STUDIES ON IRIDIUM(I), RHODIUM(I) AND RUTHENIUM(II) METALLOCAVITANDS DERIVED FROM RESORCIN[4]ARENE.

Sasa Korom

Dipòsit Legal: T 1597-2015

Saša Korom

Studies on Iridium(I), Rhodium(I) and Ruthenium(II) Metallocavitands Derived from Resorcin[4]arene

DOCTORAL THESIS
Supervised by Prof. Dr. Pablo Ballester Balaguer

UNIVERSITAT ROVIRA I VIRGILI

Tarragona 2015

UNIVERSITAT ROVIRA I VIRGILI

DEPARTAMENT DE QUIMICA ANALITICA I QUIMICA ORGANICA

C/ Marcel.lí Domingo s/n
Campus Sescelades
43007 Tarragona
Tel. 34 977 55 97 69
Fax 34 977 55 84 46
e-mail: secqaqo@urv.net

ICIQ
Institut Català d'Investigació Química

Prof. Dr. PABLO BALLESTER BALAGUER, Group leader at the Institute of Chemical Research of Catalonia (ICIQ) and Research Professor of the Catalan Institution for Research and Advanced Studies (ICREA), CERTIFIES that the present work entitled "Studies on Iridium(I), Rhodium(I) and Ruthenium(II) Metallocavitands Derived from Resorcin[4]arene" contains the research work carried out by Saša Korom under his supervision in his research group at the ICIQ and fulfils all requirements to be eligible for the Doctorate Award.

Tarragona, 13 April 2015.

Doctoral Thesis Supervisor

Prof. Dr. Pablo Ballester Balaguer

Somewhere, something incredible is waiting to be known.
- Carl Sagan -

The good thing about science is that it's true whether or not you believe in it.
- Neil deGrasse Tyson -

The science of today is the technology of tomorrow.
- Edward Teller -

ACKNOWLEDGEMENTS

The growing interest towards supramolecular chemistry stems back to a bioorganic chemistry lecture (4th year of undergraduate studies at University of Novi Sad, Serbia) presented by Prof. Velimir Popsavin demonstrating the assembly mediated bond formation by assembler (parent) molecule **A** and components **B** and **C** in a simple synthetic self-replicating system (see the reaction scheme below). In the first stage molecule **A**, using molecular recognition (through hydrogen bonds), brings carboxylic (component **B**) and amine (component **C**) functions of two molecules in sufficient proximity to initiate a reaction between them. Upon amide bond formation, **molecular replica** dissociates and is ready to enter in a new reaction cycle together with its parent molecule (**A**).

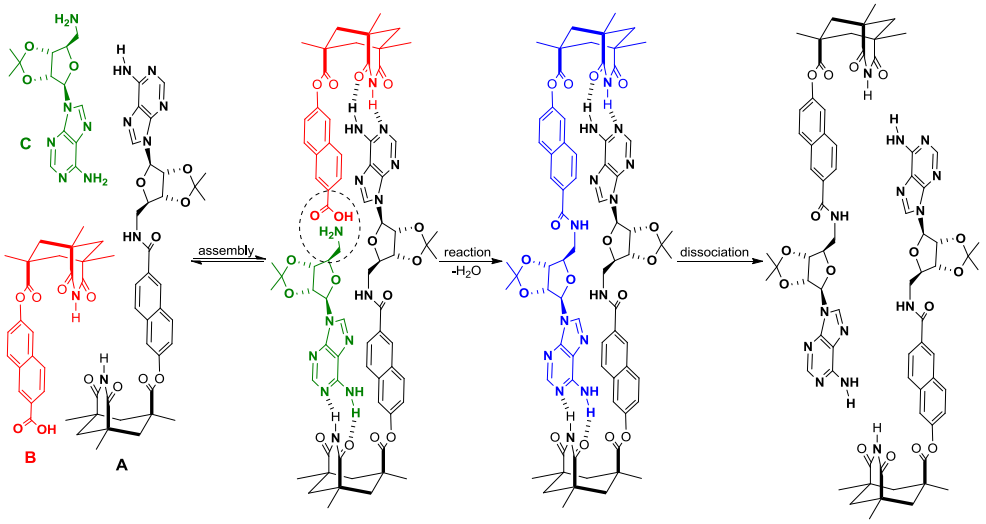

Although, at that point of time, the limited access to literature prevented me from accessing the full paper, the principle of self-replication remained in my mind sparking my interest in pursuing PhD studies in the field of supramolecular chemistry. In March 2011, Prof. Pablo Ballester gave me that opportunity by admitting me to his research group at Institute of Chemical Research of Catalonia (ICIQ). Just a few months later, ICIQ hosted the *11th International Conference on Calixarenes - Calix 11*, where I had an opportunity to listen and meet Prof. Julius Rebek, who was the principal investigator of a paper that inspired me. This event made me revisit the publication (*J. Amer. Chem. Soc.*, 1990, **112**, 1249-1250), and to my pleasant surprise I realized that the second author on the paper was actually my supervisor, Prof. Ballester, which was an amazing coincidence. Prof. Ballester is an excellent lecturer with deep understanding of supramolecular systems. His passion for science and profound didactic skills helped me understand and significantly expand my knowledge of these molecular systems, especially by assigning me research with the focus on characterization, binding and catalytic studies on metallocavitand systems. I would like to sincerely thank Prof. Ballester for this opportunity, his patience and willingness to guide me into the amazing world of supramolecular systems.

Of course, my studies and life in Tarragona would not be as amazing without my labmates sharing our everyday life and science challenges at lab PB4. I would like to use this unique opportunity to thank all past and current group members for their contribution to my life and research by naming them here: Louis Adriaenssens, Marcos Chas Pedreira, Inmaculada Pintre Gallego, Virginia Valderrey Berciano, Moira Ciardi, Mónica Espelt Ripoll, Gemma Aragay, Albano Galán, Nelson Giméz, Frank Antonio Arroyave, Daniel Hernández, José Ramón Romero, Martina Piccinno, Alejandro Díaz, Luis Escobar, as well as all ICIQ colleagues and summer fellows I didn't name here.

The smooth flow of research couldn't be imagined without the assistance of ICIQ's research support people, who I would like to sincerely thank here: Nuclear Magnetic Resonance Unit: Dr. Gabriel González, Germán Gómez and Israel Macho; High Resolution Mass Spectrometry Unit: Dr. Noemí Cabello, Sofía Arnal and Vanessa Martínez; Spectroscopy and Kinetics Unit: Dr. Fernando Bozoglian, Alexandre Cabré and Idoia Martí; Chromatography, Thermal Analysis & Electrochemistry Unit: Simona Curreli, Laura Ferreres and Maria José Hueso; X-Ray Diffraction Unit: Dr. Jordi Benet, Eduardo Carmelo Escudero, Dr. Marta Martinez and Dr. Eddy Martin; Chemical Reaction Technologies Unit: Dr. Marta Giménez, Dr. Yvette Angela Mata and Cristina Rivero. For helping me to put into reality schematics of my custom labware designs, I would like to thank: Xavier Asensio from ICIQ Glass-blowing Workshop and José Luis León from ICIQ Mechanical Workshop. I would like to thank the whole ICIQ management team whose work contributed to the quality and smooth flow of everyday ICIQ functioning.

I owe special thanks to Prof. Atsushi Urukawa for his help in attempt of getting Far InfraRed spectra, as well as, to Prof. Arjan W. Kleij, Prof. Antoni Llobet and Prof. Piet van Leeuwen for research related advices and ideas. I would also like to thank Samuel Drouet for his help in getting DPVs of my organometallic complexes and metallocavitands.

Special thanks also to our group assistant Beatriz Martín Valero for her help in all the tedious paperwork and assistance when I arrived in Tarragona and during the whole period of my studies. I would like to thank other group assistants who helped me in some way as well.

I also thank to Prof. Shannon M. Biros from Chemistry Department of the Grand Valley State University (Allendale, MI, USA) and Dr. Gemma Aragay (ICIQ) for their assistance in proofreading this thesis.

Very special thanks to my family for their constant support. Želeo bih da se najsrdačnije zahvalim mojim roditeljima, pokojnom ocu Peteru, majci Jovanki i bratu Peteru na stalnoj podršci tokom doktorskih studija u Španiji. I owe special thanks to Наталья Хоменко for her everyday support, especially during the last few months of hard work on my thesis. And not to forget, I would like to thank to all my friends in Serbia, Hungary and world-wide for their support.

This research would not be possible without funding, thus, I would like to express my sincere gratitude for financial support to: Ministerio de Economía y Competitividad (MINECO) through project CTQ2011-23014 and Severo Ochoa Excellence Accreditation 2014-2018 (SEV-2013-0319), the Generalitat de Catalunya DIUE (2009 SGR 6868), and the ICIQ Foundation in providing financial support for my scholarship and stipend during all four years of my studies at ICIQ.

The author

Table of Contents

Thesis outline

Aims of thesis

The interest of our group, when it comes to cavitand chemistry, is to direct their advancement towards more elaborated structures containing transition metals, which in turn can offer new exciting capabilities intrinsic to that metal. This can include specific geometric organization of ligating molecules around the metal center producing unique molecular motifs, or adding binding and/or catalytic capabilities to the system. Transition metals often operate between several oxidation states, which is another attractive feature begging to be explored and exploited. In the catalytic sense, coordination to transition metal(s) opens a repertoire of chemical transformations. Among other features, metal complexes can take a part in producing: self-assembly systems, self-healing materials and molecules with photo-switching or conducting capabilities.

The goal of our research was the design of new metallocavitand systems based on *d*-transition metal complexes involving iridium, rhodium and ruthenium. As cavitand framework, we selected existing non-functionalized cavitands and devised new monofunctionalized cavitands able to coordinate metals in some fashion. Our designs used three major strategies for the metal incorporation:

- Inclusion of a metal center within a supramolecular container,[1,2,3,4]
- Ligand-template directed assembly,[5]
- Direct coordination of added ligating function to the metal complex.[6,7]

Inclusion of the metal center within a supramolecular container takes advantage of cation-π interactions as the main stabilizing force between the host and the guest (cationic metal complex). Moreover, the size and the shape complementarity between the host cavity and the metal complex guest have to be taken into consideration when designing these systems.

Ligand-template directed assembly is another attractive strategy where the guest molecule, i.e. a metal center equipped with a sufficient number of donor ligands for coordination acts as a template for the assembly of the container and stays enclosed with the possibility of acting as a catalyst with the remaining coordination site, often hindered by surrounding ligands.

Direct coordination of added ligating functions to the metal center, often referred to as coordination through the first sphere, can be regarded as the formation of classic coordination compounds. It is important to note that ligating groups are often modifiers of the metal centers displaying features not shown by the naked metal or a metal ion.

Combination of these assembly strategies can offer a higher levels of cooperativity often referred to as an amplification effect.[8]

The main objectives of our research can be divided in three major areas:

- Design, synthesis and characterization,
- Binding studies, and
- Catalytic studies.

The design of a new cavitand molecule requires a thorough literature search to evaluate feasible structures with the adequate properties to fulfill the pursued goal. Molecular modeling is an important tool for the evaluation of structural congruity of the host as well as in prediction of the most appropriate structure of the guest/substrate molecule in terms of binding and/or proper orientation towards host's catalytic site. Once synthesized, cavitand molecule is thoroughly characterized in order to extract information about their true natures (sometimes contrasting theoretical predictions).

Binding properties of a cavitand as a host species is an important aspect of a structure which studies can help to pave a path towards possible applications (e.g. as a receptor/sensor, as a catalyst, etc.). Binding parameters are often obtained as thermodynamic and kinetic information through various titration experiments (NMR, UV/Vis, ITC) or VT ^{1}H NMR studies.

Catalytic studies can represent a possible important final application of the designed cavitand with significant interest for the scientific and industrial community. Since there are only few examples in the literature for the cavitand based catalytic systems,[7,9,10,11,12] these studies are still in a fledging stage and of vital fundamental importance in understanding how they work.

We believe that our modest contribution will spark scientific community and promote new ideas for further research in this branch of science.

Thesis content

The thesis is divided into four major chapters and appendix:

Chapter 1 introduces the reader to historically relevant details, such as the "birth" of cavitands and the pathways of their evolution towards receptors, molecular containers and catalysts.

Chapter 2 is the extension of our earlier studies, utilizing octaamide cavitand (**C5**) as a second-sphere ligand to coordinate Ir^{I}•COD based organometallic complexes, with the idea of studying the nature of the system and the attempt to use it as a catalyst. Unexpected behavior of the included organometallic complex led our research into a different direction, towards phenomena of supramolecular isomerism.

Chapter 3 is inspired by the same work as **Chapter 2** but with the aim to address metal leakage issues observed in the previously reported system during catalytic hydrogenation reaction. Research included modification of a single cavitand wall with the pyridyl functionality (known to weakly bind to Rh^{I} complexes) in order to increase thermodynamic stability of caviplex and prevent metal leakage during catalytic hydrogenation of norbornadiene.

Chapter 4 deals with a completely new cavitand design based on a terpyridine moiety fused onto the single cavitand wall. Fused tridentate terpyridine function is then metallated with the $RuCl_3$ to produce an organometallic complex and in a subsequent reaction reduced to Ru^{II} and coordinated to 2-(phenylazo)pyridine ligand. The first coordination sphere, occupied by a chloro ligand, was exchanged with an aqua ligand. The system was characterized and studied in terms of catalytic capabilities in epoxidation of alkenes and oxidation of choline-like alcohols.

Appendix contains information about synthetic procedures utilized for synthesis of the base cavitand frameworks.

References and notes

[1] D. Ajami, M. P. Schramm, A. Volonterio and J. Rebek, *Angew. Chem., Int. Ed.*, 2007, **46**, 242-244.
[2] M. A. Sarmentero and P. Ballester, *Org. Biomol. Chem.*, 2007, **5**, 3046-3054.
[3] E. Zuidema, M. A. Sarmentero, C. Bo and P. Ballester, *Chem.--Eur. J.*, 2008, **14**, 7285-7295.
[4] M. A. Sarmentero, H. Fernández-Pérez, E. Zuidema, C. Bo, A. Vidal-Ferran and P. Ballester, *Angew. Chem., Int. Ed.*, 2010, **49**, 7489-7492.
[5] A. W. Kleij and J. N. H. Reek, *Chem.--Eur. J.*, 2006, **12**, 4218-4227.
[6] K. Bowman-James, *Acc. Chem. Res.*, 2005, **38**, 671-678.
[7] K. E. Djernes, O. Moshe, M. Mettry, D. D. Richards and R. J. Hooley, *Org. Lett.*, 2012, **14**, 788-791.
[8] M. Roman, C. Cannizzo, T. Pinault, B. Isare, B. Andrioletti, P. van der Schoot and L. Bouteiller, *J. Am. Chem. Soc.*, 2010, **132**, 16818-16824.
[9] C. Gibson and J. Rebek, *Org. Lett.*, 2002, **4**, 1887-1890.
[10] A. Gissot and J. Rebek, *J. Am. Chem. Soc.*, 2004, **126**, 7424-7425.
[11] S. Richeter and Rebek, *J. Am. Chem. Soc.*, 2004, **126**, 16280-16281.
[12] F. H. Zelder and J. Rebek Jr, *Chem. Commun.*, 2006, 753-754.

CHAPTER 1: From resorcinol to functionalized supramolecular structures

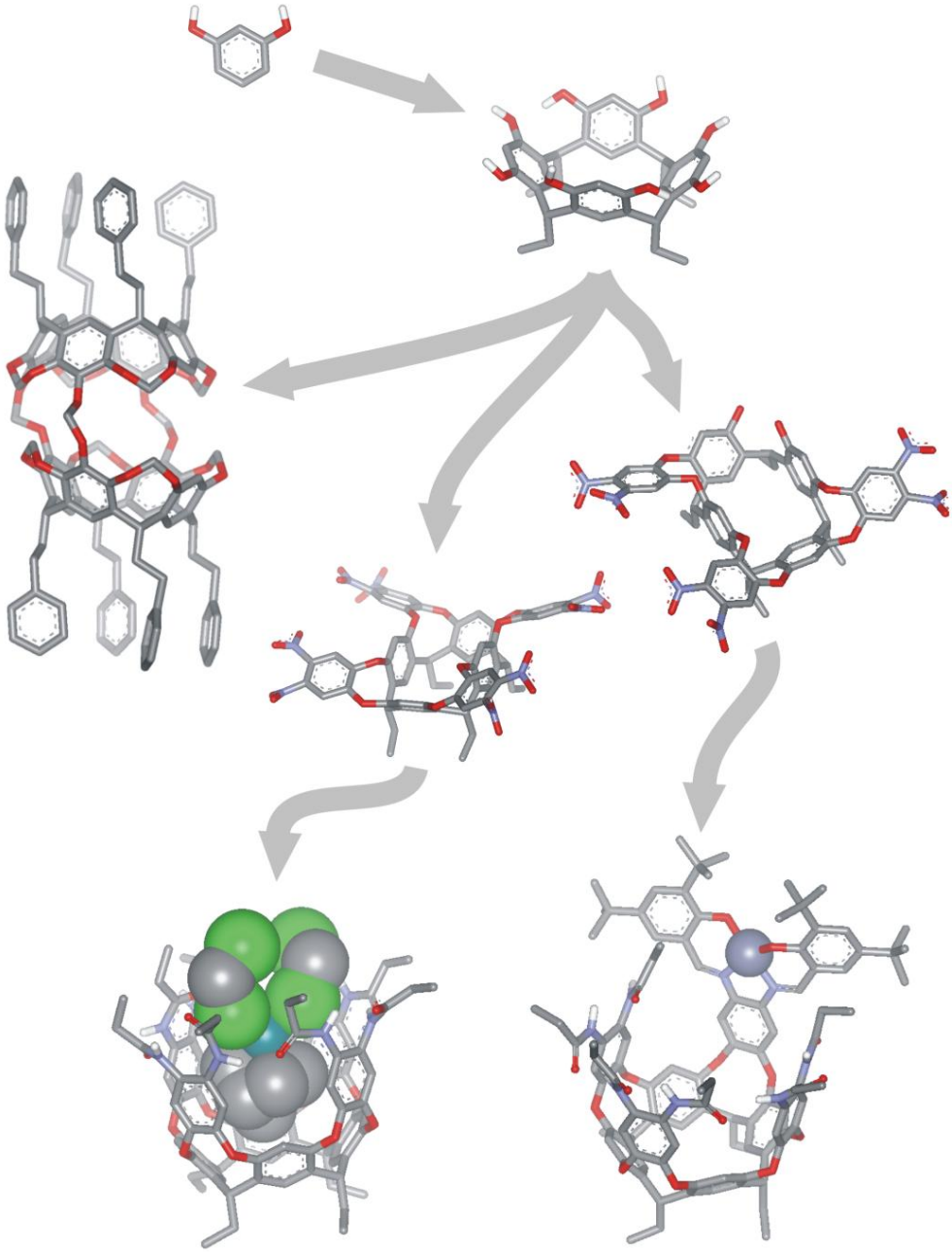

1.1 Discovery and structure elucidation

Great discoveries often come unexpected, and that's how the cavitand story begun. Although his expertize was synthesis of naturally occurring dye indigo and carbocyclic ring compounds, curiosity and delving into the unknown led the great organic chemist and Nobel prize awardee (1905) J. F. W. Adolph von Baeyer into acid catalyzed phenol-formaldehyde chemistry where he reported the formation of resin-like compounds. Since the condensation product lacked the dye properties he was looking for, Baeyer decided not to pursue any further characterization and simply concluded that he obtained the 1:1 condensation product.[1,2,3] A decade later, Michael reinvestigated the acid catalyzed reaction between benzaldehyde and resorcinol and determined the correct elemental composition of a high-melting point, crystalline product.[4] However, since at that time there were no means of estimating the molecular weight, he suggested a rather improbable structure shown in **Fig. 1**.

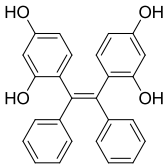

Fig. 1. Michael's proposal for the product of the acid catalyzed condensation of benzaldehyde and resorcinol.

In 1892, Caro assigned the dimeric structure to the product obtained by the acid-catalyzed condensation of resorcinol and formaldehyde, but the non-crystalline and refractory character (decomposes at 250 °C without melting) suggested that the compound had polymeric nature.[5] A few more similar experiments were carried out,[6,7,8,9,10] until Niederl and Vogel, using aliphatic aldehydes in acid-catalyzed condensation with resorcinol, determined the molecular weight for the obtained products and proposed the cyclic tetrameric structure shown in **Fig. 2**.[11]

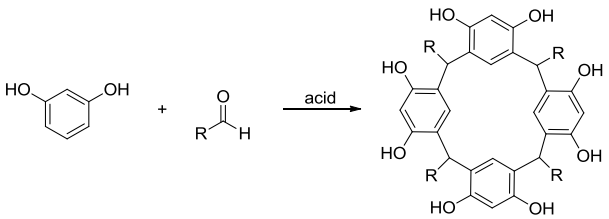

Fig. 2. Acid catalyzed condensation of resorcinol and an aldehyde.

Erdtman *et al.*[12] further corroborated these structures by mass spectrometry while Högberg investigated their stereoisomerism.[13,14] Cram *et al.* found that among several possible diastereoisomeric forms of octol (resorcin[4]arene) only one holding C_{4v} symmetry (**Fig. 3**, line drawing structure) was isolated,[15,16] and was further corroborated with solid state crystal structures.[17,18]

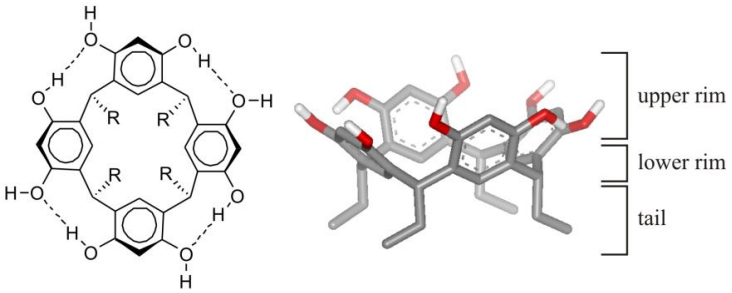

Fig. 3. Line drawing (left) and solid state (right) structures of a resorcin[4]arene. Hydrogen bonds in line drawing structure are represented as dashed lines. Nonpolar hydrogen atoms are omitted for clarity.

1.2 Structural modifications of resorcin[4]arenes

Conformational immobilization of resorcin[4]arenes was achieved by bridging OH groups of neighboring aryl rings producing convex molecules which Cram named *cavitands*. Cram defined them as *a class of synthetic organic compounds that contain enforced cavities large enough to accommodate simple organic molecules or ions*.[15,19] He introduced some terms as *the upper rim*, assigned to a wider opened part of the structure, and *the lower rim*, assigned to a narrow closed part of the structure (**Fig. 3**, solid state structure). The *lower rim* contains groups referred to as *tails* located on the methine bridges which originate from the aldehyde used in condensation reaction (**Fig. 3**, R groups in the line drawing structure and ethyl group in the solid state structure).

Chemical groups present on the *tails* can provide cavitands with: an ability to either covalently[20,21] or by non-specific interactions[22,23] attach to a solid surface; to become a starting point for divergent dendronization;[24] to increase the solubility in polar[25,30] or nonpolar solvents;[28,31] to add the redox capabilities;[40] etc.

Numerous reports testify the great efforts dedicated towards the use of different aldehydes to afford different lower rim functionalization, often requiring the optimization of the reaction conditions.[25,26] Among countless examples of used aldehydes, the most common include: (a) simple aliphatic aldehydes from ethanal to undecanal[27,28,29]; (b) functionalized aliphatic aldehydes such as 5-chloropentanal,[15] 4-hydroxybutanal,[30] and 2-sulfonatoethanal;[31] (c) aryl aldehydes such as phenylethanal;[15] (d) unsaturated aliphatic aldehydes such as 9-decenal;[25] (e) benzaldehydes, including those with substituents such as alkyl or arylalkyl,[32] OH,[33,34] NO_2,[35] halogen,[15] CN,[15] NH_2,[36] $B(OR)_2$,[37] crown ether[38] and glycosyl;[25] (f) heterocyclic aldehydes;[39] (g) ferrocenylaldehyde,[40] and others.

When *the upper rim* of the cavitand is bridged with aromatic molecules (e.g. quinoxaline, benzene, pyrazine) in order to increase its depth, these aromatic groups are

often referred to as *walls* or *panels*. Studies by Cram *et al.*[15] showed that cavitand structures containing aromatic *walls* (such as quinoxaline) can exist in two conformations referred to as *the vase* and *the kite* (**Fig. 4**). These conformations are found to play a key role in the guest binding process (also referred to as *host/guest formation* or *inclusion*), as well as, during the chemical exchange process with the same or different guest molecules present in the free form in solution.

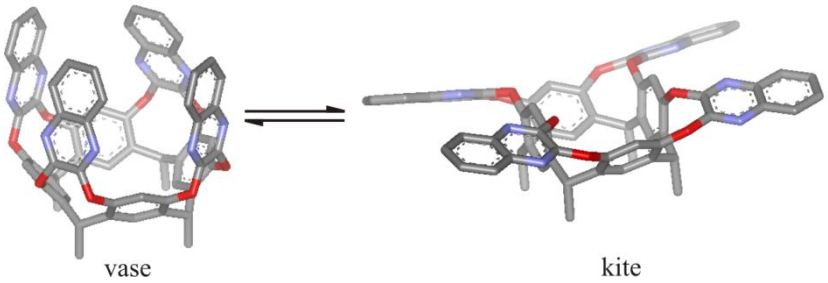

Fig. 4. Conformational change from vase to kite for quinoxaline-bridged cavitand.[41]

Moreover, Cram *et al.* converted *cavitands* into even more complex, spherically shaped structures, which he named *carcerands*.[42]

The extraordinarily complete and wide-range investigation of these structures presented the base for the 1987 Nobel Prize in Chemistry awarded to Donald Cram[43] and shared with Charles Pedersen[44] and Jean-Marie Lehn.[45]

1.3 Molecular recognition

When two atoms share their valence electrons in order to achieve a stable electronic configuration, the sharing of electrons is referred to as covalent bond.[46] There are two types of covalent bonds: nonpolar, established between two atoms with equal and polar established between two atoms with unequal electronegativity. The coordination bond (referred to as dipolar or dative-covalent bond) is a special case where one atom shares two electrons with the other atom in order to achieve a stable electronic configuration.

When two molecules approach each other in space, they can establish one or more intermolecular interactions. These interactions are weaker than covalent bonds and can be classified into three major groups (**Fig. 5**):[46,47]

- Van der Waals interactions: induced dipole – induced dipole (London dispersion force), induced dipole – dipole (Debye force) and dipole – dipole (Keesom interaction);

- Ion – induced dipole and ion – dipole interactions;
- Hydrogen bonding (also referred to as a strong electrostatic dipole – dipole interaction).

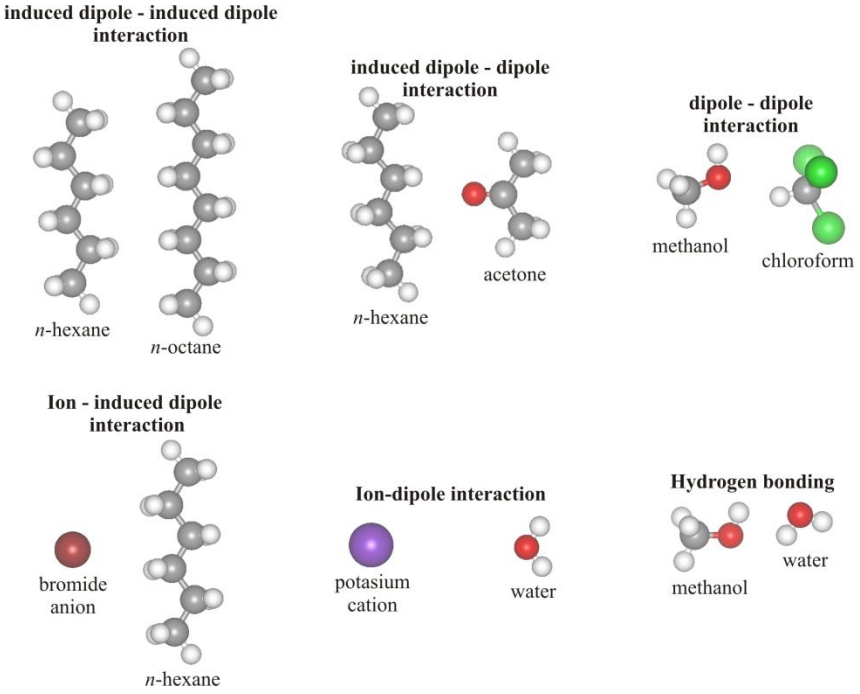

Fig. 5. MM3 energy-minimized examples of the intermolecular interactions. All molecules are presented as scaled balls and sticks.

In the biological systems, molecular recognition plays an essential role in: self-replication, information processing and metabolism.[48] Molecular recognition occurs largely by specific interactions between biological molecules.

The idea that molecular recognition lies in the complementarity of interacting surfaces was first time described by Emil Fischer, who proposed that the enzyme and the substrate fit together like *lock and key*.[49] A modern view on molecular recognition, namely *induced fit model*, represents an improvement of the *lock and key model* and takes into account that the interacting molecules are flexible and that host molecule can change shape during the recognition process.[50]

Molecular recognition applied in synthetic systems started in 1967 when Pedersen reported about stoichiometric complexes of ammonium salts with crown ethers in solution.[51] Among the most important weak interactions exploited by artificial systems are: H bonding,[52,53] π-π (often referred to as π-π stacking),[54] CH-π,[54] cation-π[55] and anion-π[56,57,58] interactions.

Lehn defined molecular recognition as *the energy and the information involved in the binding and selection of a substrate, by a given receptor molecule, which might also involve a specific function*.[45] He stated that mere binding is not recognition, although it is often taken as such. Lehn also stated that *the recognition process implies binding through a structurally well-defined set of intermolecular interactions and which is characterized by its kinetic and thermodynamic stability and selectivity*.[45,59,60]

The first evidence for the host/guest complex formation between a lipophilic resorcin[4]arene and neutral polar molecules of biological origin in apolar media was provided by Aoyama *et al.* in 1988.[28,29] They showed the ability of resorcin[4]arene to extract polar carbon hydrates, vitamins and hemin from a neat or a polar phase into a nonpolar phase by establishment of hydrogen bonds in the complex. In 1997, Atwood *et al.* successfully crystalized the resorcin[4]arene from hot nitrobenzene and demonstrated spontaneous self-assembly leading to formation of a discrete spherical molecular structure composed of six resorcin[4]arene units interlocked by formation of hydrogen bonds with eight water molecules and with a volume close to 1400 $Å^3$ (**Fig. 6**).[61]

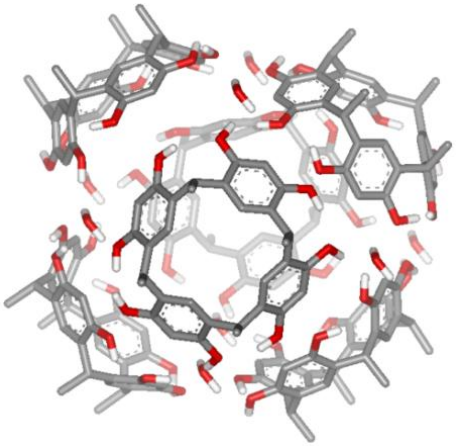

Fig. 6. Crystal structure of the hexameric assembly composed of hydrogen bond interlocked resorcin[4]arene units and water molecules. Nonpolar hydrogen atoms and guest molecules are omitted for clarity.

With the development of DOSY NMR technique, the formation of hexameric assembly was found to be responsible for the complexation of sugars in the solution.[62]

In 1989, Cram *et al.* devised a resorcin[4]arene host with a methylene bridged upper rim and showed its ability to bind an acetonitrile molecule in carbon tetrachloride medium with association constant K_a = 313 M^{-1}.[63] Variable temperature studies revealed thermodynamic parameters, yielding ΔH = -6.2 kcal mol^{-1} and ΔS = -11.4 cal mol^{-1} K^{-1}. At 273 K this gives ΔG of -3.1 kcal mol^{-1}, showing that a half of the enthalpy gain of the binding is paid for the entropic cost associated to the process.

The same year, Dalcanale *et al.* reported a crystal structure of the host/guest complex of a quinoxaline bridged resorcin[4]arene with one included acetone molecule (**C1**, **Fig. 7**). They found that C=O bond from the acetone guest is oriented in a parallel disposition to the axis of the cavity and that the two methyl groups point towards two quinoxaline walls. In these conditions, the hydrogen atoms of the methyl groups interact with the π-electrons of the quinoxaline. The attractive CH_3-π interaction has proven to be one of the driving forces responsible for the complexation of neutral molecules.[64] It was also shown that quinoxaline bridged resorcin[4]arene is able to bind aromatic guests (e.g. benzene, toluene, fluorobenzene), not only in a liquid, but also in the solid and in the gas phase.[65] The crystal structure of the complex with fluorobenzene revealed that the C-F axis is inclined 19.2° with respect to the normal reference plane and points the F atom toward the portal of the vase, a geometry guided by CH-π and π-π interactions (**C2**, **Fig. 7**).[66]

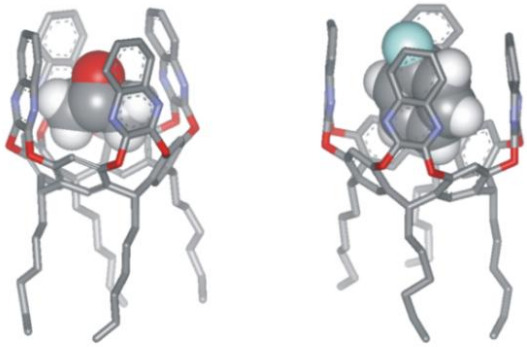

Fig. 7. Crystal structures of complexes **C1** and **C2**. Hydrogen atoms are omitted for clarity. Guest molecules are presented as CPK models.

Size and shape selectivity in cavitand systems has been well documented by Rebek *et al.* who did a wide-range inclusion studies involving 27 guest molecules.[67] They showed that complexing properties of a molecular capsule can be estimated based on the packing coefficient of the guest in the internal cavity of the host. They found out that the best binding is reached when the packing coefficient (the ratio of the guest volume to the host cavity volume) is in the range of 0.55 ± 0.09, which corresponds to the packing coefficient of most organic liquids. They also proposed that the same rule can be applied in the binding of substrates in natural biological systems. Of course, exceptions to this rule can be found in the literature. For example, Rebek *et al.* described a system based on an extended resorcin[4]arene capsule[68] and a similar self-assembled system[69] that showed packing coefficient values as high as 0.79,[70] comparable to those in the solid state.[71] The rationale for such a high packing coefficient in the case of pyrazine-imide bridged resorcin[4]arene (**Fig. 8**), lies in three important features: 1) the high congruency between capsular host, [2.2]-paracyclophane as a guest and bromotrichloromethane acting as a co-guest; 2) dipole - dipole attractive forces between electron-rich outer surface of the [2.2]-paracyclophane's aromatic rings and electron-deficient surfaces of the pyrazine-imide walls; and 3) presence

of eight bifurcating hydrogen bonds established between the two cavitand units that hold up the whole assembly and compresses the included guest and co-guest molecules.

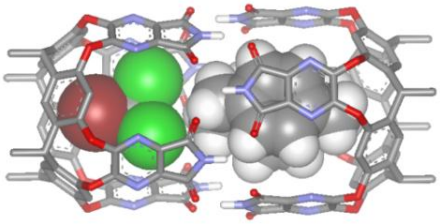

Fig. 8. Energy-minimized structure of the host/guest complex composed of a capsular host comprised of two pyrazine-imide bridged resorcin[4]arene cavitands with included [2.2]-paracyclophane as a guest and bromotrichloromethane as a co-guest. Nonpolar hydrogen atoms of a capsule are omitted for clarity. Guest and co-guest molecules are presented as CPK models.

1.4 Motional dynamics within the confined space

In 1991, Cram *et al.* worked with the carcerand **H1** (**Fig. 9**) and decided to explore the physical effects of the unique inner space (the cavity) on small incarcerated molecules.[72] They predicted that this environment would differ significantly from those imposed by the bulk solvent.

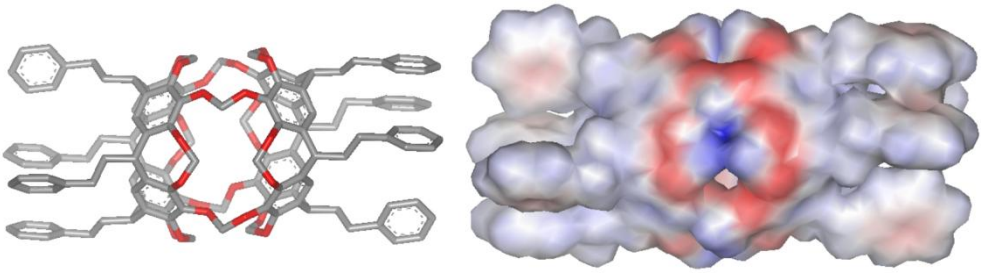

Fig. 9. Solid state structure of the carcerand **H1** presented as a stick model (left) and as an electrostatic map limited by Van der Waals radii (right). Hydrogen atoms in the stick model and the included guest in both models are omitted for clarity.

Using dynamic ^{1}H NMR experiments, they obtained rotational barriers of small molecules such as *N*,*N*-dimethylformamide and *N*,*N*-dimethylacetamide included within carcerand **H1** in nitrobenzene solution. In the case of incarcerated *N*,*N*-dimethylformamide, they found that the coalescence of two CH_3 resonances occurred at 140 °C and gave the free energy of activation ($\Delta G^{\ddagger}$) of 18.9 kcal mol^{-1}, while for *N*,*N*-dimethylformamide free in solution coalescence happened at 120 °C, corresponding to $\Delta G^{\ddagger}$ of 20.2 kcal mol^{-1}. The coalescence temperature for CH_3 groups in *N*,*N*-dimethylacetamide free in solution was at 63 °C ($\Delta G^{\ddagger}$ = 18 kcal mol^{-1}), while for the incarcerated molecule coalescence occurred at 190 °C ($\Delta G^{\ddagger}$ = 20.3 kcal mol^{-1}). To explain the lower energetic rotational barrier for the incarcerated *N*,*N*-dimethylformamide the results were fitted with C-N rotational barriers of

amides, which decrease in the order: polar solvents > nonpolar solvents > gas phase. By fitting *N*,*N*-dimethylformamide results in stated correlation they found that barrier of the rotation around C-N bond decreases in the order: polar solvent > carcerand inner phase > vacuum. Molecular modeling of *N*,*N*-dimethylformamide incarcerated in **H1** showed that the carcerand's inner phase has some characteristics of a vacuum and guest occupation of volume, leaving rotational parts of the guest less encumbered by the sides of container compared to the bulk solvent (nitrobenzene). In contrast, molecular modeling of *N*,*N*-dimethylacetamide in **H1** can barely be assembled due to compression of the container sides against the guest parts. Furthermore, $(CH_3)_2N$- plane is 90° bent against $COCH_3$ plane, requiring more deformation in the host for rotation to happen. Thus, depending on the guest, the cavity of the carcerand can be designed to be vacuum-like, liquid-like or even solid-like.

When the upper rim of resorcin[4]arene is bridged by four aromatic walls, each containing two amide groups, a new class of deep cavitands is obtained (**Fig. 10**).[73]

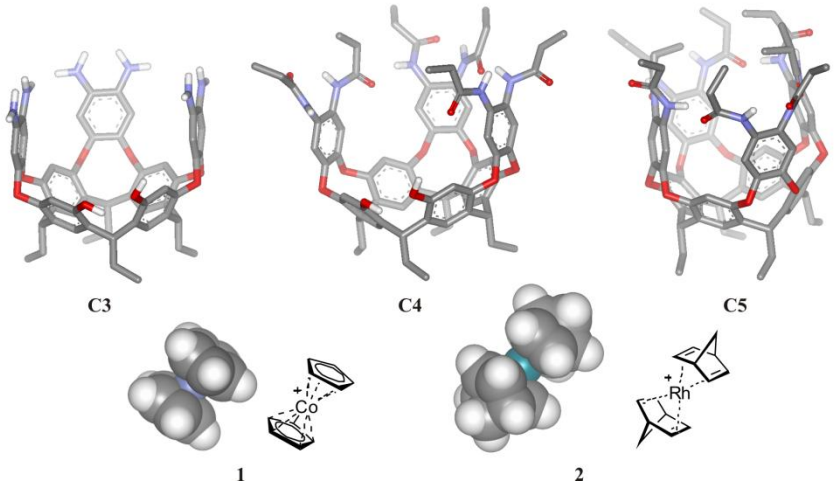

Fig. 10. Energy-minimized structure of cavitand **C3**, cobaltocenium cation **1** and Rh^{I}•$(NBD)_2$ cation **2**; solid state structures of cavitands **C4** and **C5**. Hydrogen atoms and guest molecules of cavitands are omitted for clarity. Guest molecules are presented as CPK and as line drawing models.

In 2006, Ballester *et al.* became interested in hexaaminediol cavitand **C3**,[74] previously synthesized by Rebek *et al.* as an intermediate species that was never studied in depth.[75] The scoop-like interior of the cavitand **C3** was shown to complex positively charged species, such as tetramethylammonium cation, with a high association constant (K_a = 5.1 x 10^5 M^{-1} in methanol).[74] Ballester *et al.* was also interested in the binding studies of cavitands **C3** and **C4** with organometallic complexes, such as cationic cobaltocenium (**1**) and their alkylated derivatives.[76,77] Metallocene caviplexes showed high association constants ranging from 10^3 to 10^5 M^{-1} in methanol. These high association constants were attributed to the combination of the three forms of stabilizing interactions: cation-π, CH-π and π-π. Reduction to cobaltocene weakened the binding by two orders of magnitude, due

to elimination of cation-π interactions. EXSY NMR experiments revealed that all used metallocenes and their alkylated derivatives tumble fast (on the ^{1}H NMR timescale) within the cavitand interior even at 200 K. In a later study, elongated Rh^I•$(NBD)_2$ cation (**2**) was included into a symmetrical octaamide cavitand **C5**. EXSY studies showed cross-peaks between both, upper and lower, norbornadiene ligands of included cation **2**, indicating tumbling slow on the ^{1}H NMR timescale (k_{exch} = 0.4 s^{-1}, ΔG = 18 kcal mol^{-1}).[78]

1.5 Emergence of idea of cavitands as reaction vessels

Thanks to the prolific mechanistic studies on enzymes by Frank H. Westheimer,[79,80,81,82,83,84] in early 1970 a new area of bioorganic chemistry emerged related to enzyme mimicry. Cyclic tetrameric structures (molecular baskets) appeared to the best candidates for this purpose due to the resemblance to the enzyme hydrophobic pockets. The basic idea of enzyme mimicry was to construct a synthetic receptor for a substrate molecule and equip it with appropriate functional groups for interacting with the substrate molecules. The recognition event would bring reactive groups in close spatial proximity that would facilitate product formation followed by dissociation from the cavity and catalyst recovery (**Fig. 11**).[85]

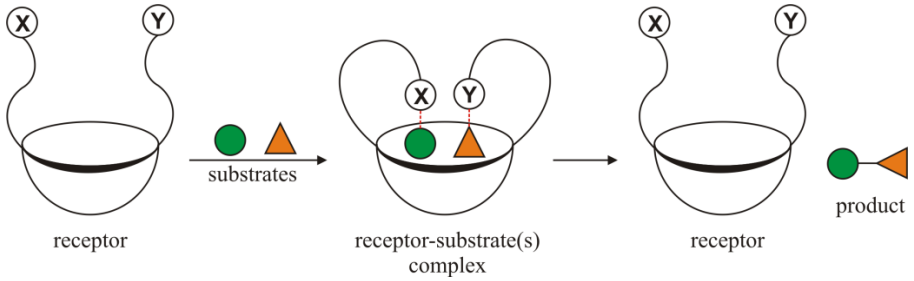

Fig. 11. Schematic representation of the enzyme mimicry by functionalized molecular basket.

1.6 Carcerands and hemicarcerands as reaction vessels

Prior to cavitand based catalytic studies, dimeric structures, carcerands and hemicarcerands, found an application as reaction vessels. Unlike carcerands, which offered almost permanent enclosure of the guest molecules, the hemicarcerands lacked one bridge, connecting two cavitand units. As a consequence, the absence of the fourth bridge created a portal that allowed easier guest/substrate exchange (**Fig. 12**, structures).

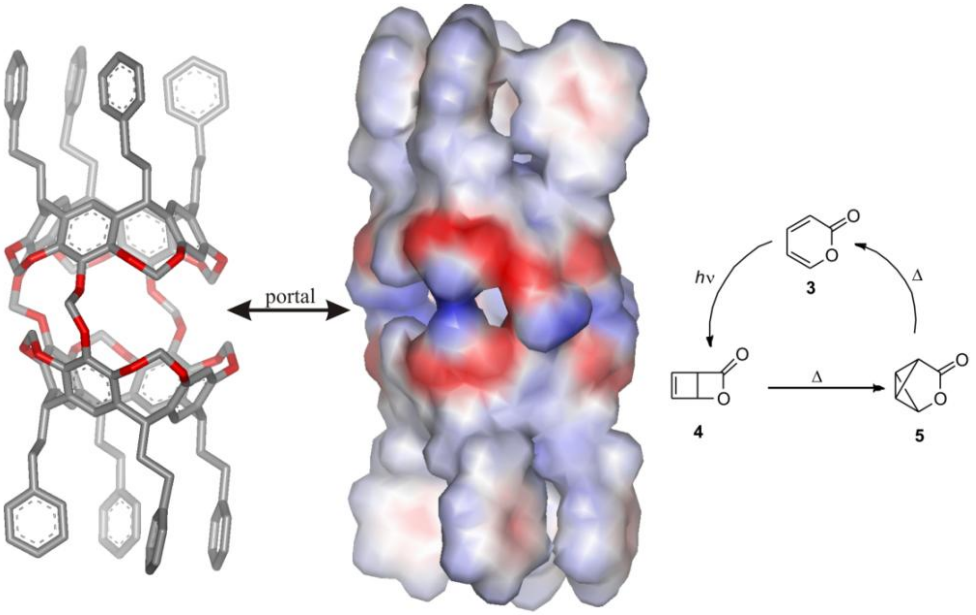

Fig. 12. Solid state structure of the hemicarcerand **H2** presented as a stick model (left) and as an electrostatic map limited by Van der Waals radii (middle); scheme of photochemical/thermal interconversions of α-pyrone **3** (right). Hydrogen atoms in the stick model and the guest molecules in the both models are omitted for clarity.

In the following text two earliest examples of cavitand based reaction vessels are briefly presented.

In 1964, Corey *et al.* reported the photochemical conversion of α-pyrone **3** to rearranged lactone **4**, which when heated gave a new lactone **5** (**Fig. 12**, reaction scheme).[86,87] Lactone **5** can be converted back to starting α-pyrone **3** by vacuum flash pyrolysis at 600 °C.[88,89]

When irradiated (75 W xenon arc lamp fitted with a filter for $\lambda < 300$ nm) solution of hemicarciplex **3⊂H2** (in chloroform-*d* at 25 °C), in one hour was quantitatively converted to **4⊂H2**.[90] ^{1}H NMR spectra showed initial broad signals for the **3⊂H2** complex due to restricted motion of α-pyrone within hemicarcerand inner space, which sharpens when heated at 60 °C. Upon completion of the photochemical reaction, complex **4⊂H2** was observed, owing sharp but doubled signals. Doubling was an indication of the tight fitting of a lactone **4** within host **H2**, with a rotation that was slow on the ^{1}H NMR timescale. When hemicarciplex **4⊂H2** was heated as a solid for 17 h at 90 °C, 80% of the complex was converted to **5⊂H2**, 13% remained as **4⊂H2**, and 7% reconverted to **3⊂H2**. The formation of lactone **5** was corroborated by the disappearance of doublets corresponding to guest **4** and the appearance of new spectral signals coincident with free **5**, with host's shielding taken into account. The reaction cycle, in the cavity of the host, was completed by heating **5⊂H2** as a solid at 140 °C for 20 h, yielding starting **3⊂H2** hemicarciplex.

In 1994, Cram *et al.* reported that carcerand host **H3** (**Fig. 13**) readily incarcerates phenols **6-9**, as well as aniline **14** and nitrobenzene **15** at high temperatures producing carciplexes **guest⊂H3**, stable at temperatures lower than 100 °C, which they fully characterized.[91] They also attempted to reduce incarcerated nitrobenzene **15** and instead of getting aniline **14**, they obtained partially reduced product *N*-phenylhydroxylamine **16** incarcerated within the host **H3**.[92] Incarcerated hydroquinones **6-9** were quantitatively converted to corresponding incarcerated quinones **10-13** at 25 °C using both $Ce(NH_4)_2(NO_2)_6$-silica-gel-CCl_4 and $Tl(CF_3COO)_3$-CCl_4-CH_3OH as oxidants. When a methanol solution of SmI_2 was added to these solutions, all guests were converted back to the initial incarcerated hydroquinones **6-9**. Since the interior of carcerand **H3** was too small to accommodate substrate and reagent at the same time, they concluded that the reaction mechanism involved electron, proton and water transfer between the solution phase containing redox reagent and the inner phase of the carciplex **H3** containing the substrate molecule.

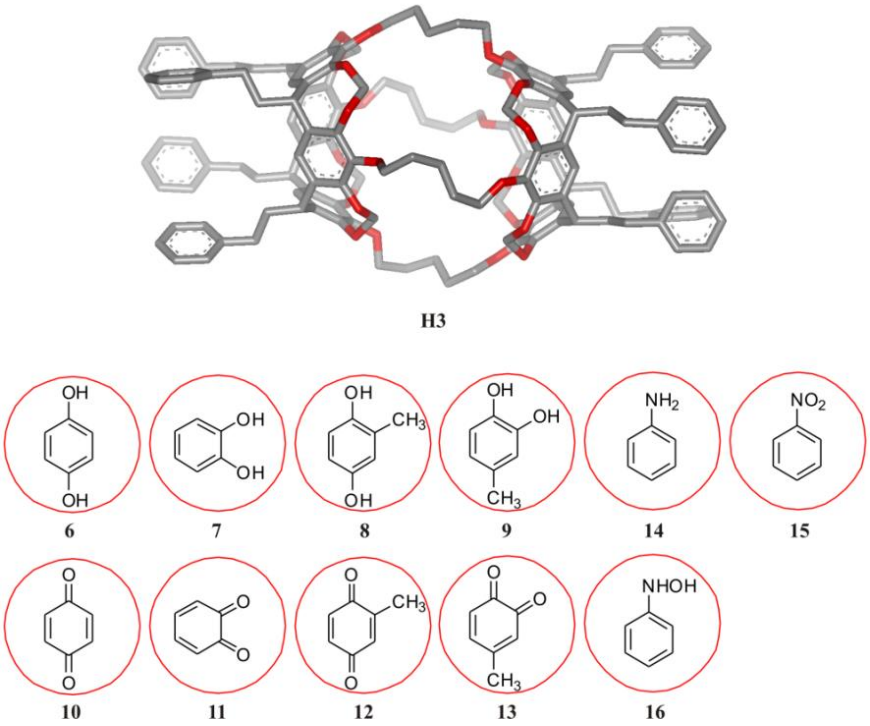

Fig. 13. Solid state structure of hemicarcerand **H3** presented as a stick model and guest (substrate) molecules. Hydrogen atoms and guest molecule in a stick model are omitted for clarity.

1.7 Cavitands as catalysts

Although molecular recognition has a long history,[93] a sizeable receptor able to completely and reversibly wrap around the guest molecule was reported for the first time in 1995 by Rebek *et al.*[94] They demonstrated size and shape selectivity towards specific guest molecules, but their structures lacked of appropriately positioned reactive functions.

It took them five additional years to develop a cavitand that was able to expose included molecule(s) to the attached catalytic group. The cavitand required for monofunctionalization was encountered by an accident, during the purification of the octanitro cavitand **C6** (**Fig. 14**). Besides cavitand **C6**, Rebek *et al.* managed to isolate cavitand **C7** which lacked the fourth wall.[95] Using the same strategy to obtain octaamide cavitand **C5** (**Fig. 10**), which involved subsequent reduction and acylation, they produced hexaamidediol cavitand **C4** (**Fig. 10**), which showed distinctive recognition characterstics.[74,76,77]

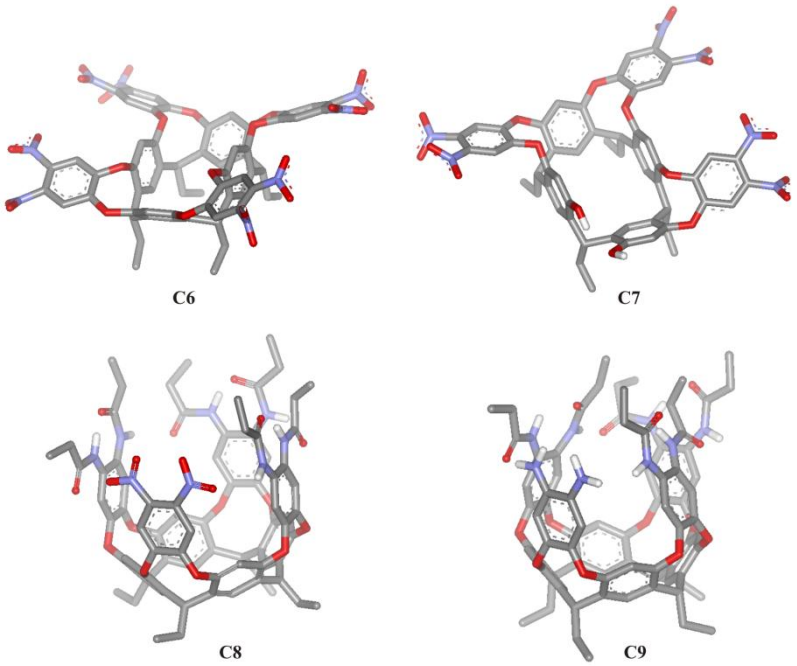

Fig. 14. Solid state structures of the cavitands **C6** and **C7** and energy-minimized structures of cavitands **C8** and **C9**. Nonpolar hydrogen atoms and guest molecules are omitted for clarity.

The addition of the fourth wall to cavitand **C4** yielded hexaamidedinitro cavitand **C8**, and in subsequent reduction gave the hexaamidediamine cavitand **C9**, a common precursor for the monofunctionalized cavitands next to the cavitand **C4**.[96] Some reported monofunctionalized cavitands include: the self-complementary structure **C10**,[95,96] (**Fig. 15**)

the introverted acid **C11**,[97] the dipyrrole **C12**,[98] the porphyrin **C13**,[99,100] the phenanthroline **C14**[101] and others.

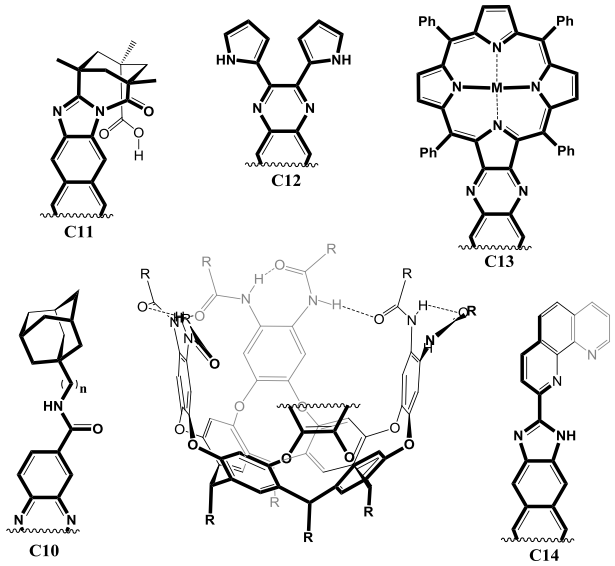

Fig. 15. Structures of cavitands **C10**-**C14**. Nonpolar hydrogen atoms are omitted for clarity.

The first example of a monofunctionalized cavitand bearing the catalytic group was reported in 2002.[102] The design was inspired by the work of Pfaltz *et al.* who reported the use of chiral ligand **21** chelated to Pd^{II} as a catalyst in allylic alkylation reactions (**Fig. 16**).[103] Palladium catalyzed reactions of monosubstituted allylic substrates (**17** or **18**) with nucleophiles, typically result in linear products (**19**).[104,105] In contrast, aryl-substituted allyl acetates (R = Ar) yield predominantly branched isomers (**20**). Inspired by this work, Rebek *et al.* developed the diphenyl-oxazoline decorated cavitand **C15** and tested it in catalysis against a model system based on the ligand **22**.

The authors expected that geminal phenyl groups positioned at the oxazoline moiety would destabilize the η^3-complex and the transition state leading to the isomer **B** (**Fig. 17**). In this way, the equilibrium would be moved towards the formation of η^3-complex **A**, with the R group oriented towards cavitand interior (CH_3-π interactions), allowing predominant formation of the linear product **19**.

Catalytic trials involving Pd^{II}•**22** and **C16** (Pd^{II}•**C15**) complexes as catalysts in alkylation of **23a**-**e** with dimethyl malonate as a nucleophile (**Fig. 18**, reaction) revealed that both systems catalyzed exclusive formation of the linear product. Contrary to ligand **22**, reaction rates varied significantly with different substrates when **C15** was employed as a ligand. Conversion of substrates **23b** and **23c** was complete in two days while rates of conversion of bulkier ones (**23d** and **23e**) were four times slower. Interestingly, rate for the smaller substrate **23a** was the lowest.

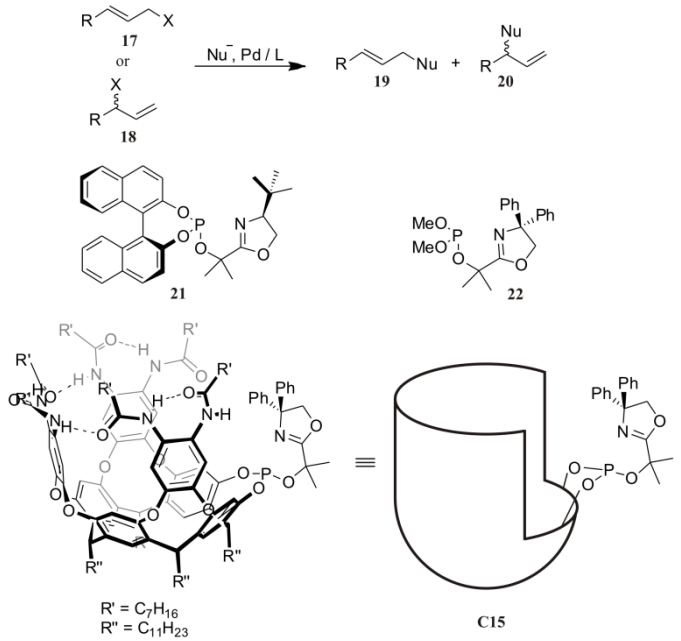

Fig. 16. Palladium catalyzed allylic alkylation (top). Structures of Pfaltz's ligand **21**, ligand **22** and cavitand **C15**. Nonpolar hydrogen atoms are omitted for clarity.

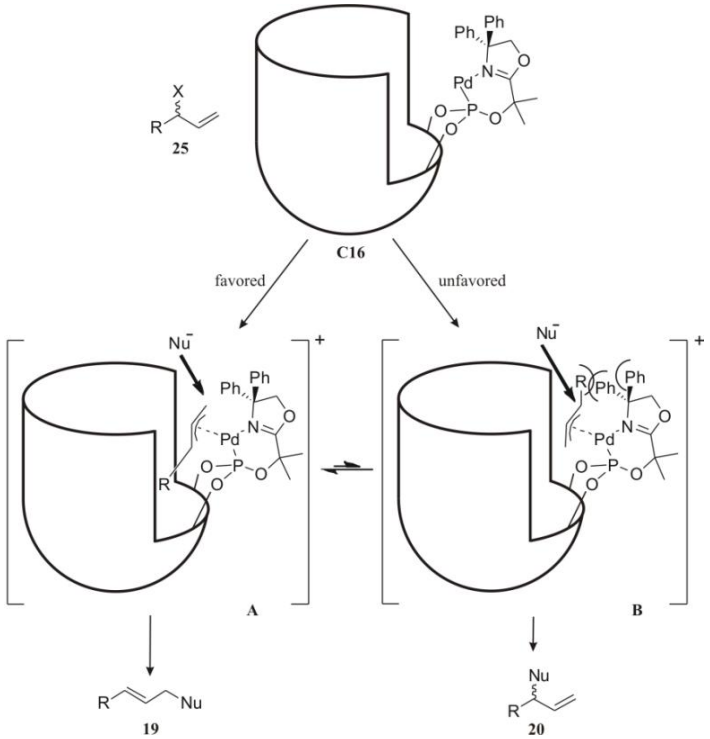

Fig. 17. Predicted nucleophilic attacks on η^3-complexes **A** and **B**. η^3-complexe **B** is shown with steric hindrances that favor an equilibrium towards formation of η^3-complexe **A** resulting in formation of the linear product **19**.

To address selectivity preferences, the set of competitive experiments was performed and obtained η^3-complexes analyzed by ESI-MS. When Pd^{II}•**22** was employed as catalyst, the ratio of intermediate species was 1:1. The lack of selectivity was explained due to the minor structural differences in the ligand **22** and both transition states with bound substrates.

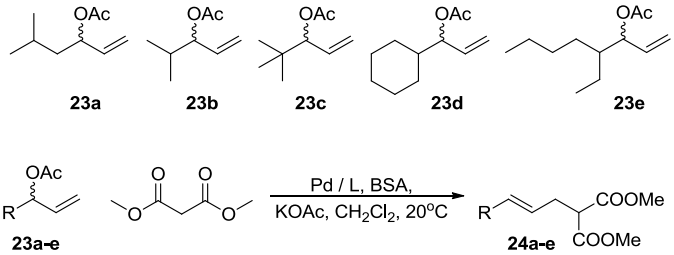

Fig. 18. Top: Substrate molecules used in alkylation catalytic studies; Bottom: Reaction with malonate as a nucleophile. BSA – *N*,*O*-bis(trimethylsilyl)acetamide.

On the contrary, the distribution of allyl η^3-intermediates for Pd^{II}•**C15** (**C16**) complexes differed significantly. They observed a clear dependence on the connectivity of the homoallylic carbon and the rate of the oxidative addition decreasing in the order: **23a** (secondary) > **23b** (tertiary) > **23c** (quaternary). To examine the ability of complex **C16** to stabilize the transition state of the oxidative addition for different tertiary connected homoallylic carbons, they found that it decreases in the order: cyclohexyl (**23d**) > iso-propyl (**23b**) > 1-ethylpentyl (**23e**).

Although metallocavitand Pd^{II}•**C15** (**C16**) didn't show remarkable increase in catalytic rates, the presence of a cavity allowed **C16** to exhibit subtle substrate specificity that distinguishes between closely related structures.

In another example, the point of interest for Rebek *et al.* was the enzyme choline acetyltransferase[106] mimicry. For this study, cavitand **C17**[107] (**Fig. 19**) was designed to possess two important elements: a cavity as a recognition point for trimethylalkyl-ammonium knob,[108,109,110,111] and a Zn^{II} coordinated to salphen group to facilitate the acyl group transfer.[112,113,114] Authors predicted that formed caviplex **26**⊂**C17** (**Fig. 19**, reaction scheme) would coordinate acetyl anhydride (**28**) forming caviplex **26**⊂**28**•**C17**. In the next stage, Zn^{II} would facilitate transfer of the acyl group from acid anhydride (**28**) to the choline (**26**) generating **27**⊂**C17** caviplex. Finally, exchange with the new molecule of choline (**26**) would release the product (**27**) allowing catalyst recovery and reaction turnover.[115]

To ensure a weak binding and to promote catalytic turnover, the reaction was performed in DMSO-d_6. Results showed significant acceleration when 0.4 mol-% of catalyst **C17** was added. With the addition of a higher amounts of the catalyst (2 mol-%), reaction acceleration reached 1900-fold increase and was comparable with the rates

observed when DMAP (**29**, 4-dimethylaminopyridine) was used as a catalyst. Interestingly, with 2 mol-% of **25** only 140-fold acceleration was observed. Presence of the cavitand **C5** alone or in combination with catalysts **25** or **29** actually slowed down the acylation reaction.

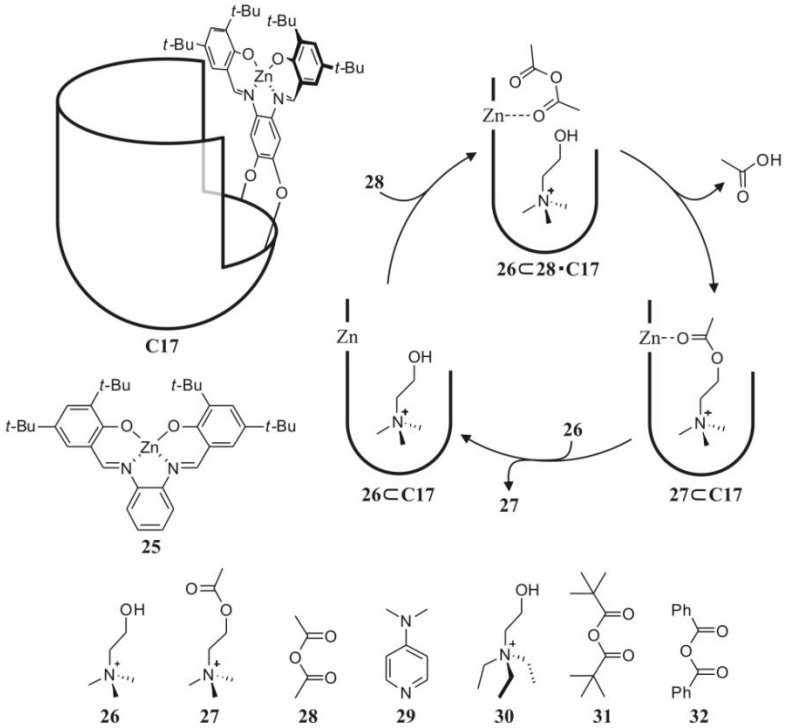

Fig. 19. Top right: schematic representation of catalytic esterification cycle; left and bottom: molecules used in this research.

When acylation of bulkier alcohol **30** was catalyzed by **25**, similar acceleration rates to the ones obtained with choline (**26**) were observed. On the other side, cavitand **C17** showed a higher acceleration rates for **26** acylation over **30**. Since no inclusion was observed for alcohol **30**, the higher acceleration rate for **26** was attributed to a lower inhibition of catalyst **C17** by product **27**. Bulkier anhydrides showed slower kinetics, and in the case of acylation of **26** showed the following relative reactivity: **28** : **32** : **31** = 15 : 2 : 1.

In conclusion, the authors demonstrated the importance of the adequate position and recognition of the catalytic centers in order to increase the rate of esterification, and demonstrated substrate size discrimination.

Finally, we will examine an example developed by Ballester *et al.*, where cavitand **C5** (**Fig. 10**) acted as a second-sphere ligand for Rh^{I}•$(NBD)_2$ complex **2** (**Fig. 20**).[78]

^{1}H NMR studies showed that this system exists in two forms. In the dominating form, cationic Rh^I•$(NBD)_2$ complex **2** is fully included in the interior of the cavitand **C5** producing a caviplex Rh^I•$(NBD)_2$⊂**C5**, **C18**. As mentioned in section **1.4**, cross-peaks observed in the EXSY NMR spectra were indication of the tumbling motion of **2** (slow on the ^{1}H NMR timescale). Beside **C18** species, a small amount of partially dissociated species was also detected where the coordination sphere of Rh^I is, probably, saturated with solvent molecules, methylene chloride-d_2 in this case, producing a caviplex $(CD_2Cl_2)_2$•Rh^I•$(NBD)_2$⊂**C5**, **C19**.

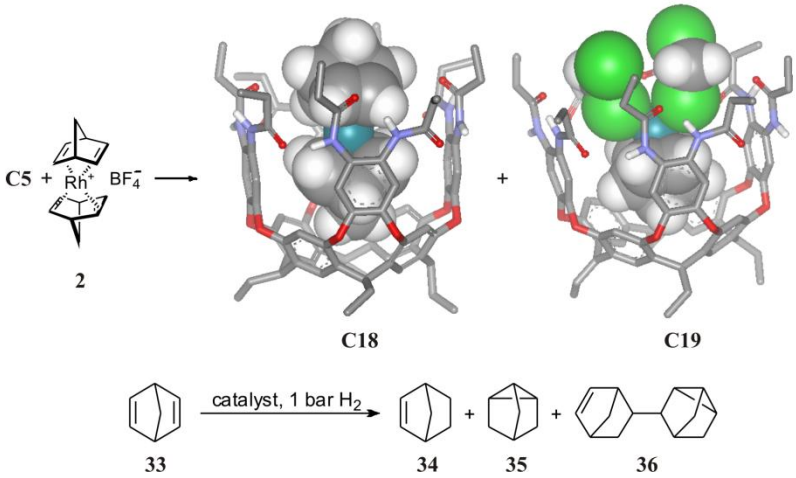

Fig. 20. Top: structures of caviplex catalysts **C18** and **C19** with nonpolar hydrogen atoms omitted for clarity. Guest molecules are presented as CPK models. Bottom scheme: catalyzed reaction.

The obtained caviplex system was found to be catalytically competent in hydrogenation of norbornadiene **33** (**Fig. 20**, reaction scheme), yielding product distribution significantly different to the one obtained when organometallic complex **2** alone was used as a catalyst. GC/FID analysis of reaction crude after 1 h of exposure to 1 atm of hydrogen showed the following product distribution: 58% of norbornene (**34**), 39% of dimer (**36**) and 3% of nortricyclene (**35**). Compared to the product distribution obtained when organometallic complex **2** was used as a catalyst (> 80% of **36**)[116] a clear significant change in selectivity can be noticed. Authors hypothesized that dimer **36** produced by caviplex system was catalyzed by a small amount of Rh^I complex dissociated from caviplexes to the bulk of solution during reaction.

1.8 References and notes

[1] A. Baeyer, *Ber. Dtsch. Chem. Ges.*, 1872, **5**, 25-26.
[2] A. Baeyer, *Ber. Dtsch. Chem. Ges.*, 1872, **5**, 280-282.

[3] A. Baeyer, *Ber. Dtsch. Chem. Ges.*, 1872, **5**, 1094-1100.
[4] A. Michael, *Am. Chem. J.*, 1883, **5**, 338-353.
[5] N. Caro, *Ber. Dtsch. Chem. Ges.*, 1892, **25**, 939-949.
[6] R. Möhlau and P. Koch, *Ber. Dtsch. Chem. Ges.*, 1894, **27**, 2887-2897.
[7] H. H. Wenzke and J. A. Nieuwland, *J. Am. Chem. Soc.*, 1924, **46**, 177-181.
[8] S. A. Flood and J. A. Nieuwland, *J. Am. Chem. Soc.*, 1928, **50**, 2566-2573.
[9] W. C. Harden and E. E. Reid, *J. Am. Chem. Soc.*, 1932, **54**, 4325-4334.
[10] C. Liebermann and S. Lindenbaum, *Ber. Dtsch. Chem. Ges.*, 1904, **37**, 1171-1180.
[11] J. B. Niederl and H. J. Vogel, *J. Am. Chem. Soc.*, 1940, **62**, 2512-2514.
[12] H. Erdtman, F. Haglid and R. Ryhage, *Acta Chem. Scand.*, 1964, **18**, 1249-1254.
[13] A. G. S. Högberg, *J. Org. Chem.*, 1980, **45**, 4498-4500.
[14] A. G. S. Högberg, *J. Am. Chem. Soc.*, 1980, **102**, 6046-6050.
[15] J. R. Moran, S. Karbach and D. J. Cram, *J. Am. Chem. Soc.*, 1982, **104**, 5826-5828.
[16] L. M. Tunstad, J. A. Tucker, E. Dalcanale, J. Weiser, J. A. Bryant, J. C. Sherman, R. C. Helgeson, C. B. Knobler and D. J. Cram, *J. Org. Chem.*, 1989, **54**, 1305-1312.
[17] J. R. Moran, J. L. Ericson, E. Dalcanale, J. A. Bryant, C. B. Knobler and D. J. Cram, *J. Am. Chem. Soc.*, 1991, **113**, 5707-5714.
[18] D. J. Cram, H. J. Choi, J. A. Bryant and C. B. Knobler, *J. Am. Chem. Soc.*, 1992, **114**, 7748-7765.
[19] D. J. Cram, *Science*, 1983, **219**, 1177-1183.
[20] G. G. Condorelli, A. Motta, M. Favazza, I. L. Fragalà, M. Busi, E. Menozzi, E. Dalcanale and L. Cristofolini, *Langmuir*, 2006, **22**, 11126-11133.
[21] M. Busi, M. Laurenti, G. G. Condorelli, A. Motta, M. Favazza, I. L. Fragalà, M. Montalti, L. Prodi and E. Dalcanale, *Chem. Eur. J.*, 2007, **13**, 6891-6898.
[22] E. B. Feresenbet, M. Busi, F. Ugozzoli, E. Dalcanale and D. K. Shenoy, *Sensor Letters*, 2004, **2**, 186-193.
[23] E. Menozzi, R. Pinalli, E. A. Speets, B. J. Ravoo, E. Dalcanale and D. N. Reinhoudt, *Chem. Eur. J.*, 2004, **10**, 2199-2206.
[24] L. R. MacGillivray and J. L. Atwood, *Nature*, 1997, **389**, 469-472.
[25] A. D. M. Curtis, *Tetrahedron Lett.*, 1997, **38**, 4295-4296.
[26] E. U. Thoden van Velzen, J. F. J. Engbersen and D. N. Reinhoudt, *J. Am. Chem. Soc.*, 1994, **116**, 3597-3598.
[27] D. J. Cram, S. Karbach, H. E. Kim, C. B. Knobler, E. F. Maverick, J. L. Ericson and R. C. Helgeson, *J. Am. Chem. Soc.*, 1988, **110**, 2229-2237.
[28] Y. Aoyama, Y. Tanaka, H. Toi and H. Ogoshi, *J. Am. Chem. Soc.*, 1988, **110**, 634-635.
[29] Y. Aoyama, Y. Tanaka and S. Sugahara, *J. Am. Chem. Soc.*, 1989, **111**, 5397-5404.
[30] B. C. Gibb, R. G. Chapman and J. C. Sherman, *J. Org. Chem.*, 1996, **61**, 1505-1509.
[31] K. Kobayashi, Y. Asakawa, Y. Kato and Y. Aoyama, *J. Am. Chem. Soc.*, 1992, **114**, 10307-10313.
[32] U. Schneider and H.-J. Schneider, *Chem. Ber.*, 1994, **127**, 2455-2469.

[33] A. Shivanyuk, V. Böhmer, W. Vogt and E. F. Paulus, *Angew. Chem., Int. Ed. Engl.*, 1997, **36**, 1301-1303.
[34] Y. Yamakawa, M. Ueda, R. Nagahata, K. Takeuchi and M. Asai, *J. Chem. Soc., Perkin Trans. 1*, 1998, 4135-4140.
[35] F. Weinelt and H. J. Schneider, *J. Org. Chem.*, 1991, **56**, 5527-5535.
[36] T. Kijima, Y. Kato, K. Ohe, M. Machida, Y. Matsushita and T. Matsui, *Bull. Chem. Soc. Jpn.*, 1994, **67**, 2125-2129.
[37] P. T. Lewis, C. J. Davis, M. C. Saraiva, W. D. Treleaven, T. D. McCarley and R. M. Strongin, *J. Org. Chem.*, 1997, **62**, 6110-6111.
[38] P. D. Beer, E. L. Tite and A. Ibbotson, *J. Chem. Soc., Chem. Commun.*, 1989, 1874-1876.
[39] R. J. M. Egberink, P. L. H. M. Cobben, W. Verboom, S. Harkema and D. N. Reinhoudt, *J. Incl. Phenom. Macrocycl. Chem.*, 1992, **12**, 151-158.
[40] P. D. Beer, E. L. Tite, M. G. B. Drew and A. Ibbotson, *J. Chem. Soc., Dalton Trans.*, 1990, 2543-2550.
[41] P. J. Skinner, A. G. Cheetham, A. Beeby, V. Gramlich and F. Diederich, *Helv. Chim. Acta*, 2001, **84**, 2146-2153.
[42] D. J. Cram, S. Karbach, Y. H. Kim, L. Baczynskyj and G. W. Kallemeyn, *J. Am. Chem. Soc.*, 1985, **107**, 2575-2576.
[43] D. J. Cram, *Angew. Chem., Int. Ed. Engl.*, 1988, **27**, 1009-1020.
[44] C. J. Pedersen, *Angew. Chem., Int. Ed. Engl.*, 1988, **27**, 1021-1027.
[45] J.-M. Lehn, *Angew. Chem., Int. Ed. Engl.*, 1988, **27**, 89-112.
[46] P. Atkins and J. de Paula, *Physical Chemistry*, W. H. Freeman and Company, New York, 2006.
[47] F. L. Leite, C. C. Bueno, A. L. Da Róz, E. C. Ziemath and O. N. Oliveira, *Int. J. Mol. Sci.*, 2012, **13**, 12773-12856.
[48] D. Voet and J. G. Voet, *Biochemistry*, Wiley, 2010.
[49] E. Fischer, *Ber. Dtsch. Chem. Ges.*, 1894, **27**, 2985-2993.
[50] D. E. Koshland, *Proc.Natl. Acad. Sci.*, 1958, **44**, 98-104.
[51] C. J. Pedersen, *J. Am. Chem. Soc.*, 1967, **89**, 7017-7036.
[52] J. Lehn, *Science*, 1993, **260**, 1762-1763.
[53] R. C. Helgeson, C. B. Knobler and D. J. Cram, *J. Chem. Soc., Chem. Commun.*, 1995, 307-308.
[54] H. H. Wenzke and J. A. Nieuwland, *J. Am. Chem. Soc.*, 1924, **46**, 177-181.
[55] J. C. Ma and D. A. Dougherty, *Chem. Rev.*, 1997, **97**, 1303-1324.
[56] S. A. Flood and J. A. Nieuwland, *J. Am. Chem. Soc.*, 1928, **50**, 2566-2573.
[57] W. C. Harden and E. E. Reid, *J. Am. Chem. Soc.*, 1932, **54**, 4325-4334.
[58] B. Nilsson, *Acta Chem. Scand.*, 1968, **22**, 732-747.
[59] J. Lehn, *Science*, 1993, **260**, 1762-1763.
[60] J.-M. Lehn, *Supramolecular Chemistry: Concepts and Perspectives*, VCH, Weinheim, 1995.

[61] L. R. MacGillivray and J. L. Atwood, *Nature*, 1997, **389**, 469-472.
[62] T. Evan-Salem, I. Baruch, L. Avram, Y. Cohen, L. C. Palmer and J. Rebek, *Proc.Natl. Acad. Sci.*, 2006, **103**, 12296-12300.
[63] J. A. Tucker, C. B. Knobler, K. N. Trueblood and D. J. Cram, *J. Am. Chem. Soc.*, 1989, **111**, 3688-3699.
[64] E. Dalcanale, P. Soncini, G. Bacchilega and F. Ugozzoli, *J. Chem. Soc., Chem. Commun.*, 1989, 500-502.
[65] M. Vincenti, E. Dalcanale, P. Soncini and G. Guglielmetti, *J. Am. Chem. Soc.*, 1990, **112**, 445-447.
[66] P. Soncini, S. Bonsignore, E. Dalcanale and F. Ugozzoli, *J. Org. Chem.*, 1992, **57**, 4608-4612.
[67] S. Mecozzi and J. J. Rebek, *Chem. Eur. J.*, 1998, **4**, 1016-1022.
[68] T. Heinz, D. M. Rudkevich and J. Rebek, *Nature*, 1998, **394**, 764-766.
[69] F. L. Leite, C. C. Bueno, A. L. Da Róz, E. C. Ziemath and O. N. Oliveira, *Int. J. Mol. Sci.*, 2012, **13**, 12773-12856.
[70] A. Scarso, H. Onagi and J. Rebek, *J. Am. Chem. Soc.*, 2004, **126**, 12728-12729.
[71] A. I. Kitaigorodsky, *Molecular Crystals and Molecules*, Academic Press, London, 1973.
[72] J. C. Sherman, C. B. Knobler and D. J. Cram, *J. Am. Chem. Soc.*, 1991, **113**, 2194-2204.
[73] D. M. Rudkevich, G. Hilmersson and J. Rebek, *J. Am. Chem. Soc.*, 1998, **120**, 12216-12225.
[74] P. Ballester and M. A. Sarmentero, *Org. Lett.*, 2006, **8**, 3477-3480.
[75] P. Amrhein, A. Shivanyuk, D. W. Johnson and J. Rebek, *J. Am. Chem. Soc.*, 2002, **124**, 10349-10358.
[76] M. A. Sarmentero and P. Ballester, *Org. Biomol. Chem.*, 2007, **5**, 3046-3054.
[77] E. Zuidema, M. A. Sarmentero, C. Bo and P. Ballester, *Chem.--Eur. J.*, 2008, **14**, 7285-7295.
[78] M. A. Sarmentero, H. Fernández-Pérez, E. Zuidema, C. Bo, A. Vidal-Ferran and P. Ballester, *Angew. Chem., Int. Ed.*, 2010, **49**, 7489-7492.
[79] F. H. Westheimer, H. F. Fisher, E. E. Conn and B. Vennesland, *J. Am. Chem. Soc.*, 1951, **73**, 2403-2403.
[80] H. F. Fisher, E. E. Conn, B. Vennesland and F. H. Westheimer, *J. Biol. Chem.*, 1953, **202**, 687-697.
[81] F. A. Loewus, F. H. Westheimer and B. Vennesland, *J. Am. Chem. Soc.*, 1953, **75**, 5018-5023.
[82] F. C. Kokesh and F. H. Westheimer, *J. Am. Chem. Soc.*, 1971, **93**, 7270-7274.
[83] F. H. Westheimer and D. E. Schmidt, *Biochemistry*, 1971, **10**, 1249-1253.
[84] B. Zerner, *Bioorg. Chem.*, 1992, **20**, 269-284.
[85] C. D. Gutsche, *Calixarenes: An Introduction*, The Royal Society of Chemistry, 2008.
[86] E. J. Corey and J. Streith, *J. Am. Chem. Soc.*, 1964, **86**, 950-951.
[87] E. J. Corey and W. H. Pirkle, *Tetrahedron Lett.*, 1967, **8**, 5255-5256.

[88] G. Maier, M. Hoppe, K. Lanz and H. P. Reisenauer, *Tetrahedron Lett.*, 1984, **25**, 5645-5648.
[89] J. Kreile, N. Münzel, A. Schweig and H. Specht, *Chem. Phys. Lett.*, 1986, **124**, 140-146.
[90] D. J. Cram, M. E. Tanner and R. Thomas, *Angew. Chem., Int. Ed. Engl.*, 1991, **30**, 1024-1027.
[91] T. A. Robbins, C. B. Knobler, D. R. Bellew and D. J. Cram, *J. Am. Chem. Soc.*, 1994, **116**, 111-122.
[92] T. A. Robbins and D. J. Cram, *J. Am. Chem. Soc.*, 1993, **115**, 12199-12199.
[93] D. J. Cram and J. M. Cram, *Container Molecules and Their Guests*, Royal Society of Chemistry, Los Angeles, USA, 1994.
[94] R. S. Meissner, J. Rebek and J. de Mendoza, *Science*, 1995, **270**, 1485-1488.
[95] A. R. Renslo, D. M. Rudkevich and J. Rebek, *J. Am. Chem. Soc.*, 1999, **121**, 7459-7460.
[96] A. R. Renslo, F. C. Tucci, D. M. Rudkevich and J. Rebek, *J. Am. Chem. Soc.*, 2000, **122**, 4573-4582.
[97] A. R. Renslo and J. J. Rebek, *Angew. Chem., Int. Ed. Engl.*, 2000, **39**, 3281-3283.
[98] U. Lücking, D. M. Rudkevich and J. Rebek Jr., *Tetrahedron Lett.*, 2000, **41**, 9547-9551.
[99] S. D. Starnes, D. M. Rudkevich and J. Rebek, *Org. Lett.*, 2000, **2**, 1995-1998.
[100] S. D. Starnes, D. M. Rudkevich and J. Rebek, *J. Am. Chem. Soc.*, 2001, **123**, 4659-4669.
[101] U. Lücking, J. Chen, D. M. Rudkevich and J. Rebek, *J. Am. Chem. Soc.*, 2001, **123**, 9929-9934.
[102] C. Gibson and J. Rebek, *Org. Lett.*, 2002, **4**, 1887-1890.
[103] R. Prétôt and A. Pfaltz, *Angew. Chem., Int. Ed. Engl.*, 1998, **37**, 323-325.
[104] B. Åkemark, K. Zetterberg, S. Hansson, B. Krakenberger and A. Vitagliano, *J. Organomet. Chem.*, 1987, **335**, 133-142.
[105] M. P. T. Sjoegren, S. Hansson, B. Aakermark and A. Vitagliano, *Organometallics*, 1994, **13**, 1963-1971.
[106] D. Nachmansohn and A. L. Machado, *J. Neurophysiol.*, 1943, **6**, 397-403.
[107] S. Richeter and Rebek, *J. Am. Chem. Soc.*, 2004, **126**, 16280-16281.
[108] E. A. Castro, M. Cubillos and J. G. Santos, *J. Org. Chem.*, 2001, **66**, 6000-6003.
[109] A. Gissot and J. Rebek, *J. Am. Chem. Soc.*, 2004, **126**, 7424-7425.
[110] J. L. Atwood and A. Szumna, *J. Am. Chem. Soc.*, 2002, **124**, 10646-10647.
[111] P. Ballester, A. Shivanyuk, A. R. Far and J. Rebek, *J. Am. Chem. Soc.*, 2002, **124**, 14014-14016.
[112] L. G. Mackay, R. S. Wylie and J. K. M. Sanders, *J. Am. Chem. Soc.*, 1994, **116**, 3141-3142.
[113] B. M. Trost and T. Mino, *J. Am. Chem. Soc.*, 2003, **125**, 2410-2411.
[114] N. C. Gianneschi, S. T. Nguyen and C. A. Mirkin, *J. Am. Chem. Soc.*, 2005, **127**, 1644-1645.
[115] F. H. Zelder and J. Rebek Jr, *Chem. Commun.*, 2006, 753-754.
[116] R. J. Roth and T. J. Katz, *Tetrahedron Lett.*, 1972, **13**, 2503-2504.

CHAPTER 2: Motion and isomerism of Ir^{I}•COD included in Rebek's self-folding octaamide cavitand

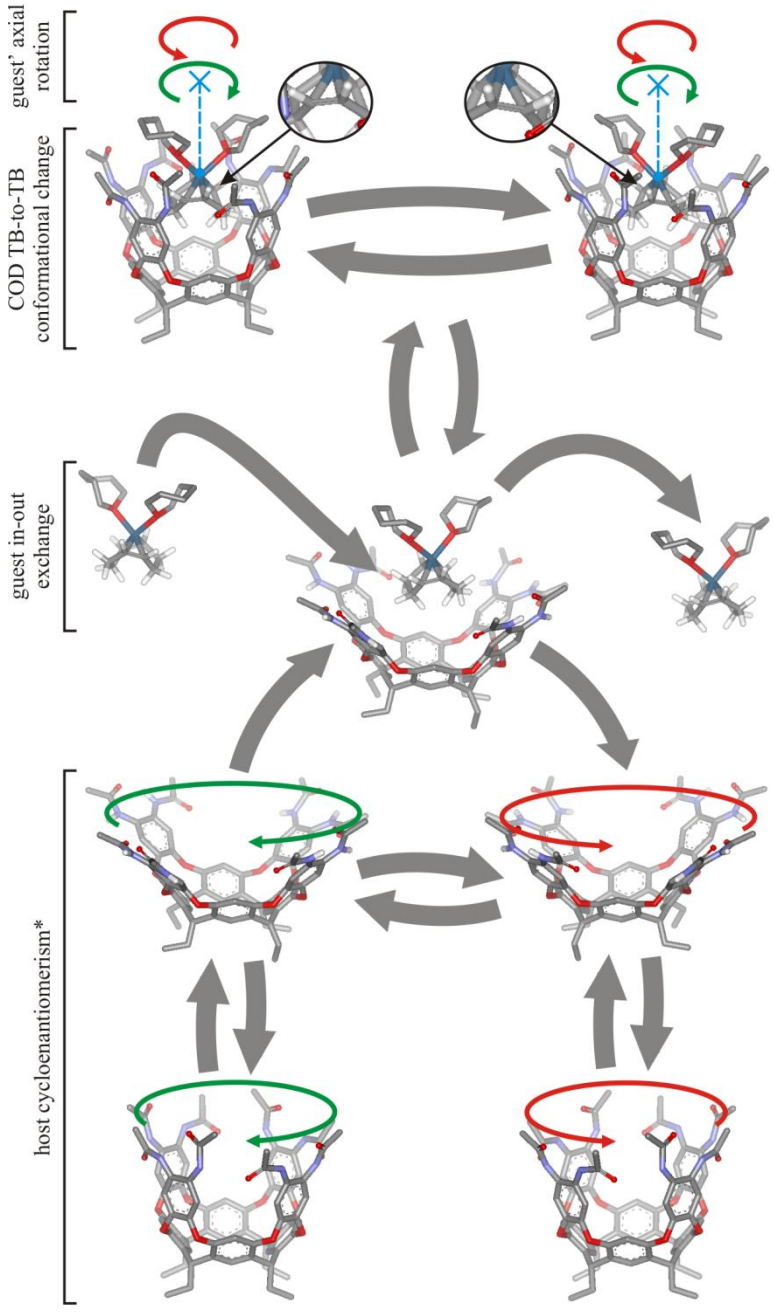

* with or without included guest molecule

2.1 Introduction

In our previous work, we learned that cavitand **C5** acted as a second sphere ligand for the organometallic complex Rh^{I}•$(NBD)_2$, **2** (**Fig. 21**) and the inclusion process produced a mixture of two caviplexes.[1] The analysis of the caviplex distribution using ^{1}H NMR spectroscopy showed that the included bis-norbornadiene Rh^{I} complex Rh^{I}•$(NBD)_2$⊂**C5** (**2**⊂**C5**) was the dominant species over the caviplex having dissociated one of the NBD ligands from the Rh^{I} metal center. The caviplex mixture showed catalytic competence in the hydrogenation of NBD significantly altering the selectivity of the reaction compared to that of the organometallic complex free in solution. These results urged us to continue our investigations using organometallic complexes of other metals with different sizes and shapes but suitable for inclusion within the cavitand **C5**. We selected Ir^{I} organometallic complex Ir^{I}•$(COD)_2$, **37** having bulkier but conformationally flexible COD ligand *vs* more compact and conformationally rigid NBD used in previous studies. In this chapter, we disclose the characterization studies of the Ir^{I}•COD caviplex. The obtained results lead our research into a direction very different from the catalysis, and prompted us to investigate the motion and the conformational interconversion experienced by the organometallic Ir^{I}•COD complex included into cavitand **C5**.

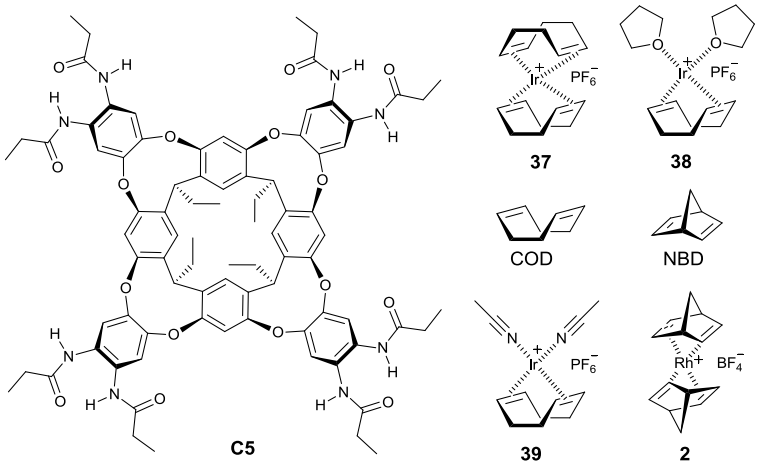

Fig. 21. Line drawing structures of self-folding octaamide cavitand **C5**; cationic complexes: Ir^{I}•$(COD)_2$, **37**; $(THF)_2$•Ir^{I}•COD, **38**; $(CH_3CN)_2$•Ir^{I}•COD, **39**; Rh^{I}•$(NBD)_2$, **2** and ligands: 1,5-cyclooctadiene (COD) and 2,5-norbornadiene (NBD).

2.2 Results and discussion

The cavitand **C5** belongs to a class of molecular structures stemming from the resorcin[4]arene scaffold with the addition of four aromatic walls at the upper rim in order to additionally elaborate its aromatic cavity. Each aryl wall is functionalized with two

amide groups. Accordingly, the presence of both, H-bond donors and H-bond acceptors, allows amide groups installed at the upper rim of the cavitand to be unidirectionally oriented by establishing two types of H-bonds: *intraannular* (between amide couples on the same wall) and *interannular* (between amide groups of the neighboring walls).[2] The formation of a belt of eight hydrogen bonds at the upper rim of **C5** induces the cavitand to adopt the *vase* conformation.[3,4] In nonpolar solvents (e.g. chloroform-*d*) and at room temperature, two types of hydrogen bonds (*intraanular* and *internanular*) are involved in a chemical exchange process that is slow on the ^{1}H NMR timescale. Thus, NH protons of amide groups resonate as two separate signals in the ^{1}H NMR spectrum of **C5**. Each signal integrates for four hydrogen atoms (**Fig. 22**, a). The number of proton signals observed in the ^{1}H NMR spectrum of **C5** is diagnostic of C_4 symmetry. The array of hydrogen bonds orients eight amide groups in a unidirectional manner. The unidirectional orientation of amides can have either a clockwise (*P*) or a counterclockwise (*M*) sense of rotation when **C5** is observed from the top of its aromatic cavity. This element of asymmetry renders cavitand **C5** inherently chiral and the compound exists as two cycloenantiomers (**Fig. 23**). It is worthwhile to note that when two cycloenantiomers of **C5** are involved in slow chemical exchange on the ^{1}H NMR timescale, aromatic protons H^1 and H^2 also become diastereotopic, because they experience different magnetic environments by being close to the NH (hydrogen bond donor) or to the C=O (hydrogen bond acceptor) functions of amide groups. Thus, they are expected to resonate as separated signals.

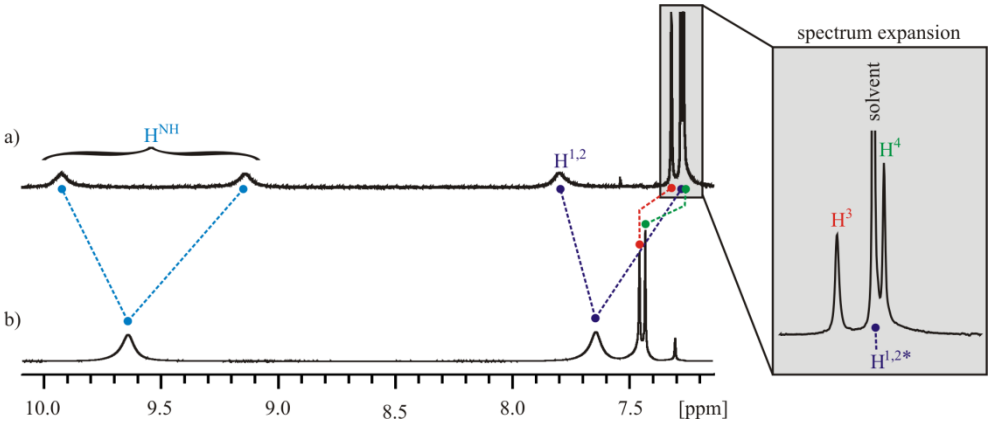

Fig. 22. ^{1}H NMR spectra of the cavitand **C5** at room temperature in: a) chloroform-*d*, and, b) THF-d_8 solutions. Note: the second $H^{1,2}$ signal is hidden under the solvent signal (confirmed by NOESY).

In a polar solvent (e.g THF-d_8), the energy barrier for the interconversion between two cycloenantiomers is reduced. A probable explanation has to do with the participation of solvent molecules in hydrogen bonding interactions with amide groups of the cavitand in the transition state. For this reason, at room temperature, NH protons appear as a broad singlet (**Fig. 22**, b).

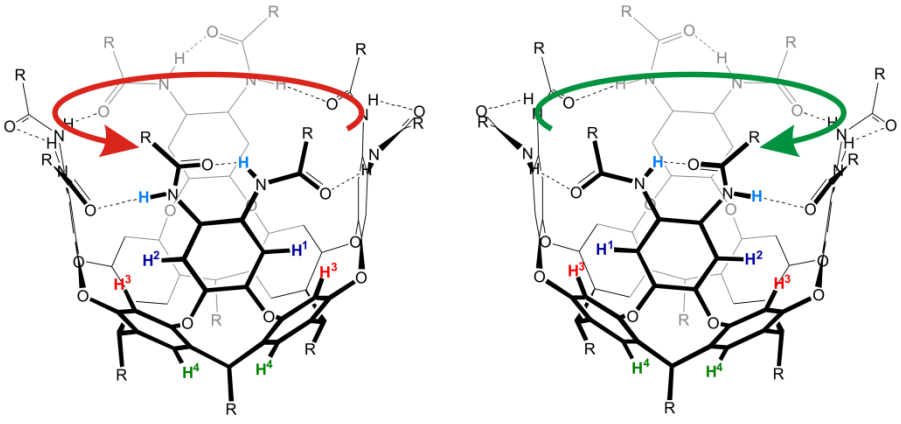

Fig. 23. Cycloenantiomers of the cavitand **C5** with colored arrows depicting directionality of hydrogen bonds. Aromatic double bonds and most of nonpolar hydrogen atoms are omitted for clarity. R is an ethyl group.

When the temperature of the solution is increased the broad NH singlet sharpens. Conversely, when the temperature is lowered below 273 K, the signal of the NH protons splits into two because the interconversion between two cycloenantiomers becomes slow on the ^{1}H NMR timescale (**Fig. 24**).

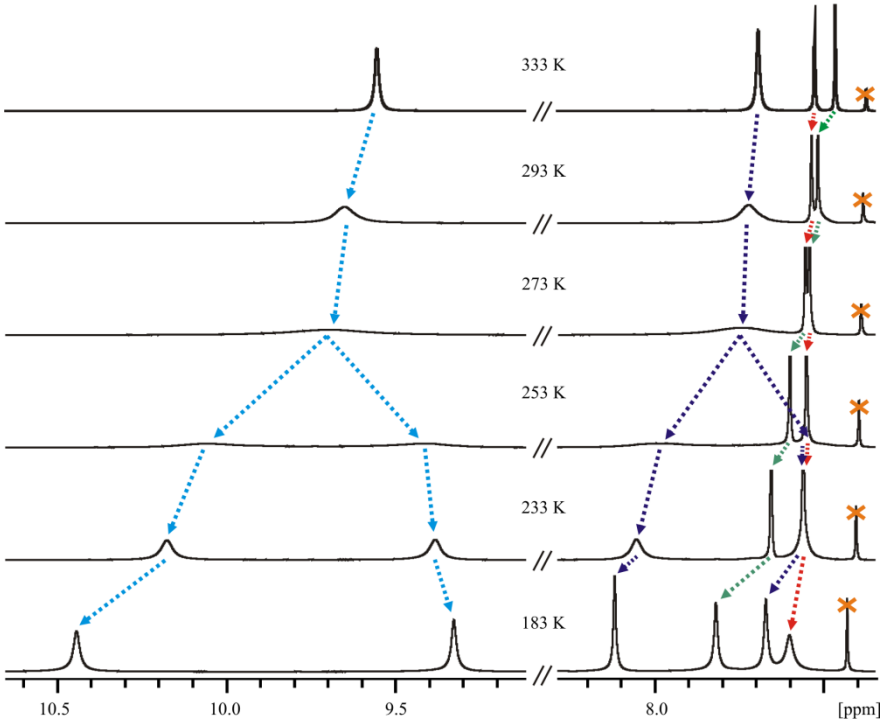

Fig. 24. Selected downfield regions of VT ^{1}H NMR experiments performed on cavitand **C5** (2.2 μmol) in THF-d_8 (550 μL). Designations: ■ - NH proton signals, ■ - $H^{1,2}$ proton, ■ - H^{3} proton and ■ - H^{4} proton signals, X - artefact.

A similar splitting trend is followed by the singlet assigned to aromatic protons $H^{1,2}$ which become diastereotopic. Using the coalescence temperature method, we determined that the energy barrier for the interconversion between two cycloenantiomers in THF-d_8 solution was around 13 kcal mol^{-1}. This value was approximately 5 kcal mol^{-1} lower than the energy barrier measured for the same interconversion in nonpolar solvents.[4,5,6] The measured energy barrier is the sum of energies required to break the belt of eight hydrogen bonds at the upper rim of **C5**, which stabilizes its vase conformation, and for the vase-to-kite interconversion (10 - 12 kcal mol^{-1}).[7,6,8] Not surprisingly, the measured energy barrier coincides with the calculated one for the exchange of included compounds (*vide infra*). We estimated that the energy required to break the hydrogen bonded belt of the cavitand in THF-d_8 solution is close to 1 kcal mol^{-1}.

At room temperature, the addition of 0.8 equivalents of the organometallic complex Ir^{I}•$(COD)_2$, **37** to a 1 mM THF-d_8 solution of the cavitand **C5** induced the observation of separate proton signals for free and bound host. Amide NH protons of the bound host split into four signals (**Fig. 25**, b, ▲ - NH protons; see **Fig. 23** for proton designations). The same signal splitting trend is followed by $H^{1,2}$ protons (▲), while protons H^3 (▲) and H^4 (▲) split into two signals.

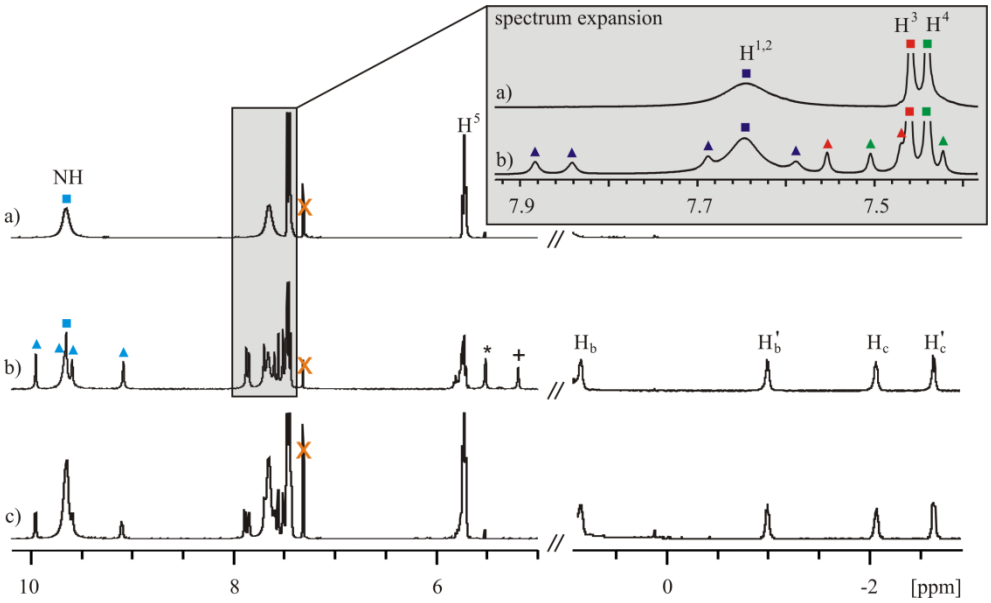

Fig. 25. Selected regions of ^{1}H NMR spectra for: a) the free host **C5** (4 mM in THF-d_8), b) the mixture of the free host **C5** and the host/guest complex **38**⊂**C5**, c) the mixture of the free host **C5** and the host/guest complex **39**⊂**C5**. Solutions were prepared by mixing the host **C5** (2.2 µmol) and the appropriate guest (**37** or **39**, 1.8 µmol) in THF-d_8 (550 µL) at 298 K. Designations: free host (■ - NH, ■ - $H^{1,2}$, ■ -H^3 and ■ - H^4), bound host (▲ - NH, ▲ - $H^{1,2}$, ▲ - H^3 and ▲ - H^4), X - artefact, * - free COD, + - free **37**.

Concomitantly, we observed the emergence of a new set of four highly upfield shifted proton signals (designated as H_b, H_b', H_c and H_c'). We assigned these signals to protons of

the guest included in the aromatic cavity of **C5** (**Fig. 25**, b). NOESY and ROESY experiments (see Supporting Information) revealed the presence of cross-peaks due to chemical exchange between proton pairs H_b' / H_c' and H_b / H_c of the included guest, suggesting their chemical exchange slow on the ^{1}H NMR timescale. Additionally, we observed a third pair of protons for the included guest (designated as H_a / H_a'), which were buried under intense proton signals of the ethyl groups of the free and the bound host. This latter pair was also involved in a slow chemical exchange process on the ^{1}H NMR timescale. ^{13}C-^{1}H HSQC experiment (see Supporting Information) showed single cross peaks between two different sp^2 carbons and each one of H_a and H_a' protons. On the other hand, two sp^3 carbons showed pairs of cross-peaks with couples H_b / H_b' and H_c / H_c'. The four upfield shifted signals assigned to protons of the included guest had the same integral value, which also coincided with those measured for each one of the four NH signals corresponding to the bound host.

It is worth noting, that signals corresponding to protons in the free COD (**Fig. 25**, b, designated with *) were also detected in the ^{1}H NMR spectrum of the mixture. However, the exact amount of the free COD was difficult to determine by integration owing to the interference of other proton signals. The dissociation of the COD suggested that the structure of Ir^I complex included in the cavitand **C5** possessed a single COD molecule as a ligand. This hypothesis was substantiated, by performing an inclusion experiment using the heteroleptic $(CH_3CN)_2$•Ir^I•COD complex, **39** dissolved in THF-d_8. The ^{1}H NMR spectrum of the inclusion complex $(CH_3CN)_2$•Ir^I•COD⊂**C5** was superimposable with that obtained for the inclusion complex starting from the Ir^I•$(COD)_2$, **37** (**Fig. 25**, c). This result, evidenced that the cavitand **C5** in the presence of the organometallic Ir^I•$(COD)_2$ complex **37** formed the Ir^I•COD⊂**C5** caviplex in which one of the CODs was dissociated.

It is important to note that the organometallic complex Ir^I•$(COD)_2$, **37** when dissolved in THF-d_8 showed partial dissociation (≈ 15 %) of one of the COD ligands, implying the formation of a heteroleptic complex, most likely, with two solvent molecules (THF-d_8)$_2$•Ir^I•COD, **38**. This dissociation process of one COD ligand was not observed when methylene chloride-d_2 was used as a solvent. Furthermore, the solvent molecules (THF-d_8) did not exchange acetonitrile or COD ligands from the first coordination sphere of the $(CH_3CN)_2$•Ir^I•COD complex, **39**. Taken in concert, these observations allowed us to hypothesize that the formation of **38**⊂**C5** caviplex did not imply the inclusion of the homoleptic Ir^I•$(COD)_2$ complex **37** followed by dissociation of one of the COD ligands but rather the direct inclusion of the heteroleptic (THF-d_8)$_2$•Ir^I•COD complex **38** present in low concentration in the solution. Moreover, the addition of incremental amounts of COD to the solution containing the (THF-d_8)$_2$•Ir^I•COD⊂**C5** caviplex induced the diminution of the intensity of proton signals of the host/guest complex at the expense of an increase in signal intensities assigned to protons of the free host and the free guest. The proposed process is schematized in **Fig. 26**.

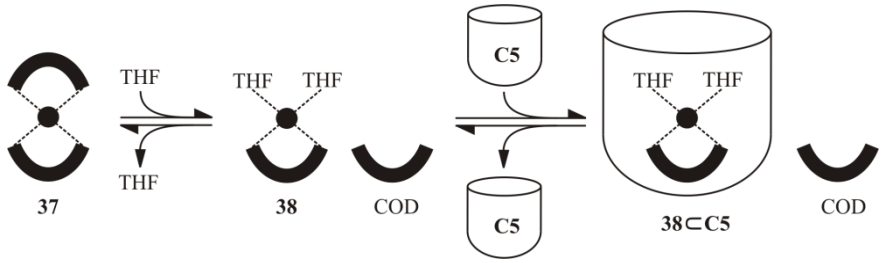

Fig. 26. Schematic representation of proposed inclusion equilibria.

To understand the splitting pattern observed for protons of the included (THF-d_8)$_2$•Ir^{I}•COD, **38** or (CH$_3$CN)$_2$•Ir^{I}•COD, **39** guests we need to recall conformational features displayed by the COD free in the solution and when metal-chelated. Experimental and theoretical studies proposed that the lowest conformation energy for the free COD is the twisted-boat (TB) conformation (**Fig. 27**).[9,10,11,12] Results derived from variable-temperature NMR experiments supported the existence of COD in the TB conformation featuring C_2 symmetry as the lowest energy conformer.[11] The TB-to-TB interconversion process can proceed through three different processes: a) via skew-like transition state of a D_2 symmetry b) via a C_{2v} symmetric boat-like transition state, and, c) via an intermediate chair minimum of a C_{2h} symmetry and two transition states skew or boat-like. The first process a) has the lowest calculated free enthalpy and is used to interpret a coalescence observed in the ^{1}H NMR spectrum at 96 K (ΔG = 4.4 kcal mol^{-1}). The chair process b) or a combination of the skew and the boat processes c) are offered to explain the second observed coalescence process in the ^{1}H NMR spectrum at 105 K (ΔG = 4.9 kcal mol^{-1}).

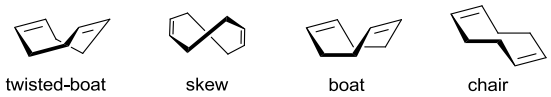

Fig. 27. Line drawing structures of four different COD conformers.

At the low temperature, the reduced rate of interconversion between the two TB conformers leads to the presence of *persistent conformational chirality*,[13,14] a phenomena characteristic for molecules devoid of stereocenters but with the restricted rotation around their chemical bonds. Therefore, each of the two possible TB conformers represents an enantioconformer. To assign the absolute configuration to each conformer we applied rules of the axial chirality by looking at the TB conformer of the COD through the single bond connecting two methylenes as shown in **Fig. 28**.

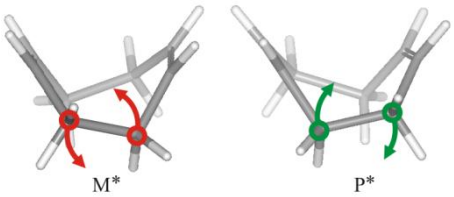

Fig. 28. Persistent conformational chirality of the COD TB conformers at the temperature below coalescence.

As the temperature increases to above the coalescence temperature, the TB-to-TB interconversion becomes fast on the NMR timescale and the number of proton signals observed in the ^{1}H NMR spectrum of the free COD is consistent with the boat-like C_{2v} symmetry. To the best of our knowledge, we are not aware of any studies performed on mono- or bis-COD Ir^I complexes addressing the interconversion between TB conformers of the metal-chelated COD ligand. Theoretical predictions using DFT calculations at the PB86 level of theory with def2svp basis set showed the TB-to-TB exchange barrier for the organometallic complex Ir^I•COD in the gas phase to be close to 2 kcal mol^{-1}. Although most publications depict the line drawing structure of the COD ligand in the boat conformation, a search in the CCDC (Cambridge Crystallographic Data Centre) rapidly identified X-ray crystal structures of iridium complexes showing the existence of metal-chelated COD ligands adopting the TB conformation in the solid state (**Fig. 29**).[15,16]

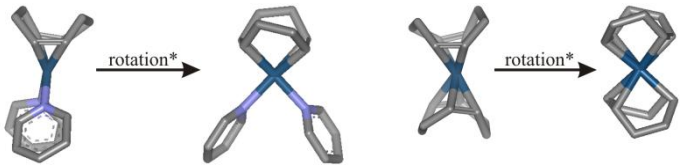

Fig. 29. Solid state structures for two Ir^I complexes (CCDC: JAMJOW and TUQWOS respectively) displaying the metal-chelated COD in the TB conformation. Hydrogen atoms and counterions are omitted for clarity. Designation: * - rotation of a molecule around its axial axis for ≈ 90°

Molecular modeling studies (MM3 as implemented in SCIGRESS v3.0), showed that in the energy-minimized structure of the host/guest complex (THF-d_8)$_2$•Ir^I•COD⊂**C5** the COD ligand adopted the TB conformation (**Fig. 30**).[17]

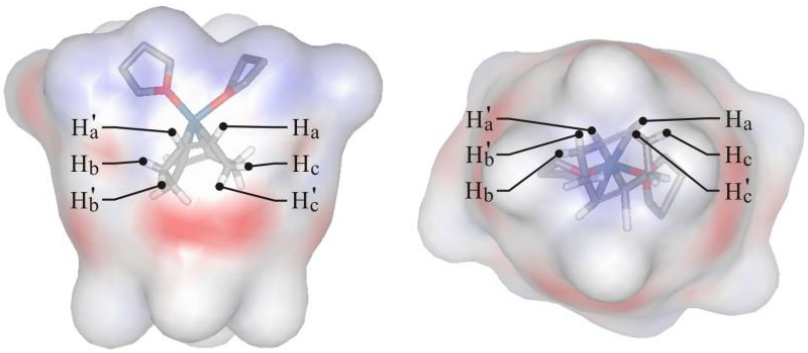

Fig. 30. MM3 energy-minimized structure of the host/guest complex (THF)$_2$•Ir^I•COD⊂**C5**, **38**⊂**C5** with designated guest COD protons. Host molecule **C5** was presented as a transparent electrostatic potential map surface. Hydrogen atoms on THF ligands are omitted for clarity.

In this conformation, the Ir^I•COD complex features a C_2 symmetry, instead of the expected C_{2v} for the COD in the boat-like conformation, and should provide a set of six different proton signals in the ^{1}H NMR spectrum, two corresponding to the chemically non-

equivalent vinylic groups and four for equatorially and axially oriented protons in two chemically non-equivalent methylenes. We were surprised to see that at room temperature the predicted number of proton signals for the included Ir^{I}•COD coincided with that expected for the COD in TB conformation. Our anticipation was that at room temperature the TB-to-TB interconversion process of the chelated COD in the included Ir^{I}•COD complex should be fast on the NMR timescale. If this was the case, protons of the included organometallic complex should provide a set of only three different signals (vinyl, axial and equatorial methylene protons) in agreement with its C_{2v}-like symmetry. In fact, this is the typical pattern of protons observed in the ^{1}H NMR spectra of Ir^{I}•COD complexes free in solution.

We are convinced (*vide infra*) that indeed the TB-to-TB interconversion process of the included Ir^{I}•COD is fast on the NMR timescale and that, as mentioned above, the observation of six different signals for its protons was due to the chiral nature of the container (**Fig. 31**, b).

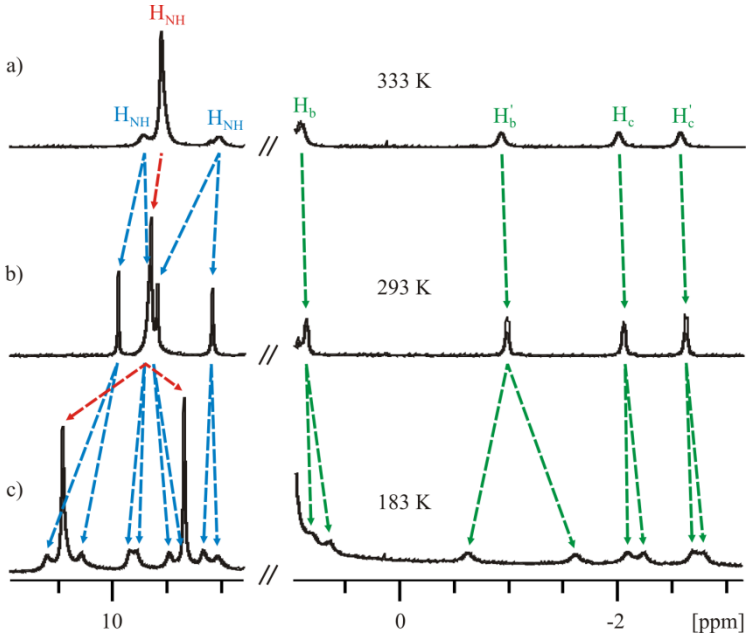

Fig. 31. VT ^{1}H NMR profile of the host/guest complex **38**⊂**C5** at: a) 333 K, b) 293 K, and c) 183 K. The host/guest complex was made by mixing the host **C5** (2.2 μmol) and the guest **37** (1.8 μmol) in THF-d_8 (550 μL). Signal splitting patterns for: ■ – the included Ir^{I}•COD, ■ – NHs of the bound host **C5**, ■ – NHs of the free host **C5**.

The asymmetry of the cavitand stems from the unidirectional orientation of amide groups and the existence of a slow interconversion process (on the NMR timescale) between two cycloenantiomers. This feature of the container renders protons of the included guest diastereotopic. We were also astonished to observe that the inclusion of the Ir^{I}•COD complex into **C5** disrupted the C_4 symmetry of the bound host previously observed

for inclusion complexes with other guests.[1,18] The ^{1}H NMR spectra of inclusion complexes of **C5** usually showed either one or two signals for NH amide protons at the upper rim depending on the rate constant for the interconversion process between two cycloenantiomers. The unique pattern of four signals observed for NH amide protons of the bound host in the (THF-d_8)$_2$•Ir^I•COD⊂**C5** complex showed an integration ratio of 2:2:2:2.[17] NH protons, enclosed in green and orange circles in **Fig. 32**, become chemically non-equivalent if both the spinning rate of the included Ir^I•COD along the axial axis of **C5** and that for the cycloenantiomer interconversion are slow on the NMR timescale.

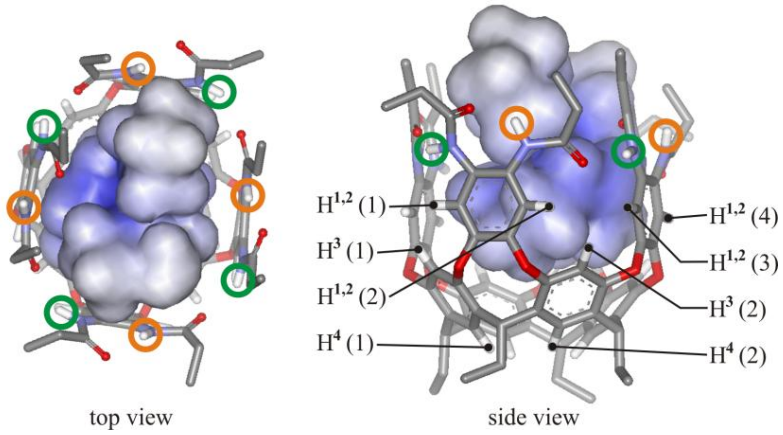

Fig. 32. MM3 energy-minimized structure of the host/guest complex (THF)$_2$•Ir^I•COD⊂**C5**, **38**⊂**C5** with designated HN and aromatic protons. Guest molecule was presented as an electrostatic potential map limited by van der Waals radii. Hydrogen atoms on ethyl groups of the host are omitted for clarity.

In complete agreement with both processes, being slow on the NMR timescale, we also observed eight different signals for aromatic protons of the bound **C5** (**Fig. 25**, b). Four signals were assigned to diastereotopic H^{1,2} protons, while a set of other two signals to H^3 and H^4 protons of two adjacent walls.

The reasons for the slow spinning of the Ir^I•COD included in **C5** are not clear to us. There are no apparent steric clashes between the guest and the host that could slow down the spinning process. We expect the existence of attractive forces between the electron rich inner surface of the cavitand and the outer electron-poor surface of the cationic organometallic complex (cation-π and CH-π interactions). Most likely, as the guest rotates around host's axial axis some of CH-π interactions weaken and the energy of the complex increases to a transition state close to 45º; further rotation leads to the next energy degenerated minimum found at 90º from the starting point. The pattern of cross peaks due to chemical exchange of amide NH signals evidenced that the spinning and the cycloenantiomerization processes were both slow on the ^{1}H NMR timescale. Unfortunately, the cross-peak overlap for different processes and the existence of an additional in-out chemical exchange process involving NH signals prohibited determination of corresponding energy barriers. Interestingly, the EXSY experiment (see Supporting

Information) showed a beautiful and clean pattern of cross peaks between diastereotopic protons of the included guest owing to the interconversion process between two cycloenantiomers of the container. We determined the barrier for the cycloenantiomerization process in the Ir^{I}•COD⊂**C5** complex to be ΔG = 19 kcal mol^{-1} (298 K) from integrals of diagonal and cross peaks corresponding to protons of the included guest.

From a separate EXSY experiment (see Supporting Information) performed on a solution of **C5** containing a large excess of the Ir^{I}•COD complex (10 equiv) and using selected exchange signals between the free and bound guest, we calculated an energy barrier for the in-out exchange process of ΔG = 17 kcal mol^{-1} (298 K).

The observed slow exchange for the in-out process is a surprising result owing to the open end of the container and a perfect accommodation of the included Ir^{I}•COD. As already reported by Rebek *et al.*,[6,8] the exchange dynamics must be controlled by the mechanism of *hostage exchange* and not by the thermodynamic stability of the complex. The lowest energy pathway for the in-out exchange of the included guest requires the bound host to change conformation from *vase* to *kite*. To pull apart the vase conformer four *interannular* hydrogen bonds must be broken and this raises the energetic price of the motion. The coincidence in energy barriers for the interconversion between the change in the sense of direction of the amide carbonyls and the exchange between the free and bound guest support this mechanism.[8,19]

When the temperature is raised to 333 K (**Fig. 31**, a), diastereotopic aromatic proton signals of the bound cavitand showed coalescence and only two broad signals were observed for NH protons. This observation indicates that while the axial rotation of the included guest is fast on the NMR timescale, the interconversion between two cycloenantiomers of the bound **C5** was still slow. Consequently, the number of signals for protons of the included guest was maintained from the room temperature up to 333 K.

Finally, lowering the temperature below 213 K (**Fig. 31**, c) induced the splitting of most signals for protons in the bound host and in the included guest. A likely explanation has to do with the existence of slow exchange on the ^{1}H NMR timescale between two chiral TB conformations of the chelated COD ligand in the included Ir^{I}•COD complex. When this process becomes slow on the NMR timescale, a new asymmetry element (persistent conformational chirality) is added to the inclusion complex (THF-d_8)$_2$•Ir^{I}•COD⊂**C5** in addition to the one provided by the unidirectional orientation of amide groups. In short, at 213 K the (THF-d_8)$_2$•Ir^{I}•COD⊂**C5** complex is present in solution as a mixture of two racemic diastereoisomers (**Fig. 33**).[20,21]

Using the coalescence temperature method, we calculated the energy barrier for the TB-to-TB exchange in the chelated COD included in the **C5** to be ΔG = 8.6 kcal mol^{-1}. This value corresponds to an increase of close to 4 kcal mol^{-1} compared to the same process for

the COD free in solution. We suggest that a diminution of attractive CH-π interactions on moving from the ground-state to the transition-state and/or the worst fit of the transition-state in the cavitand **C5** could be responsible for the larger energy barrier measured for the TB-to-TB conformational exchange in the included Ir^{I}•COD.

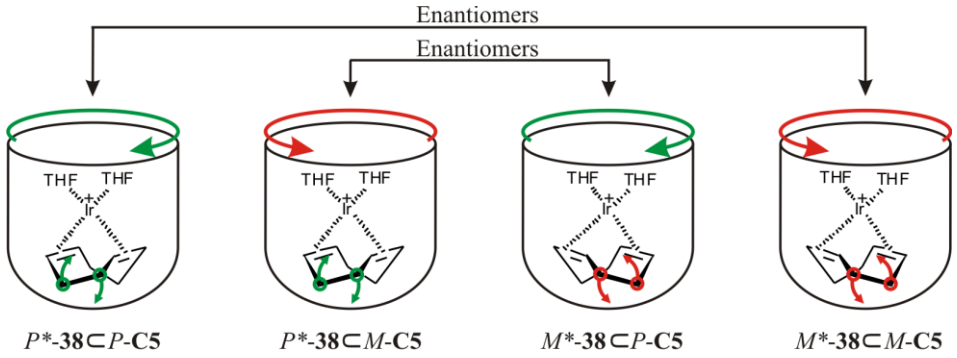

Fig. 33. Diastereoisomeric forms of $(THF)_2$•Ir^{I}•COD⊂**C5**, **38**⊂**C5** caviplex. Chiralities of amide upper rim of the host **C5** and the COD ligand of the guest **38** are depicted with colored arrows.

To assess thermodynamic characteristics of the $(CH_3CN)_2$•Ir^{I}•COD⊂**C5**, **39**⊂**C5** complex we first determined integral values for free and bound species at all temperatures where these signals were integrable. The best diagnostic signals for the free and the bound host were NH proton signals. Likewise, we determined integral values for the free organometallic complex $(CH_3CN)_2$•Ir^{I}•COD, **39** by integrating alkene proton signal from the coordinated COD and normalized it by dividing it by two. The bound Ir^{I} complex we determined by integrating a signal belonging to COD methylene proton Hb'. From ratios of the free and the bound host, as well as from ratios of the free and the bound guest we obtained the fraction values for each component. Multiplying these fractions to initial concentrations of the host and the guest, we obtained their equilibria concentrations at each temperature. Using the formula below, we calculated an equilibria constant for each temperature.

$$K_{\mathrm{eq}} = \frac{[\mathrm{Ir^{I}} \bullet \mathrm{COD}\subset\mathbf{C5}]}{[\mathbf{C5}][\mathrm{Ir^{I}} \bullet \mathrm{COD}]}$$

By plotting calculated equilibria constants in the function of inverse temperatures we constructed the Van't Hoff plot (**Fig. 34**) and from the linear fit we determined the intercept and the slope.

To calculate the enthalpy (ΔH), the entropy (ΔS) and the free energy (ΔG) of the $(CH_3CN)_2$•Ir^{I}•COD⊂**C5** complex, we combined equation for the Gibbs free energy

$$\Delta G = \Delta H - \mathrm{T}\Delta S$$

with Gibbs free energy isotherm equation

$$\Delta G = \mathrm{RT}\ln(K_{\mathrm{eq}})$$

where R is a gas constant (1.987 cal mol^{-1} K^{-1}). This gave us

$$\ln(K_{\mathrm{eq}}) = -\frac{\Delta H}{\mathrm{RT}} + \frac{\Delta S}{\mathrm{R}}$$

from this equation follows that

$$\Delta H = -\mathrm{R} * \mathrm{slope} = -1.987\ \mathrm{cal\ mol^{-1}K^{-1}} * (-2951.23\ \mathrm{K}) = 5.9\ \mathrm{kcal\ mol^{-1}}$$

$$\Delta S = \mathrm{R} * \mathrm{intercept} = -1.987\ \mathrm{cal\ mol^{-1}K^{-1}} * 17.04 = 33.9\ \mathrm{cal\ mol^{-1}K^{-1}}$$

at room temperature (298 K) we have

$$\Delta G(298\ \mathrm{K}) = \Delta H - 298 * \Delta S$$

$$\Delta G(298\ \mathrm{K}) = 5.9 - 298 * 0.0339 = 5.9 - 10.1 = -4.2\ \mathrm{kcal\ mol^{-1}}$$

These values show that formation of inclusion complex is endothermic and driven by the entropy.

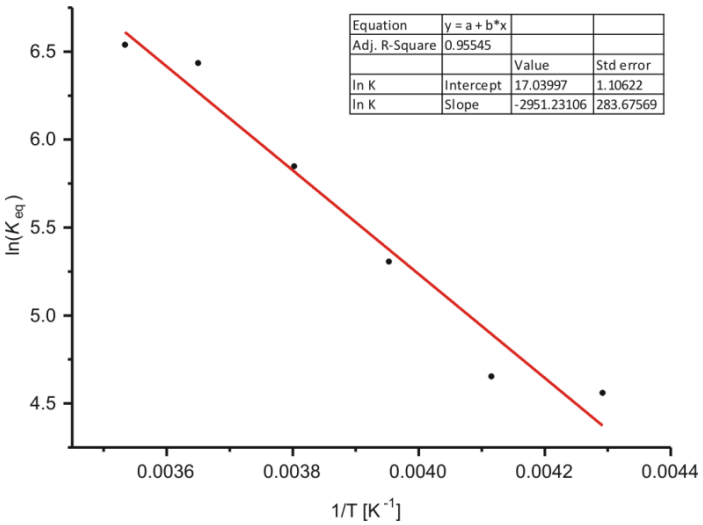

Fig. 34. Van't Hoff plot for **39**$^{+}$⊂**C5** system.

Finally, by adding incremental amounts of the NBD ligand to a solution containing the host/guest complex $(CH_3CN)_2$•Ir^{I}•COD⊂**C5** we observed gradual disappearance of four upfield signals of the included COD, being replaced by two singlets. Likewise, four NH proton signals were replaced by singlets of two new species possessing the same ratio for

integrals as observed for their corresponding upfield signals. Finally, eight diastereotopic aromatic proton signals ($H^{1,2}$, H^3 and H^4) merged producing two sets of three singlets for each of the two present species.

As expected, the NBD ligand fully transligates COD ligand producing two new host/guest complexes Ir^{I}•$(NBD)_2$⊂**C5** and $(THF\text{-}d_8)_2$•Ir^{I}•NBD⊂**C5** in 4.5 to 1 ratio. Furthermore, singlets corresponding to amide NHs in both complexes indicated restoration of C_{4v} symmetry and fast chemical exchange betweeen two cycloenantiomers. To the best of our knowledge, there are only few reports for the synthesis of the $Ir^{I}(NBD)_2$ complexes.[22,23] We conclude that the obtained inclusion complexes were a combination of the mono- and bis-NBD chelated Ir^{I}. This result was in complete agreement with our previous report on the inclusion of Rh^{I}•$(NBD)_2$ by the host **C5**.[1]

2.3 Conclusions

Using experimental and theoretical studies, we characterized caviplex **38⊂C5**. VT ^{1}H NMR studies allowed us to calculate the increase of TB-to-TB conformational exchange barrier caused by the constrained space of the host **C5**. Results showed an increase of close to 4 kcal mol^{-1} compared to free COD. The reduced rate of exchange between two COD TB conformers gave us a unique opportunity to study persistent conformational chirality of coordinated COD as well as a whole system's motional dynamics.

2.4 Experimental section

2.4.1 General information and instrumentation

All reagents and solvents were obtained from commercial suppliers and were used without further purification unless otherwise stated. Compounds **C5**, **37** and **39** were synthesized according to published procedures.[6,24,25] ^{1}H, NOESY (EXSY), ROESY, HSQC and VT NMR spectra were recorded on a Bruker Avance 400 or a Bruker Avance 500 spectrometer. Deuterated THF was purchased from Deutero GmbH and dried over sodium prior to use, while deuterated methylene chloride was purchased from Sigma-Aldrich and used without any purification. Chemical shifts are given in ppm and peaks were referenced relative to the solvent residual peak (δ_{CDCl3} = 7.28 ppm, δ_{CD2Cl2} = 5.32 ppm, $\delta_{THF\text{-}d8}$ = 1.73 and 3.58 ppm). Handling with air and moisture sensitive complexes was performed in the glovebox under nitrogen atmosphere and samples transferred to a J. Young NMR tube.

2.5 Supporting information

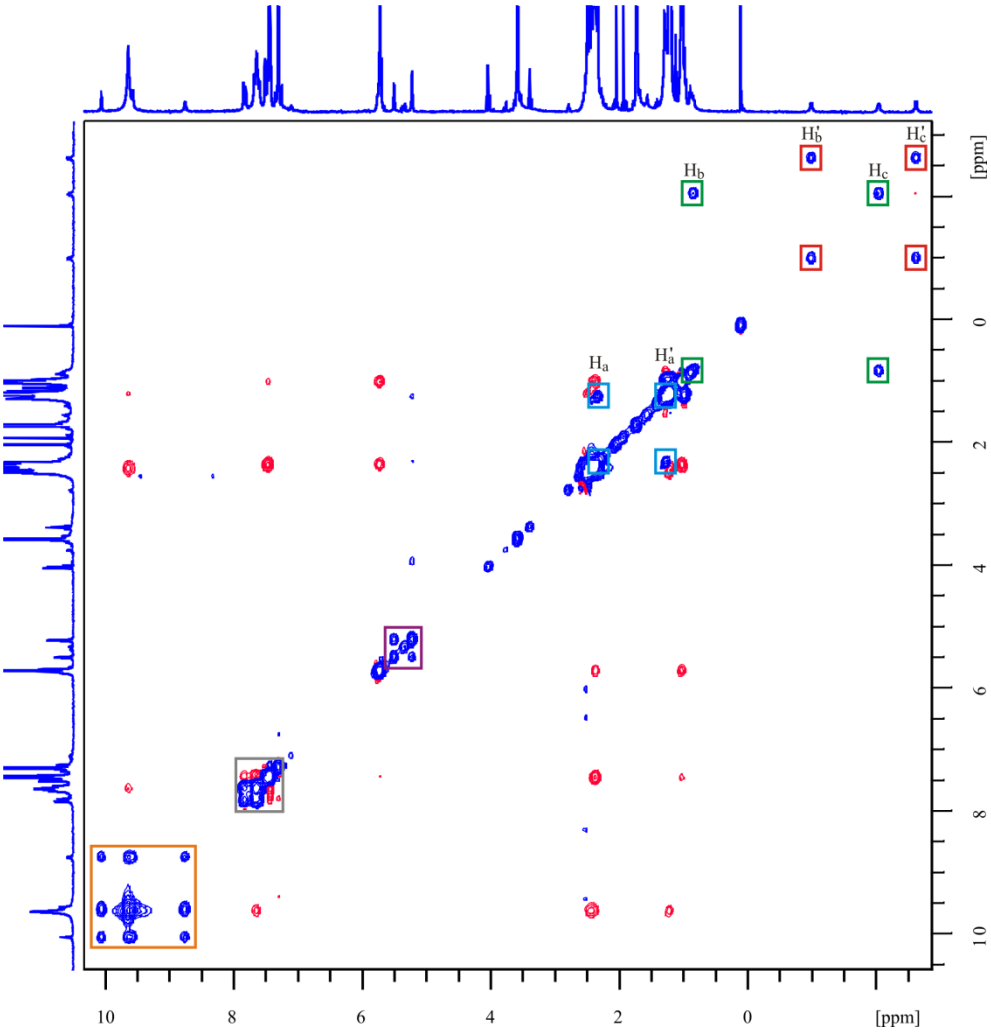

Fig. 35. ^{1}H-^{1}H NOESY NMR spectrum (d8 = 300 ms) of a mixture of host **C5** and host/guest complex (THF-d_8)$_2$•Ir^{I}•COD⊂**C5**, **38**⊂**C5**, prepared by dissolving a cavitand **C5** (2.2 µmol) and an organometallic complex Ir^{I}•(COD)$_2$, **37** (1.8 µmol) in THF-d_8 (550 µL).

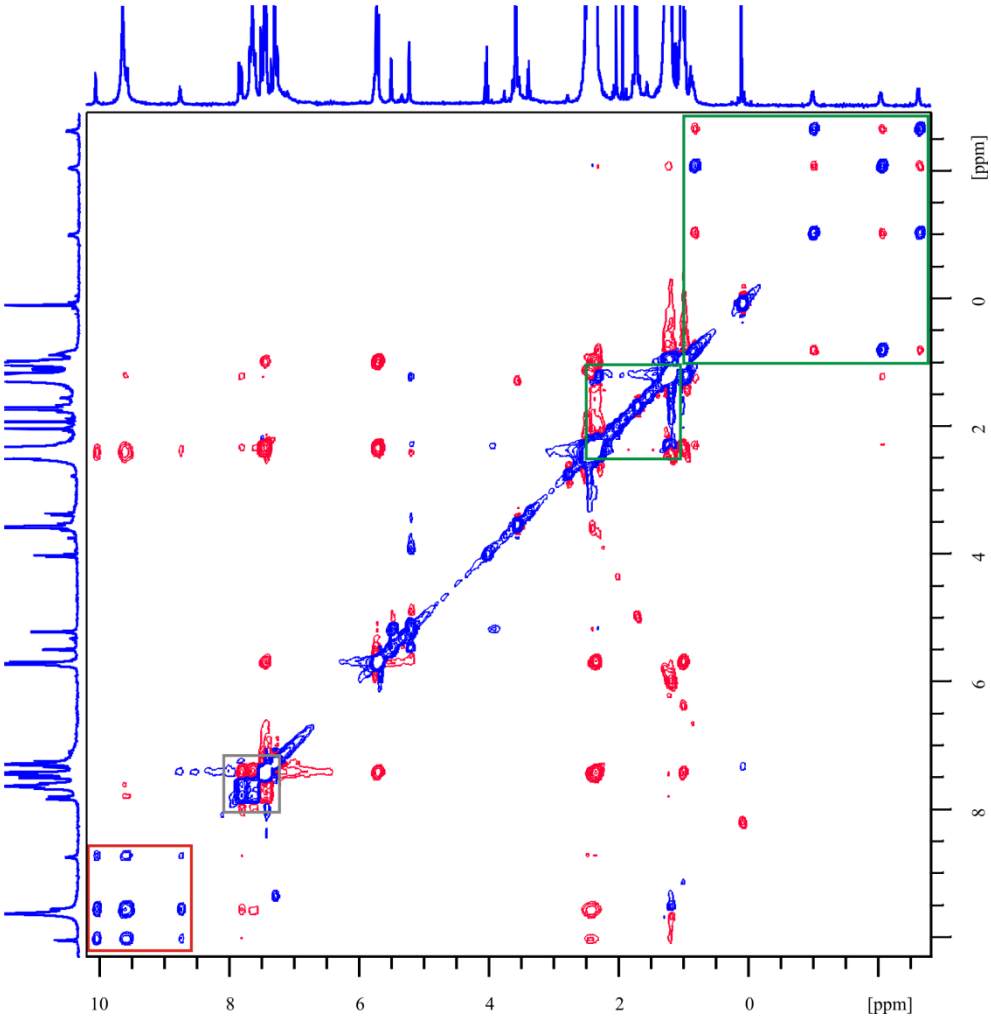

Fig. 36. ^{1}H-^{1}H ROESY NMR spectrum (p15 = 300 ms) of a mixture of host **C5** and host/guest complex (THF-d_8)$_2$•Ir^{I}•COD⊂**C5**, **38**⊂**C5**, prepared by dissolving a cavitand **C5** (2.2 μmol) and an organometallic complex Ir^{I}•(COD)$_2$, **37** (1.8 μmol) in THF-d_8 (550 μL). Chemically exchanging protons are marked in blue, while proximity (NOE) protons in red.

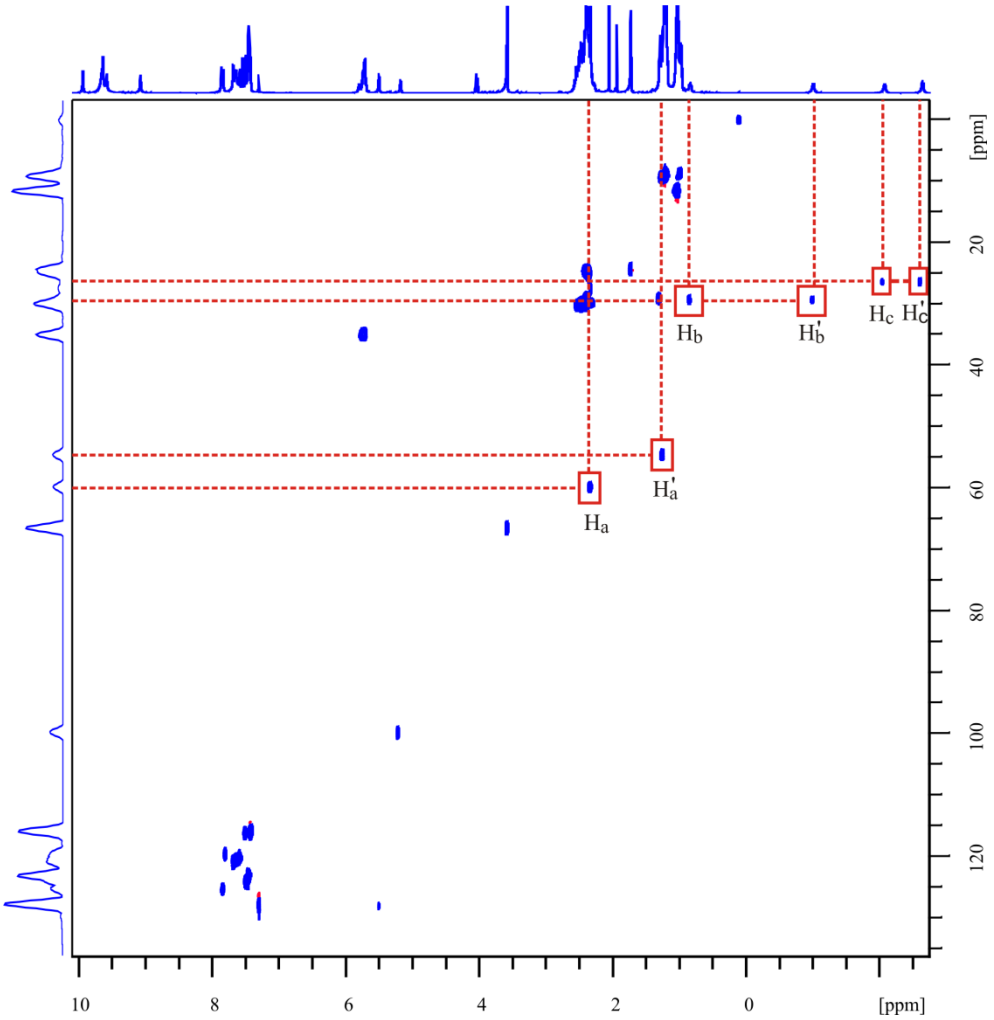

Fig. 37. ^{1}H-^{13}C HSQC NMR spectrum of a mixture of host **C5** and host/guest complex (THF-d_8)$_2$•Ir^{I}•COD⊂**C5**, **38**⊂**C5**, prepared by dissolving a cavitand **C5** (2.2 μmol) and an organometallic complex Ir^{I}•(COD)$_2$, **37** (1.8 μmol) in THF-d_8 (550 μL).

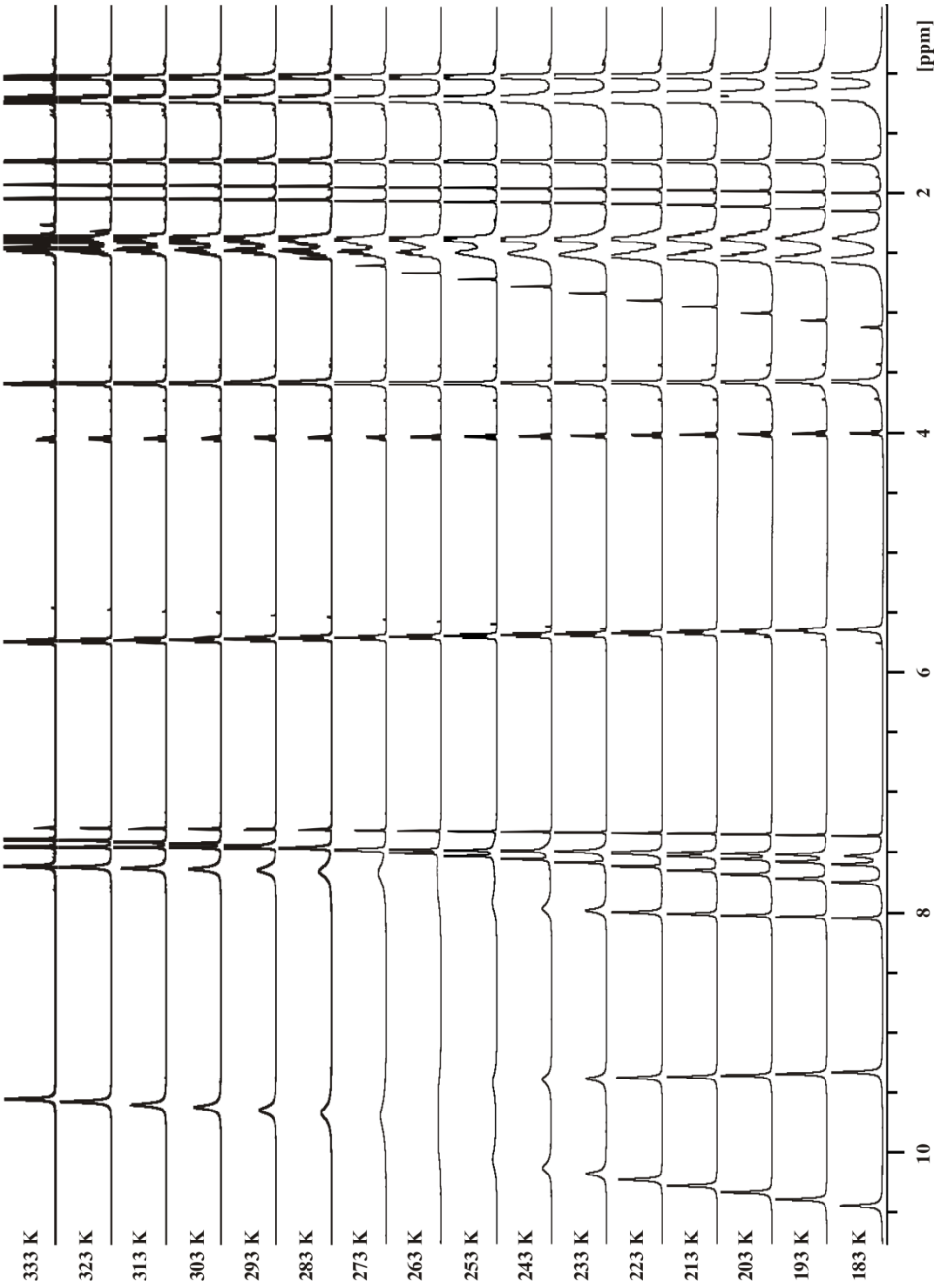

Fig. 38. Full VT ^{1}H NMR profile for a host **C5** (2.2 μmol) dissolved in THF-d_8 (550 μL).

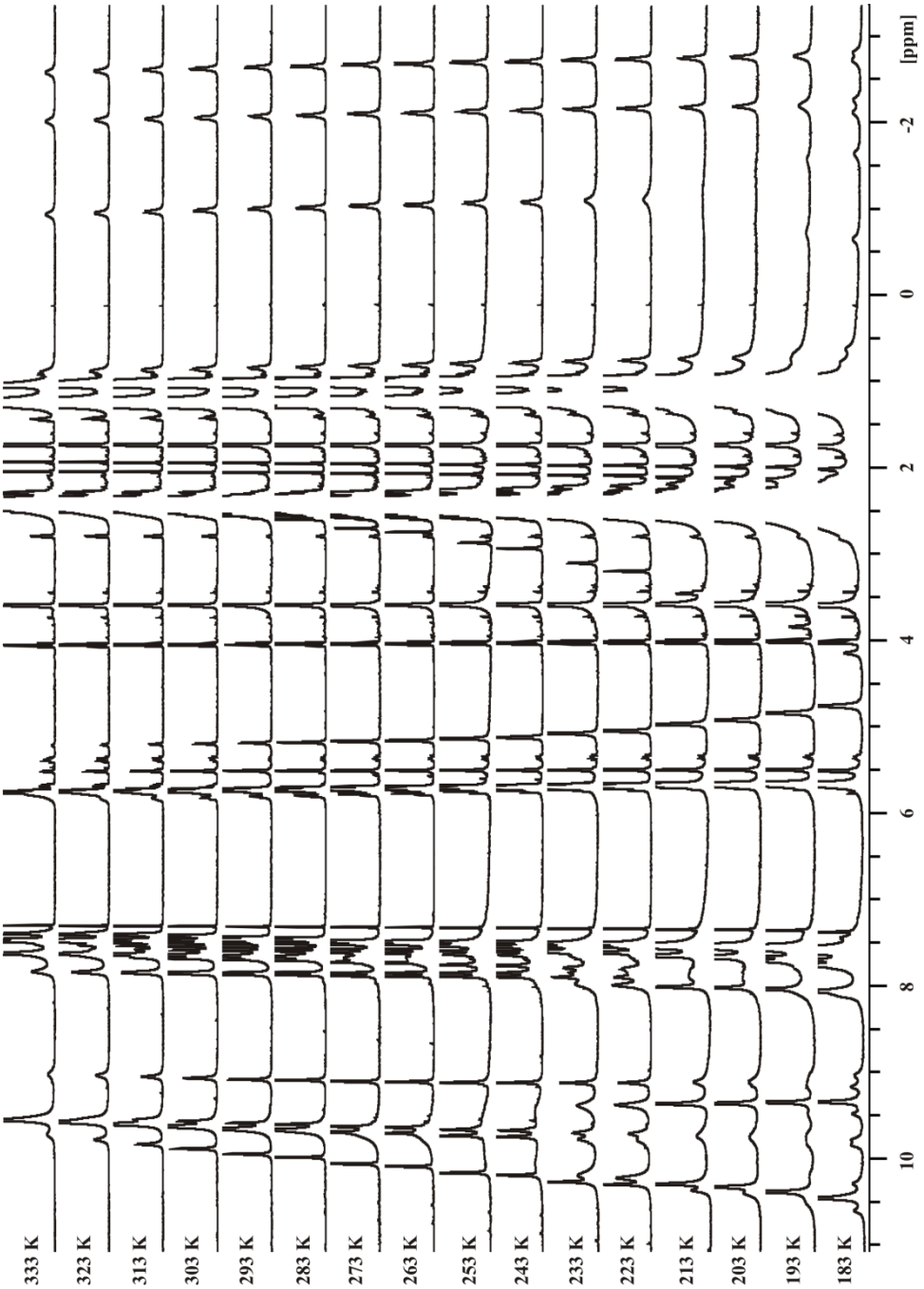

Fig. 39. Full VT ^{1}H NMR profile for a mixture of host **C5** and host/guest complex (THF-d_8)$_2$•Ir^{I}•COD⊂**C5**, **38**⊂**C5**, prepared by dissolving a cavitand **C5** (2.2 μmol) and an organometallic complex Ir^{I}•(COD)$_2$, **37** (1.8 μmol) in THF-d_8 (550 μL).

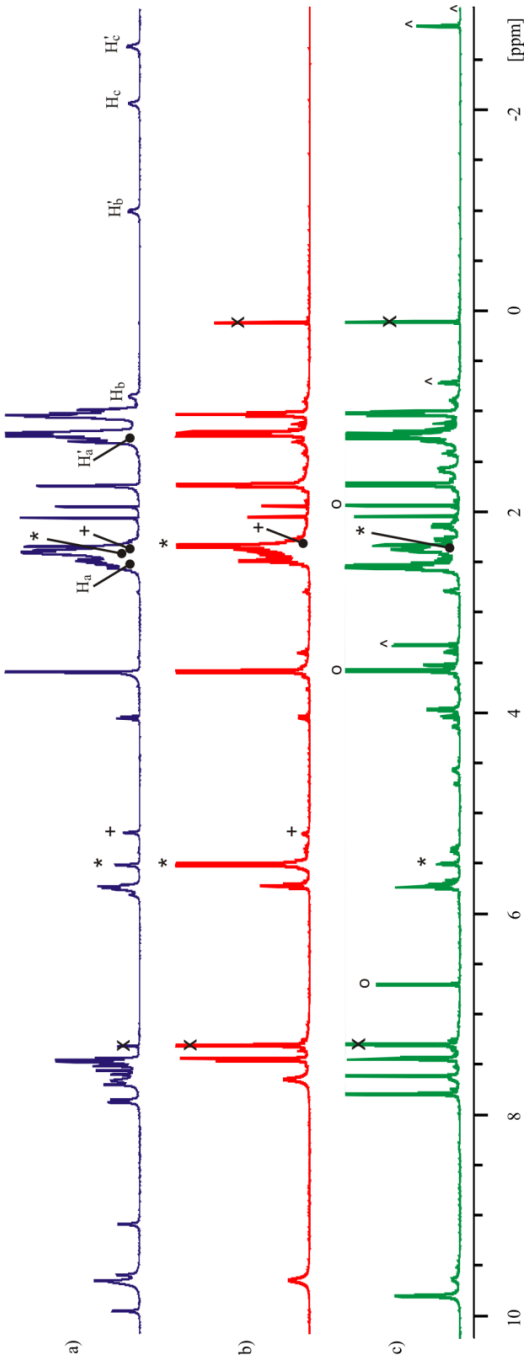

Fig. 40. Titration of: (a) a mixture of host **C5** and host/guest complex (THF-d_8)$_2$•Ir^I•COD⊂**C5**, **38**⊂**C5** prepared by dissolving a cavitand **C5** (2.2 μmol) and an organometallic complex Ir^I•(COD)$_2$, **37** (1.8 μmol) in THF-d_8 (550 μL) with (b) 10 equiv. of COD, and (c) 3.2 equiv. of NBD. Designations: * - the free COD; + - the free Ir^I•(COD)$_2$, **37**; o - the free NBD; ^ - inclusion signals for a mixture of host **C5** and host/guest complexes Ir^I•(NBD)$_2$⊂**C5** and (THF-d_8)$_2$•Ir^I•(NBD)$_2$⊂**C5**; X - artefact.

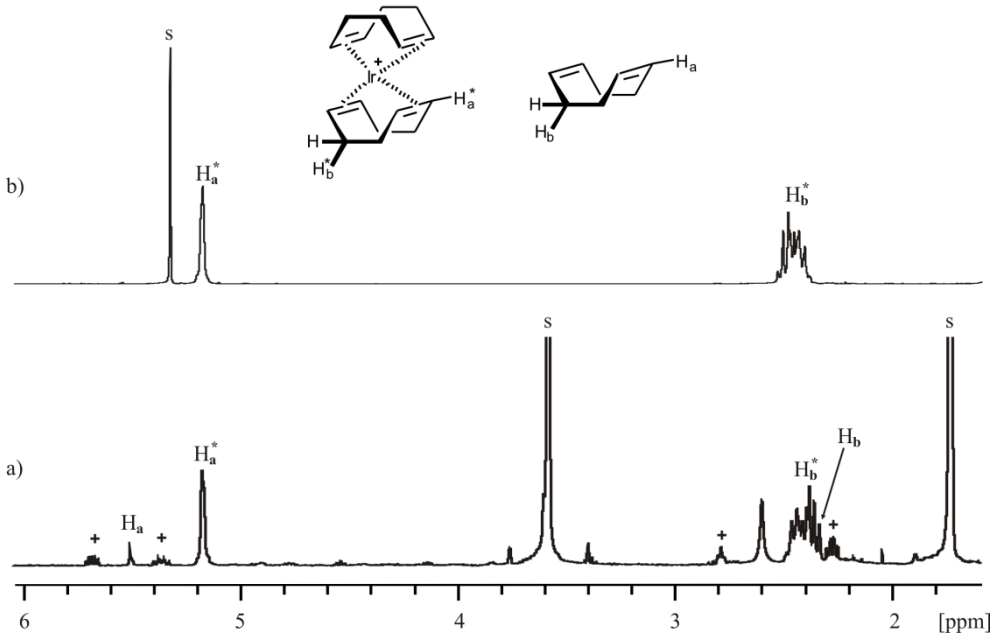

Fig. 41. ^{1}H NMR spectra of the guest Ir^I•$(COD)_2$, **37** dissolved in: a) THF-d_8 and b) methylene chloride-d_2. Designations: s - solvent residual signal(s); + - signals belonging to partially transligated complex **37**.

Table 1. DFT calculation data for the simplified version of **38**⊂**C5** (ethyl groups were replaced by methyl and THF ligands were replaced by dimethyl ether molecules) performed at PB86 level of theory using def2svp basis set.

Row	Symbol	X	Y	Z	Row	Symbol	X	Y	Z
1	C	2.5574	-0.5861	-4.9762	21	C	3.9543	3.3116	0.8373
2	C	2.6522	-1.8881	-4.4467	22	C	4.7135	2.1057	0.8478
3	C	3.4824	-2.0605	-3.316	23	C	4.9813	1.4537	-0.3768
4	C	4.182	-0.9824	-2.7537	24	C	4.4946	1.9478	-1.5955
5	C	4.0481	0.3017	-3.3031	25	C	-2.5574	0.5861	-4.9762
6	C	3.236	0.5271	-4.4391	26	C	-2.6522	1.8881	-4.4467
7	C	3.1423	-3.7293	-1.6205	27	C	-3.4824	2.0605	-3.316
8	C	3.8137	-3.4868	-0.4169	28	C	-4.182	0.9824	-2.7537
9	C	3.3154	-3.9473	0.819	29	C	-4.0481	-0.3017	-3.3031
10	C	2.1037	-4.6968	0.8374	30	C	-3.236	-0.5271	-4.4391
11	C	1.4457	-4.9623	-0.3839	31	C	-3.1423	3.7293	-1.6205
12	C	1.9391	-4.4802	-1.6036	32	C	-3.8137	3.4868	-0.4169
13	C	0.6102	2.5556	-4.9728	33	C	-3.3154	3.9473	0.819
14	C	1.9111	2.6645	-4.4428	34	C	-2.1037	4.6968	0.8374
15	C	2.0767	3.4929	-3.3099	35	C	-1.4457	4.9623	-0.3839
16	C	0.992	4.1877	-2.7542	36	C	-1.9391	4.4802	-1.6036
17	C	-0.2902	4.0431	-3.3065	37	C	-0.6102	-2.5556	-4.9728
18	C	-0.5105	3.2229	-4.4382	38	C	-1.9111	-2.6645	-4.4428
19	C	3.7449	3.1535	-1.6074	39	C	-2.0767	-3.4929	-3.3099
20	C	3.4988	3.8178	-0.3993	40	C	-0.992	-4.1877	-2.7542

Row	Symbol	X	Y	Z	Row	Symbol	X	Y	Z
41	C	0.2902	-4.0431	-3.3065	87	O	-0.6825	-5.0555	1.8049
42	C	0.5105	-3.2229	-4.4382	88	C	0.1885	-6.0968	3.8112
43	C	-3.7449	-3.1535	-1.6074	89	H	4.8715	-1.1492	-1.9157
44	C	-3.4988	-3.8178	-0.3993	90	C	3.1157	1.9308	-5.0424
45	C	-3.9543	-3.3116	0.8373	91	H	4.7703	-2.946	-0.4398
46	C	-4.7135	-2.1057	0.8478	92	H	0.5338	-5.5715	-0.3751
47	C	-4.9813	-1.4537	-0.3768	93	H	1.1518	4.8819	-1.9186
48	C	-4.4946	-1.9478	-1.5955	94	C	-1.9124	3.0905	-5.0464
49	O	3.686	-3.3497	-2.8259	95	H	2.9508	4.7707	-0.4163
50	O	1.3406	-4.8097	-2.8006	96	H	5.5955	0.5445	-0.3732
51	O	-3.363	-3.7012	-2.8109	97	H	-4.8715	1.1492	-1.9157
52	C	-4.3575	-4.4108	3.0717	98	C	-3.1157	-1.9308	-5.0424
53	C	-5.4147	-0.3388	2.4903	99	H	-4.7703	2.946	-0.4398
54	O	-4.8188	-1.3481	-2.7928	100	H	-0.5338	5.5715	-0.3751
55	O	-3.686	3.3497	-2.8259	101	H	-1.1518	-4.8819	-1.9186
56	C	-4.4547	4.3805	3.031	102	C	1.9124	-3.0905	-5.0464
57	C	-0.318	5.4032	2.4595	103	H	-2.9508	-4.7707	-0.4163
58	O	-1.3406	4.8097	-2.8006	104	H	-5.5955	-0.5445	-0.3732
59	O	3.363	3.7012	-2.8109	105	H	4.5514	-2.664	1.8977
60	O	4.8188	1.3481	-2.7928	106	H	2.3977	-5.5208	2.6919
61	N	4.0797	-3.5852	1.9711	107	H	-2.6478	-4.5145	1.9296
62	N	1.615	-5.2058	2.0639	108	H	-5.5734	-2.4197	2.6828
63	N	-3.576	-4.0536	1.9973	109	H	-4.5514	2.664	1.8977
64	N	-5.2502	-1.6273	2.0669	110	H	-2.3977	5.5208	2.6919
65	N	-4.0797	3.5852	1.9711	111	H	2.6478	4.5145	1.9296
66	N	-1.615	5.2058	2.0639	112	H	5.5734	2.4197	2.6828
67	N	3.576	4.0536	1.9973	113	H	-4.3698	-6.3538	3.9769
68	N	5.2502	1.6273	2.0669	114	H	-2.7001	-5.7019	3.7476
69	C	-3.7435	-5.4355	4.0091	115	H	-3.7906	-5.0543	5.0513
70	O	-5.4969	-3.962	3.2806	116	H	-5.6405	0.4378	4.5031
71	O	-4.9792	0.6644	1.8891	117	H	-7.167	0.2819	3.5853
72	C	-6.1938	-0.2146	3.7949	118	H	-6.3995	-1.1911	4.2807
73	O	-3.975	5.5023	3.2577	119	H	-5.7974	2.7506	3.6775
74	O	0.6825	5.0555	1.8049	120	H	-6.4521	4.4279	3.8072
75	C	-5.5404	3.801	3.9222	121	H	-5.2302	3.8853	4.9852
76	C	-0.1885	6.0968	3.8112	122	H	-1.1644	6.3178	4.2913
77	C	4.3575	4.4108	3.0717	123	H	0.3614	7.0531	3.6741
78	O	5.4969	3.962	3.2806	124	H	0.418	5.4652	4.4952
79	C	3.7435	5.4355	4.0091	125	H	2.7001	5.7019	3.7476
80	C	5.4147	0.3388	2.4903	126	H	4.3698	6.3538	3.9769
81	O	4.9792	-0.6644	1.8891	127	H	3.7906	5.0543	5.0513
82	C	6.1938	0.2146	3.7949	128	H	5.6405	-0.4378	4.5031
83	C	4.4547	-4.3805	3.031	129	H	7.167	-0.2819	3.5853
84	C	5.5404	-3.801	3.9222	130	H	6.3995	1.1911	4.2807
85	O	3.975	-5.5023	3.2577	131	H	6.4521	-4.4279	3.8072
86	C	0.318	-5.4032	2.4595	132	H	5.2302	-3.8853	4.9852

Row	Symbol	X	Y	Z	Row	Symbol	X	Y	Z
133	H	5.7974	-2.7506	3.6775	167	C	1.3179	0.8026	0.0507
134	H	-0.418	-5.4652	4.4952	168	H	1.2855	-2.2035	1.9053
135	H	1.1644	-6.3178	4.2913	169	H	0.2565	-2.2099	-0.5806
136	H	-0.3614	-7.0531	3.6741	170	C	-1.3179	-0.8026	0.0507
137	H	-2.4717	3.9851	-4.7091	171	H	-2.5171	0.1121	1.6967
138	C	-1.9134	3.0999	-6.5867	172	H	-1.2855	2.2035	1.9053
139	H	-4.0097	-2.486	-4.6969	173	H	-0.2565	2.2099	-0.5806
140	C	-3.1333	-1.9407	-6.5825	174	H	0.7198	2.784	0.7817
141	C	1.9134	-3.0999	-6.5867	175	H	2.5171	-0.1121	1.6967
142	H	2.4717	-3.9851	-4.7091	176	H	2.2806	1.2979	-0.1749
143	H	4.0097	2.486	-4.6969	177	H	1.056	0.2192	-0.857
144	C	3.1333	1.9407	-6.5825	178	H	-0.7198	-2.784	0.7817
145	H	1.9263	-0.4302	-5.8649	179	H	-2.2806	-1.2979	-0.1749
146	H	0.4623	1.9213	-5.8604	180	H	-1.056	-0.2192	-0.857
147	H	-1.9263	0.4302	-5.8649	181	Ir	0	0	2.727
148	H	-0.4623	-1.9213	-5.8604	182	O	1.3432	-0.576	4.4622
149	H	-1.3773	2.236	-7.0359	183	O	-1.3432	0.576	4.4622
150	H	-2.9568	3.0768	-6.9689	184	C	1.9218	0.5934	5.0705
151	H	-1.4274	4.0249	-6.9652	185	C	2.264	-1.6783	4.4013
152	H	-3.1145	-2.9863	-6.9589	186	C	-1.9218	-0.5934	5.0705
153	H	-2.271	-1.4087	-7.0395	187	C	-2.264	1.6783	4.4013
154	H	-4.0595	-1.455	-6.9586	188	H	2.746	1.0004	4.4414
155	H	2.9568	-3.0768	-6.9689	189	H	2.3072	0.3286	6.0816
156	H	1.3773	-2.236	-7.0359	190	H	1.1113	1.3408	5.1669
157	H	1.4274	-4.0249	-6.9652	191	H	3.0906	-1.4694	3.6858
158	H	3.1145	2.9863	-6.9589	192	H	2.6736	-1.863	5.4198
159	H	2.271	1.4087	-7.0395	193	H	1.6955	-2.5669	4.0669
160	H	4.0595	1.455	-6.9586	194	H	-2.746	-1.0004	4.4414
161	C	0.7921	-1.3868	1.343	195	H	-2.3072	-0.3286	6.0816
162	C	-0.2492	-1.8738	0.3553	196	H	-1.1113	-1.3408	5.1669
163	C	-1.5143	0.15	1.2282	197	H	-3.0906	1.4694	3.6858
164	C	-0.7921	1.3868	1.343	198	H	-2.6736	1.863	5.4198
165	C	0.2492	1.8738	0.3553	199	H	-1.6955	2.5669	4.0669
166	C	1.5143	-0.15	1.2282					

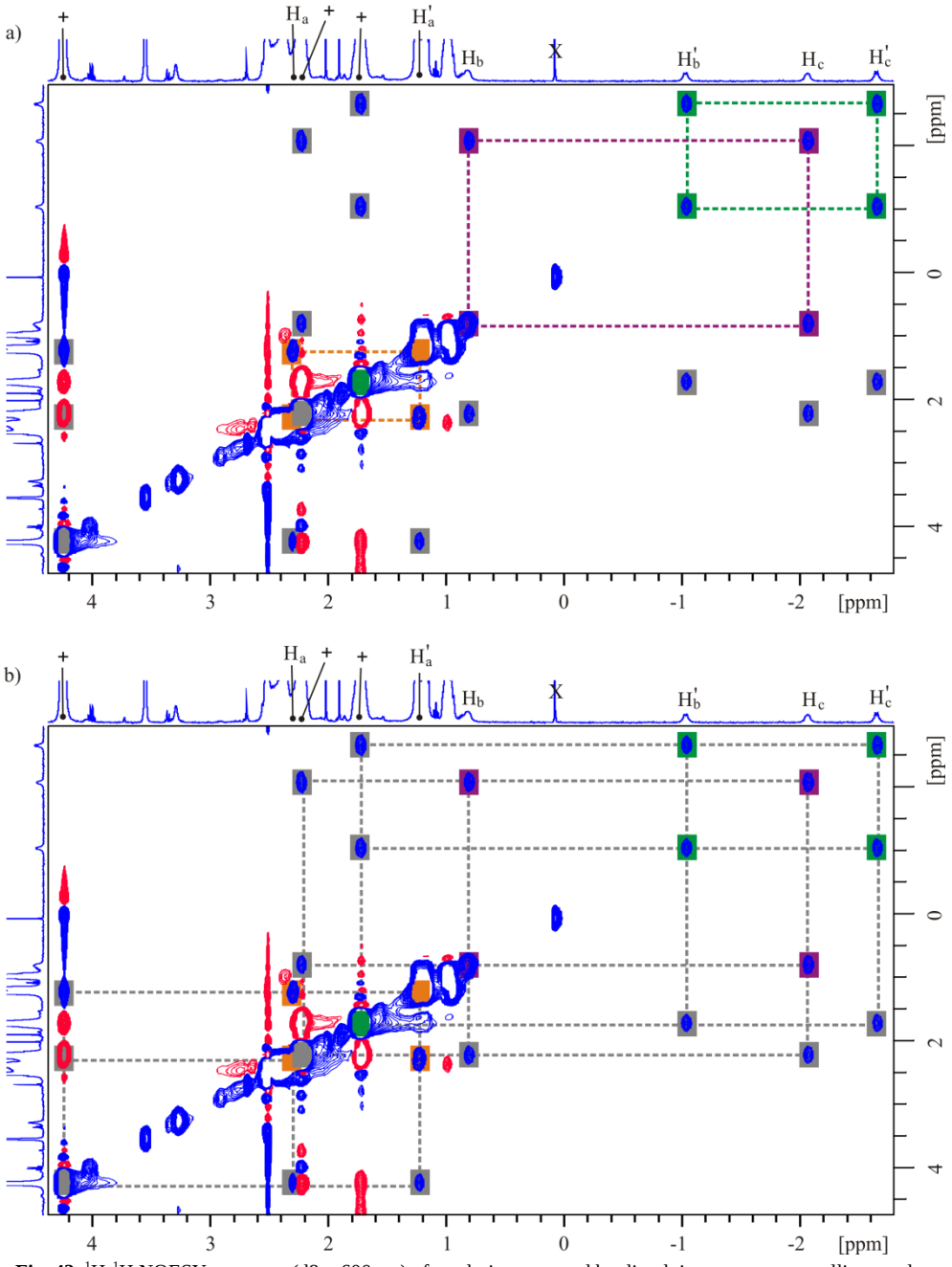

Fig. 42. ^{1}H-^{1}H NOESY spectrum (d8 = 600 ms) of a solution prepared by dissolving an organometallic complex $(CH_3CN)_2$•Ir^{I}•COD, **39** (4.2 μmol) and a cavitand **C5** (0.4 μmol) in THF-d_8 (500 μL): Cross-peaks related to: a) cycloenantiomerism, and b) organometallic complex in-out exchange. Designations: + - free organometallic complex $(CH_3CN)_2$•Ir^{I}•COD, **39**, X - artefact.

Table 2. Integral, percent and concentration values determined for the free and the bound cavitand **C5** at different temperatures.

	NH integrals		calculated %		concentrations [M]	
T [K]	free **C5**	bound **C5**	free **C5**	bound **C5**	free **C5**	bound **C5**
283	6.05	1.36	22.48	77.52	3.1E-03	9.0E-04
274	13.00	4.00	30.77	69.23	2.8E-03	1.2E-03
263	16.00	4.00	25.00	75.00	3.0E-03	1.0E-03
253	16.50	3.20	19.39	80.61	3.2E-03	7.8E-04
243	30.60	4.30	14.05	85.95	3.4E-03	5.6E-04
233	34.60	4.20	12.14	87.86	3.5E-03	4.9E-04

Table 3. Integral, percent and concentration values determined for the free and the bound organometallic complex Ir^{I}•COD at different temperatures.

	Ir^{I} integrals		calculated %		concentrations [M]	
T [K]	free Ir^{I}	bound Ir^{I}	free Ir^{I}	bound Ir^{I}	free Ir^{I}	bound Ir^{I}
283	0.34	0.05	12.82	87.18	4.2E-04	2.9E-03
274	1.00	0.28	21.81	78.19	7.1E-04	2.6E-03
263	0.92	0.38	29.42	70.58	9.6E-04	2.3E-03
253	0.81	0.47	36.47	63.53	1.2E-03	2.1E-03
243	1.00	0.91	47.64	52.36	1.6E-03	1.7E-03
233	1.10	0.87	44.16	55.84	1.4E-03	1.8E-03

Table 4. Calculated values for $\ln(K_{eq})$ in the function of the inverse temperature.

T [K]	K_{eq}	1/T [K^{-1}]	$\ln(K_{eq})$
283	691.7	0.0035	6.54
274	623.1	0.0036	6.43
263	346.5	0.0038	5.85
253	201.7	0.0040	5.31
243	104.9	0.0041	4.65
233	95.7	0.0043	4.56

2.6 References and notes

[1] M. A. Sarmentero, H. Fernández-Pérez, E. Zuidema, C. Bo, A. Vidal-Ferran and P. Ballester, *Angew. Chem., Int. Ed.*, 2010, **49**, 7489-7492.
[2] R. G. Chapman and J. C. Sherman, *J. Org. Chem.*, 2000, **65**, 513-516.

[3] J. R. Moran, J. L. Ericson, E. Dalcanale, J. A. Bryant, C. B. Knobler and D. J. Cram, *J. Am. Chem. Soc.*, 1991, **113**, 5707-5714.
[4] D. J. Cram, H. J. Choi, J. A. Bryant and C. B. Knobler, *J. Am. Chem. Soc.*, 1992, **114**, 7748-7765.
[5] J. R. Moran, J. L. Ericson, E. Dalcanale, J. A. Bryant, C. B. Knobler and D. J. Cram, *J. Am. Chem. Soc.*, 1991, **113**, 5707-5714.
[6] D. M. Rudkevich, G. Hilmersson and J. Rebek, *J. Am. Chem. Soc.*, 1998, **120**, 12216-12225.
[7] J. R. Moran, S. Karbach and D. J. Cram, *J. Am. Chem. Soc.*, 1982, **104**, 5826-5828.
[8] D. M. Rudkevich, G. Hilmersson and J. Rebek, *J. Am. Chem. Soc.*, 1997, **119**, 9911-9912.
[9] K. Hagen, L. Hedberg and K. Hedberg, *J. Phys. Chem.*, 1982, **86**, 117-121.
[10] W. R. Rocha and W. B. De Almeida, *J. Comput. Chem.*, 1997, **18**, 254-259.
[11] F. A. L. Anet and L. Kozerski, *J. Am. Chem. Soc.*, 1973, **95**, 3407-3408.
[12] O. Ermer, *J. Am. Chem. Soc.*, 1976, **98**, 3964-3970.
[13] O. Pattawong, M. Q. Salih, N. T. Rosson, C. M. Beaudry and P. H.-Y. Cheong, *Org. Biomol. Chem.*, 2014, **12**, 3303-3309.
[14] L. Lunazzi, M. Mancinelli and A. Mazzanti, *J. Org. Chem.*, 2008, **73**, 5354-5359.
[15] M. S. Abbassioun, P. B. Hitchcock and P. A. Chaloner, Acta Crystallogr. Sect. C, 1989, **45**, 953-954.
[16] D. H. Woodmansee, M.-A. Muller, M. Neuburger and A. Pfaltz, *Chem. Sci.*, 2010, **1**, 72-78.
[17] Theoretical predictions using DFT calculations at the PB86 level of theory with def2svp basis set confirmed TB conformation of the guest $(CH_3\text{-O-}CH_3)_2$•Ir^I•COD included within cavitand **C5** (with methyl groups instead of ethyl). Using this energy-optimized structure, we calculated theoretical NMR spectrum, where NH, aromatic and COD signals coincided well with experimentally determined values.
[18] E. Zuidema, M. A. Sarmentero, C. Bo and P. Ballester, *Chem.--Eur. J.*, 2008, **14**, 7285-7295.
[19] R. J. Hooley, H. J. Van Anda and J. Rebek, *J. Am. Chem. Soc.*, 2007, **129**, 13464-13473.
[20] D. Fiedler, R. G. Bergman and K. N. Raymond, *Angew. Chem., Int. Ed.*, 2006, **45**, 745-748.
[21] D. J. Cram, M. E. Tanner and R. Thomas, *Angew. Chem., Int. Ed. Engl.*, 1991, **30**, 1024-1027.
[22] A. B. Chaplin, J. C. Green and A. S. Weller, *J. Am. Chem. Soc.*, 2011, **133**, 13162-13168.
[23] T. J. Malosh, J. R. Shapley, R. J. Lawson, D. N. T. Hay and T. N. Rohrabaugh Jr, *J. Organomet. Chem.*, 2013, **745–746**, 98-105.
[24] A. Dervisi, C. Carcedo and L.-l. Ooi, *Adv. Synth. Catal.*, 2006, **348**, 175-183.
[25] V. W. Day, W. G. Klemperer and D. J. Main, *Inorg. Chem.*, 1990, **29**, 2345-2355.

CHAPTER 3: Pyridyl-decorated self-folding heptaamide cavitands as ligands in the rhodium-catalyzed hydrogenation of norbornadiene

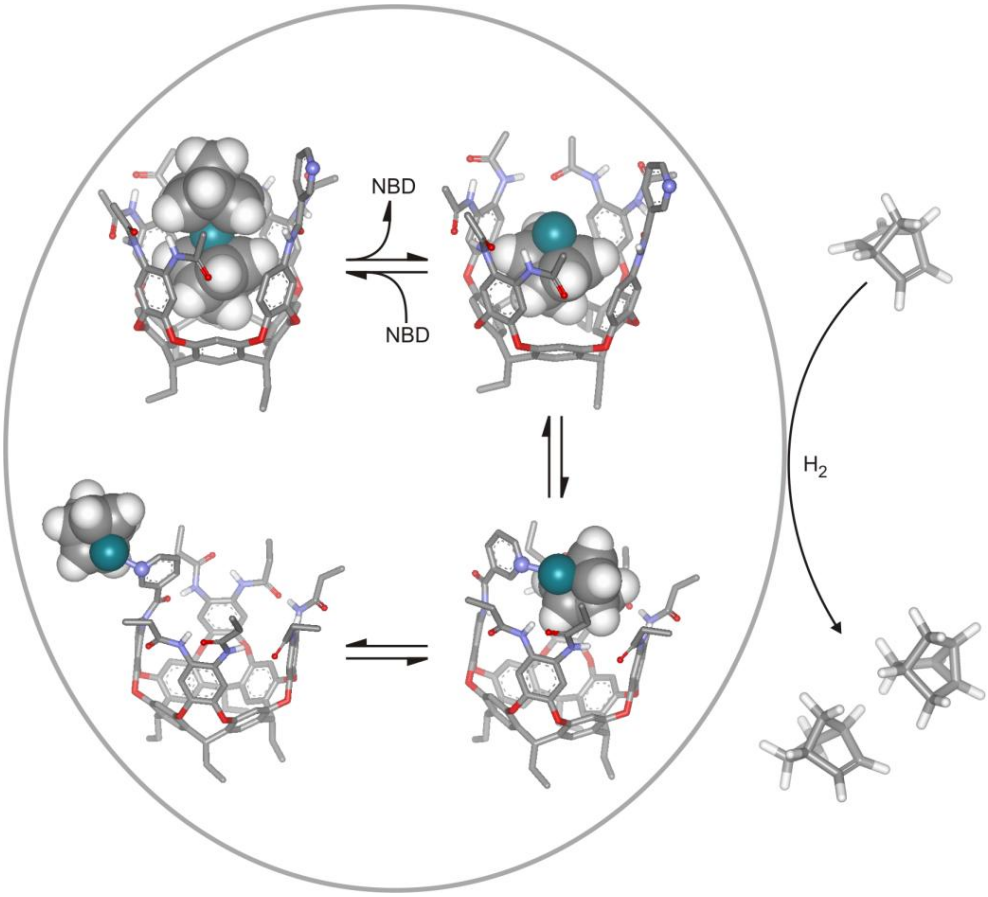

[§] This chapter was published in *Eur. J. Org. Chem.* **2014**, 4276-4282.

3.1 Introduction

The application of supramolecular concepts to catalysis is targeted through different approaches.[1,2,3,4,5,6,7] Among them, the encapsulation of catalytic metal centers within molecular assemblies has proved to be highly efficient.[8,9,10] By this approach, the stability,[11,12] reactivity[13] and selectivity[11,14,15] normally observed for the catalytic metal center free in solution can be radically altered and modified.

Encapsulation of a catalytic metal center has been achieved successfully through ligand-template directed assembly of the container.[16,17,18] Alternatively, an organometallic complex can be used in the form of a guest of a molecular or supramolecular container.[19] In the latter case, the molecular vessel acts as a second coordination sphere ligand. Recently, one of us[11] reported that self-folding octaamide cavitand **C5**[20,21] (**Fig. 43**), based on a resorcin[4]arene scaffold, binds the organometallic complex Rh^{I}•$(NBD)_2$, **2** with high affinity in methylene chloride solution. The binding process mainly produces a 1:1 inclusion complex Rh^{I}•$(NBD)_2$⊂**C5**, **2**⊂**C5** (**C18**, **Fig. 20**). The inclusion process, however, also induces the partial dissociation of one of the NBD ligands of **2**, affording in small quantity another inclusion complex - $(CD_2Cl_2)_2$•Rh^{I}•NBD⊂**C5** (**C19**, **Fig. 20**).

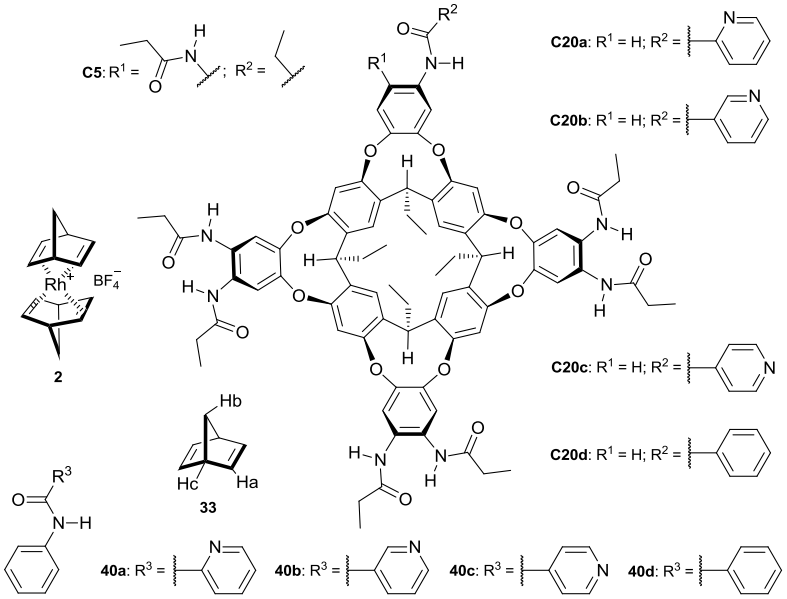

Fig. 43. Molecular structures of self-folding cavitands octaamide **C5** and heptaamides **C20a-d**, together with the cationic Rh^{I} complex **2**, norbornadiene (NBD, **33**), and monoamides **40a-d** used as model systems.

Interestingly, the mixture of two inclusion cationic Rh^{I} complexes was found to be catalytically competent in the hydrogenation of NBD. When the hydrogenation is performed on a laboratory scale, with the supramolecular system **C5** (1.2 mol-%) and **2** (1.0 mol-%), the GC/FID analysis of the crude product reveals that it is composed of norbornene

(**34**, 58%), nortricycline (**35**, 3%), and dimer **36** (39%, **Fig. 44**). This finding constitutes a remarkable result because the hydrogenation of NBD promoted by **2** alone (1 mol-%) produces almost exclusively dimer **36** as the result of the known reductive NBD dimerization.[22] We hypothesized that the dimer **36** also detected in the NBD catalytic hydrogenation in the presence of the mixture of inclusion complexes **2**⊂**C5** and $(CD_2Cl_2)_2$•Rh^I•NBD⊂**C5** must be produced by the presence of a small quantity of **2** that is released into the solution during hydrogenation.

Fig. 44. Line drawing structures of norbornene **34**, nortricyclene **35**, dimer **36** and dimer **41**.

In this work, we disclose the synthesis of a series of regioisomeric heptaamide self-folding cavitands **C20a-c**, which are structurally related to **C5** but each possess a single pyridyl residue installed at the upper rim.

In addition, we report the results obtained for the Rh^I catalyzed hydrogenation of NBD in the presence of these heptaamide cavitands **C20** as ligands. The design of the unimolecular pyridyl containers **C20** for the inclusion of the Rh^I metal center is based on the combination of two supramolecular strategies: (a) ligand-templated assembly, and (b) use of an organometallic cationic complex as the guest in the molecular container. Our expectations were that the pyridyl residue would be able to act in a cooperative manner with the electron-rich interior of the cavitand (cation-π), thus increasing the thermodynamic stabilities of Rh^I caviplexes derived from **C20** relative to the previously reported system based on the non-functionalized octaamide cavitand **C5**. If this was the case, the release of **2** or Rh^I•NBD complexes in solution during the hydrogenation should be reduced, and the formation of dimer **36** might even be eliminated.

3.2 Results and discussion

3.2.1 Synthesis and characterization

The regioisomeric pyridyl cavitands **C20a-c** and the phenyl heptaamide cavitand **C20d** were prepared by acylation of the known monoamino hexaamide cavitand **C23**[23] (see Supporting Information) with the corresponding acylpyridyl or benzoyl chlorides, respectively. We used Schotten-Baumann conditions to perform the reactions. The yields ranged from 70-85%. Cavitand **C20d**, with a phenyl group instead of a pyridyl residue, was prepared as a reference model system. By analogous synthetic procedures, a series of *N*-phenylpyridinecarboxamides **40a-c** and the *N*-phenylbenzamide (**40d**) were produced as additional reference systems (See **Fig. 43** for structures).

The X-ray structures of cavitands **C20a**, **C20b** and **C20d** revealed that they each adopted the vase conformation in the solid state. This conformation is stabilized by the formation of an array of six intramolecular hydrogen bonds between the amide functions at the upper rim.[20] In the case of **C20a** and **C20b**, one molecule of the crystallization solvent is included in the aromatic cavity. It is worth noting that cavitands **C20** are chiral molecules possessing two elements of asymmetry. The nonsymmetric substitution of one of the four phenyldioxo bridges creates asymmetry in the covalent structure of a cavitand **C20**, resulting in chiral stereogenic carbon atoms (**Fig. 45**, side views). In this sense, enantiomers of **C20** can easily be differentiated by the reverse absolute configurations of the methine carbon atom (*R* or *S*) embedded in the nine-membered ring encompassing the phenyldioxo bridge with the single amide.

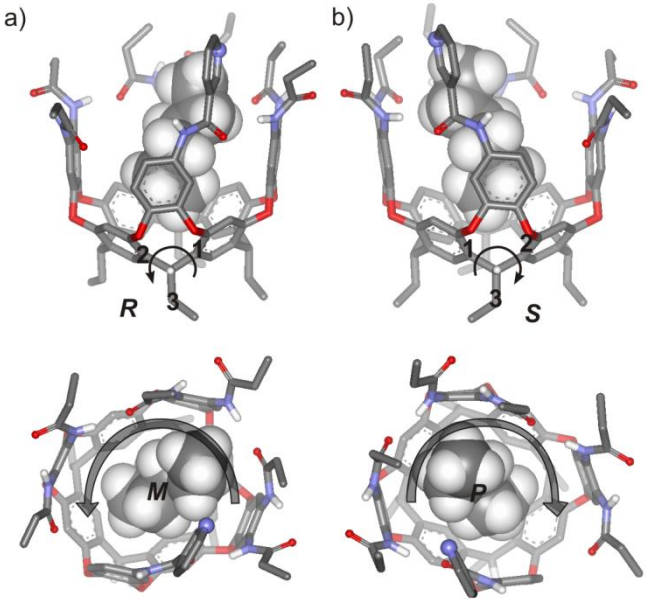

Fig. 45. Side and top views of the X-ray structures of the racemic pair of diastereoisomers present in the crystal packing of **C20b**: a) *M*,*R*-**C20b** and b) *P*,*S*-**C20b**. Nonpolar hydrogen atoms of **C20b** have been omitted for clarity. The included hexane molecule (from the solvent) is shown as a CPK model. Nitrogen atoms of the pyridyl residues are highlighted as larger balls.

The other asymmetry is of supramolecular origin.[24] It originates from the unidirectional orientation of carbonyl groups of the amides at the upper rim (**Fig. 45** top views). The amides' directionality derives from the formation of an intramolecular belt of hydrogen bonds.[25] Because of this second element of asymmetry, cavitands **C20** can exist as mixtures of two diastereoisomeric pairs of mutual enantiomers (four diastereomers). Interestingly, only one of two possible racemic pairs is detected in the packing of single crystals obtained for **C20b** and **C20d** [(*M*,*R*)-**C20** and (*P*,*S*)-**C20**]. The preferred sense of orientation (*P*/*M*) of the belt of hydrogen-bonded amides is controlled by the favoured role of the single amide as hydrogen bond acceptor.

In the particular case of **C20a**, the crystal packing shows that the aromatic cavity is filled with one acetone molecule and also with the ethyl group of an adjacent cavitand molecule, forming a dimeric aggregate (**Fig. 46**).

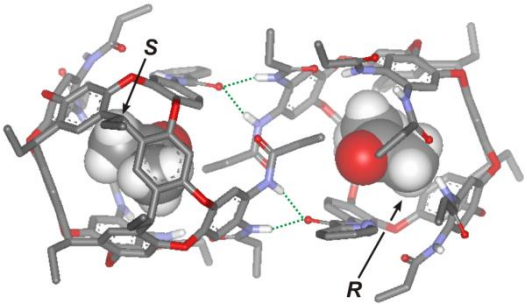

Fig. 46. Solid-state structure of the dimer of **C20a**. Bifurcated hydrogen bonds are depicted as green dotted lines. The molecule of acetone (from the solvent) included in **C20a** is shown as a CPK model. Nonpolar hydrogen atoms in **C20a** have been omitted for clarity. Nitrogen atoms of the pyridyl residues are highlighted as larger balls.

The dimer is held together by four bifurcated intermolecular hydrogen bonds established between the carbonyl oxygen atom of the single-amide group of each monomer and the NH groups of two amide groups of the adjacent **C20a** molecule. The intermolecular interactions disrupt the unidirectional orientation of the amide groups at the upper rim of **C20a**. Two enantiomers of **C20a** are present in each dimer.

The ^{1}H NMR spectra of methylene chloride-*d* solutions of cavitands **C20a-d** each feature a single set of proton signals consistent with C_1 symmetry. The signals of the amide protons are downfield-shifted, suggesting their involvement in hydrogen bonding. The four chemically non-equivalent methine protons resonate at $\delta \approx 5.6$ ppm. Taken together, these results suggest that cavitands **C20** exist as enantiomeric pairs of single diastereoisomers in solution, adopting the vase conformation.[26] These results are in agreement with the solid-state data and with reported findings for related heptaamide cavitands.[23]

3.2.2 Binding studies

Simple molecular modeling studies suggested two different geometries (*endo* and *exo*) for the coordination complexes formed through the interaction of the pyridyl nitrogen atom in **C20a** and **C20b** and the rhodium metal of Rh^{I}•NBD. The formation of the N-Rh^{I} bond induces the dissociation of one NBD ligand in **2** (*vide infra*). In the *exo* binding geometry the Rh^{I}•NBD unit would point away from the aromatic cavity (**Fig. 47**, d).

Conversely, in the *endo* conformer the Rh^{I}•NBD unit is directed towards the aromatic cavity (**Fig. 47**, c). Compound **C20c**, with the nitrogen atom in the *para* position of the

pyridyl substituent, would be expected to direct the Rh^{I}•NBD unit away from the aromatic cavity in any of its conformers.

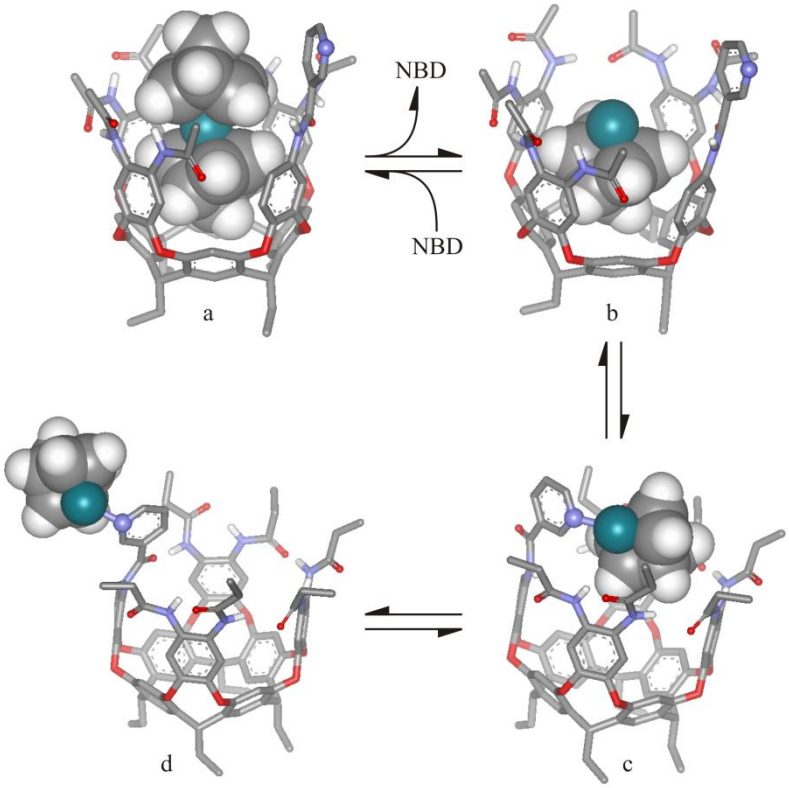

Fig. 47. Energy-minimized structures of different metallo-complexes resulting from the interaction of **C20b** with **2**: (a) **2**⊂**C20b**, (b) Rh^{I}•NBD⊂**C20b**, (c) *endo*-NBD•Rh^{I}•**C20b**, and (d) *exo*-NBD•Rh^{I}•**C20b**. The Rh^{I} metal and the NBD ligands are shown as CPK models; **C20b** is displayed in stick representation. Nonpolar hydrogen atoms in **C20b** have been omitted for clarity. Nitrogen atoms of the pyridyl residues are highlighted as larger balls.

For the three pyridyl cavitands **C20a-c**, owing to the weak coordination interaction that exists between Rh^{I} and nitrogen atoms,[27] it is sensible to consider the direct inclusion of **2** (**Fig. 47**, a) or Rh^{I}•NBD (**Fig. 47**, b) in their aromatic cavities without assistance of the coordination bond with the pyridyl nitrogen atom.

The calculated energies (MM3 as implemented in SCIGRESS v3.0) for the complexes of **C20a**/**C20b** with Rh^{I}•NBD in *exo* and *endo* coordination geometries indicate that the former is energetically preferred for the caviplex NBD•Rh^{I}•**C20a** whereas the latter is favored in the case of NBD•Rh^{I}•**C20b**.

Because the *endo*-NBD•Rh^{I}•**C20b** complex features a cooperative binding mode, which combines the formation of a coordination N-Rh^{I} bond with cation-π interactions, we expected that its thermodynamic and kinetic properties would be improved in relation to those of **C20a** or the parent **2**⊂**C5** complex. This improvement should translate into

reduced leaking of Rh^{I}•NBD into the bulk solution under hydrogenation conditions. A recent computational study showed that the reductive dimerization of NBD to afford dimer **36** requires the coordination of three NBD molecules to the Rh^{I} center.[28] For steric reasons, three molecules of NBD cannot coordinate simultaneously to Rh^{I} if the metal center is included in the cavity of **C5** or **C20**. In short, cavitand **C20b** stands out as an ideal candidate to suppress the formation of dimer **36** observed in the rhodium-catalyzed hydrogenation of NBD.

With the aim of studying the binding properties (towards **2**) of the pyridyl carboxamide residues installed at the upper rim of cavitands **C20a-c** in isolation from those of the close-by aromatic cavity, we synthesized pyridyl carboxamides **40a-d** (**Fig. 43**) as model systems and studied their binding properties. The interaction between **40a-d** and **2** were probed by ^{1}H NMR spectroscopy. The addition of 0.8 equiv. of **2** to separate methylene chloride solutions of the three pyridine carboxamides **40a-c** (4.5 mM) induced significant changes in the chemical shifts of the signals of the amide NH and pyridyl protons relative to those in the free ligands. The results of the titration experiments indicate that the coordination of carboxamides **40a-c** to **2** induces different levels of dissociation of one of the NBD ligands, yielding free NBD and the 1:1 heteroleptic complexes NBD•Rh^{I}•**40a-c**. The complexes are each stabilized by the formation of a N-Rh^{I} coordination bond. The protons of the free and the bound NBDs are observed as separate signals, indicating that they are involved in a chemical exchange process that is slow on the NMR timescale. Conversely, a single set of proton signals is observed for each of the *N*-phenylpyridyl carboxamides **40a-c**. Moreover, the extent to which the 1:1 complexes NBD•Rh^{I}•**40a-c** are formed in equimolar solutions depend on the position of the nitrogen atom in the pyridyl substituent of the ligand. In the case of **40a**, in which the pyridyl nitrogen atom is *ortho* to the amide function, the complex NBD•Rh^{I}•**40a** is formed quantitatively in an equimolar mixture of partners. Most likely, this is due to the existence of a ditopic interaction between the ligand **40a** and the Rh^{I} metal center. Additional evidence for Rh^{I} coordination to the carbonyl oxygen in NBD•Rh^{I}•**40a** was provided by the downfield shift experienced by the amide NH. In striking contrast, ligand **40d**, lacking the pyridyl residue, induces the dissociation of **2** into NBD and the formation of NBD•Rh^{I}•**40d** to a minimum extent. Therefore, ligand **40d** must coordinate to the Rh^{I} through its carbonyl oxygen atom. It is worth mentioning that in this latter case the chemical exchange processes both of free and bound NBD and of free and bound ligand **40d** are slow on the NMR timescale.

Next, we investigated the binding properties of the cavitand series **C20** towards **2**. Using 1D and 2D ^{1}H-NMR spectroscopy, we analyzed the compositions of separate methylene chloride-*d* solutions containing 1 equiv. of **2** and 1.2 equiv. of each cavitand **C20a-d**. In all cases, the proton signals corresponding to the free NBD (**33**) were easily identified (H_a, H_b and H_c; see the Supporting Information). This observation parallels the findings made with the model system **40a-c**. In short, the coordination of the pyridyl substituents in cavitands **C20a-c** with **2** induces the dissociation of one of their NBD

ligands to different extents. The presence of cross-peaks in EXSY experiments revealed that the protons of free NBD were involved in chemical exchange processes with bound NBD molecules in more than one magnetic environment. The olefinic proton (H_a) of the free NBD was the best signal to analyze the multi-site exchange systems. In the case of **C20a** (2-carboxypyridine cavitand) interacting with **2**, 1 equiv. of the free NBD is released and found to exchange with NBD units in two different bound states. The quantitative dissociation of **2** is in agreement with the result obtained for the model **40a**. Most likely, the ditopic (N,O) metal-ligand interaction present in the NBD•Rh^I•**C20a** complex is responsible for its high thermodynamic stability. On the basis of the molecular modeling studies discussed above, we assigned *endo* and *exo* geometries to the two coordination complexes of NBD•Rh^I•**C20a**. The two complexes are engaged in a chemical exchange process. The complexes' interconversion is slow on the NMR timescale because it must occur through a sizeable conformational change of the cavitand (vase-to-kite) rather than by a simple C-C bond rotation. The small integral measured for the signal that resonates furthest upfield (δ = -2.64 ppm) is assigned to H_c protons of the Rh^I•NBD included in the aromatic cavity of **C20a** indicates that the *exo* conformer is the major species (> 90%) in solution.

The use of cavitand **C20b** (3-carboxypyridine) produced a more complex distribution of species. From the integrals of selected proton signals, we calculated the percentages of the different species in solution to be: 62% of the *exo*-NBD•Rh^I•**C20b** conformer, 21% of the *endo*-NBD•Rh^I•**C20b** conformer, and 17% of the inclusion complex **2⊂C20b** not assisted by the formation of a coordination bond. Contrary to our expectations, the *endo*-NBD•Rh^I•**C20b** complex is not the major species in solution. Interestingly, the protons of the bound NBD in *endo*-NBD•Rh^I•**C20b** resonate as diastereotopic signals, due to cavity's chirality imparted by the unidirectional orientation of the amide groups at the upper rim. By using competitive pairwise experiments we also determined that the complexes of cavitand **C20b** had a minimal thermodynamic advantage with respect to **2⊂C5**. This result was again completely unexpected on the basis of our initial hypothesis.

The third pyridyl cavitand **C20c** (4-carboxypyridine), with its N atom pointing away from the aromatic cavity, produced a very different distribution of complexes. The major species detected in solution is the inclusion complex Rh^I•NBD⊂**C20c** (68%), which does not involve a coordination bond, probably due to geometric constrains. The coordination complex NBD•Rh^I•**C20c** (23%) and the inclusion complex **2⊂C20c** (9%) are also present in the mixture. The protons of the external NBD ligands in the last complex also resonate as diastereotopic signals.

Finally, cavitand **C20d** (carboxyphenyl) produced the inclusion complexes Rh^I•NBD⊂**C20d** (50%) and **2⊂C20d** (45%) in similar quantities, with a small amount of free **2** (5%) remaining in solution.

3.2.3 Catalysis

The coordination complexes of **40a-d** and **2** were tested as catalysts in the hydrogenation of norbornadiene **33** (1 mol-% of **2**, 1.2 mol-% of **40a-d**, room temp., 1 atm H_2). The GC/FID analysis of the hydrogenation crude products after 45 min reaction time showed significant differences in composition. The results obtained are summarized in **Table 5**.

Several conclusions can be drawn from the data: (1) the monotopic coordination of the Rh^I metal center to the pyridyl nitrogen atom in ligands **40b** and **40c** produces highly active species for the hydrogenation of NBD that exclusively yield nortricyclene (**35**, Entries 7 and 9), (2) the ditopic N,O coordination of the Rh^I center exerted by ligand **40a** hydrogenates NBD to produce a close to 1:1 mixture of norbornene (**34**) and nortricyclene (**35**, Entry 5), and (3) ligand **40d**, lacking the pyridyl group, does not have a significant effect on the catalytic properties exhibited by **2** alone (Entries 1 and 11).

It is worth noting that dimer **41** is produced in significant amounts in Entries 1 and 11. On the other hand, catalyst **2** in the absence of H_2 induces the dimerization of NBD to yield dimer **41** (Entry 2).[29]

Table 5. Percentage of NBD (**33**) consumed ("con") after 45 min reaction time and the resulting product distribution (%) for the laboratory-scale catalytic hydrogenations performed in this study (see the Supporting Information for experimental details).

Entry	System	% **33** con	Product distribution in %[a]				
			34	**35**	**36**	**41**	other
1	**2** [b]	80	0.9	1.0	73.4	24.7	0
2	**2** [c]	30	2.9	0	0	92.2	4.9
3	**C5** + **2**	55	81.7	0.7	15.6	2.0	0
4	**C20a** + **2**	30	60.1	39.9	0	0	0
5	**40a** + **2**	35	47.6	52.4	0	0	0
6	**C20b** + **2**	35	42.4	57.6	0	0	0
7	**40b** + **2**	30	0	100	0	0	0
8	**C20c** + **2**	60	18.3	81.7	0	0	0
9	**40c** + **2**	50	0	100	0	0	0
10	**C20d** + **2**	60	64.6	0	35.4	0	0
11	**40d** + **2**	75	1.1	1.3	72.9	23.5	1.2

[a] Values (%) are corrected under the assumption that the response factor of the dimer is twice that of the monomer. [b] Without preactivation of catalyst. [c] No hydrogen.

We learned during the course of this study that the reaction conditions used to perform the hydrogenation experiments result in a slow diffusion of hydrogen[30] into the reaction mixture. For this reason, and in the particular case of catalyst **2**, we must conclude that the reactions producing the hydrogenated dimer **36** and non-hydrogenated **41** become competitive. Next, we evaluated the catalytic performances of the caviplex systems in the

hydrogenation of NBD under reaction and analytical conditions identical to those above (1 mol-% of **2** and 1.2 mol-% of **C20a-d** at room temp. and under 1 atm H_2).

The **C20a+2** system (Entry 4) produces norbornene (**34**) and nortricyclene (**35**) in a 3:2 ratio. This result corresponds to a moderate increase in the amount of norbornene produced relative to the model system (Entry 5). We ascribe this increase in norbornene production to a high catalytic activity of the *endo*-NBD•Rh^I•**C20a** complex present in solution in a low amount (< 10%). At the first sight, the system **C20b+2** seems to be less efficient in the production of norbornene than **C20a+2**. However, if the product distribution obtained for **C20b+2** is compared with that of the corresponding model systems **40b+2** then the opposite conclusion is reached. As we did for the **C20a+2** system, we also ascribe the norbornene production for **C20b+2** to the *endo*-NBD•Rh^I•**C20b** complex, now present in solution in larger amounts (21%). Consistently with this explanation, the system **C20c+2**, lacking an *endo* geometry complex assisted by N-coordination, is less effective in norbornene production. Probably, the inclusion complexes of **C20c** are competent in norbornene production but they are less active than the N-coordinated counterparts NBD•Rh^I•**C20c** that mainly yields notricyclene (**35**).

Finally, the results obtained for the system **C20d**+**2** also support the competence of inclusion complexes Rh^I•NBD⊂**C20d** and **2**⊂**C20d** in the production of norbornene (**34**). However, the percentages of produced norbornene are lower than for the system **C5**+**2**. We explain this result by considering that the elimination in **C20d** of one of the amide group at the upper rim, with respect to **C5**, distorts the aromatic cavity and makes its inclusion complexes with Rh^I•NBD thermodynamically less stable. In turn, the reduced thermodynamic stability of the inclusion complexes of **C20d** relative to **C5** translates into the presence of significant amounts of free **2** in solution, as already observed in the binding experiment. By the same token, the release of Rh^I•NBD or **2** into solution during hydrogenation must be favored for **C20d** in relation to **C5**. The low levels of nortricyclene (**35**) present in the crude products of Entries 1, 2, 3, 10 and 11 attest that the *exo* species with N coordination to the Rh^I metal center must be responsible for its production.

3.3 Conclusions

The structural modifications of cavitand **C5** represented by the cavitand series **C20a-c** are not successful in allowing their application as ligands for the exclusive rhodium-catalyzed hydrogenation of NBD (**33**) to norbornene (**34**). The emergence of *exo* geometries in the complexes formed between **20a-c** and **2** provide a new reaction pathway that was not important in the case of **C5**. The *exo* complexes feature a coordination bond between the nitrogen atom of the pyridyl residue at the upper rim of cavitands **C20a-c** and the metal center of Rh^I•NBD. In agreement with the results obtained for the model systems

40a-c, the *exo* coordination complexes are competent in producing nortricyclene (**35**) as the main hydrogenation product of NBD. In addition, the significant levels of norbornene (**34**) produced in the hydrogenation of NBD when the supramolecular systems **C20a-d** and **2** are employed as catalysts is attributed to a reaction pathway involving the inclusion of the Rh^{I} metal center in the deep cavities of the hosts. In the *endo* complexes of **C20a** and **C20b** the cavitand may act as a first- or second-sphere ligand depending on the type of interaction established with the included rhodium center. The obtained results are not conclusive in supporting the hypothesis that *endo* complexes assisted by coordination with the pyridyl residue can also modulate the conversion of NBD into nortricyclene (**35**).

3.4 Experimental section

3.4.1 General information and instrumentation

All reagents and solvents were obtained from commercial suppliers and used without further purification unless otherwise stated. Cavitands **C5** and **C22** (see the Appendix) were synthesized by the experimental procedure published by Rebek.[21,23] Dimer molecules **36** and **41** were synthesized by the procedure published by Katz.[22,29] 1D and 2D NMR spectra were recorded with a Bruker Avance 400 or a Bruker Avance 500 spectrometer. All deuterated solvents (Sigma-Aldrich) were used without any further purification. Chemical shifts are given in ppm and peaks were referenced relative to the solvent residual peak (δ_{CD2Cl2} = 5.32 ppm, δ_{CDCl3} = 7.26 ppm, $\delta_{DMSO\text{-}d6}$ = 2.49 ppm). All NMR *J* values are given in Hz and are uncorrected. All MS were recorded with a Bruker MALDI-TOF Autoflex instrument. Product distributions were analyzed by use of an Agilent gas chromatograph 6890N with a FID detector. Melting points were determined with Mettler Toledo MP70 Melting Point System. All XRD samples were recorded with a Bruker Kappa Apex II.

3.4.2 Synthesis of cavitand molecules

The nitro group in **C22** was reduced to the corresponding amine **C23** followed by acylation using Schotten-Baumann conditions to afford the desired cavitands **C20a-d** in good yields after column chromatography purification.

A typical synthetic procedure is described. A solution of nitro cavitand **C22** (428 mg, 0.313 mmol, 1 equiv.) in THF (25 mL) was placed in a 50 mL two-necked flask. A catalytic amount of Raney-Ni (washed 4 times with THF, followed by separation with a magnet and decantation) was added to this solution. The mixture was stirred with a magnetic bar and purged with hydrogen (by passing hydrogen over the solution for a few seconds). The hydrogenation reaction was performed under hydrogen (1 atm) and at 40 °C for 2 h. The

resulting solution was filtered through a 0.45 μm syringe filter to remove the catalyst, and the solvent removed under reduced pressure, affording **C23** (410 mg, 0.306 mmol, 98%).

The amino cavitand **C23** was immediately used in the next reaction step – acylation of the amine group under Schotten-Baumann conditions to produce cavitands **C20a-d**. To obtain **C20b**, for example, the experimental procedure consisted of adding a solution of potassium carbonate (1.2 g, 8.68 mmol, 28 equiv.) in water (18 mL) to a solution of **C23** (410 mg, 0.306 mmol, 1 equiv.) in ethyl acetate (25 mL). Next, the solid nicotinoyl chloride (142 mg, 0.96 mmol, 3 equiv.) was added to the above solution in small portions with vigorous stirring. The mixture was stirred at room temperature for 16 h under nitrogen. After this time, the organic phase was separated, dried over anhydrous sodium sulfate, filtered and the solvent evaporated in vacuo. The solid residue obtained was purified by flash column chromatography on silica with a gradient of methanol (0 - 5%) in methylene chloride to afford **C20b** (390 mg, 0.27 mmol, 86%) as a solid.

By use of similar experimental procedures the cavitand **C20a** was isolated in 77% yield, **C20c** in 69% yield and **C20d** in 79% yield.

Cavitand C20a: Crystals suitable for X-ray crystal structure analysis were obtained.[31] M.p. >250 °C with decomposition.^{1}H NMR (400 MHz, CD_2Cl_2): δ = 9.79 (s, 1H), 9.56 (s, 1H), 9.54 (s, 1H), 9.13 (s, 1H), 8.99 (s, 1H), 8.72 (s, 1H), 8.59 (d, *J* = 4.2 Hz, 1H), 8.54 (s, 1H), 8.18 (d, *J* = 2.6 Hz, 1H), 8.11 (d, *J* = 7.8 Hz, 1H), 7.97 (s, 1H), 7.89 (td, *J* = 7.7, 1.7 Hz, 1H), 7.79 (s, 1H), 7.77 (s, 1H), 7.75 (s, 1H), 7.73 (s, 1H), 7.50 (ddd, *J* = 7.6, 4.8, 1.1 Hz, 1H), 7.42 (s, 1H), 7.40 (s, 1H), 7.37 (s, 1H), 7.36 (s, 1H), 7.34 (s, 1H), 7.31 (s, 1H), 7.27 (s, 1H), 7.25 (s, 1H), 7.25 (s, 1H), 7.24 (s, 1H), 6.84 (dd, *J* = 8.7, 2.2 Hz, 1H), 5.75 - 5.57 (m, 4H), 2.52 - 2.21 (m, 20H), 1.22 (ddd, *J* = 16.2, 13.0, 7.6 Hz, 15H), 1.05 (td, *J* = 7.1, 4.3 Hz, 9H), 0.99 (td, *J* = 7.2, 3.5 Hz, 6H) ppm. FTIR: ῡ = ν(C-N) 1401; ν(Ar) 1599, 892; ν(C=O) 1662; ν(alkyl) 2964, 2935, 2875; ν(-NH···O=) 3261 cm^{-1}. MS (MALDI, +): calcd for $C_{84}H_{82}N_8O_{15}$ + H^+ 1443.6; found 1443.6.

Cavitand C20b: Crystals suitable for X-ray crystal structure analysis were obtained.[31] M.p. >250 °C with decomposition. ^{1}H NMR (400 MHz, CD_2Cl_2): δ = 9.53 (s, 1H), 9.41 (s, 1H), 9.23 (s, 1H), 9.01 (s, 1H), 8.91 (s, 1H), 8.76 (s, 1H), 8.64 (dd, *J* = 4.8, 1.7 Hz, 1H), 8.49 (s, 1H), 8.10 (s, 1H), 7.78 (dt, *J* = 7.9, 1.9 Hz, 1H), 7.70 (s, 1H), 7.60 (s, 1H), 7.58 (s, 1H), 7.56 (s, 1H), 7.53 (s, 1H), 7.51 (s, 2H), 7.50 (s, 1H), 7.36 (s, 2H), 7.34 (s, 2H), 7.29 (s, 2H), 7.27 (s, 2H), 7.27 (s, 1H), 7.23 (s, 1H), 5.74 (t, *J* = 8.3 Hz, 1H), 5.67 - 5.59 (m, 2H), 5.59 - 5.52 (m, 1H), 2.62 - 2.18 (m, 18H), 1.70 (hept, *J* = 7.9 Hz, 2H), 1.37 - 0.89 (m, 27H), 0.77 (t, *J* = 7.6 Hz, 3H) ppm. FTIR: ῡ = ν(C-N) 1403; ν(Ar) 1597, 892; ν(C=O) 1664; ν(alkyl) 2967, 2934, 2872; ν(-NH···O=) 3251 cm^{-1}. MS (MALDI, +): calcd for $C_{84}H_{82}N_8O_{15}$ + H^+ 1443.6; found 1443.6.

Cavitand C20c: M.p. >250 °C with decomposition. ^{1}H NMR (500 MHz, CD_2Cl_2): δ = 9.59 (s, 1H), 9.45 (s, 1H), 9.32 (s, 1H), 8.98 (s, 1H), 8.77 - 8.72 (m, 1H), 8.61 - 8.55 (m, 2H),

8.14 (s, 1H), 7.85 - 7.81 (m, 1H), 7.71 (s, 1H), 7.58 (s, 1H), 7.56 (s, 1H), 7.55 (s, 1H), 7.54 (s, 1H), 7.52 (s, 1H), 7.50 (s, 1H), 7.37 (s, 1H), 7.35 (s, 2H), 7.34 (s, 1H), 7.32 (s, 1H), 7.30 (s, 1H), 7.29 (s, 1H), 7.28 (s, 1H), 7.27 (s, 1H), 7.24 (s, 2H), 7.23 (s, 1H), 5.73 (t, *J* = 8.4 Hz, 1H), 5.63 (dt, *J* = 12.5, 8.3 Hz, 2H), 5.57 (t, *J* = 8.3 Hz, 1H), 2.59 - 2.20 (m, 20H), 1.33 - 1.17 (m, 18H), 1.11 - 1.03 (m, 3H), 1.04 - 0.95 (m, 6H), 0.77 (t, *J* = 7.6 Hz, 3H) ppm. FTIR: $\tilde{\upsilon}$ = ν(C-N) 1401; ν(Ar) 1599, 892; ν(C=O) 1658; ν(alkyl) 2963, 2935, 2874; ν(-NH···O=) 3253 cm^{-1}. MS (MALDI, +): calcd for $C_{84}H_{82}N_8O_{15}$ + H^+ 1443.6; found 1443.6.

Cavitand C20d: Crystals suitable for X-ray crystal structure analysis were obtained.[31] M.p. >250 °C with decomposition. ^{1}H NMR (400 MHz, CD_2Cl_2): δ = 9.43 (s, 1H), 9.38 (s, 1H), 9.35 (s, 1H), 9.11 (s, 1H), 8.36 (s, 1H), 8.05 (dd, *J* = 8.3, 1.2 Hz, 1H), 7.92 (s, 1H), 7.73 (s, 1H), 7.63 (s, 1H), 7.62 (s, 1H), 7.60 (s, 1H), 7.57 (s, 1H), 7.50 (s, 1H), 7.48 (s, 1H), 7.47 (s, 2H), 7.45 (s, 2H), 7.43 (s, 1H), 7.37 (s, 1H), 7.37 (s, 1H), 7.36 (s, 1H), 7.35 (s, 2H), 7.34 (s, 2H), 7.28 (s, 1H), 7.27 (s, 1H), 7.25 (s, 1H), 5.72 (t, *J* = 8.3 Hz, 1H), 5.68 - 5.59 (m, 2H), 5.64 - 5.53 (m, 1H), 2.55 - 2.18 (m, 16H), 1.86 - 1.57 (m, 4H), 1.31 - 1.16 (m, 12H), 1.04 (ddq, *J* = 30.3, 15.6, 7.5 Hz, 15H), 0.76 (t, *J* = 7.5 Hz, 3H) ppm. FTIR: $\tilde{\upsilon}$ = ν(C-N) 1402; ν(Ar) 1598, 892; ν(C=O) 1664; ν(alkyl) 2965, 2933, 2872; ν(-NH···O=) 3249 cm^{-1}. MS (MALDI, +): calcd for $C_{84}H_{82}N_8O_{15}$ + Na^+ 1464.6; found 1464.6.

3.4.3 Synthesis of control molecules

Under Schotten-Baumann conditions analogous to those described for the synthesis of cavitands **C20a-d**, aniline was acylated to produce reference ligands **40a-d**. Crystallization from water/acetone mixtures afforded pure compounds, in 75% yield for **40a**, 64% yield for **40b**, 43% yield for **40c** and 89% yield for **40d**.

***N*-Phenylpyridine-2-carboxamide (40a)**: ^{1}H NMR (500 MHz, $CDCl_3$): δ = 10.03 (s, 1H), 8.62 (ddd, *J* = 4.7, 1.6, 0.9 Hz, 1H), 8.31 (dt, *J* = 7.8, 1.0 Hz, 1H), 7.91 (td, *J* = 7.7, 1.7 Hz, 1H), 7.79 (dt, *J* = 8.7, 1.6 Hz, 2H), 7.49 (ddd, *J* = 7.6, 4.8, 1.2 Hz, 1H), 7.43 - 7.33 (m, 2H), 7.19 - 7.10 (m, 1H) ppm.[32]

***N*-Phenylpyridine-3-carboxamide (40b)**: ^{1}H NMR (500 MHz, $CDCl_3$): δ = 9.08 (d, *J* = 1.8 Hz, 1H), 8.76 (dd, *J* = 4.8, 1.6 Hz, 1H), 8.20 (dt, *J* = 7.9, 2.0 Hz, 1H), 8.04 (s, 1H), 7.64 (d, *J* = 7.8 Hz, 2H), 7.43 (ddd, *J* = 7.9, 4.8, 0.8 Hz, 1H), 7.41 - 7.35 (m, 2H), 7.21 - 7.16 (m, 1H) ppm.[33]

***N*-Phenylpyridine-4-carboxamide (40c)**: ^{1}H NMR (500 MHz, DMSO-d_6): δ = 10.48 (s, 1H), 9.06 - 8.56 (m, 2H), 7.97 - 7.79 (m, 2H), 7.76 (d, *J* = 7.7 Hz, 2H), 7.37 (t, *J* = 7.9 Hz, 2H), 7.13 (t, *J* = 7.4 Hz, 1H) ppm.[34]

***N*-Phenylbenzamide (40d)**: ^{1}H NMR (500 MHz, $CDCl_3$): δ = 7.88 (s, 1H), 7.86 (d, *J* = 1.5 Hz, 2H), 7.65 (d, *J* = 7.8 Hz, 2H), 7.59 - 7.51 (m, 1H), 7.48 (t, *J* = 7.5 Hz, 2H), 7.41 - 7.34 (m, 2H), 7.16 (t, *J* = 7.4 Hz, 1H) ppm.[32]

3.4.4 Catalytic hydrogenation reactions

A typical laboratory-scale hydrogenation experiment consisted of dissolving **2** (20 μmol) and the appropriate cavitand or model ligand (**C5**, **C20a-d**, **40a-d**, 25 μmol) in methylene chloride (HPLC grade, 6.8 mL). The resulting solution was transferred to a 25 mL three-necked flask fitted with a hydrogen inlet. The catalyst was preactivated by purging the flask with hydrogen and stirring the mixture under 1 atm of hydrogen for 5 min. Next, neat norbornadiene (**33**, 2.12 mmol) was added in one shot, and the reaction evolution was immediately sampled by taking small aliquots of the reaction mixture (100 μL). Aliquots were taken every 15 min. Each aliquot was diluted with methylene chloride (100 μL), filtered through a silica gel plug, and analyzed by GC/FID.

3.5 Supporting information

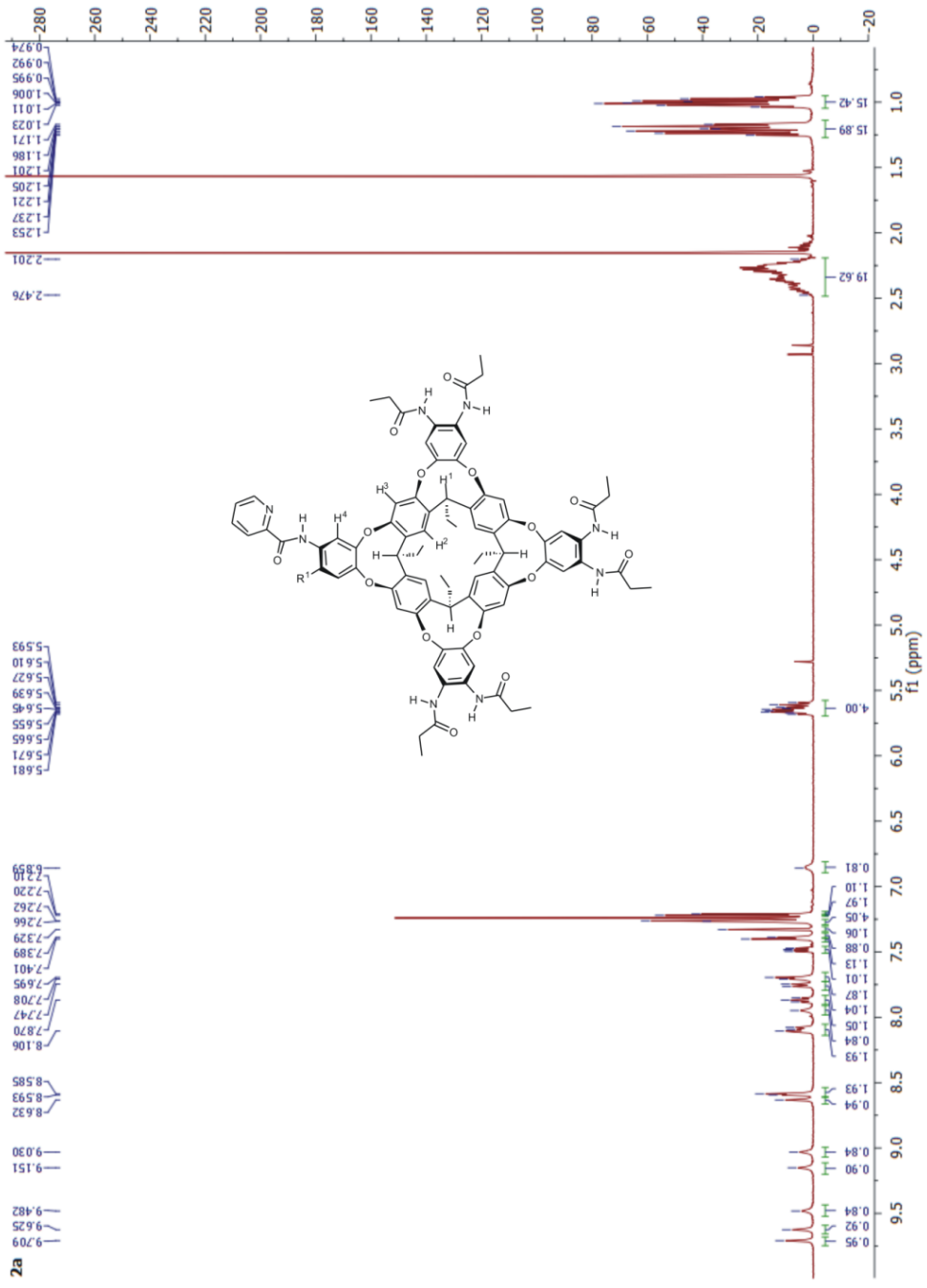

Fig. 48. ^{1}H NMR spectrum of cavitand **C20a** in CD_2Cl_2.

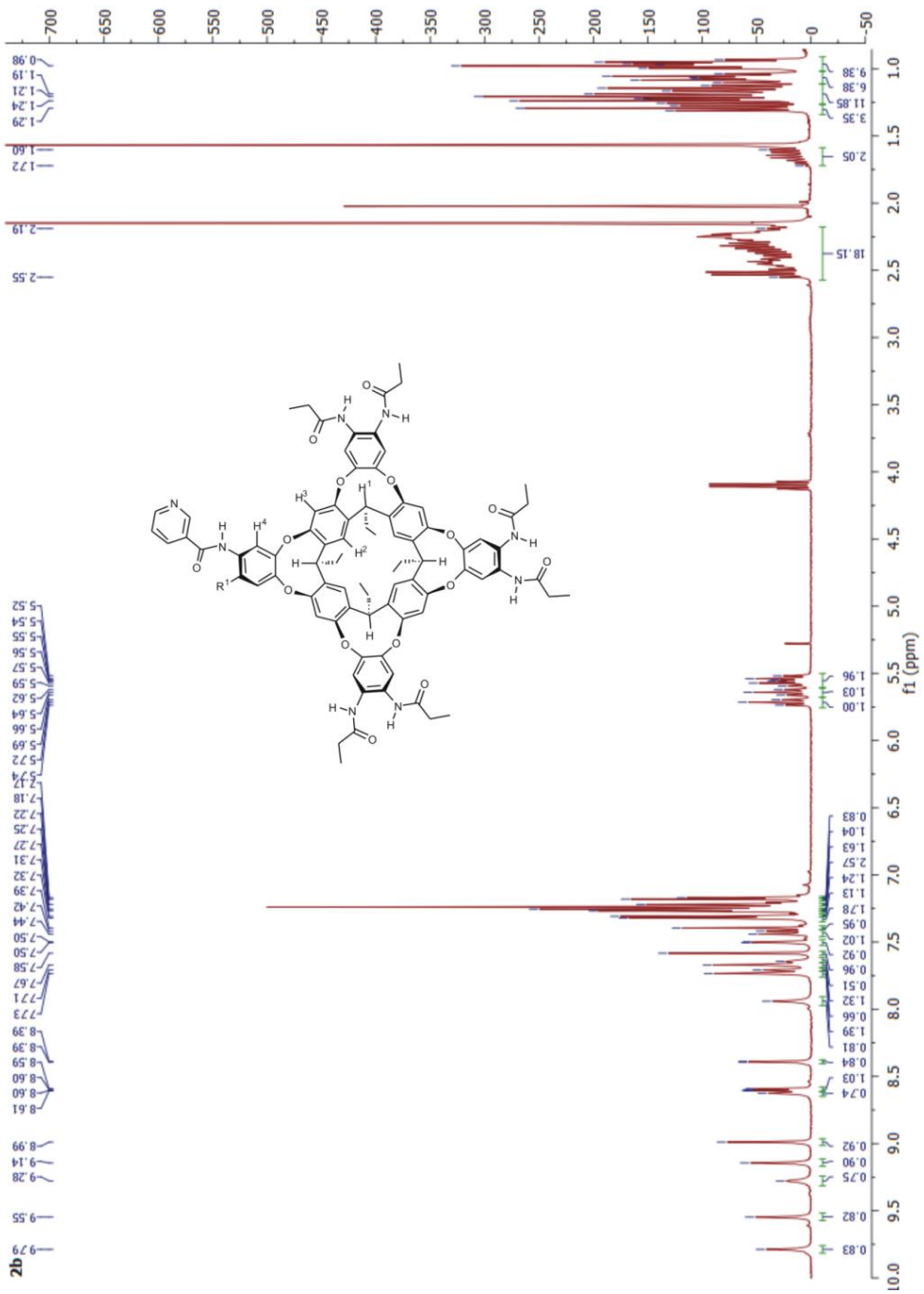

Fig. 49. ^{1}H NMR spectrum of cavitand **C20b** in CD_2Cl_2.

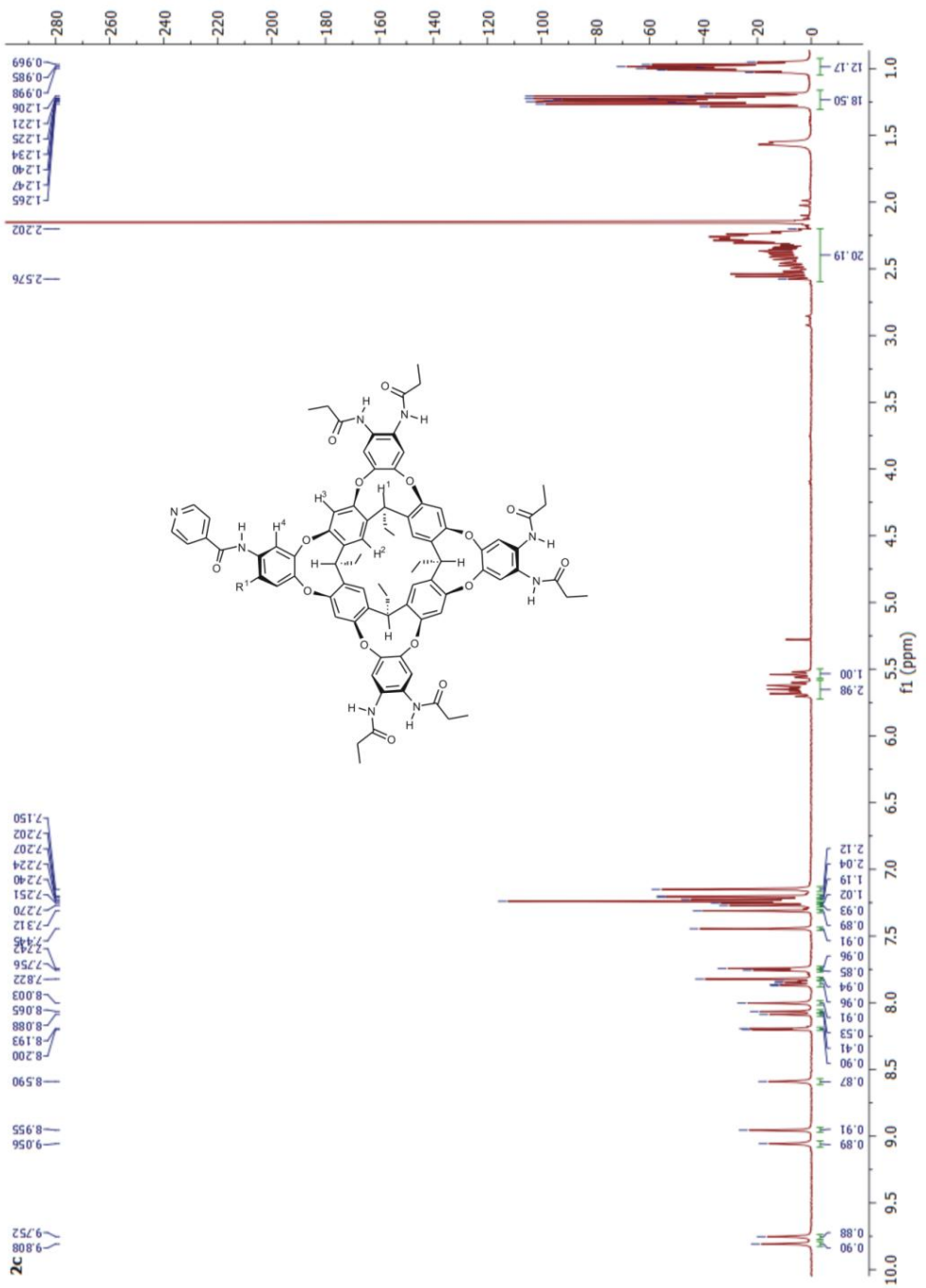

Fig. 50. ^{1}H NMR spectrum of cavitand **C20c** in CD_2Cl_2.

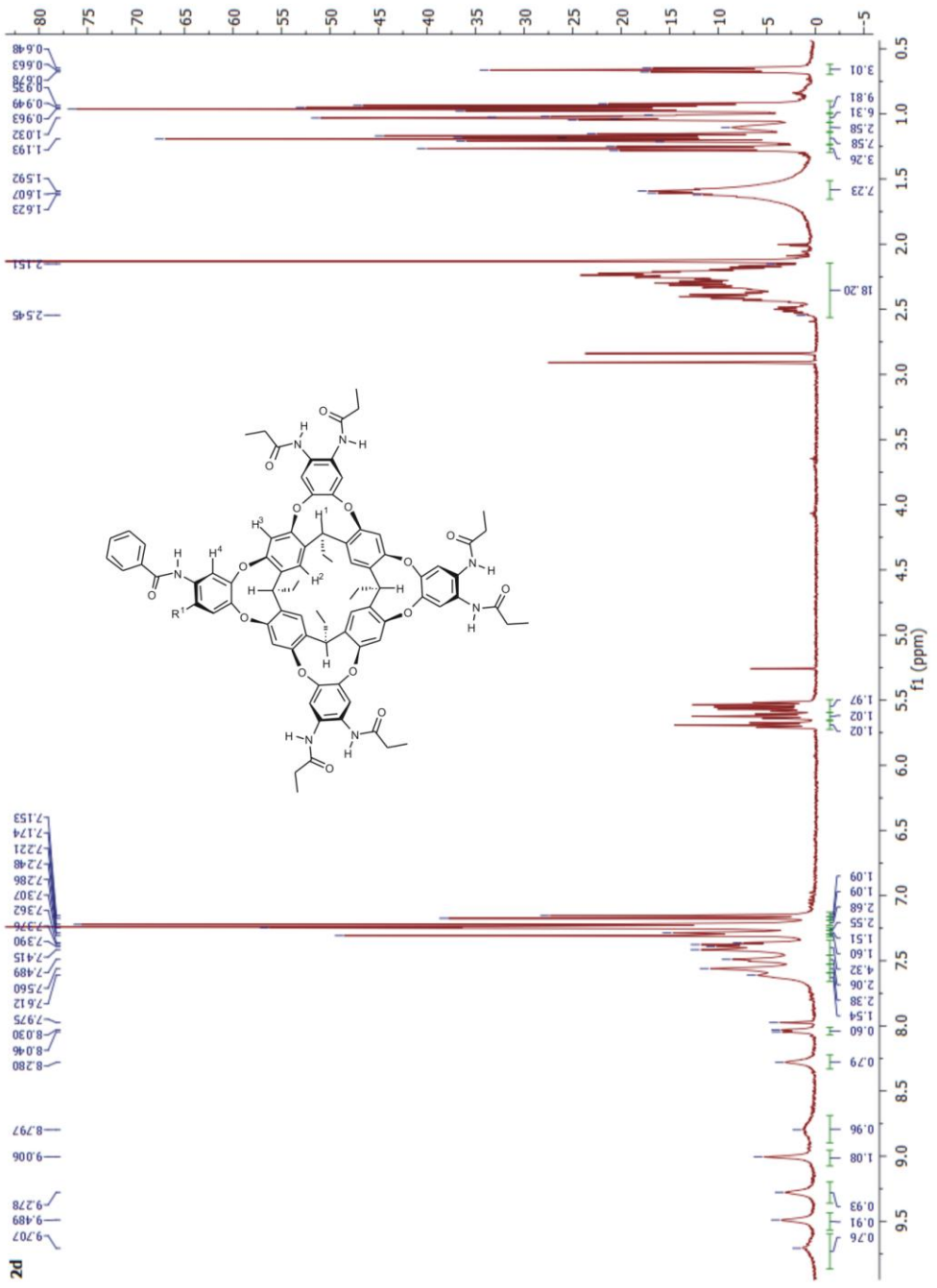

Fig. 51. ^{1}H NMR spectrum of cavitand **C20d** in CD_2Cl_2.

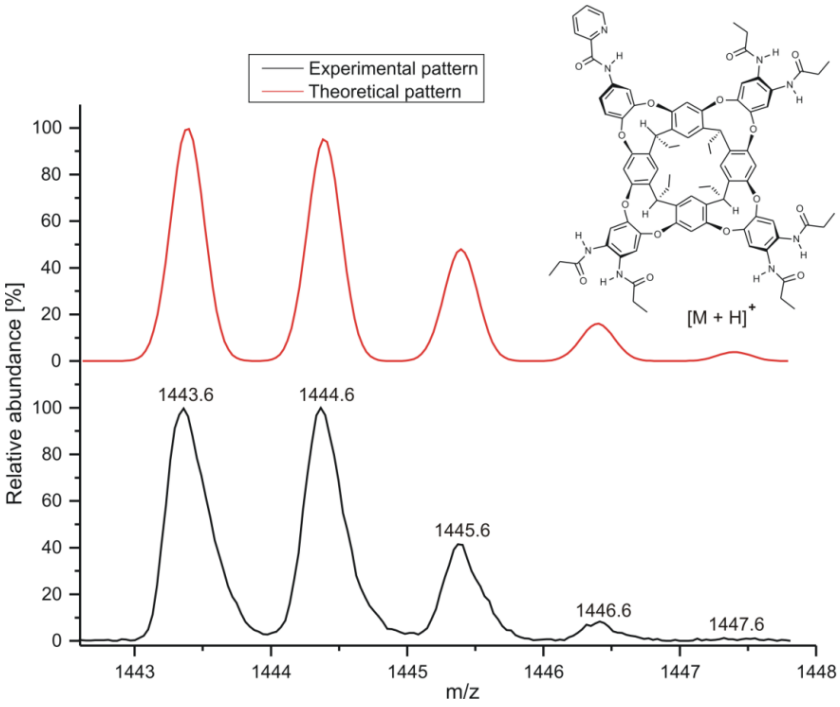

Fig. 52. MALDI-MS (+) isotopic pattern for cavitand **C20a**.

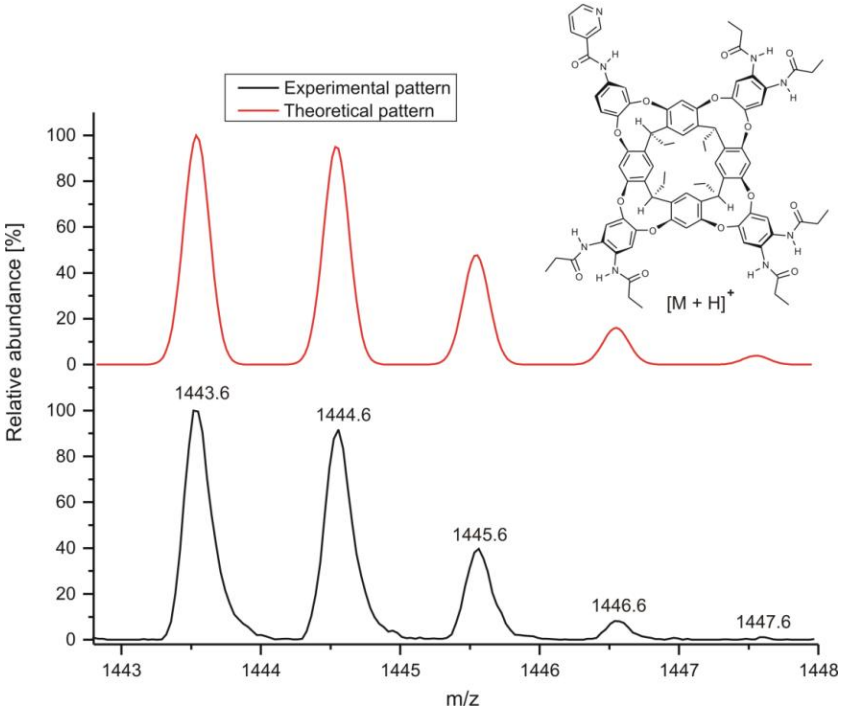

Fig. 53. MALDI-MS (+) isotopic pattern for cavitand **C20b**.

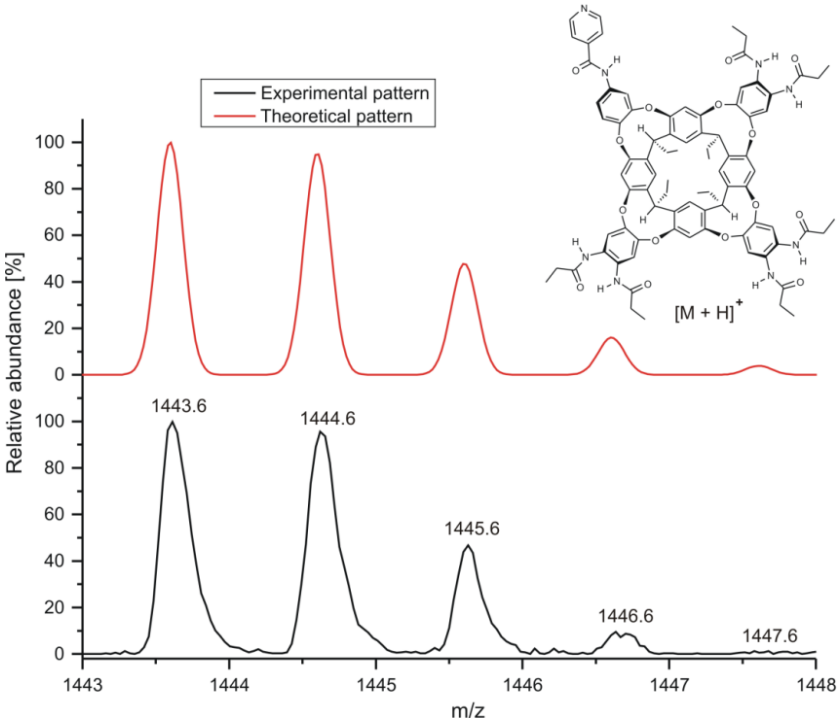

Fig. 54. MALDI-MS (+) isotopic pattern for cavitand **C20c**.

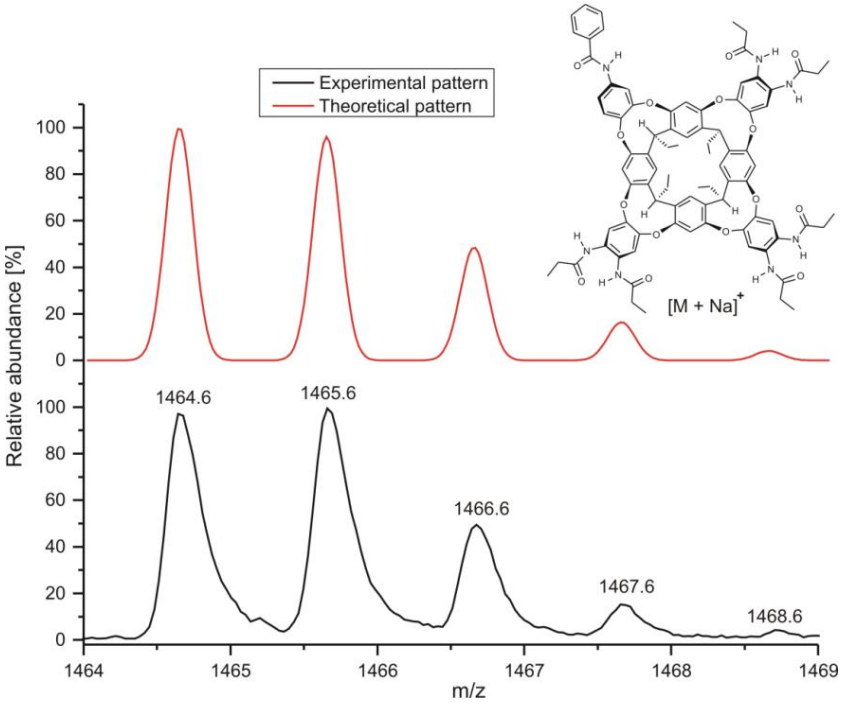

Fig. 55. MALDI-MS (+) isotopic pattern for cavitand **C20d**.

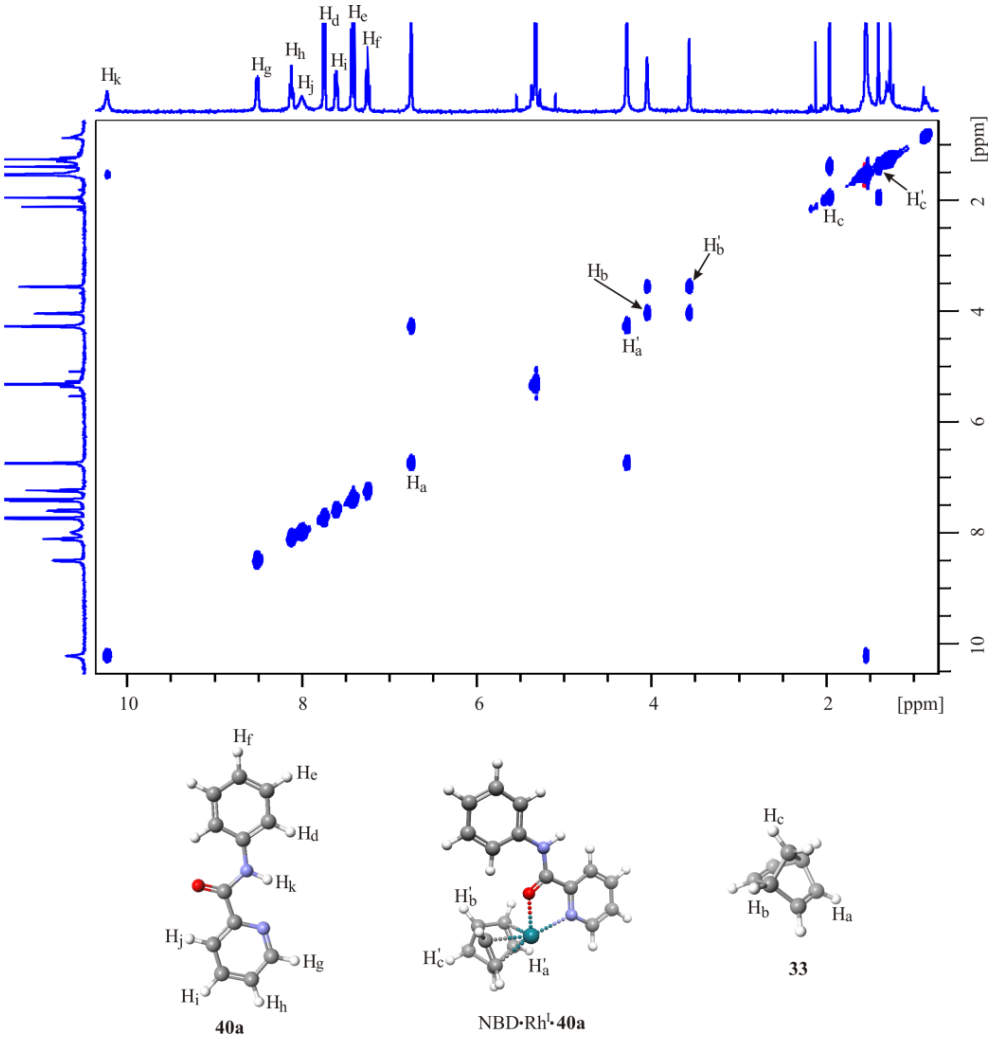

Fig. 56. ^{1}H-^{1}H NOESY NMR spectrum (d8 = 300 ms) of a complex mixture composed of a reference ligand **40a** (2.4 µmol) and an organometallic complex **2** (2.0 µmol) dissolved in CD_2Cl_2 (550 µL).

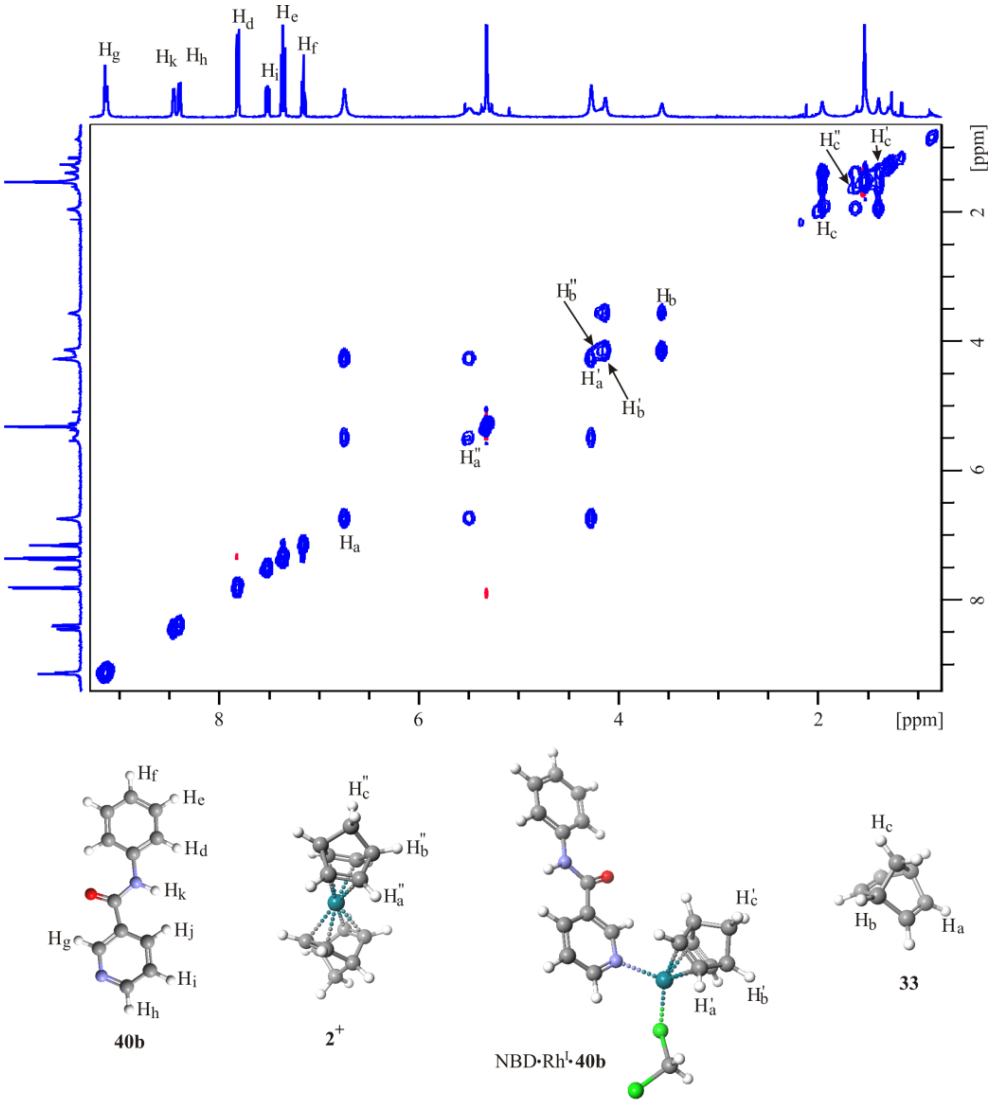

Fig. 57. ^{1}H-^{1}H NOESY NMR spectrum (d8 = 300 ms) of a complex mixture composed of a reference ligand **40b** (2.4 μmol) and an organometallic complex **2** (2.0 μmol) dissolved in CD_2Cl_2 (550 μL).

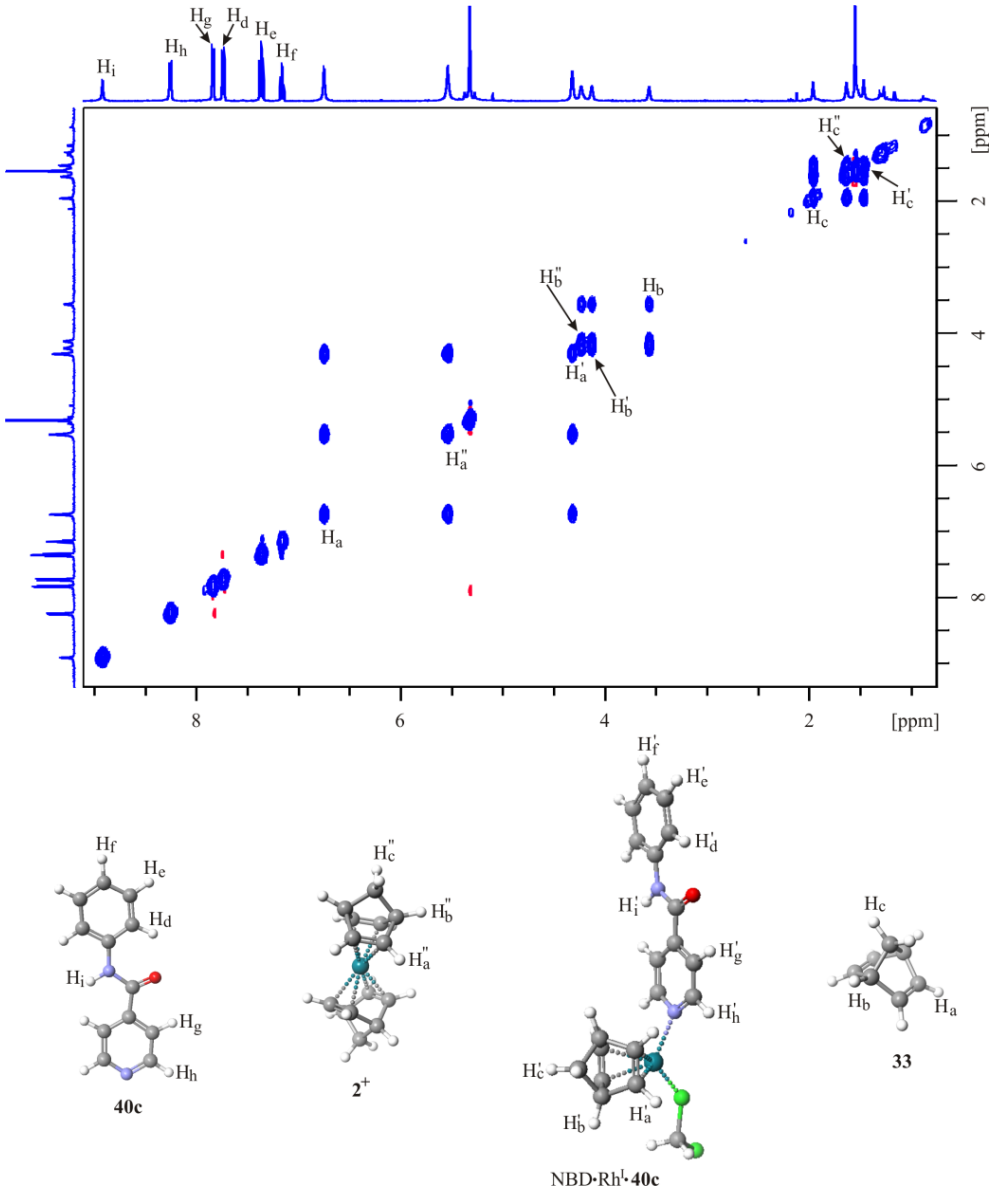

Fig. 58. ^{1}H-^{1}H NOESY NMR spectrum (d8 = 300 ms) of a complex mixture composed of a reference ligand **40c** (2.4 μmol) and an organometallic complex **2** (2.0 μmol) dissolved in CD_2Cl_2 (550 μL).

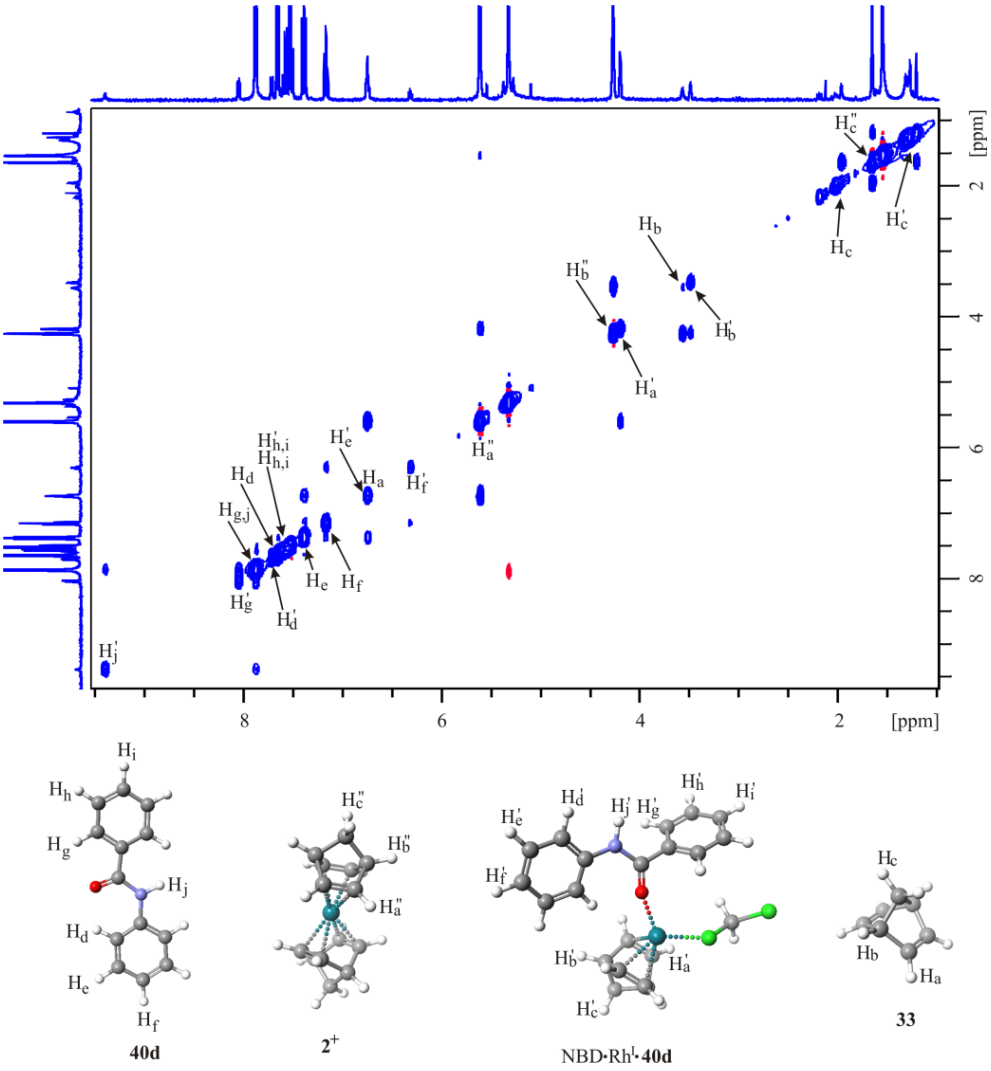

Fig. 59. ^{1}H-^{1}H NOESY NMR spectrum (d8 = 300 ms) of a complex mixture composed of a reference ligand **40d** (2.4 µmol) and an organometallic complex **2** (2.0 µmol) dissolved in CD_2Cl_2 (550 µL).

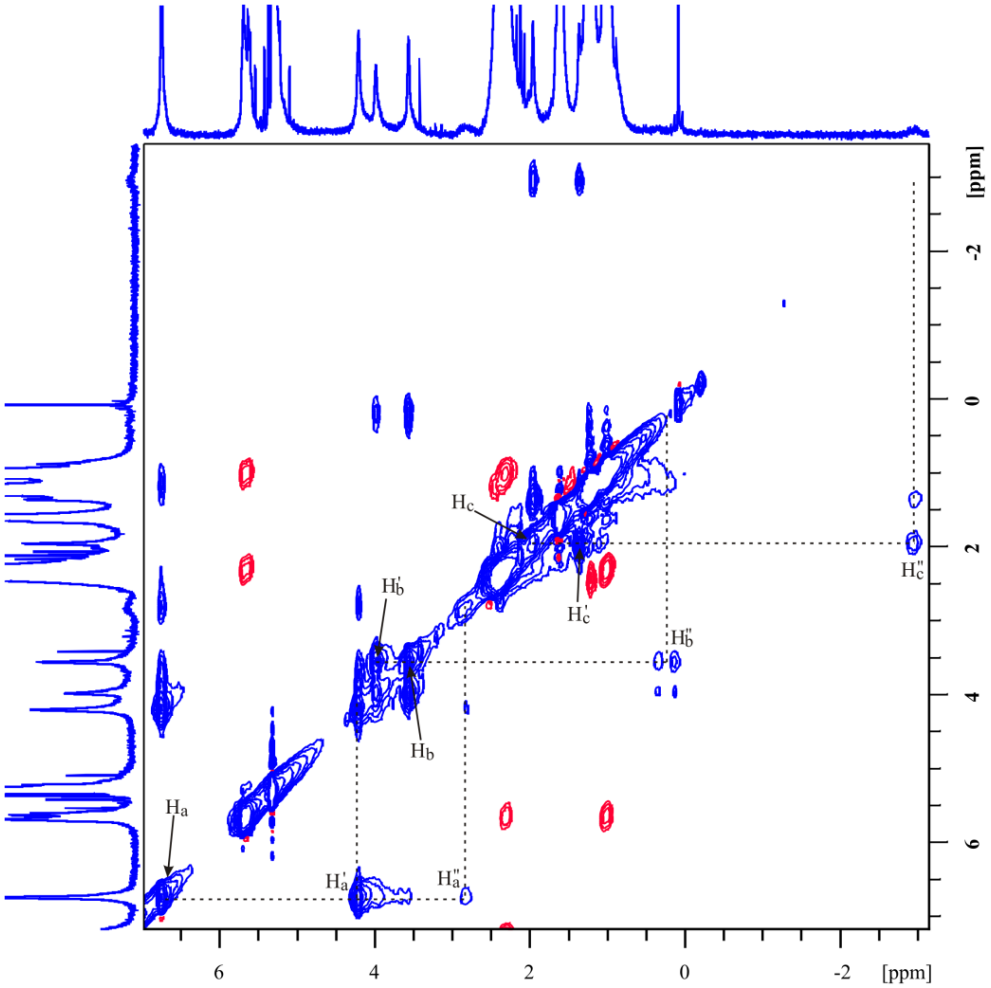

Fig. 60. ^{1}H-^{1}H NOESY NMR spectrum (d8 = 600 ms) of a complex mixture composed of a cavitand **C20a** (2.4 µmol) and an organometallic complex **2** (2.0 µmol) dissolved in CD_2Cl_2 (550 µL).

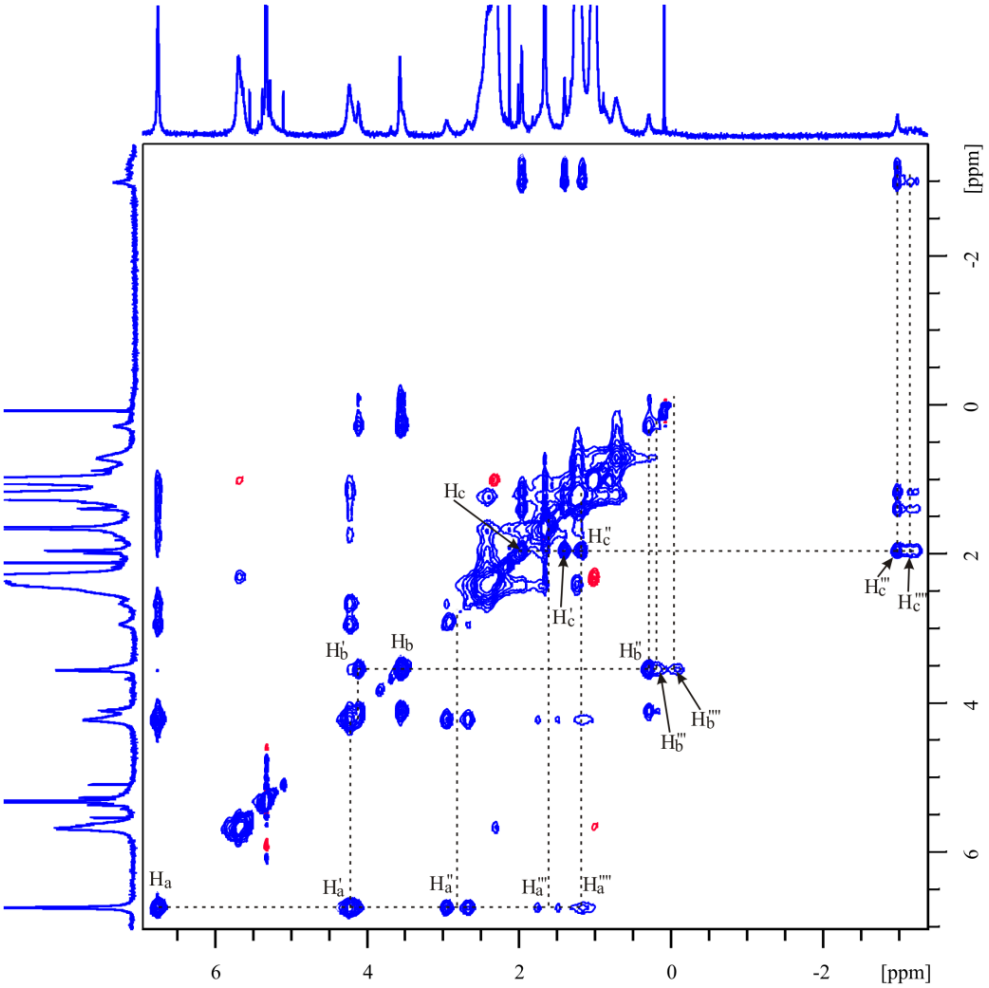

Fig. 61. ^{1}H-^{1}H NOESY NMR spectrum (d8 = 600 ms) of a complex mixture composed of a cavitand **C20b** (2.4 μmol) and an organometallic complex **2** (2.0 μmol) dissolved in of CD_2Cl_2 (550 μL).

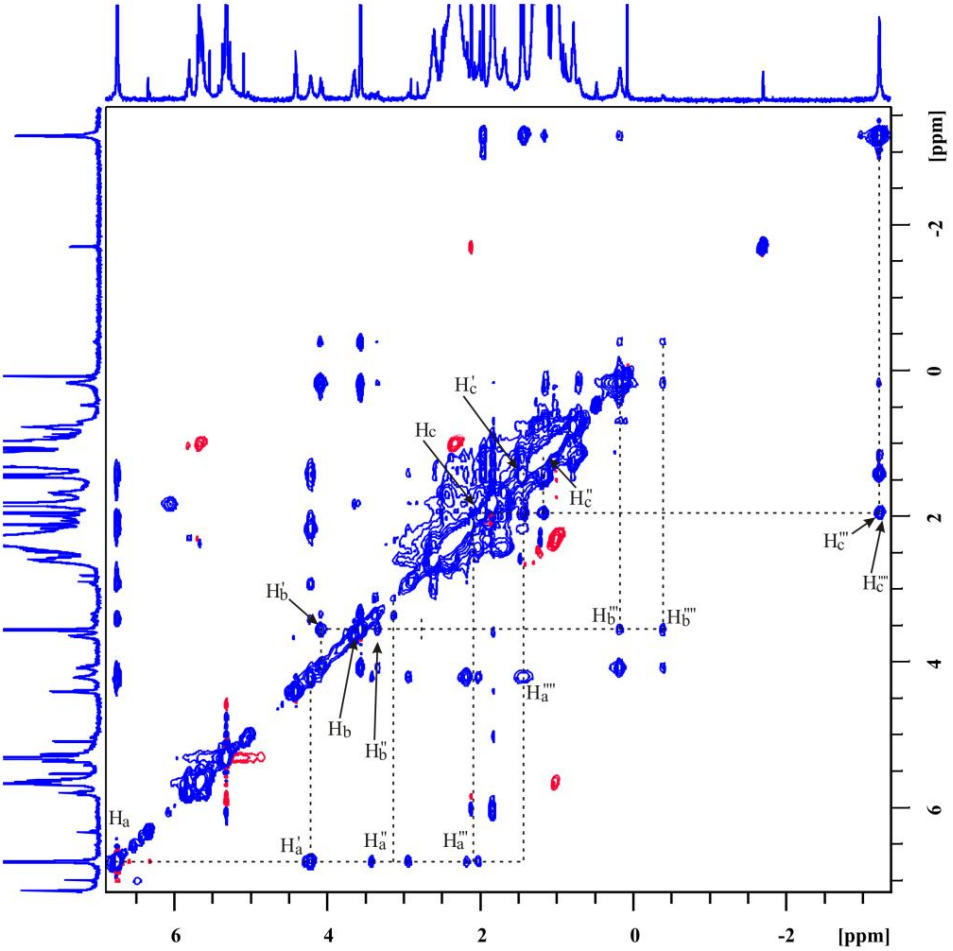

Fig. 62. ^{1}H-^{1}H NOESY NMR spectrum (d8 = 600 ms) of a complex mixture composed of a cavitand **C20c** (2.4 µmol) and an organometallic complex **2** (2.0 µmol) dissolved in CD_2Cl_2 (550 µL).

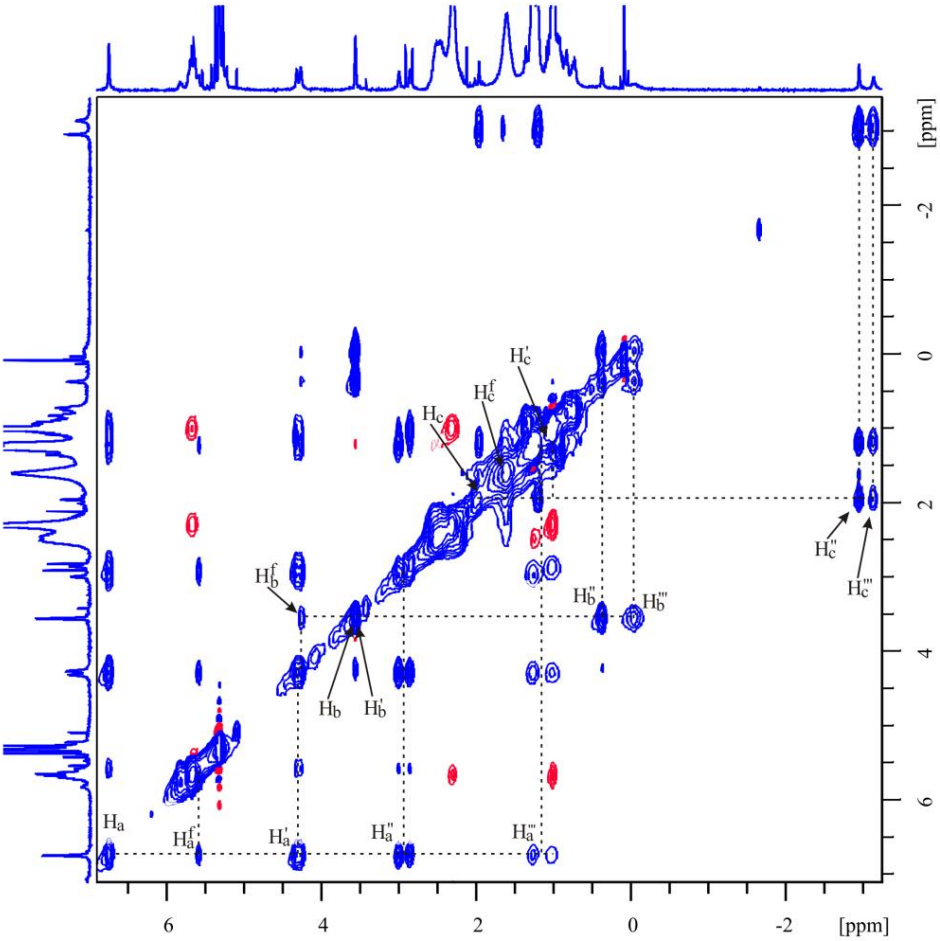

Fig. 63. ^{1}H-^{1}H NOESY NMR spectrum (d8 = 600 ms) of a complex mixture composed of a cavitand **C20d** (2.4 µmol) and an organometallic complex **2** (2.0 µmol) dissolved in CD_2Cl_2 (550 µL).

Table 6. Complex distribution (%) determined by ^{1}H NMR spectroscopy.

Systems	*exo*-NBD•Rh^{I}•**C20**	*endo*-NBD•Rh^{I}•**C20**	**2**⊂**C20**	Rh^{I}•NBD⊂**C20**	**2**
C20a+**2**	90	10	/	/	/
C20b+**2**	62	21	17	/	/
C20c+**2**	23	/	9	68	/
C20d+**2**	/	/	45	50	5

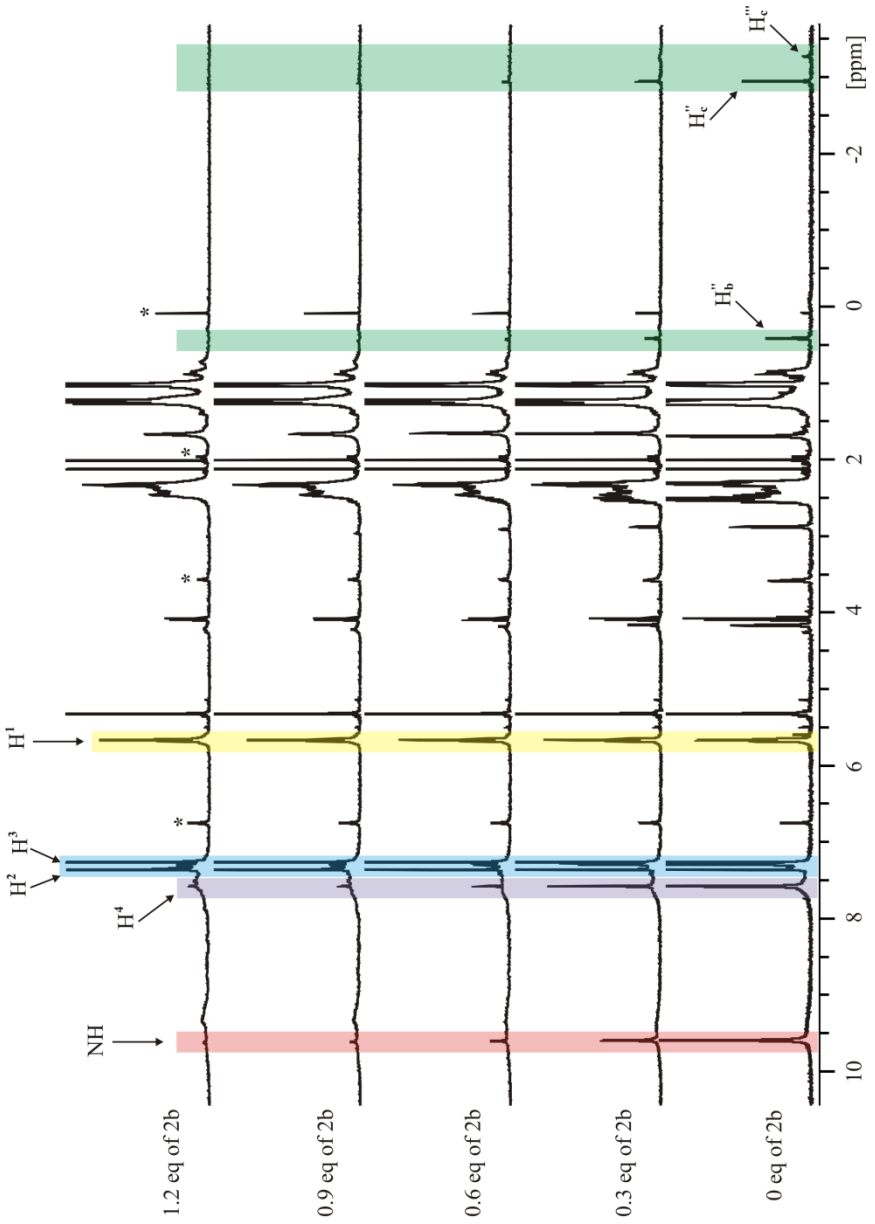

Fig. 64. Changes in ^{1}H NMR spectra (400 MHz) during titration of a caviplex system composed of an organometallic complex **2** (2.0 μmol) and a cavitand **C5** (2.4 μmol) dissolved in CD_2Cl_2 (550 μL) with the cavitand **C20b**. Designations: * - impurity. Note that H^2, H^3 and H^1 signals of caviplex **C5** coincide with signals of the free cavitand **C5**.

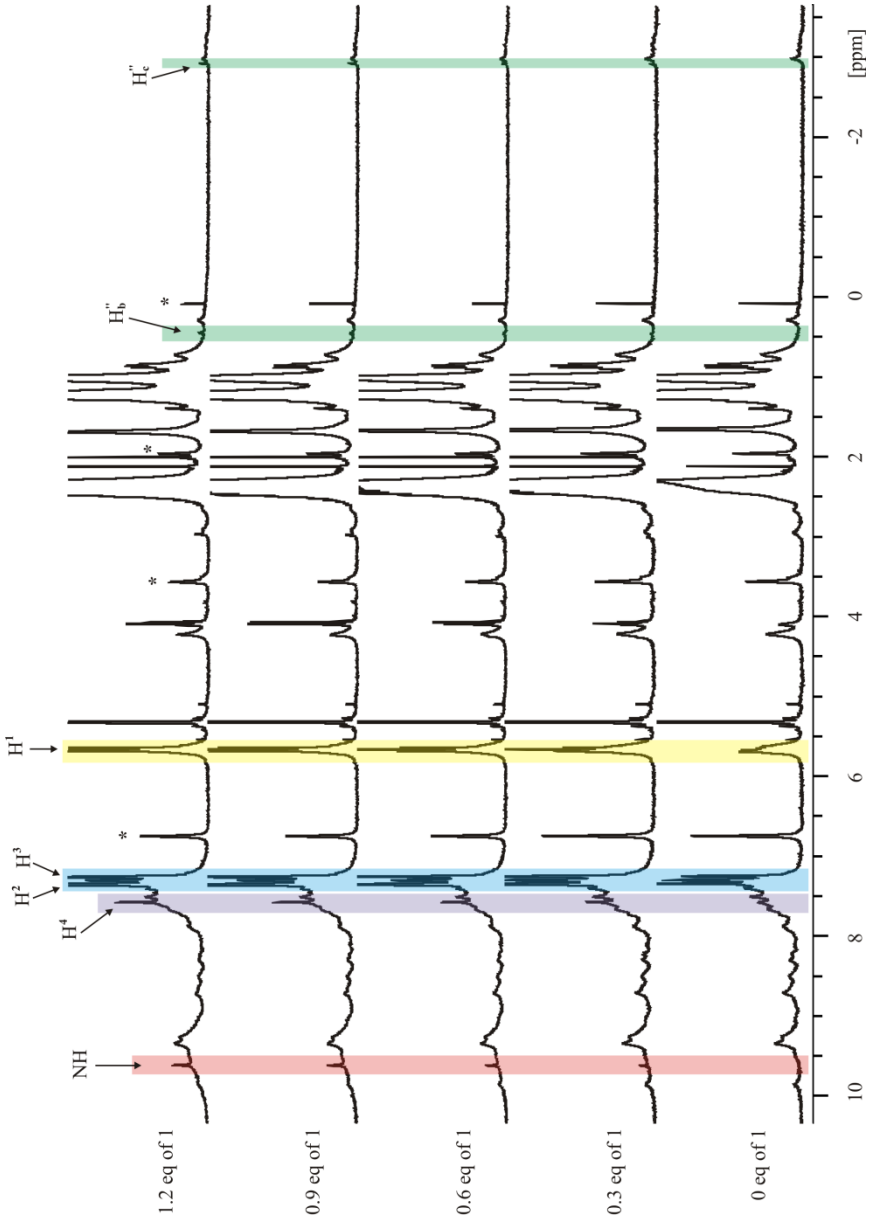

Fig. 65. Changes in ^{1}H NMR spectra (400 MHz) during titration of a caviplex system composed of an organometallic complex **2** (2.19 μmol) and a cavitand **C20b** (2.51 μmol) dissolved in CD_2Cl_2 (550 μL) with the cavitand **C5**. Designations: * - impurity. Note that H^2, H^3 and H^1 signals of caviplex **C5** coincide with signals of the free cavitand **C5**.

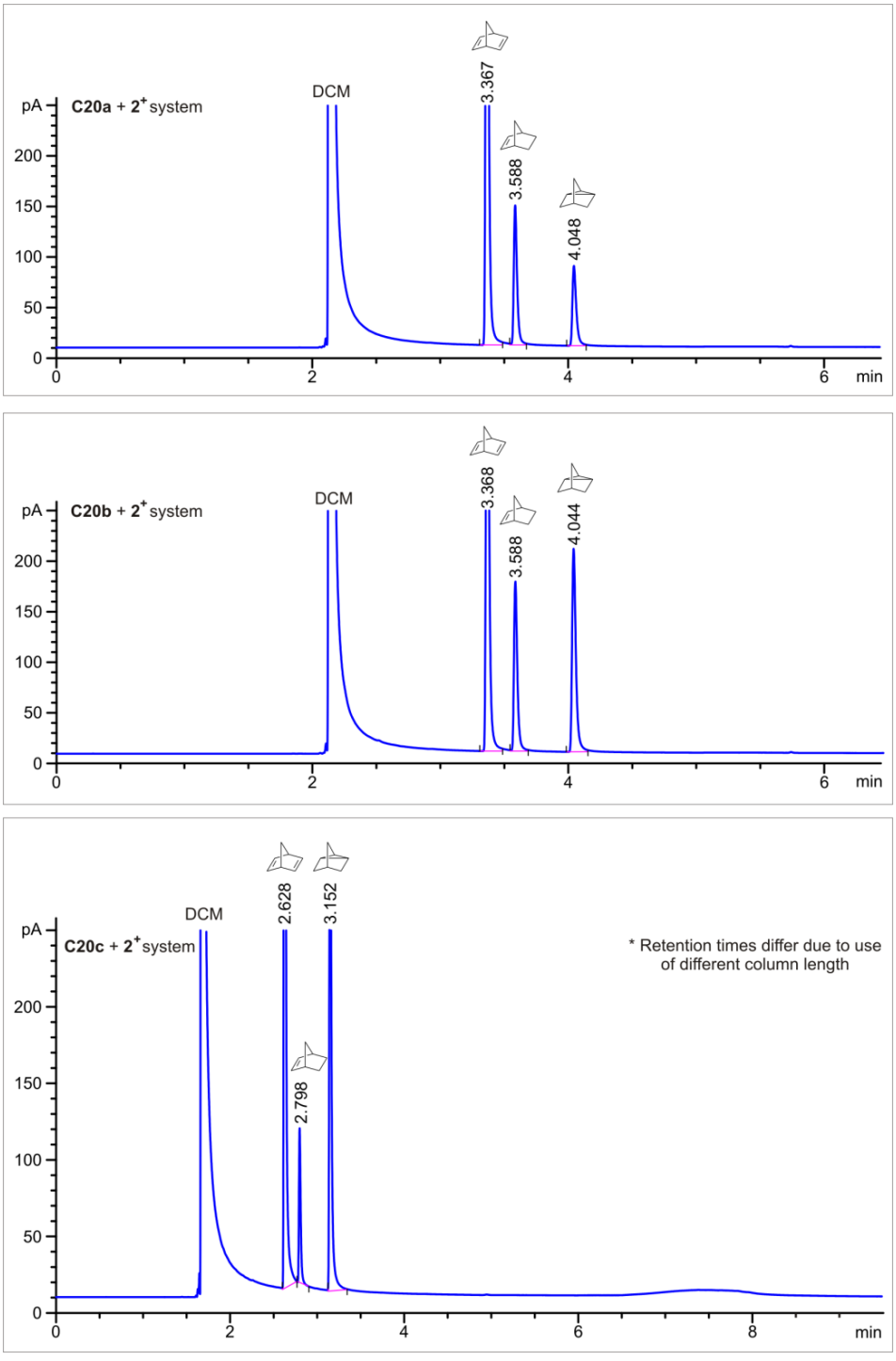

Fig. 66. GC/FID traces of product mixture after 45 min of reaction catalyzed by reaction system composed of organometallic complex **2** (20 μmol) in the presence of cavitands **C20a-c** (25 μmol) in in CH_2Cl_2 (6.8 mL).

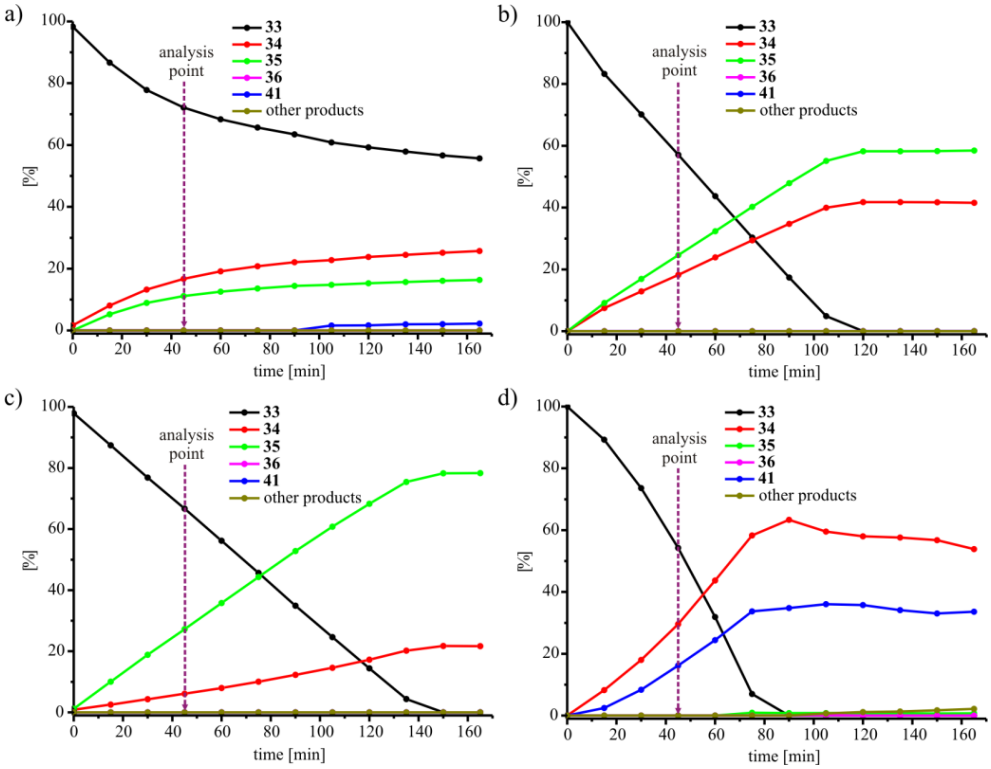

Fig. 67. Full GC/FID kinetic curves for catalytic hydrogenation (1 atm) of norbornadiene (**33**, 2.12 mmol) catalyzed by organometallic complex **2** in the presence of cavitand (25 μmol): a) **C20a**, b) **C20b**, c) **C20c**, and d) **C20a** in CH_2Cl_2 (6.8 mL). Analysis point: 45 min.

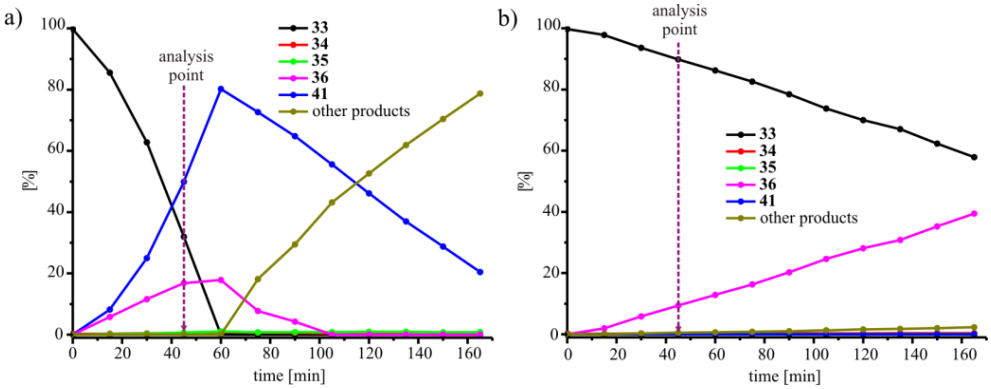

Fig. 68. Full GC/FID kinetic curves for catalytic hydrogenation (1 atm, a) and catalytic dimerization (b) of norbornadiene (**33**, 2.12 mmol) catalyzed by **2** (20 μmol) in CH_2Cl_2 (6.8 mL). Analysis point: 45 min.

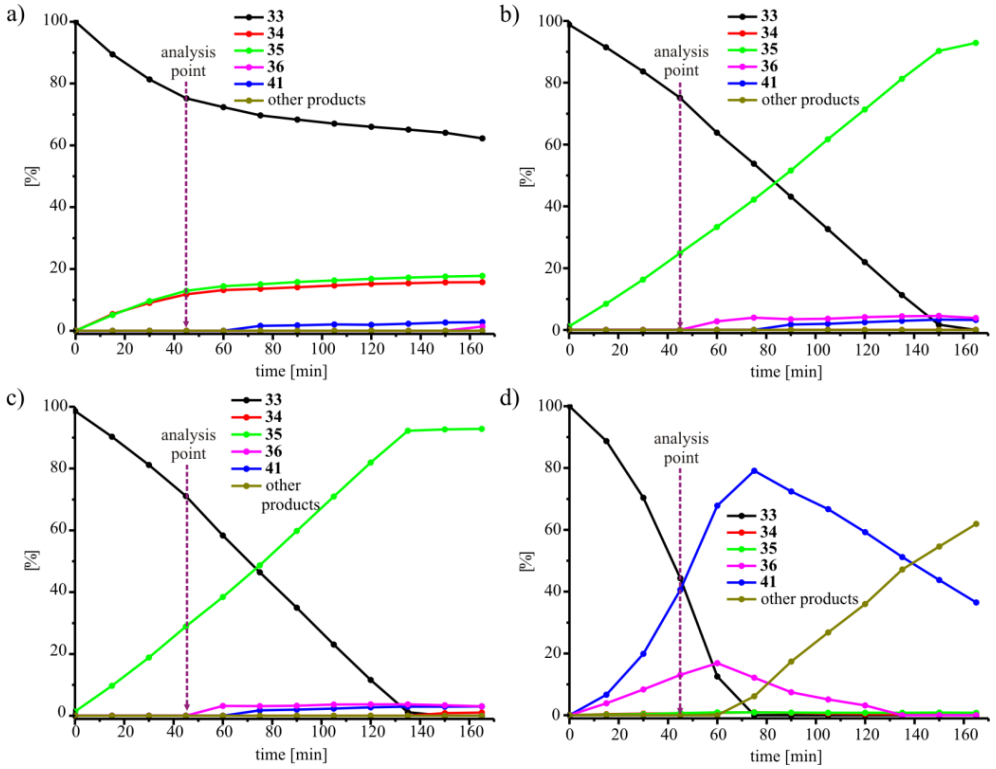

Fig. 69. Full GC/FID kinetic curves for catalytic hydrogenation (1 atm) of norbornadiene (**33**, 2.12 mmol) catalyzed by organometallic complex **2** (20 μmol) in the presence of ligand (25 μmol): a) **40a**, b) **40b**, c) **40c**, and d) **40d** in CH_2Cl_2 (6.8 mL). Analysis point: 45 min.

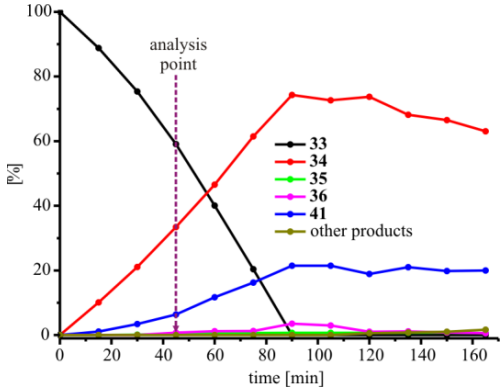

Fig. 70. Full GC/FID kinetic curves for the catalytic hydrogenation (1 atm) of norbornadiene (**33**, 2.12 mmol) catalyzed by mixture of cavitand **C5** (25 μmol) and organometallic complex **2** (20 μmol) in CH_2Cl_2 (6.8 mL). Analysis point: 45 min.

3.6 References and notes

[1] P. W. N. M. van Leeuwen, ed., *Supramolecular catalysis*, Wiley-VCH, Weinheim, 2008.
[2] M. Raynal, P. Ballester, A. Vidal-Ferran and P. W. N. M. van Leeuwen, *Chem. Soc. Rev.*, 2014, **43**, 1660-1733.
[3] M. Raynal, P. Ballester, A. Vidal-Ferran and P. W. N. M. van Leeuwen, *Chem. Soc. Rev.*, 2014, **43**, 1734-1787.
[4] A. Cavarzan, J. N. H. Reek, F. Trentin, A. Scarso and G. Strukul, *Cat. Sci. Tech.*, 2013, **3**, 2898-2901.
[5] B. W. Purse, A. Gissot and J. Rebek, *J. Am. Chem. Soc.*, 2005, **127**, 11222-11223.
[6] T. Murase, Y. Nishijima and M. Fujita, *J. Am. Chem. Soc.*, 2011, **134**, 162-164.
[7] C. J. Hastings, M. P. Backlund, R. G. Bergman and K. N. Raymond, *Angew. Chem., Int. Ed.*, 2011, **50**, 10570-10573.
[8] J. Meeuwissen and J. N. H. Reek, *Nature Chem.*, 2010, **2**, 615-621.
[9] H. J. Hwang, J. R. Carey, E. T. Brower, A. J. Gengenbach, J. A. Abramite and Y. Lu, *J. Am. Chem. Soc.*, 2005, **127**, 15356-15357.
[10] T. S. Koblenz, J. Wassenaar and J. N. H. Reek, *Chem. Soc. Rev.*, 2008, **37**, 247-262.
[11] M. A. Sarmentero, H. Fernández-Pérez, E. Zuidema, C. Bo, A. Vidal-Ferran and P. Ballester, *Angew. Chem., Int. Ed.*, 2010, **49**, 7489-7492.
[12] D. Fiedler, R. G. Bergman and K. N. Raymond, *Angew. Chem., Int. Ed.*, 2006, **45**, 745-748.
[13] Z. J. Wang, C. J. Brown, R. G. Bergman, K. N. Raymond and F. D. Toste, *J. Am. Chem. Soc.*, 2011, **133**, 7358-7360.
[14] A. Cavarzan, A. Scarso, P. Sgarbossa, G. Strukul and J. N. H. Reek, *J. Am. Chem. Soc.*, 2011, **133**, 2848-2851.
[15] V. F. Slagt, J. N. H. Reek, P. C. J. Kamer and P. W. N. M. van Leeuwen, *Angew. Chem., Int. Ed.*, 2001, **40**, 4271-4274.
[16] A. W. Kleij and J. N. H. Reek, *Chem-Eur J*, 2006, **12**, 4219-4227.
[17] V. F. Slagt, P. C. J. Kamer, P. W. N. M. van Leeuwen and J. N. H. Reek, *J. Am. Chem. Soc.*, 2004, **126**, 1526-1536.
[18] B. Kang, J. W. Kurutz, K. T. Youm, R. K. Totten, J. T. Hupp and S. T. Nguyen, *Chem. Sci.*, 2012, **3**, 1938-1944.
[19] C. J. Brown, G. M. Miller, M. W. Johnson, R. G. Bergman and K. N. Raymond, *J. Am. Chem. Soc.*, 2011, **133**, 11964-11966.
[20] D. M. Rudkevich, G. Hilmersson and J. Rebek, *J. Am. Chem. Soc.*, 1997, **119**, 9911-9912.
[21] D. M. Rudkevich, G. Hilmersson and J. Rebek, *J. Am. Chem. Soc.*, 1998, **120**, 12216-12225.
[22] R. J. Roth and T. J. Katz, *Tetrahedron Lett.*, 1972, **13**, 2503-2504.
[23] O. B. Berryman, A. C. Sather, A. Lledó and J. Rebek, *Angew. Chem., Int. Ed.*, 2011, **50**, 9400-9403.

[24] A. Szumna, *Chem. Soc. Rev.*, 2010, **39**, 4274-4285.
[25] The stereochemical designations are described in the following sequence: axial chirality (*P* or *M*) defined by the unidirectional (clockwise or counterclockwise) sense of rotation of the seven amide carbonyl groups viewed from above the cavity followed by the absolute configuration, applying the CIP rules, of the methyne (*R* or *S*) in the nine membered ring containing the asymmetric phenyldioxo bridge.
[26] J. R. Moran, J. L. Ericson, E. Dalcanale, J. A. Bryant, C. B. Knobler and D. J. Cram, *J. Am. Chem. Soc.*, 1991, **113**, 5707-5714.
[27] A. J. Pardey and C. Longo, *Coord. Chem. Rev.*, 2010, **254**, 254-272.
[28] A. Hamilton, M. Gicquel, P. Ballester and C. Bo, *Curr. Org. Chem.*, 2013, **17**, 1499-1506.
[29] J. J. Mrowca and T. J. Katz, *J. Am. Chem. Soc.*, 1966, **88**, 4012-4015.
[30] M. B. Krüger, C. Selle, D. Heller and W. Baumann, *J. Chem. Eng. Data*, 2012, **57**, 1737-1744.
[31] CCDC 990079 (**2a**), 990080 (**2b**), 990081 (**2d**) contain the supplementary crystallographic data for this paper. These data can be obtained free of charge from The Cambridge Crystallographic Data Centre via https://summary.ccdc.cam.ac.uk/structure-summary-form.
[32] L. Zhang, W. Wang, A. Wang, Y. Cui, X. Yang, Y. Huang, X. Liu, W. Liu, J.-Y. Son, H. Oji and T. Zhang, *Green Chem.*, 2013, **15**, 2680-2684.
[33] W. Fang, Q. Deng, M. Xu and T. Tu, *Org. Lett.*, 2013, **15**, 3678-3681.
[34] K. Motoshima, Y. Hiwasa, M. Yoshikawa, K. Fujimoto, A. Tai, H. Kakuta and K. Sasaki, *ChemMedChem*, 2007, **2**, 1527-1532.

CHAPTER 4: Synthesis, characterization and preliminary catalytic studies on terpyridine-functionalized self-folding hexaamide cavitand coordinated to Ru^{II} with 2-(phenylazo)pyridine as an ancillary ligand

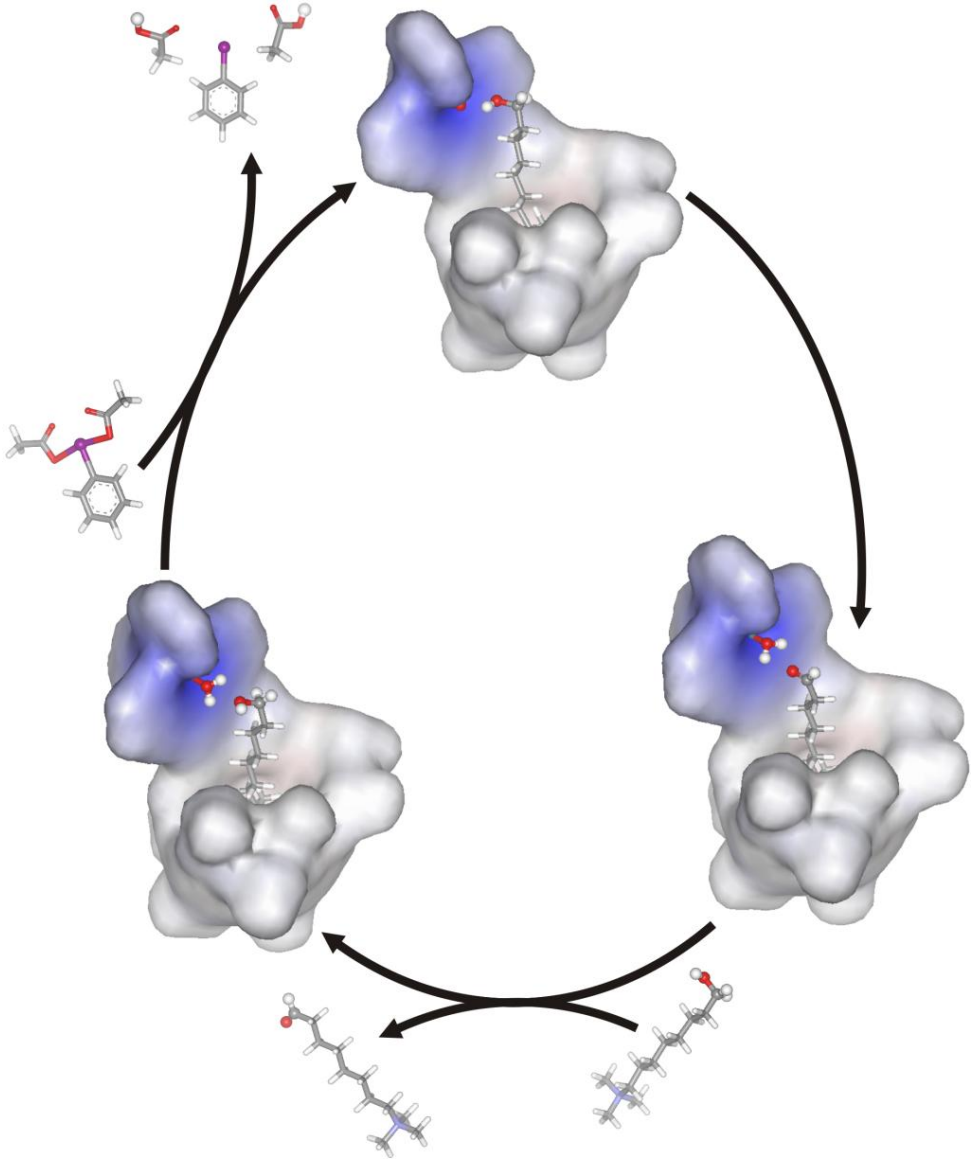

4.1 Introduction

The concept of merging molecular recognition with chemical catalysis is a growing area of interest.[1] The synthetic availability of resorcin[4]arene derived cavitands that are not symmetrically substituted[2] allowed the decoration of their structure with various functional groups, catalytic units or ligands that can coordinate a catalytic metal. Examples of these structures include oxazoline,[3] porphyrin,[4,5] salphen,[6,7] and pyridine[8] derivatives. To the best of our knowledge, only three of the resorcin[4]arene cavitands that were employed to catalyze chemical reactions contained a transition metal (Pd^{II}, Rh^{I}, Fe^{II}) coordinated to one of its modified walls.[3,8,9] Inspired by these previous findings and by the wide range of transformations catalyzed by ruthenium coordination complexes,[10] we decided to investigate the possibility of grafting a Ru^{II} organometallic complex **azpy**•Ru^{II}•(H_2O)•**tpy** (**47**) on a single wall of a resorcin[4]arene cavitand. The structure of the metallocavitand **azpy**•Ru^{II}•(H_2O)•**C24** (**C27**) that was the target of our studies is shown in **Fig. 71**.

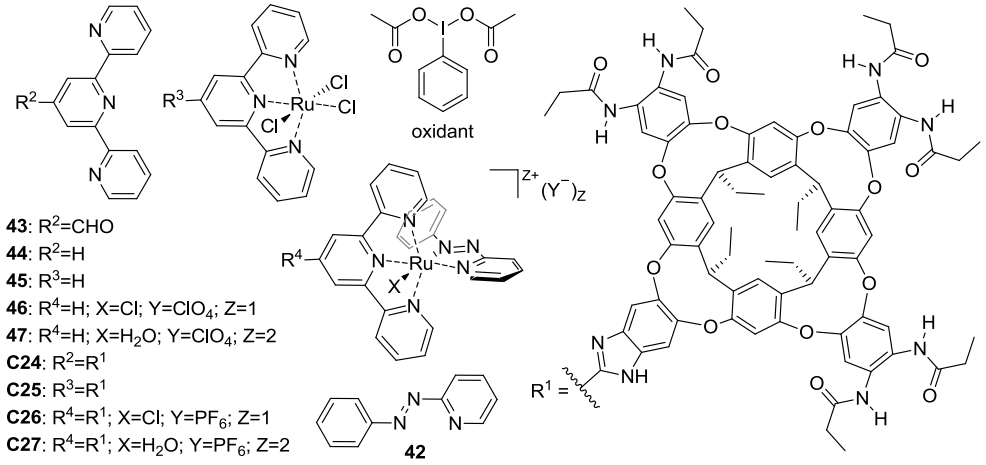

Fig. 71. Structures of a cavitand **C24**, metallocavitands Ru^{III}•Cl_3•**C24** (**C25**), **azpy**•Ru^{II}•Cl•**C24** (**C26**) and **azpy**•Ru^{II}•(H_2O)•**C24** (**C27**), model molecules 2,2':6',2"-terpyridine (**tpy**, **44**), Ru^{III}•Cl_3•**tpy** (**45**), **azpy**•Ru^{II}•Cl•**tpy** (**46**) and **azpy**•Ru^{II}•(H_2O)•**tpy** (**47**), ligand 2-(phenylazo)pyridine (**azpy**, **42**), terpyridine aldehyde (**43**), and sacrificial oxidant iodosobenzene diacetate. Metallocavitands **C26** and **C27** and model molecules **46** and **47** are presented as *trans* isomers with the regards of relationship between phenyl group from ancillary **azpy** ligand (**42**) and monodentate ligand X (Cl or H_2O).

The Ru^{II} is well recognized as a metal ion capable of entering into dπ-pπ back-bonding, in addition to the conventional σ-bonding.[11] The model used in organometallic chemistry to explain the dπ-pπ back-bonding is known as Dewar-Chatt-Duncanson model (**Fig. 72**).[12,13,14] The model states that the occupied π-orbitals on the ligand (a π-acid such as alkene or diazo compound) donate their electron density to the unoccupied s-, p_z-, d_{z2}- or hybrid sd-orbitals of the metal (σ donation) simultaneously with back-donation of electron density from occupied metal d-orbitals to the empty π*-orbital of the ligand (π back-donation). As a consequence, the C-C (alkene) / N-N (azo) bond distance of a ligand increases as a result of both, decreased electron density in the bonding π-orbital and

increased electron density in the antibonding π*-orbital. This leads to elongation of the π-bond on the ligand and therefore lowering of its vibrational frequency.

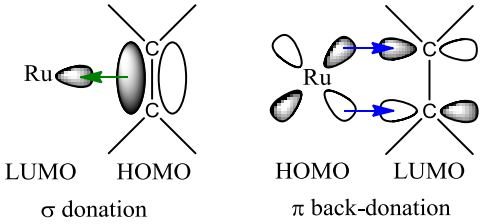

Fig. 72. Dewar-Chatt-Duncanson model for the dπ-pπ back-bonding on the example of alkene.

Our design requires the functionalization of the cavitand's structure with a single terpyridine moiety (**43**), followed by metallation with a Ru^{III}, and finally, simultaneous reduction of a metal to Ru^{II} coupled with coordination of the metal to an ancillary bidentate ligand (**azpy**, **42**, **Fig. 71**). The sixth coordination site (X) of the Ru^{II} center will be occupied by an aqua ligand. The Ru^{II}•(H_2O) complex will be converted into the catalytically active Ru^{IV}•(O) species through the intermediacy of a sacrificial chemical oxidant iodosobenzene diacetate. Ru^{IV}•(O) species are known to be catalytically active towards various oxidations. The ancillary ligand plays a crucial role in tuning the redox properties of the ruthenium metal center by promoting either one-electron transfer (via Ru^{III}) or two-electron transfer pathway(s). The ancillary ligand can also affect the selectivity of the Ru^{IV}•(O) organometallic complex by involving steric and electronic effects. In the design of our catalytic system, we selected the strong π-acid 2-(phenylazo)pyridine (**azpy**, **42**) as an ancillary ligand also known for its capability to act as both σ-donor and π-acceptor. This ligand promotes a two-step proton-coupled electron transfer (PCET), preventing the electrostatic charge buildup and thus the formation of high-energy intermediates and giving an easy access to high-valence catalytically active Ru^{IV}•(O) species.[15,16] Furthermore, due to preferred involvement of Ru^{IV}•(O) species in two-electron transfer reactions, two reaction mechanisms are possible for the epoxidation reaction and include: 1) concerted mechanism, and, 2) mechanism via metalla-oxetane.[17,18,19,20] Both pathways promote stereoselective reactions. The third mechanism, promoted by different ancillary ligands, involves one-electron transfer and formation of radical species and for this reason does not show stereoselectivity.[19,20] The Ru^{IV}•(O) species are unstable and have a high tendency to oxidize organic molecules used as substrates. After oxidation of the substrate the ruthenium metal center recovers its original oxidation state and coordinates to a new aqua ligand affording Ru^{II}•(H_2O) species that can enter the next catalytic cycle. Among numerous chemical transformations catalyzed by Ru^{II}, we decided to test the epoxidation of alkenes[15,21,22,23,24,25,26] and the oxidation of primary alcohols to aldehydes.[27,28,29,30,31,32]

4.2 Results and discussion

4.2.1 Synthesis

The synthesis of metallocavitand **C27** was tackled in a convergent manner and was divided into four stages. In the first stage, we synthesized the ancillary ligand **azpy** (**42**) following a published procedure.[11,33] The synthesis of **azpy** consisted of the base catalyzed condensation of 2-amino-pyridine with nitrosobenzene (**Scheme 1**).

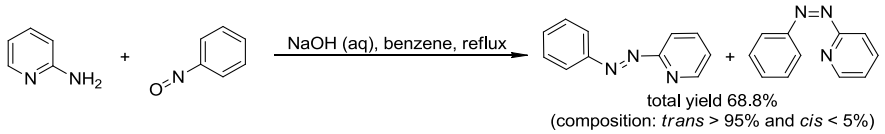

Scheme 1. Synthesis of 2-(phenylazo)pyridine (**42**).

The second stage consisted of a four-step synthesis to obtain the appropriate terpyridine molecule (**43**) equipped with an aldehyde function in the 4' position (**Scheme 2**).

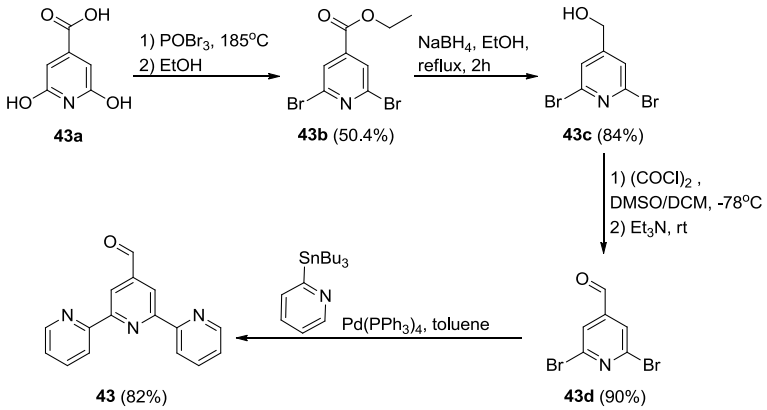

Scheme 2. Synthetic scheme for the preparation of terpyridine aldehyde **43**.

The aldehyde function is required in order to connect the terpyridine moiety to one of the cavitand's walls. In the first step of the synthesis, we performed the bromination of the phenolic and carboxylic hydroxyl groups of the 2,6-dihydroxyisonicotinic acid (**43a**) using phosphoryl bromide. The product obtained from the triple bromination was treated with ethanol yielding the corresponding ethyl ester **43b**. This procedure represents a small improvement with respect to the published one.[34,35] In the second synthetic step, the ethyl ester **43b** was reduced to the benzyl alcohol **43c** by the action of sodium borohydride. Subsequently, the primary benzyl alcohol was oxidized to the aldehyde **43d** using Swern conditions. Finally, the Stille coupling of the aldehyde **43d** with two equivalents of 2-(tributylstannyl)pyridine afforded the desired terpyridine aldehyde **43**.[36]

The third stage of our designed convergent synthesis consisted in the preparation of the hexaamidediamine cavitand **C9** following the reported procedure (**Scheme 3**).[37,38]

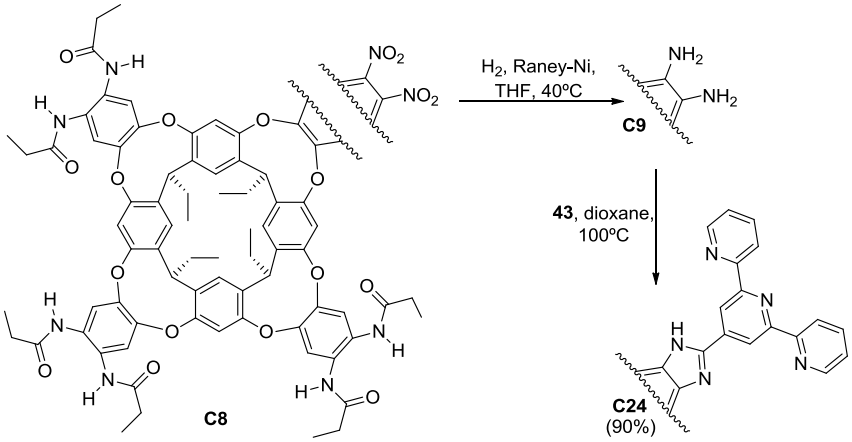

Scheme 3. Introduction of terpyridine moiety into the cavitand framework. For simplification, fragment of the modified cavitand wall is highlighted.

The coupling of the hexaamidediamine cavitand **C9** with the terpyridine aldehyde **43** by *in situ* oxidation of the intermediate imine with the present air afforded the terpyridine cavitand **C24** in good yield (90%).[38]

Finally, the incorporation of the catalytic Ru^{II} metal center to the terpyridine cavitand **C24** required three additional synthetic steps (**Scheme 4**).[39,40] In the first step, the cavitand **C24** was refluxed with $RuCl_3$ in ethanol solution, affording the metallocavitand Ru^{III}•Cl_3•**C24** (**C25**) in 83% yield. Second, the introduction of an ancillary ligand was performed by refluxing, also in ethanol solution, the metallated cavitand Ru^{III}•Cl_3•**C24** (**C25**) with the ligand **azpy** (**42**). The chelation of the ancillary ligand, in the presence of triethylamine, produced the concomitant reduction of the metal center from Ru^{III} to Ru^{II}. In the workup of the reaction we also carried out the exchange of the chloride anion by a less-coordinating counterpart (PF_6^-). Although we were able to purify and isolate the organometallic complex *trans*-**azpy**•Ru^{II}•Cl•**tpy** (**46**, **Scheme 4**) using both crystallization and column chromatography on silica, this was not the case with the cavitand analogue **azpy**•Ru^{II}•Cl•**C24** (**C26**). The only purification option we were able to apply was column chromatography on basic alumina. First, unreacted **azpy** (**42**) and a mixture of isomeric forms (*cis*-*trans*-*cis*- and *trans*-*trans*-*trans*-) of (**azpy**)$_2$•Ru^{II}•Cl_2 as a blue solution eluted from the column, followed by a dark pink fraction corresponding to the metallocavitand **C26** (88%), possibly as a mixture of *cis* and *trans* isomeric forms.[41]

Once we obtained the **azpy**•Ru^{II}•Cl•**C24** (**C26**) cavitand, all that was left was the substitution of the coordinated chloro by an aqua ligand. This exchange was performed using $AgPF_6$ in the presence of water furnishing the **azpy**•Ru^{II}•(H_2O)•**C24** (**C27**) metallocavitand in 99% yield.

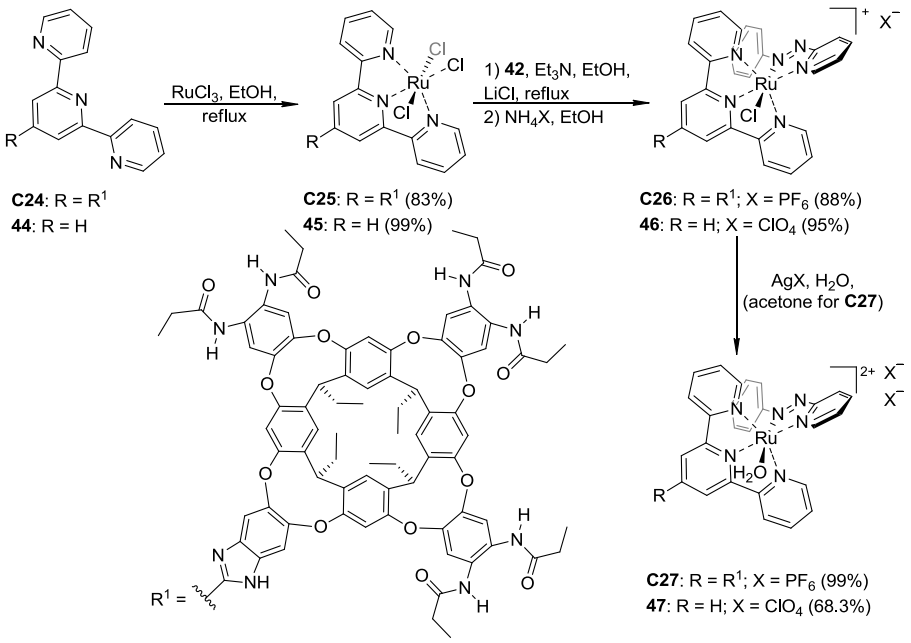

Scheme 4. Metallation of the terpyridine moiety. The metallocavitand and the organometallic complex are presented in their *trans* forms.

The model complex **azpy**•Ru^{II}•(H_2O)•**tpy** (**47**, **Scheme 4**) was produced starting from 2,2':6',2''-terpyridine (**tpy**, **44**) using an analogous synthetic procedure to the one described for the cavitand **C27** with the difference of producing ClO_4^- salts.[40] This Ru^{II} complex (**47**) was used as a reference in the characterization and catalytic studies of the Ru^{II} cavitand **C27**.

4.2.2 Characterization

Cavitand **C24**: A careful examination of the downfield region of the ^1H NMR spectrum of the cavitand **C24** in chloroform-*d* solution at room temperature revealed the presence of separate signals for each one of the six NH protons and all its aromatic protons (**Fig. 73**, see Supporting Information for full spectrum).

The number of proton signals was consistent with a C_1 symmetry indicating a slow interconversion on the NMR timescale between two senses of unidirectional orientation of amide groups. This unidirectional orientation of amides is induced by the formation of an array of hydrogen bonds at the upper rim of cavitand **C24**. The preferred sense of orientation of amides is dictated by hydrogen-bonding characteristics of the tautomeric form in the imidazole unit. The unidirectional orientation of amides in **C24** is the origin of an asymmetry element that renders this compound as a mixture of two cycloenantiomers.

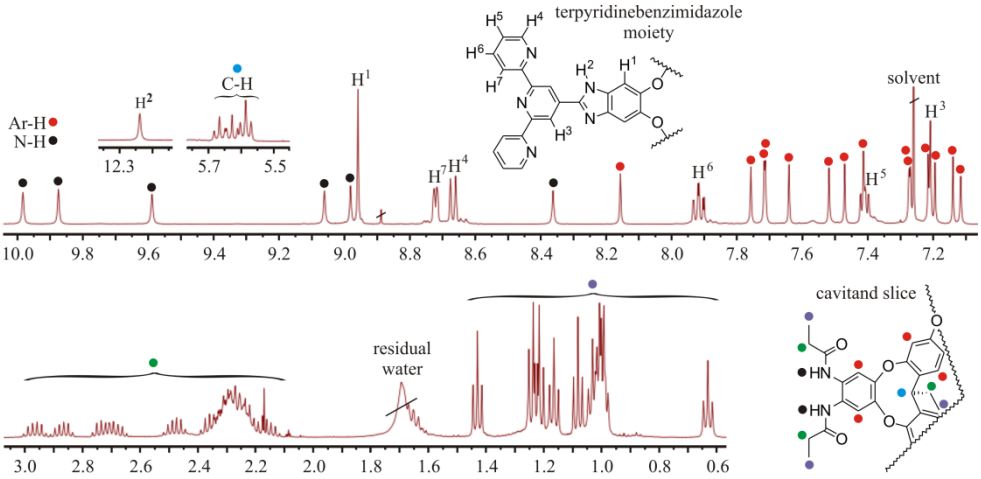

Fig. 73. Selected downfield and upfield regions of ^{1}H NMR spectrum of cavitand **C24** in $CDCl_3$.

The NOESY spectrum of the cavitand **C24** showed a cross-peak between the imidazole proton (H^2) and the residual water signal indicating chemical exchange of acidic imidazole proton with protons from residual water. A close analysis of the downfield region of the NOESY spectrum for NH signals showed the existence of chemical exchange cross-peaks between three different pairs of NHs (1-5, 2-6, 3-4, **Fig. 74**, left).

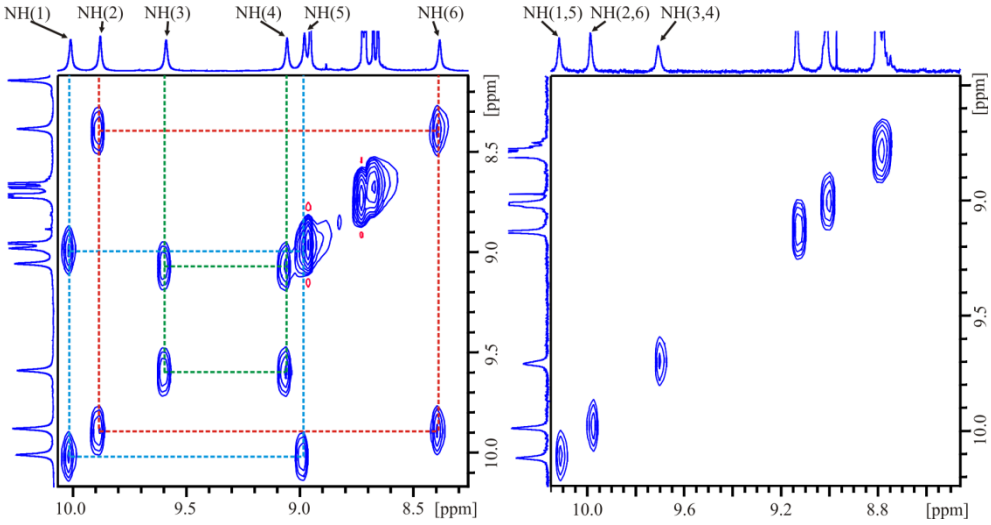

Fig. 74. Zoom in of the NOESY spectrum of the NH region for the cavitand **C24** in $CDCl_3$ (left) and acetone-d_6 (right).

This is the expected result of the slow interconversion on the NMR timescale between two possible cycloenantiomers of the cavitand **C24**, having clockwise and counterclockwise sense of direction of the hydrogen-bonded array of amides. An EXSY experiment performed at 298 K allowed us to calculate the interconversion rate of 1 s^{-1} corresponding to an energy barrier of 15 kcal mol^{-1}.

A change of solvent from nonpolar chloroform-*d* or methylene chloride-d_2 to polar acetone-d_6, increased the rate of interconversion between two cycloenantiomers of **C24**. Thus, in acetone-d_6 solution at room temperature we observed only three signals for NH protons instead of the six detected in the nonpolar solvents (**Fig. 74**, right).

The vase conformation of the cavitand **C24** in the solid-state was corroborated by XRD analysis of the obtained single crystals (**Fig. 75**). The examination of the crystal structure showed that the vase conformation of the cavitand **C24** was stabilized by the formation of an array of seven intramolecular hydrogen bonds between six amides and acidic benzimidazole hydrogen atom as suggested from the studies in solution. The examination of two cavitand molecules facing each other shows that each has a delocalized solvent molecule included in the aromatic cavity and between their upper rims (**Fig. 75**, a). Chirality analysis shows that two cavitands **C24**, that face each other, are enantiomers (*P*,*R*-**C24** and *M*,*S*-**C24**). The present elements of asymmetry are given on an example of *P*,*R*-**C24** enantiomer (**Fig. 75**, b and c).

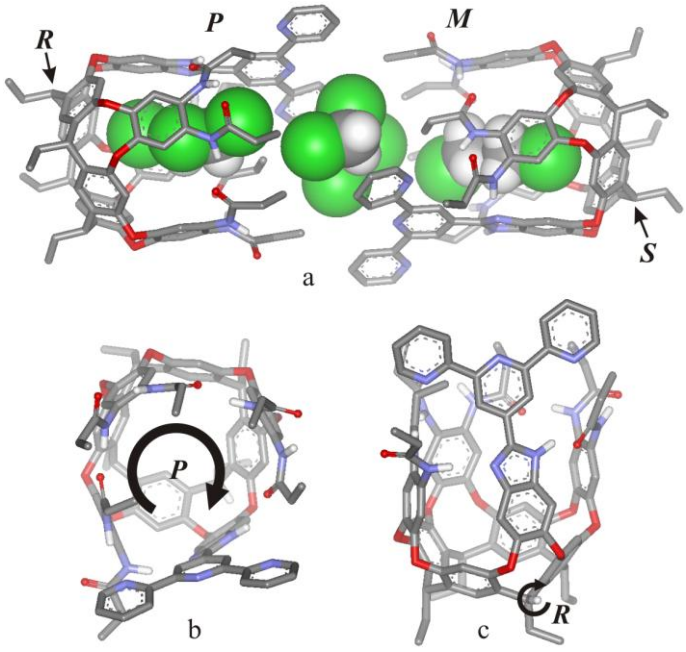

Fig. 75. a) Position of the two cavitand **C24** enantiomers in the crystal structure. Stereochemical designations: b) axial chirality, and c) absolute configuration of methyne carbon determined by CIP rules. Nonpolar hydrogen atoms are omitted for clarity. Delocalized solvent molecules are presented as CPK models.

The high resolution ESI-MS (+) analysis of the cavitand **C24** provided an experimental accurate mass for the monoisotopic peak corresponding to the $[M + H]^+$ ion that deviated less than 6 ppm from the calculated value. Not surprisingly, the isotopic pattern measured for the $[M + H]^+$ ion matched nicely with the theoretical one (**Fig. 76**).

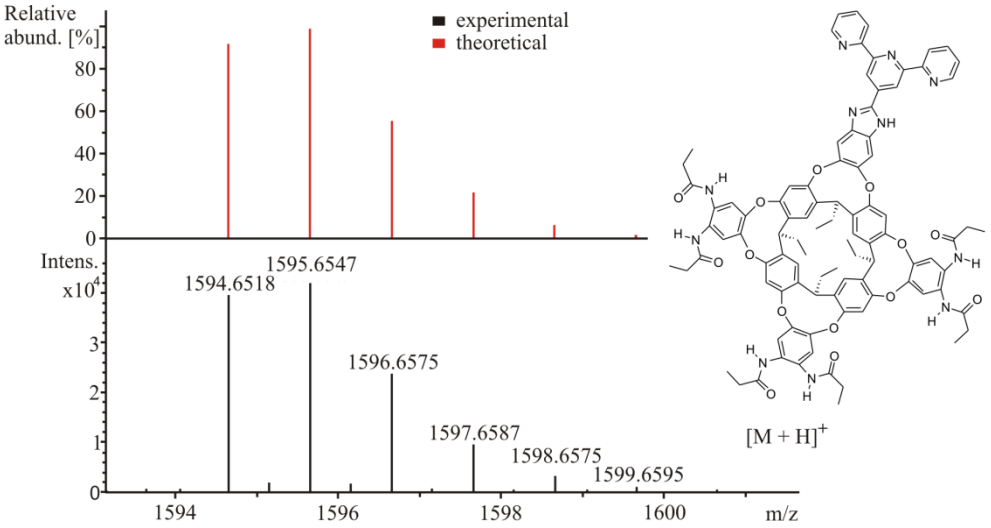

Fig. 76. ESI-MS (+) isotopic pattern for the cavitand **C24**.

To monitor the changes induced by coordination of the terpyridine unit in **C24** with Ru^{II}, we used UV/Vis spectroscopy. The UV-Vis spectrum of cavitand **C24** showed two absorption bands centered at 333 and 283 nm. In contrast, the absorption spectrum of 2,2':6',2''-terpyridine (**tpy**, **44**) consisted of a band centered at 281 nm with a shoulder (**Fig. 77**). For comparison purposes we also measured the absorption spectrum of octaamide cavitand **C5**. The spectrum of the octaamide cavitand **C5** showed two overlapping absorption bands with maxima at 285 and 277 nm, respectively.

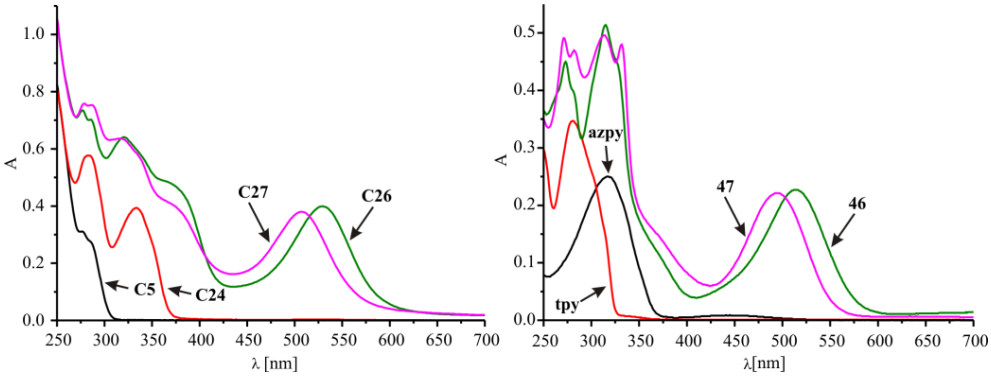

Fig. 77. UV/Vis spectra of 20 μM methylene chloride solutions of: (left) octaamide (**C5**) and terpyridine (**C24**) cavitands, metallocavitands **azpy**•Ru^{II}•Cl•**C24** (**C26**), and **azpy**•Ru^{II}•(H_2O)•**C24** (**C27**); (right) ligands **azpy** (**42**) and 2,2':6',2''-terpyridine (**tpy**, **44**), and organometallic complexes **azpy**•Ru^{II}•Cl•**tpy** (**46**), and **azpy**•Ru^{II}•(H_2O)•**tpy** (**47**).

Metallocavitand **C25**: The complexation of the cavitand **C24** to $RuCl_3$ afforded Ru^{III}•Cl_3•**C24** (**C25**) metallocavitand as a brown solid. The ^1H NMR analysis of the metallocavitand solution revealed broad signals that, in the most part, were impossible to assign (**Fig. 78**). As could be expected, the coordination of **C24** to the paramagnetic Ru^{III}

was mainly responsible for the broadening of proton signals, however other processes like aggregation (*vide infra*) or conformational exchange cannot be excluded as additional causes of the observed broadening. In any case, the coordination of the Ru^{III} to the terpyridine unit induced the most significant changes in chemical shifts and broadening to its protons. Terpyridine protons resonated as broad signals that were shifted highly upfield due to the paramagnetic nature of Ru^{III}.

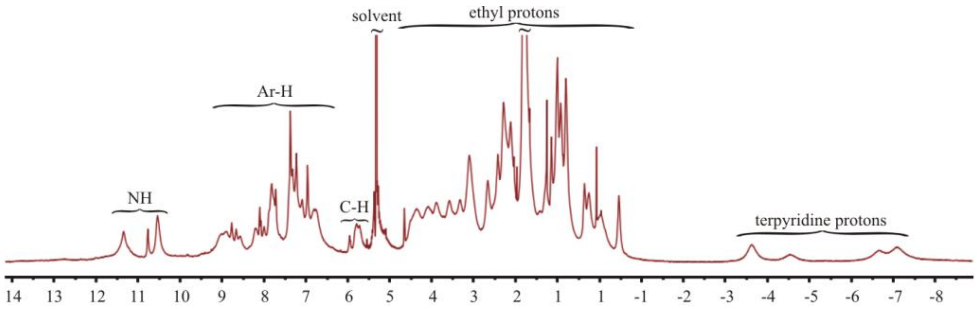

Fig. 78. ^{1}H NMR spectrum (optimized for paramagnetic species) of metallocavitand **C25** in CD_2Cl_2.

Single crystals suitable for X-ray analysis of the Ru^{III}•Cl_3•**C24** (**C25**) metallocavitand were grown from ethanol solution by slow evaporation. In the solid state, the packing of the lattice showed three molecules of metallocavitand **C25**, with two molecules engaged in formation of a dimer-like arrangement where metallated terpyridine groups of adjacent molecules partially occupied each other's cavity (**Fig. 79**, a). Such geometry disrupted the hydrogen bonded array of amide groups that maintained the vase conformation of the metallocavitand, yielding a structure with two aromatic walls in the equatorial conformation (kite) and the other two in the axial conformation (vase) (**Fig. 79**, b).

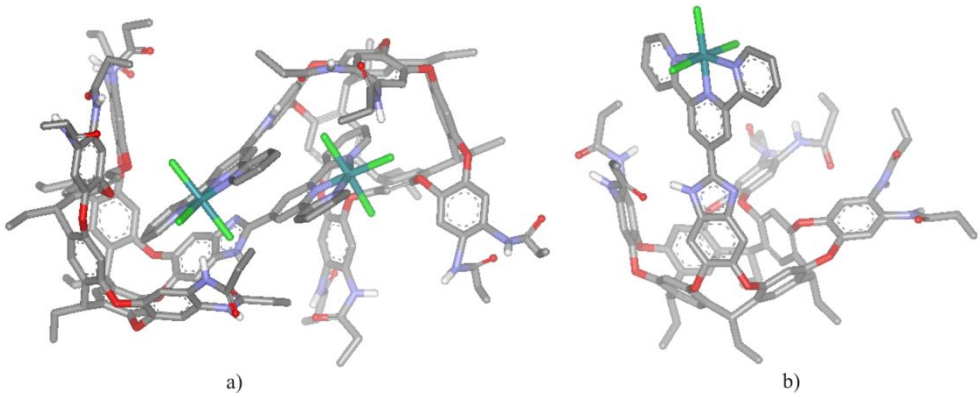

Fig. 79. The organization of two metallocavitand Ru^{III}•Cl_3•**C24** (**C25**) molecules in a solid state structure: a) a dimer-like packing, and b) a structure of a single molecule. Nonpolar hydrogen atoms are omitted for clarity.

The third metallocavitand molecule (**Fig. 80**, red molecule) was oriented in the lattice in such a way to allow π-π stacking interaction of one of its aromatic walls that is in the kite

conformation with one of the pyridyl groups from the terpyridine moiety of the neighboring metallocavitand.

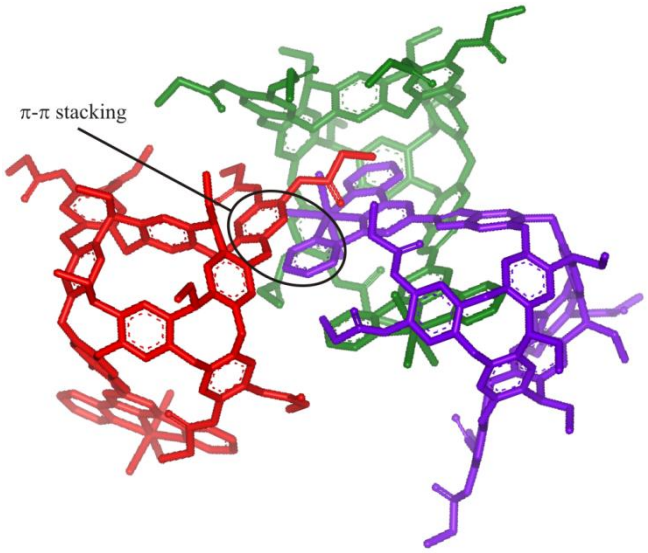

Fig. 80. The organization of metallocavitand Ru^{III}•Cl_3•**C24** (**C25**) units in the crystal lattice. For clarity, each metallocavitand molecule is presented in a different color. The π-π interaction of the third molecule (colorred in red) is highlighted.

The MALDI-MS (+) analysis of the Ru^{III}•Cl_3•**C24** (**C25**) metallocavitand provided a good match between experimental and theoretical isotopic patterns for the ion-peak $[M - Cl]^+$ (**Fig. 81**).

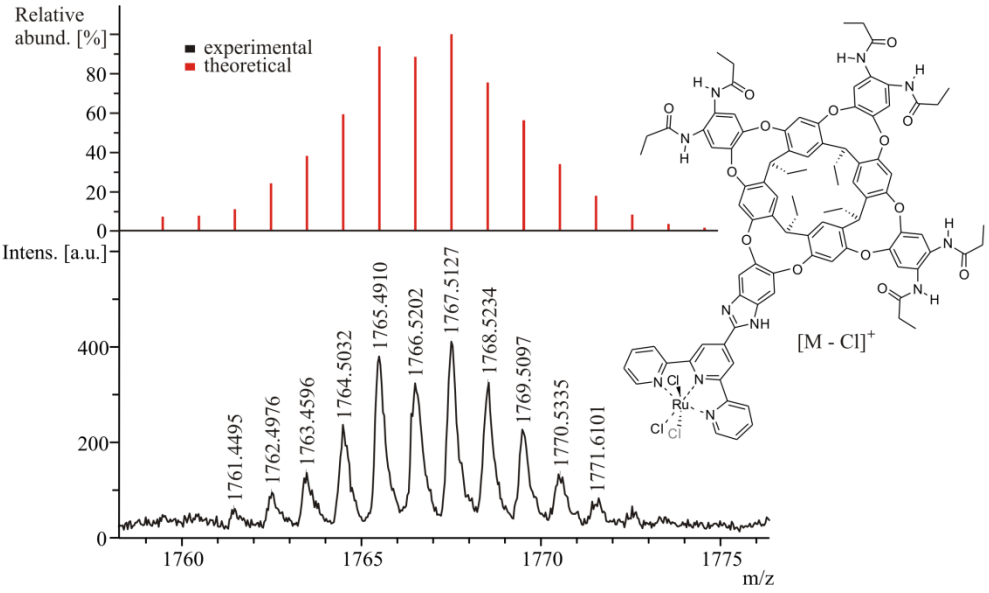

Fig. 81. MALDI-MS (+) isotopic pattern for Ru^{III}•Cl_3•**C24** (**C25**) metallocavitand.

Organometallic complex **46** and metallocavitand **C26**: The ^{1}H NMR spectrum of the model organometallic complex **azpy**•Ru^{II}•Cl•**tpy** (**46**) showed sharp signals that were easily assigned to the exclusive formation of the *trans*- isomer.[41] The aromatic region of the ^{1}H NMR spectrum of *trans*-**azpy**•Ru^{II}•Cl•**tpy** together with their proton assignment is depicted in the **Fig. 82**.[40]

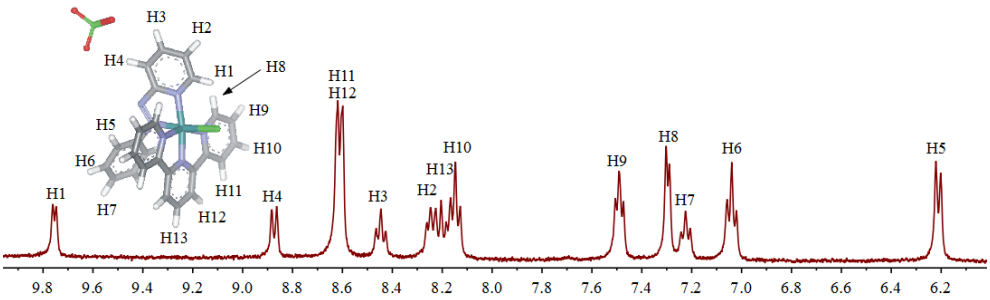

Fig. 82. ^{1}H NMR spectrum of *trans*-**azpy**•Ru^{II}•Cl•**tpy** (**46**) in DMSO-d_6 solution. Inset: X-ray structure of the organometallic complex *trans*-**azpy**•Ru^{II}•Cl•**tpy** (**46**).

The most interesting resonance in the spectrum is that of H1. The aromatic proton is deshielded by the magnetic anisotropy of the chloro ligand and resonates at 9.75 ppm. For two possible isomers of the **azpy** (**42**) ligand, only the *trans*-**azpy**•Ru^{II}•Cl•**tpy** presents this interaction and thus the chemical shift of H1 was a characteristic of the binding geometry.[40] The formation of the *trans*-**azpy**•Ru^{II}•Cl•**tpy** complex was also corroborated by XRD analysis of a single crystal grown from acetonitrile solution (**Fig. 82**, inset).

Unfortunately, the assignment of the signals of the ^{1}H NMR spectrum of the cavitand **azpy**•Ru^{II}•Cl•**C24** (**C26**) was not possible owing to their broadening and ill-defined nature, possibly due to dynamic processes present in the structure. It was evidenced that the highly upfield shifted signals observed for the paramagnetic metallocavitand Ru^{III}•Cl$_3$•**C24** (**C25**) assigned to aromatic protons in the **tpy** unit were no longer present in the upfield region of the ^{1}H NMR spectrum of **azpy**•Ru^{II}•Cl•**C24** (**Fig. 83**, a).

The feature that remained constant in the ^{1}H NMR spectra of structurally diverse ruthenium-metallocavitands Ru^{III}•Cl$_3$•**C24** (**C25**), **azpy**•Ru^{II}•Cl•**C24** (**C26**) and **azpy**•Ru^{II}•(H$_2$O)•**C24** (**C27**) was the observation of a broad singlet resonating at ≈ 5.6 ppm that was assigned to methine protons of the metallocavitands. We assumed that the observation of this signal was indicative of the existence, in solution, of certain proportion of the cavitand in the vase conformation.

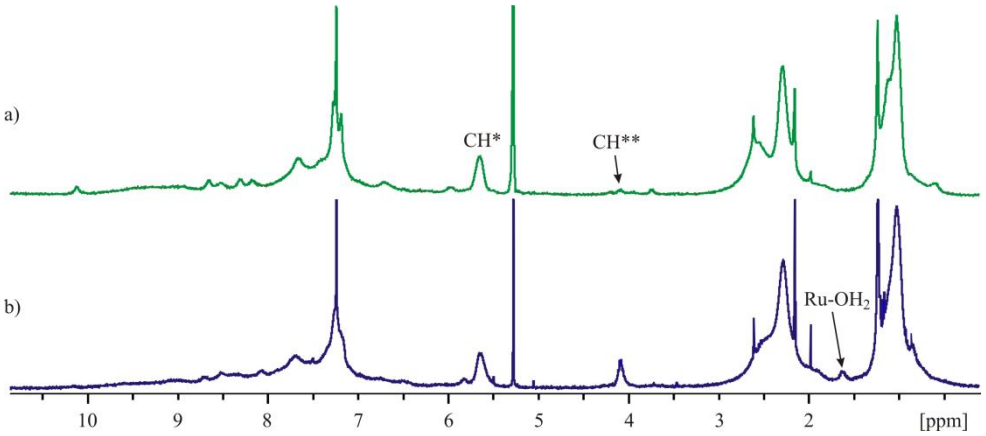

Fig. 83. ^{1}H NMR spectrum of metallocavitands: a) **azpy**•Ru^{II}•Cl•**C24** (**C26**) and b) **azpy**•Ru^{II}•(H_2O)•**C24** (**C27**) in $CDCl_3$. Designations: CH* - methine in the vase and CH** - the kite conformation, Ru-OH_2 - coordinated water.

The analysis of NOESY spectrum shows several cross-peaks, which with the help of a ROESY spectrum appear to be associated with mutual proximity between methylene, methyl, methine and probably terpyridine hydrogen atoms (**Fig. 84**).

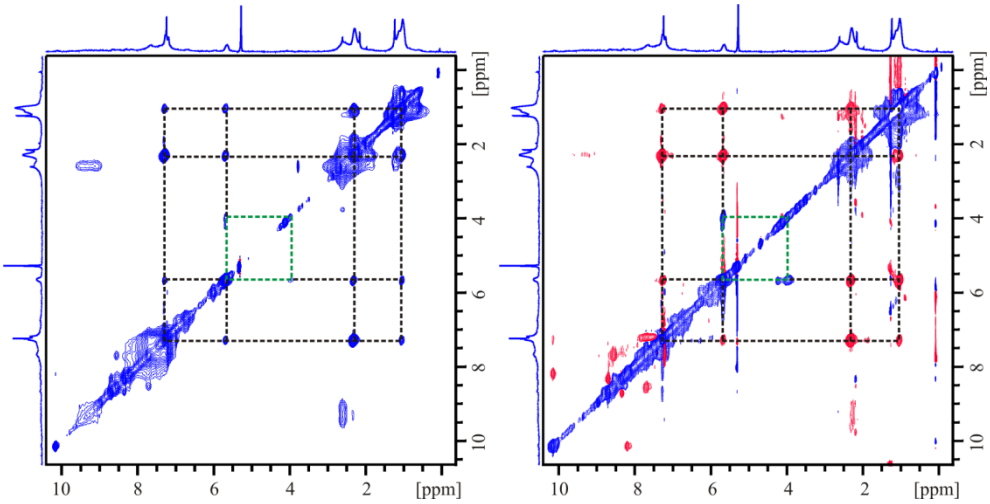

Fig. 84. ^{1}H-^{1}H NOESY (left) and ^{1}H-^{1}H ROESY (right) spectra of metallocavitand **azpy**•Ru^{II}•Cl•**C24** (**C26**) in $CDCl_3$. Vase to kite conformational exchange is depicted with green dashed lines. Proximities are depicted with black dashed lines.

Moreover, the NOESY spectrum of the cavitand **azpy**•Ru^{II}•Cl•**C24** (**C26**) showed several cross-peaks that were indicative of the spatial proximity between methine protons and protons of the ethyl feet. The ROESY spectrum corroborated the NOE results. Of special importance is the observation of a NOE cross-peak between methine protons and one signal assigned to aromatic protons of the cavitand **azpy**•Ru^{II}•Cl•**C24**. This observation suggested that at least one aromatic wall of the cavitand adopted an equatorial orientation (kite) as already observed in the X-ray structure of the parent Ru^{III}•Cl_3•**C24** metallocavitand

(**Fig. 79**, b). This hypothesis was substantiated by the existence of a chemical exchange process, easily detected in the ROESY spectrum due to the positive nature of the cross-peaks, between methine protons in rings including bridging phenyl groups in axial orientation (vase) and broad signals resonating close to 4 ppm that were assigned to similar protons belonging to macrocycles with bridging phenyl groups in the equatorial orientation (kite) (**Fig. 84**, green dashed lines). All efforts to obtain better defined signals in the NMR spectra by performing VT experiments were unsuccessful.

All attempts to produce single crystals of cavitand **azpy**•Ru^{II}•Cl•**C24** suitable for XRD analysis were unsuccessful. However, we obtained a high resolution MALDI-MS (+) spectra showing the expected isotopic pattern for the mono-cationic species $[M - PF_6]^+$ of the metallocavitand **C26** (**Fig. 85**).

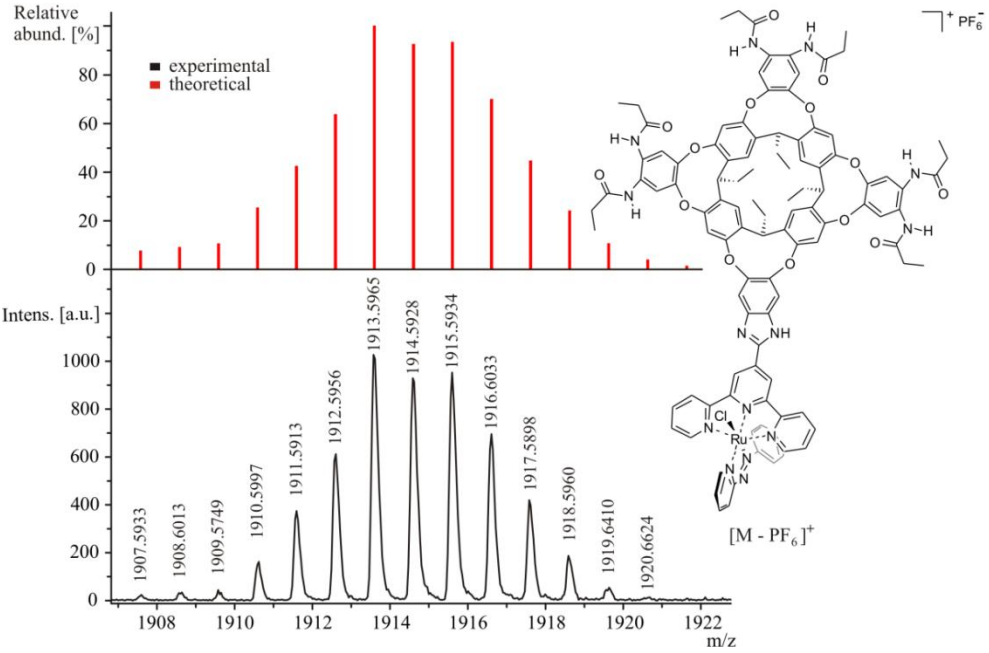

Fig. 85. MALDI-MS (+) isotopic pattern for the **azpy**•Ru^{II}•Cl•**C24** (**C26**) metallocavitand.

The UV/Vis spectrum of the **azpy**•Ru^{II}•Cl•**C24** (**C26**) metallocavitand (**Fig. 77**) showed a MLCT (Metal-to-Ligand Charge-Transfer) band centered at 529 nm. A similar MLCT band is observed in the absorption spectrum of the reference organometallic complex *trans*-**azpy**•Ru^{II}•Cl•**tpy** (**46**) (513 nm). Other absorption bands are also coincident in the spectra of two Ru^{II} complexes. In short, all the described characterization data are in agreement with the structure of **azpy**•Ru^{II}•Cl•**C24** (**C26**) for the solid isolated in the reaction of Ru^{III}•Cl_3•**C24** (**C25**) and **azpy** (**42**). Unfortunately, the **azpy**•Ru^{II}•Cl•**C24** (**C26**) complex was probably obtained as a mixture of *cis*- and *trans*- isomers that are involved in a conformational equilibrium between equatorial and axial oriented bridging phenyl groups that is intermediate on the NMR timescale.

Redox active species are routinely characterized by their redox potential. Despite all our attempts, we couldn't obtain well defined cyclic voltammograms (CV) of the ruthenium metallocavitand species. Instead, we utilized differential pulse voltammetry (DPV) for their redox characterization. The reference organometallic complex *trans*-**azpy**•Ru^{II}•Cl•**tpy** (**46**) showed a peak with a maximum at 0.99 V, while metallocavitand **azpy**•Ru^{II}•Cl•**C24** (**C26**) showed a broad wave composed of two superimposed components. The wave maximum was achieved with a current intensity of 1.08 V (**Fig. 86**). The presence of two maxima could be an indication of the presence of two possible isomeric forms of the metallocavitand **azpy**•Ru^{II}•Cl•**C24** (**C26**).[41,42]

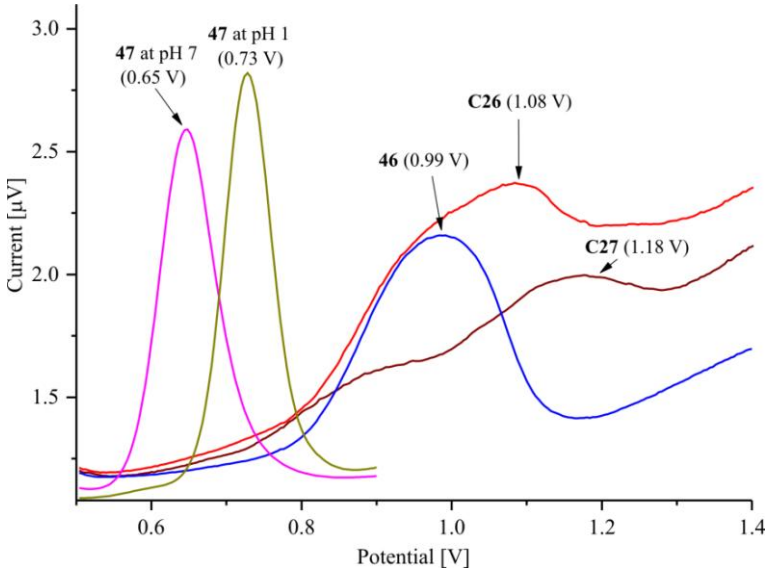

Fig. 86. Differential Pulse Voltammograms (DPV) for metallocavitands **azpy**•Ru^{II}•Cl•**C24** (**C26**) in acetonitrile and **azpy**•Ru^{II}•(H_2O)•**C24** (**C27**) in chloroform, organometallic complexes *trans*-**azpy**•Ru^{II}•Cl•**tpy** (**46**) in acetonitrile and *trans*-**azpy**•Ru^{II}•(H_2O)•**tpy** (**47**) in water at pH 7 and pH 1 ($HClO_4$). Supporting electrolytes: for both metallocavitand solutions: Bu_4N•PF_6 (0.1 M), for organometallic complex **46**: Bu_4N•ClO_4 (0.1 M), and for organometallic complex **47**: $NaClO_4$ (0.1 M). Reference electrode: $Hg/HgSO_4$; working electrode: glassy carbon; counter electrode: platinum.

The inspection of the Infrared (IR) spectrum of the organometallic complex *trans*-**azpy**•Ru^{II}•Cl•**tpy** (**46**) in the region between 3150 - 3500 cm^{-1} (**Fig. 87**) showed the complete absence of vibrational bands. The IR spectrum of the metallocavitand **azpy**•Ru^{II}•Cl•**C24** (**C26**) in the same region featured a broad band at ≈ 3240 cm^{-1} that was assigned to the vibration (stretch) of NHs of hydrogen bonded amides.[8] Finally, the N=N stretching frequency of the coordinated ancillary ligand is appreciably lower for both, organometallic complex **azpy**•Ru^{II}•Cl•**tpy** (1296 cm^{-1}) and metallocavitand counterpart (1272 cm^{-1}), compared to that of free **azpy** (**42**) ligand (1420 cm^{-1}), due to back-bonding effect as predicted by Dewar-Chatt-Duncanson's model.

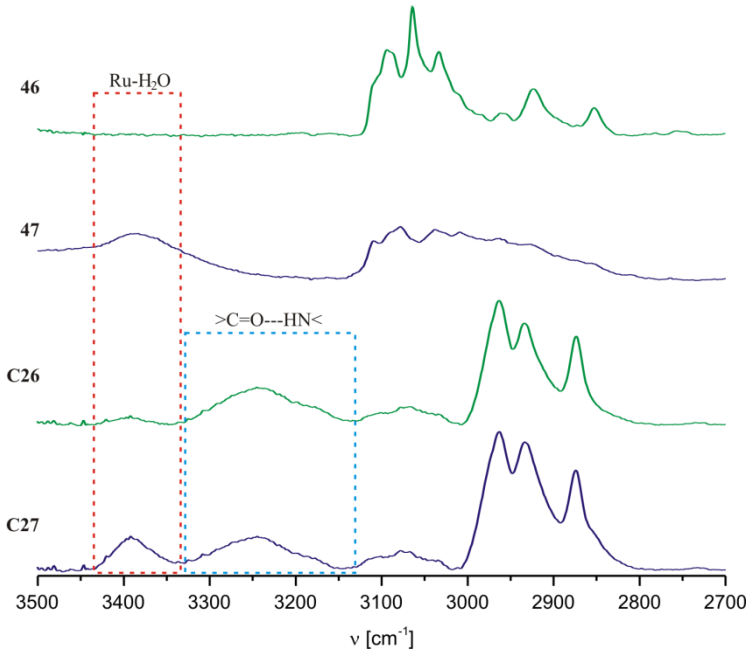

Fig. 87. Selected region of the IR spectra for model systems *trans*-**azpy**•Ru^{II}•Cl•**tpy** (**46**) and *trans*-**azpy**•Ru^{II}•(H_2O)•**tpy** (**47**) and metallocavitands **azpy**•Ru^{II}•Cl•**C24** (**C26**) and **azpy**•Ru^{II}•(H_2O)•**C24** (**C27**) with highlighted positions of Ru^{II}-H_2O and amide hydrogen bond stretches.

Organometallic complex **47** and metallocavitand **C27**: The substitution of the chloro anionic ligand of the purple metallocavitand **azpy**•Ru^{II}•Cl•**C24** (**C26**) by an aqua ligand was achieved by treating it with an excess of $AgPF_6$ in acetone solution in the presence of water. The reaction induced the precipitation of AgCl with a concomitant change in the color of the solution from purple to maroon that is characteristic of the **azpy**•Ru^{II}•(H_2O)•**C24** (**C27**). After removal of the precipitate, the solution was concentrated and added drop-wise to water causing precipitation of the metallocavitand **C27** as a brown solid. Using a related procedure but starting from the reference organometallic complex *trans*-**azpy**•Ru^{II}•Cl•**tpy** (**46**), we obtained the corresponding aqua complex *trans*-**azpy**•Ru^{II}•(H_2O)•**tpy** (**47**) used as a control molecule in the following catalytic reactions. The ^{1}H NMR spectrum of the *trans*-**azpy**•Ru^{II}•(H_2O)•**tpy** (**47**) complex in deuterium oxide solution displayed sharp and well resolved signals that were easily assigned (**Fig. 88**). The H1 proton resonated highly downfield, which was indicative of the *trans*-geometry of the isolated complex. The *trans*- geometry of the aqua complex was also evidenced in the solid state by solving the diffraction data of a single crystal grown from a water solution (**Fig. 88**, inset).

In contrast, the ^{1}H NMR spectrum of the aqua metallocavitand **azpy**•Ru^{II}•(H_2O)•**C24** (**C27**) in chloroform-*d* solution showed broad and ill-defined signals. This observation was not completely unexpected given the observed broadening of signals in the ^{1}H NMR spectrum of the parent metallocavitand **azpy**•Ru^{II}•Cl•**C24** (**C26**) (**Fig. 83**, b). Two new

broad singlets resonating at 4.08 and 1.67 ppm, respectively, are observed in the ^{1}H NMR spectrum of the aqua cavitand complex **azpy**•Ru^{II}•(H_2O)•**C24** compared to that of **azpy**•Ru^{II}•Cl•**C24**.

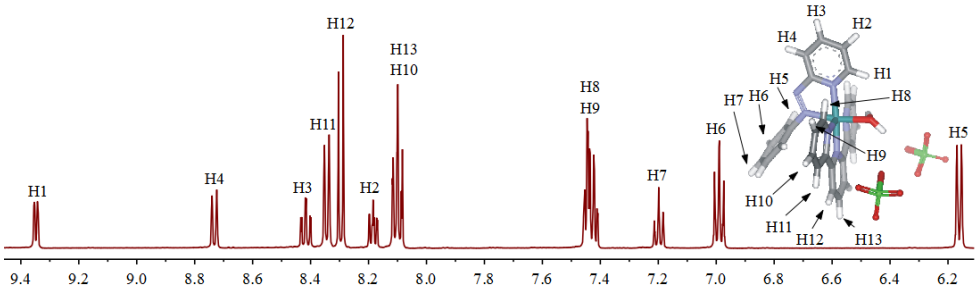

Fig. 88. ^{1}H NMR spectrum of *trans*-**azpy**•Ru^{II}•(H_2O)•**tpy** (**47**) in D_2O. Inset: X-ray structure of the organometallic complex *trans*-**azpy**•Ru^{II}•(H_2O)•**tpy** (**47**).

The NOESY/ROESY spectra of the **azpy**•Ru^{II}•(H_2O)•**C24** (**C27**) complex showed an analogous chemical exchange process between vase-kite conformers previously observed for the metallocavitand **azpy**•Ru^{II}•Cl•**C24** (**C26**). However, in the case of **azpy**•Ru^{II}•(H_2O)•**C24** (**C27**) the intensity of the signal resonating at 4.08 ppm, which was assigned to conformers having one or more bridging phenyl units in the equatorial conformation (kite), is larger than in the case of **azpy**•Ru^{II}•Cl•**C24** (**C26**) metallocavitand. The signal appearing at 1.67 ppm was assigned to protons of the aqua ligand.

All attempts to obtain single crystals of **azpy**•Ru^{II}•(H_2O)•**C24** suitable for X-ray analysis were unsuccessful. Interestingly, in the high resolution ESI-MS (+) spectrum of the solid isolated as the aqua complex **azpy**•Ru^{II}•(H_2O)•**C24** (**C27**) was observed as a set of peaks that fitted nicely to the theoretical isotopic pattern calculated for the mono-cationic species [M - 2PF_6 - H]$^+$ (**Fig. 89**). The analogous species was observed in the ESI-MS (+) spectrum of the reference organometallic complex **azpy**•Ru^{II}•(H_2O)•**tpy** (**47**).

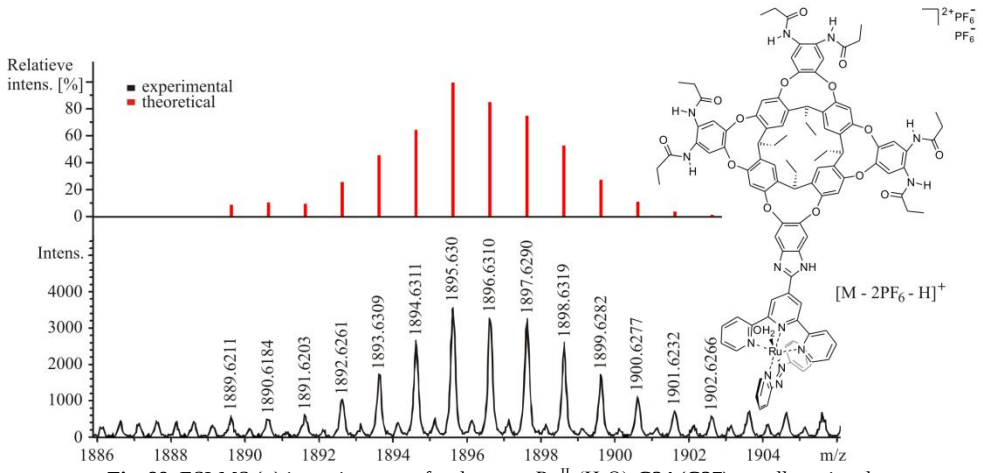

Fig. 89. ESI-MS (+) isotopic pattern for the **azpy**•Ru^{II}•(H_2O)•**C24** (**C27**) metallocavitand.

The absorption spectrum of the aqua metallocavitand **azpy**•Ru^{II}•(H_2O)•**C24** (**C27**) (**Fig. 77**) showed a blue-shift for the MLCT band (502 nm) compared to the maximum of the band for the parent **azpy**•Ru^{II}•Cl•**C24** (**C26**) (529 nm). The same blue-shifting trend for the MLCT band was observed for the reference organometallic aqua complex **azpy**•Ru^{II}•(H_2O)•**tpy** (**47**) (494 nm) when compared to parent chloro complex **azpy**•Ru^{II}•Cl•**tpy** (**46**) (513 nm).

The DPV voltammogram of the aqua metallocavitand **azpy**•Ru^{II}•(H_2O)•**C24** (**C27**) showed two broad peaks with the maximum occurring at a potential of 1.18 V. Finally, the IR spectrum of **azpy**•Ru^{II}•(H_2O)•**C24** (**Fig. 87**) displayed two broad bands in the 3150 - 3500 cm^{-1} region, one corresponding to the stretching of hydrogen bonded NHs at ≈ 3240 cm^{-1} and the other centered at 3393 cm^{-1} that was assigned to the OH vibration of the aqua ligand. This is in a good agreement with the equivalent signal observed for the OH vibration of the control molecule **azpy**•Ru^{II}•(H_2O)•**tpy** (**47**) (3390 cm^{-1}).

4.2.3 Catalytic epoxidation of alkenes

The initial trials of the epoxidation reactions were attempted using chloro cavitand **azpy**•Ru^{II}Cl•**C24** (**C26**) as a catalyst. We hoped to be able to generate the catalytically active aqua complex **azpy**•Ru^{II}•(H_2O)•**C24** (**C27**) *in situ*. Unfortunately, the experimental conditions we used for the reaction (5 mol-% of catalyst; room temperature; NMR scale; methylene chloride-d_2 as a solvent; 2 equivalents of iodosobenzene diacetate as an oxidant; 40 mM water; 5.5 mM styrene as a substrate) did not allow us to detect the formation of the epoxide product using ^{1}H NMR spectroscopy. We reasoned that this observation indicated that the chloro metallocavitand **azpy**•Ru^{II}Cl•**C24** (**C26**) did not experience the expected ligand exchange to produce *in situ* the aqua derivative **azpy**•Ru^{II}•(H_2O)•**C24** (**C27**). For this reason, we decided to undertake the epoxidation reactions using the pre-formed aqua complexes **azpy**•Ru^{II}•(H_2O)•**C24** (**C27**) and the control molecule **azpy**•Ru^{II}•(H_2O)•**tpy** (**47**) produced in a separated step.

The initial test studies of the epoxidation reaction were performed using styrene (**48**), *trans*-β-methylstyrene (**49**) and the trimethylalkylammonium salt **50** containing a terminal benzylic *Z*-alkene as model substrates (**Scheme 5**).

The structure of alkene **50** is not the most ideal to achieve the simultaneous complexation of its trimethylalkylammonium knob in the aromatic cavity of the metallocavitand **azpy**•Ru^{II}•(H_2O)•**C24** (**C27**), and the placement of the terminal alkene in an optimum position to the catalytic ruthenium center for the epoxidation reaction to occur. However, we decided to use alkene **50** as a model substrate owing to the simplicity of its synthesis from the commercially available starting material. Moreover, we were interested

in evaluating the effect that the presence of the tetraalkylammonium group in the substrate could exert on the epoxidation reaction rate.

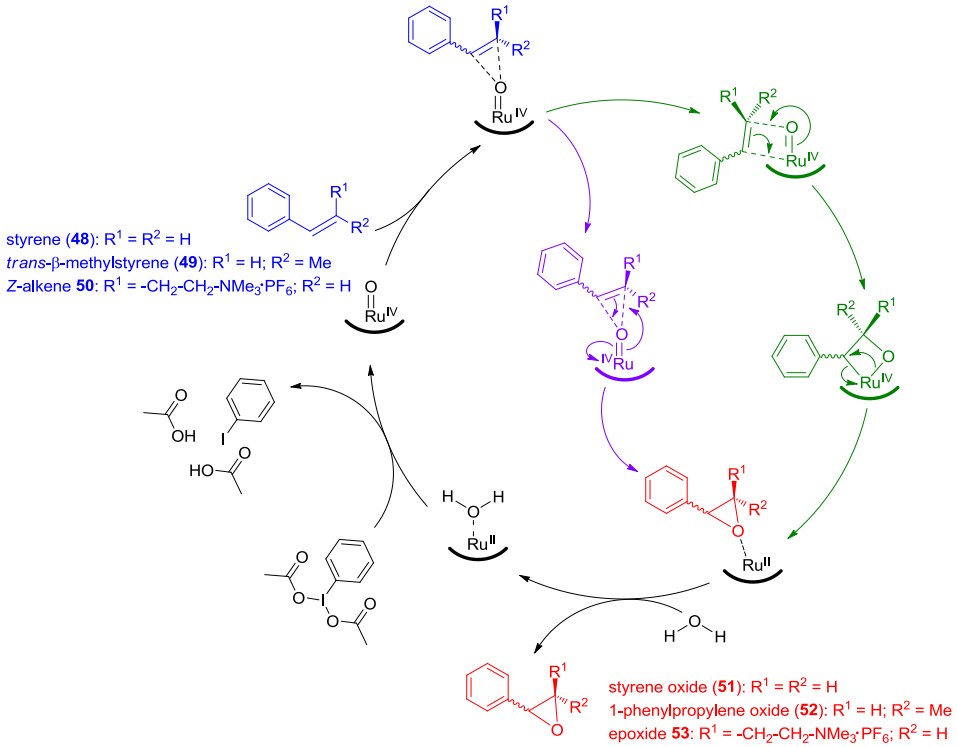

Scheme 5. Proposed concerted (purple) and metalla-oxetane (green) mechanisms for catalytic epoxidation reaction of styrene (**48**), *trans*-β-methylstyrene (**49**) and *Z*-alkene **50** exerted by a Ru^{II}•(H_2O) complex in the presence of iodosobenzene diacetate as a sacrificial oxidant.[17,18,19,20]

The progress of the epoxidation reaction was monitored using ^1H NMR spectroscopy (**Fig. 90**, styrene example). As diagnostic signals of the consumption of the sacrificial oxidant we selected those of the *ortho*- protons in the iodosobenzene diacetate. The monitoring of the disappearance of the starting material and the product formation relied on diagnostic proton signals of their alkene and epoxide groups, respectively.

Separate catalytic epoxidation reactions of styrene (**48**, 5.5 mM) using 5 mol-% of the control catalyst **azpy**•Ru^{II}•(H_2O)•**tpy** (**47**) and metallocavitand **azpy**•Ru^{II}•(H_2O)•**C24** (**C27**), showed, after 70 minutes of reaction, a slow formation of styrene oxide **51** (< 1.0 mM) in both cases (**Fig. 91**).

The analysis of the data for both systems indicated discrepancy in rates of alkene disappearance and epoxide formation. After 70 min of reaction both catalytic systems consumed ≈ 20 % of styrene (**48**) forming ≈ 15 % of styrene oxide (**51**). Careful analysis of NMR spectra indicated presence of ≈ 4% of phenylacetaldehyde (**54**) and acetophenone (**54b**), products of Meinwald rearrangement (**Scheme 6**).[43]

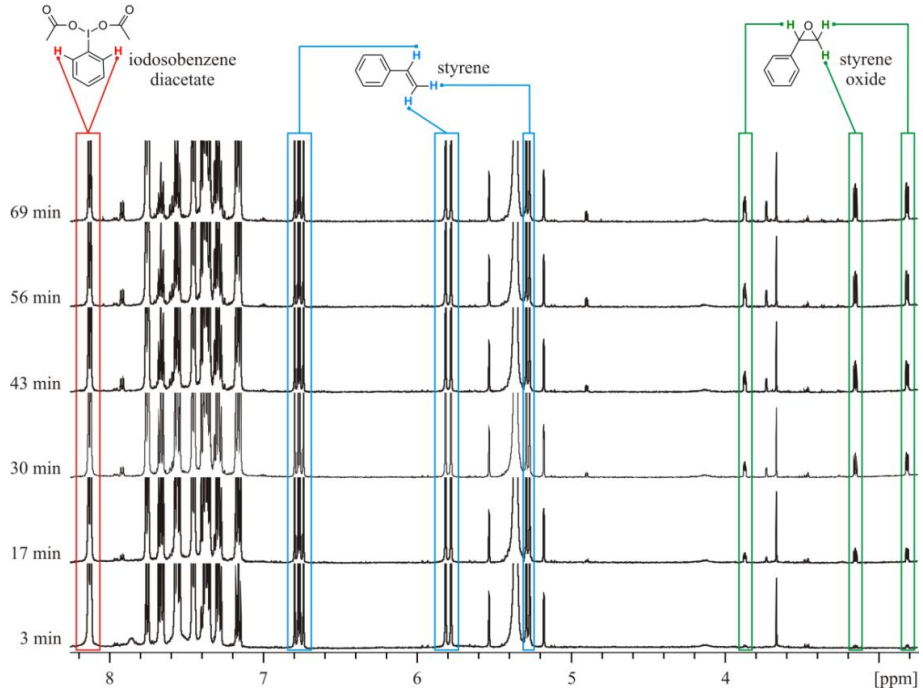

Fig. 90. Few selected time dependent ^{1}H NMR spectra for catalytic epoxidation of styrene (**48**, 5.5 mM) catalyzed by **azpy**•Ru^{II}•(H_2O)•**C24** (**C27**, 5 mol-%) in the presence of iodosobenzene diacetate as an oxidant (11 mM) and water (40 mM) in CD_2Cl_2 (550 μL).

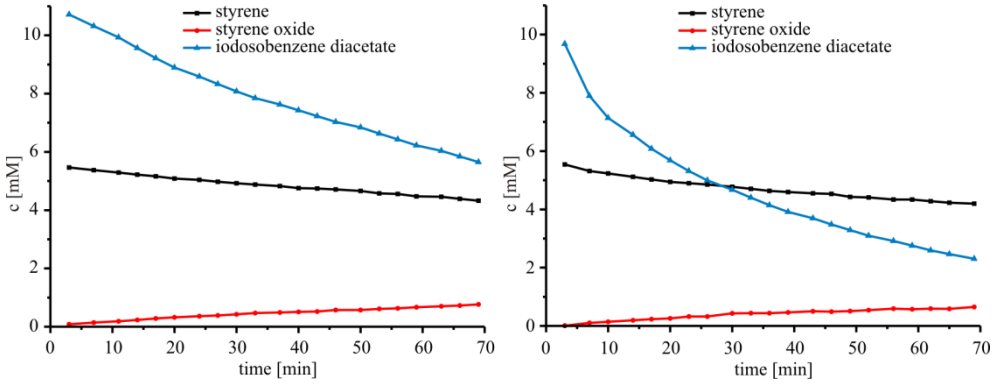

Fig. 91. Plots of the concentration changes measured for the epoxidation reaction of styrene (**48**, 5.5 mM) catalyzed by **azpy**•Ru^{II}•(H_2O)•**tpy** (**47**, 5 mol-%, left) and **azpy**•Ru^{II}•(H_2O)•**C24** (**C27**, 5 mol-%, right) in the presence of iodosobenzene diacetate as an oxidant (11 mM) and water (40 mM) in CD_2Cl_2 (550 μL).

Although the Meinwald rearrangement is usually carried out in the presence of stoichiometric (or even excess) amount of Lewis acids such as methylaluminium *bis*(4-bromo-2,6-di-*tert*-butylphenoxide) (MABR),[44] BF_3•Et_2O,[45] $MgBr_2$,[46] lithium salts[47,48] and $InCl_3$,[49] in recent years a few transition metal complexes, such as $Pd(OAc)_2$[50,51] and ruthenoporphyrins[20,52] also showed this type of catalysis. Besides these carbonyl

compounds we also detected traces (≈ 1%) of phenylacetic acid, a product of phenylacetaldehyde (**54**) oxidation.

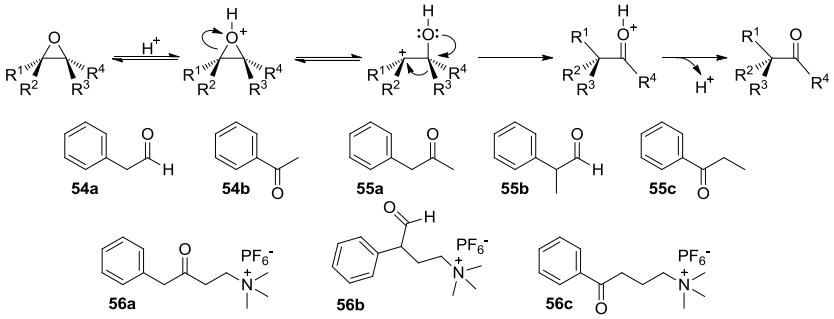

Scheme 6. Meinwald rearrangement mechanism of the epoxide catalyzed by an (Lewis) acid. Structure of possible rearrangement products coming from styrene (**48**): phenylacetaldehyde (**54a**) and acetophenone (**54b**); from *trans*-β-methylstyrene (**49**): phenylacetone (**55a**), 2-phenylpropionaldehyde (**55b**) and propiophenone (**55c**); and from and *Z*-alkene **50**: ketones **56a**, **56c** and aldehyde **56b**.

In addition, rates of the epoxidation reactions are almost identical (within experimental error) for two employed catalysts: **azpy**•Ru^{II}•(H_2O)•**tpy** (**47**) and **azpy**•Ru^{II}•(H_2O)•**C24** (**C27**). It is worth noting that the initial rate for the consumption of the sacrificial oxidant is significantly larger in the case of the catalytic aqua metallocavitand **azpy**•Ru^{II}•(H_2O)•**C24** (**C27**). This observation hints to the presence of additional oxidation reactions in this latter case. To investigate this claim, we performed the reaction with both catalysts under identical conditions but in the absence of a substrate (**Fig. 92**).

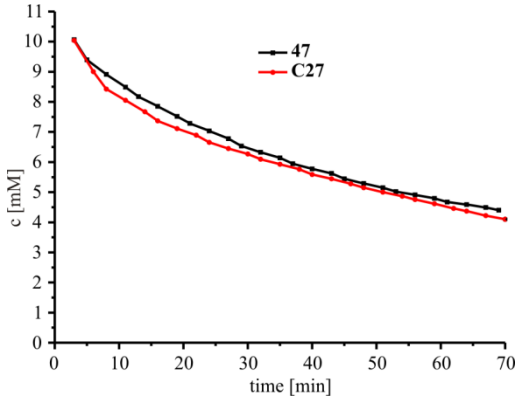

Fig. 92. Plots of the concentration change of iodosobenzene diacetate (11 mM) in the presence of **azpy**•Ru^{II}•(H_2O)•**tpy** (**47**, 5 mol-%, black) and **azpy**•Ru^{II}•(H_2O)•**C24** (**C27**, 5 mol-%, red) and water (40 mM) in CD_2Cl_2 (550 μL) solution.

Surprisingly, when substrate was absent, rates of sacrificial oxidant consumption were almost identical regardless of the used catalyst. Our initial hypothesis was that the catalyst experiences self-oxidation that would produce catalytically inactive species and either slow down or completely suppress the epoxidation reaction. However, in that case the resulting species must be considered as catalytically competent because the rate of the reaction does

not seem to be altered. A more plausible answer lies in our second hypothesis - water oxidation. Although typical water oxidation using Ru^{II}•(H_2O) complexes as catalysts are usually conducted in water solutions at pH 1,[40,53,54,55,56] we cannot exclude the possibility of this reaction being responsible for the high oxidant consumption. It is important to note that no oxidant consumption was detected by ^1H NMR in the absence of catalyst. Taken into account rates of styrene oxide (**51**) formation and the oxidant consumption, we can infer that water oxidation accounts for most of the oxidant consumption.

In order to explore the epoxidation reaction of non-terminal alkenes we used *trans*-β-methylstyrene (**49**, **Scheme 5**). The epoxidation reaction of *trans*-β-methylstyrene (**49**) was performed using identical catalytic conditions to those described for styrene (**48**). The product of the epoxidation reaction was 1-phenylpropylene oxide, possibly as a mixture of stereoisomers (*cis*, *trans*) (**Fig. 93**).

The initial reaction rates for *trans*-β-methylstyrene (**49**) consumption and 1-phenylpropylene oxide (**52**) formation are similar to those recorded for styrene (**48**). Interestingly, the rates of oxidant consumption are approximately three times lower than in the case of styrene (**48**) reaction. We believe that carbonyl compounds generated by Meinwald rearrangement of the epoxide **52** (**Scheme 6**, products **55a-c**) could bear responsibility in affecting the rate of the fastest reaction - the oxidant decomposition, by competitive coordination to the ruthenium metal center with the water molecule.

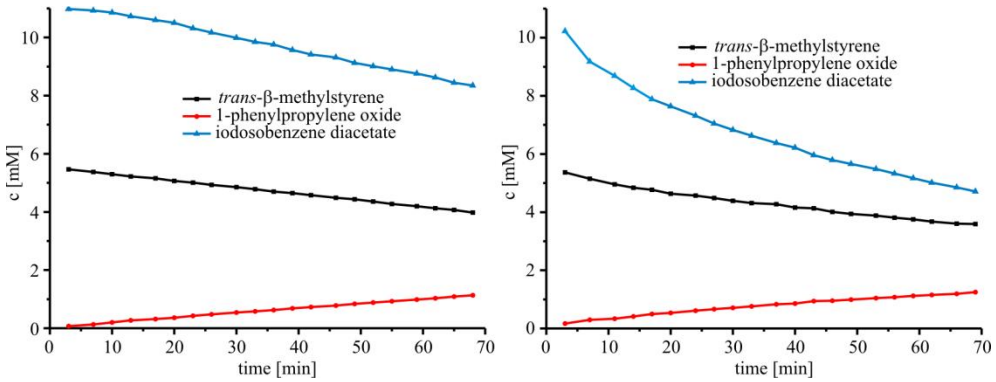

Fig. 93. Plots of the concentration changes measured in the reaction of epoxidation of *trans*-β-methylstyrene (5.5 mM) catalyzed by **azpy**•Ru^{II}•(H_2O)•**tpy** (**47**, 5 mol-%, left) and **azpy**•Ru^{II}•(H_2O)•**C24** (**C27**, 5 mol-%, right) in the presence of iodosobenzene diacetate as an oxidant (11 mM) and water (40 mM) in CD_2Cl_2 (550 μL).

The increase of catalyst content from 5 to 10 mol-% of **azpy**•Ru^{II}•(H_2O)•**C24** (**C27**) doubled the rates of the substrate (**49**) consumption and the epoxide (**52**) formation (**Fig. 94**). On the other hand, the consumption of the sacrificial oxidant increased by a factor of 1.7.

Further doubling of the catalyst **azpy**•Ru^{II}•(H_2O)•**C24** content to 20 mol-%, did not bring significant change in substrate/product rates. Results indicated only a slight increase in the oxidant consumption (by a factor of 2.2 compared to 5 mol-% catalysis).

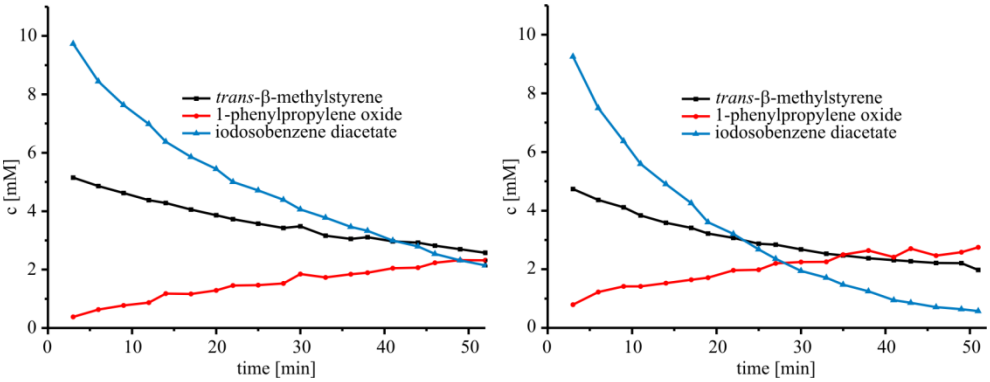

Fig. 94. Plots of the changes in concentrations for the epoxidation reactions of *trans*-β-methylstyrene (**49**, 5.5 mM) catalyzed by 10 mol-% (left) and 20 mol-% (right) of **azpy**•Ru^{II}•(H_2O)•**C24** (**C27**) in the presence of iodosobenzene diacetate as an oxidant (11 mM) and water (40 mM) in CD_2Cl_2 (550 μL).

For the last epoxidation trial, we synthesized the trimethylalkylammonium terminal alkene **50** (**Scheme 5**). The synthesis consisted of three steps (**Scheme 7**). First, the Wittig reaction of benzaldehyde with the phosphorous ylide, prepared by reaction of the phosphonium salt **50a** with one equiv. of *n*-BuLi at -78 °C,[57] produced the dimethylamine *Z*-alkene **50b**. Next, dimethylamine **50b** was quaternized by treatment with the excess of methyl iodide yielding the corresponding trimethylalkylammonium derivative as the iodide salt **50c**. Finally, the iodide anion of **50c** was exchanged by reaction with $AgPF_6$ salt to obtain the corresponding trimethylalkylammonium PF_6 salt **50**.

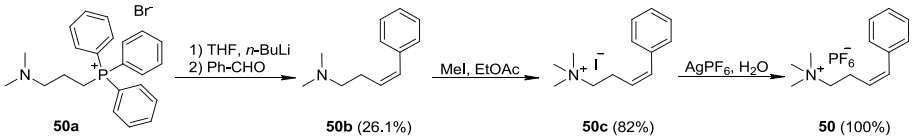

Scheme 7. Synthesis of *Z*-alkene salt **50**.

The reaction of *Z*-alkene **50** with *m*-CPBA (*meta*-chloroperbenzoic acid, Prilezhaev reaction) produced the epoxide **53** containing both PF_6 and meta-chlorobenzoate (coming from reduced *m*-CPBA) anions (**Scheme 8**).

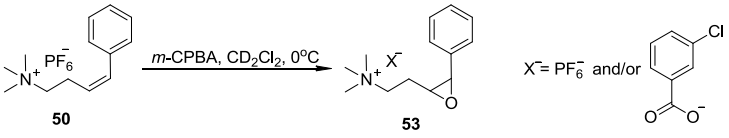

Scheme 8. Synthesis of the reference epoxide **53** by action of *m*-CPBA (Prilezhaev reaction).

The identity of the both, *Z*-alkene **50** and epoxide **53** were confirmed by ^{1}H NMR and high resolution ESI-MS. The epoxide compound **53** was used in the assignment of proton

signals of the product obtained in the epoxidation reaction of *Z*-alkene **50** catalyzed by the aqua complexes **azpy**•Ru^{II}•(H_2O)•**C24** (**C27**) and **azpy**•Ru^{II}•(H_2O)•**tpy** (**47**).[58]

We performed the epoxidation reactions of the trimethylammonium containing *Z*-alkene **50** under identical conditions described above for styrene (**48**) and *trans*-β-methylstyrene (**49**) using the metallocavitand **azpy**•Ru^{II}•(H_2O)•**C24** (**C27**) and the reference organometallic complex **azpy**•Ru^{II}•(H_2O)•**tpy** (**47**) as catalysts. Examination of reaction curves and initial reaction rates revealed behavior identical to epoxidation reaction of *trans*-β-methylstyrene (**49**). This finding suggests that the presence of the trimethylalkylammonium knob didn't have a significant effect on the catalysis. The identical consumption rate of the sacrificial oxidant compared to the *trans*-β-methylstyrene (**49**) epoxidation reaction suggested presence of carbonyl compounds (**Scheme 6**, products **56a-c**) coming from Meinwald rearrangement, that were, possibly, responsible for reduced oxidant decomposition.

The increase of catalyst **azpy**•Ru^{II}•(H_2O)•**C24** (**C27**) content from 5 to 10 and 20 mol-% yielded exactly the same behavior observed in *trans*-β-methylstyrene (**49**) epoxidation reaction additionally corroborating the unimportance of added trimethylammonium function for the epoxidation reaction.

We also investigated the effect of increased amounts of the sacrificial oxidant on epoxidation reaction rates catalyzed by 5 mol-% of the metallocavitand **azpy**•Ru^{II}•(H_2O)•**C24** (**C27**) catalyst by doubling and quadrupling it compared to the initially used amount (**Fig. 95**).

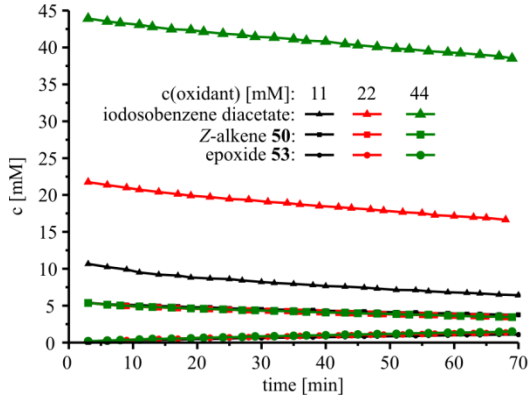

Fig. 95. Plots of changes in concentration of different species in the epoxidation reaction of *Z*-alkene **50** (5.5 mM) catalysed by **azpy**•Ru^{II}•(H_2O)•**C24** (**C27**, 5 mol-%) in the presence of: 11 (▲■●), 22 (▲■●) and 44 (▲■●) mM iodosobenzene diacetate as an oxidant and water (40 mM) in CD_2Cl_2 (550 μL).

We found that the increase in oxidant content brought up a negligible effect on epoxidation rates indicating the rate law of the reaction is zero order with respect to the

sacrificial oxidant. Furthermore, the increase of the oxidant content didn't yield observable changes on the initial rates of the oxidant consumption.

The result indicates that even with 2 equiv. (11 mM) of the sacrificial oxidant and in the presence of 5.5 mM of alkene (**50**), 5 mol-% of the catalyst **azpy**•Ru^{II}•(H_2O)•**C24** achieves its full capacity within the investigated time frame of the reaction. The capacity of investigated Ru^{II}•(H_2O) catalysts include: 1) oxidation of water as the dominant process, 2) slow epoxidation of investigated substrates, and 3) Meinwald rearrangement of the epoxide to produce carbonyl compounds.

Finally, the treatment of *Z*-alkene **50** with the sacrificial oxidant alone did not produce detectable amounts of epoxide **53**, by ^1H NMR spectroscopy, demonstrating the required intermediacy of the catalyst for the epoxidation reaction to take place.

4.2.4 Catalytic oxidation of alcohols

The second benchmark reaction that was studied to assess the efficiency and selectivity of the metallocavitand **azpy**•Ru^{II}•(H_2O)•**C24** (**C27**) was the oxidation of primary alcohols to afford aldehydes. We selected four primary alcohols as starting materials (**Scheme 9**).

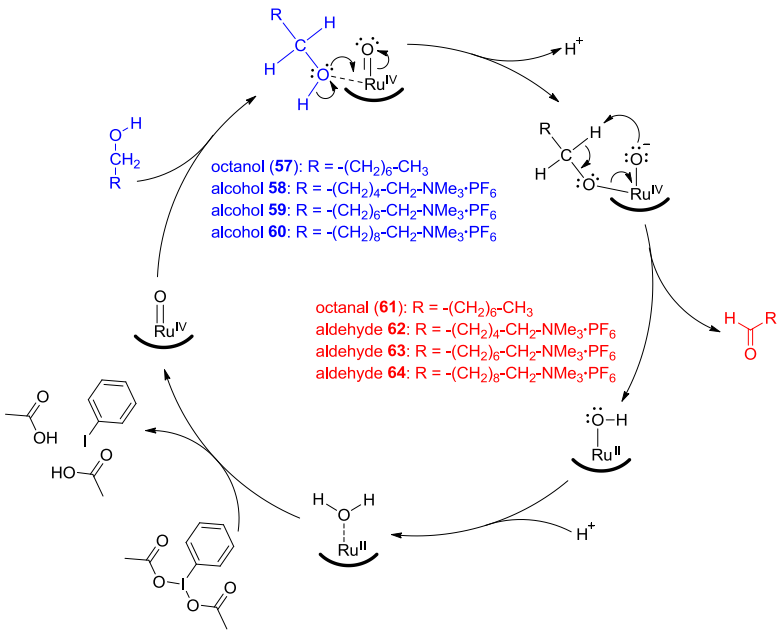

Scheme 9. Catalytic cycle proposed for alcohol (octanol (**57**), **58**, **59** and **60**) oxidation reaction catalyzed by Ru^{II}•OH_2 species in the presence of iodosobenzene diacetate as a sacrificial oxidant.[59,60]

Octanol (**57**) was selected as a reference substrate. The remaining three substrates contained a trimethylalkylammonium knob that spanned from the primary alcohol through a different numbers of methylene units.

Molecular modelling studies (PM6 as implemented in SCIGRESS v3.0) indicated that primary alcohol **59** was the best fit in its fully extended conformation to span the distance between the aromatic cavity and catalytic center of the metallocavitand **azpy**•Ru^{II}•(H_2O)•**C24** (**C27**). The aqua ligand bound to the catalytic metal center could interact with the alcohol group of the guest either through hydrogen bond interactions (**Fig. 96**, a) or by being substituted through coordication with alcoholic OH group (**Fig. 96**, b).

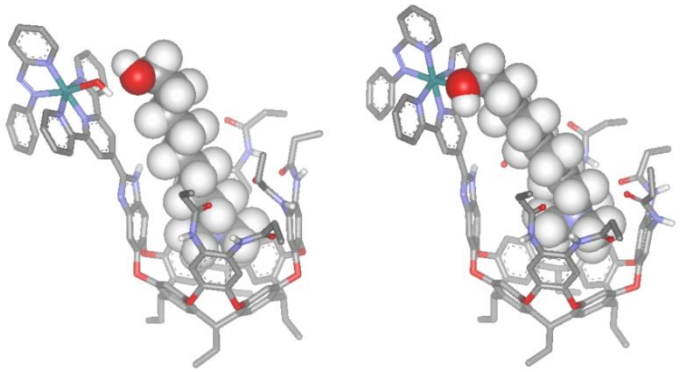

Fig. 96. PM6 energy optimized structures of **59**⊂*trans*-**azpy**•Ru^{II}•(H_2O)•**C24** complex with (a) and without (b) coordination to Ru^{II} center. Nonpolar hydrogen atoms of the host and all counterions are omitted for clarity. The guest molecule is presented as a CPK model.

The other primary alcohols **58** and **60** feature shorter and longer distances, respectively, between their trimethylammonium and hydroxyl groups. We expected that the metallocavitand **azpy**•Ru^{II}•(H_2O)•**C24** (**C27**) should behave as a selective catalyst for the oxidation of the primary alcohol **59** compared to the two other counterparts **58** and **60**.

The progress of the alcohol oxidation reaction was monitored using ^1H NMR spectroscopy (**Fig. 97**, alcohol **59** example). As diagnostic signals of the consumption of the sacrificial oxidant we selected those of the *ortho*- protons in the iodosobenzene diacetate. The monitoring of the appearance of the product relied on diagnostic proton signals of the aldehyde proton. The identity of aldehyde proton signal was corroborated by synthesis of the aldehyde **63**, starting from alcohol **59**, by using Swern oxidation reaction (**Scheme 10**).

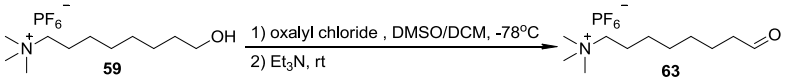

Scheme 10. Synthesis of the reference aldehyde **63**.

The formation of aldehyde **63** was identified in the reaction mixture by ^{1}H NMR and confirmed by ESI-MS after HPLC separation (see the Supporting Information).

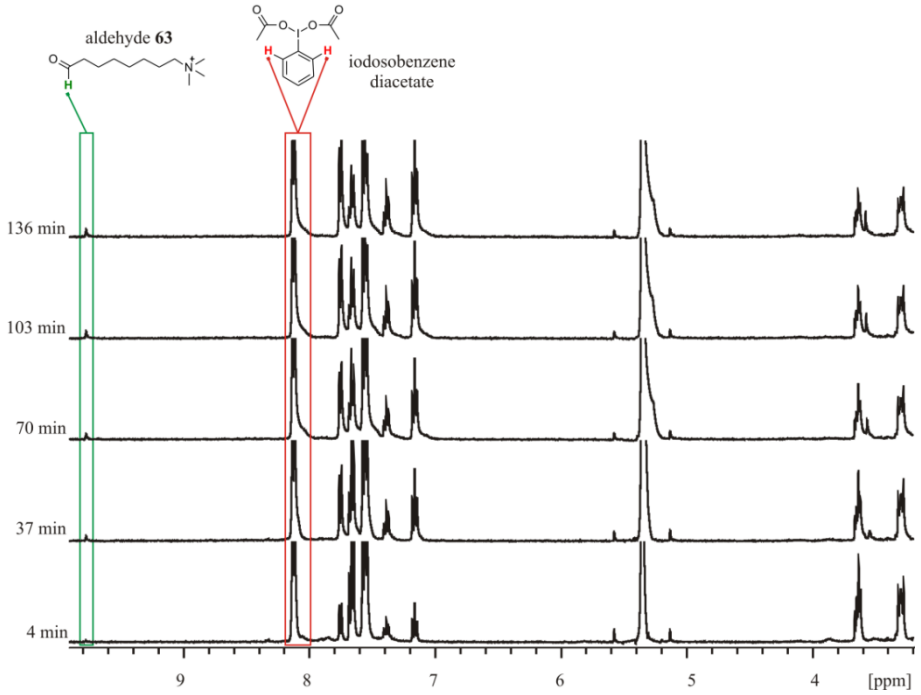

Fig. 97. Few time dependent ^{1}H NMR spectra for catalytic oxidation of alcohol **59** (6 mM) catalyzed by **azpy**•Ru^{II}•(H_2O)•**C24** (**C27**, 5 mol-%) in the presence of iodosobenzene diacetate (18 mM) in CD_2Cl_2 (500 μL).

Surprisingly, the oxidation reaction of octanol (**57**) catalyzed by 5 mol-% of the reference ruthenium compound **azpy**•Ru^{II}•(H_2O)•**tpy** (**47**) in the presence of iodosobenzene diacetate as a sacrificial oxidant (no addition of water) proceeded at a much lower rate than the analogous reaction catalyzed by metallocavitand **azpy**•Ru^{II}•(H_2O)•**C24** (**C27**, **Fig. 98**).

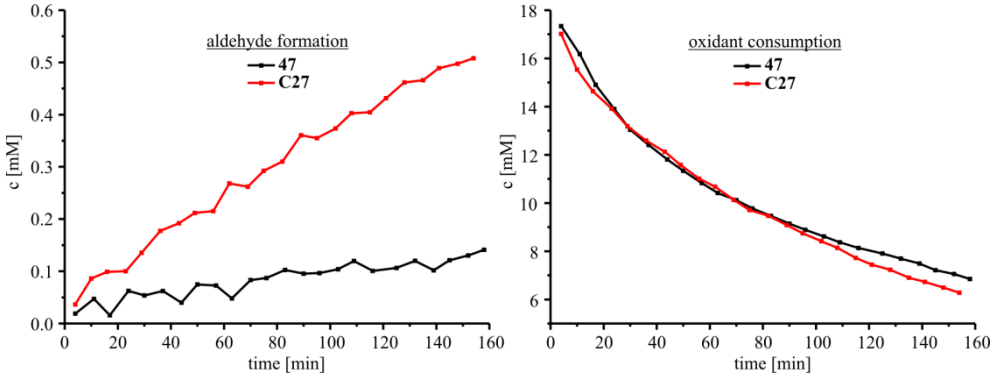

Fig. 98. Plots of changes in the concentration of the octanal (**61**) produced in the oxidation of the octanol (**57**, 6 mM) catalyzed by **azpy**•Ru^{II}•(H_2O)•**tpy** (**47**, 5 mol-%, black) and **azpy**•Ru^{II}•(H_2O)•**C24** (**C27**, 5 mol-%, red) in the presence of iodosobenzene diacetate as an oxidant (18 mM) in CD_2Cl_2 (500 μL).

This represented a completely unexpected result for us. Providing a reasonable explanation to this fact is not easy. However, we surmise that competitive water oxidation reactions may take place in solution. This secondary reaction must be more efficient in the case of the more hydrophilic catalyst **azpy**•Ru^{II}•(H_2O)•**tpy** (**47**), which in turn reduces the amount of available catalyst in solution to perform the alcohol oxidation. Interestingly, the rates of consumption of the sacrificial oxidant were completely analogous in both catalyzed reactions.

Alcohols **58**, **59** and **60** were prepared in two synthetic steps starting from the corresponding bromo-alcohol derivatives **58a**, **59a** and **60a** (**Scheme 11**). The synthesis of the ammonium alcohols began with the introduction of the quaternary trimethylammonium knob by the direct substitution reaction of the bromo substituent with trimethylamine affording **58b**, **59b** and **60b**. Next, we exchanged the bromide anion with the PF_6 counterpart in order to eliminate possibility of coordination with Ru^{II} and to increase the solubility of the ammonium salts in nonpolar organic solvents.

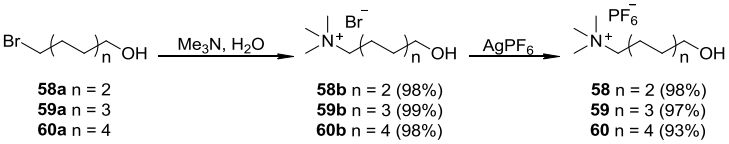

58a n = 2 | **58b** n = 2 (98%) | **58** n = 2 (98%)
59a n = 3 | **59b** n = 3 (99%) | **59** n = 3 (97%)
60a n = 4 | **60b** n = 4 (98%) | **60** n = 4 (93%)

Scheme 11. Synthesis of substrate alcohols **58**, **59** and **60**.

The formation of the inclusion complex **59**⊂**azpy**•Ru^{II}•(H_2O)•**C24** was evidenced by the presence, in the ^1H NMR spectrum of an equimolar mixture, of multiple and broad upfield signals resonating at ≈ -0.7 ppm that were assigned to the trimethylalkylammonium knob included in the aromatic cavity of the metallocavitand **azpy**•Ru^{II}•(H_2O)•**C24** (**C27**). The NOESY spectrum of an equimolar mixture of **azpy**•Ru^{II}•(H_2O)•**C24** (**C27**) and **59** showed the presence of cross-peaks between the bound and the free guest that were indicative of the existence of a chemical exchange process that was slow on the ^1H NMR timescale (**Fig. 99**). It is important to notice that multiple signals were observed for the protons of the bound trimethylammonium groups. Most likely, this is due to the presence of the **59**⊂**azpy**•Ru^{II}•(H_2O)•**C24** complex as a mixture of conformers of the two possible enantiomers[41] of **C27**.

The oxidation reactions of alcohol **59** catalyzed by 5 mol-% of the reference catalyst **azpy**•Ru^{II}•(H_2O)•**tpy** (**47**) or the metallocavitand **azpy**•Ru^{II}•(H_2O)•**C24** (**C27**) provided similar results to those obtained in the oxidation of octanol (**57**). That is the metallocavitand catalyst **azpy**•Ru^{II}•(H_2O)•**C24** outperformed the reference catalysts (**47**). This trend was also observed in the oxidation of alcohols **58** and **60**. Although the oxidation reaction of alcohol **59** catalyzed by metallocavitand **azpy**•Ru^{II}•(H_2O)•**C24** is somewhat faster than the corresponding oxidations of the alcohols **58** and **60**, the difference in rates are not very

significant. The introduction of additional water to the reaction mixture facilitated the oxidation of the alcohols, where water probably acted as a proton acceptor (**Fig. 100**).

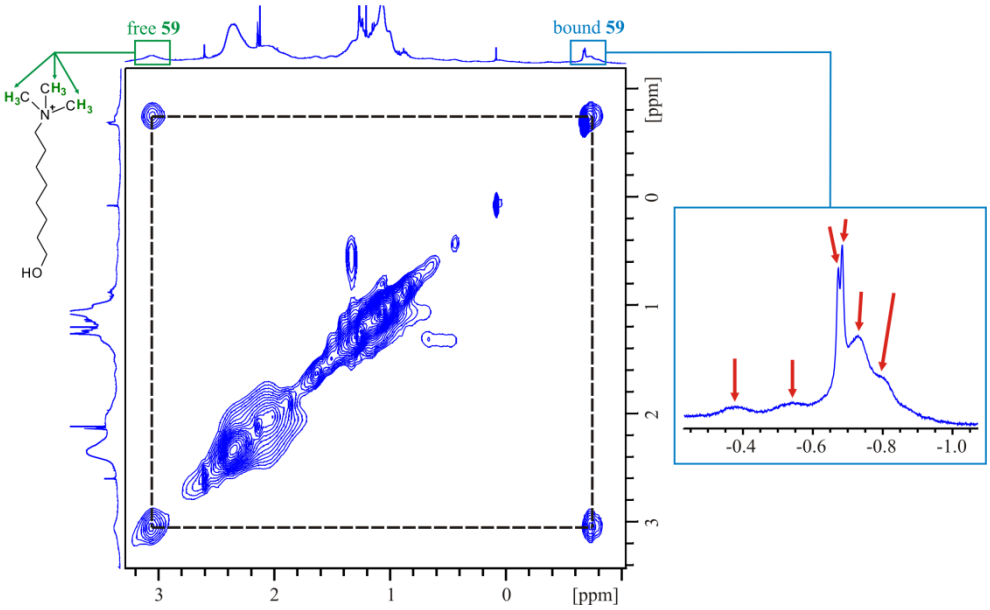

Fig. 99. Expanded region of the NOESY spectrum acquired from an equimolar solution of the alcohol **59** (4.6 mM) and **azpy**•Ru^{II}•(H_2O)•**C24** (**C27**) in CD_2Cl_2 (500 µL). Cross-peak indicating chemical exchange between free and bound **59** is indicated with black dashed lines.

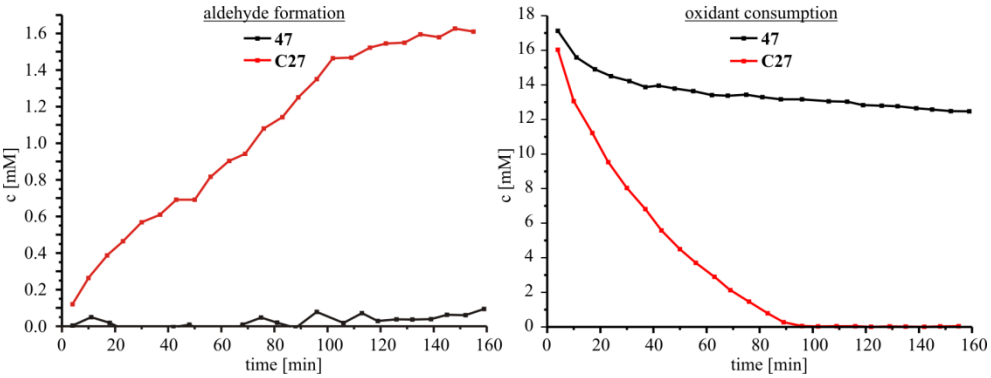

Fig. 100. Plots of changes in the concentration of the aldehyde **63** produced in the oxidation of the alcohol **59** (6 mM) catalyzed by **azpy**•Ru^{II}•(H_2O)•**tpy** (**47**, 5 mol-%, black) and **azpy**•Ru^{II}•(H_2O)•**C24** (**C27**, 5 mol-%, red) in the presence of iodosobenzene diacetate as an oxidant (18 mM) and water (112 mM) in CD_2Cl_2 (500 µL).

However, it is difficult to extract the general conclusion from the behavior of the decomposition/consumption rates of the sacrificial oxidant observed in the different oxidation reactions we performed. In short, although the metallocavitand **azpy**•Ru^{II}•(H_2O)•**C24** (**C27**) is a better catalyst for the oxidation of the studied primary alcohols than the reference organometallic complex **azpy**•Ru^{II}•(H_2O)•**tpy** (**47**), we did not observed any selectivity in the oxidation reactions of the series of trimethylalkylammonium

alcohols (**58**, **59** and **60**). Moreover, the oxidation of octanol (**57**) catalyzed by metallocavitand **azpy**•Ru^{II}•(H_2O)•**C24** occurred at a similar rate to the ones observed for the trimethylammonium analogues. We must conclude that the epoxidation and the oxidation reactions mediated by the metallocavitand **azpy**•Ru^{II}•(H_2O)•**C24** (**C27**) did not show significant signs of the involvement of supramolecular catalysis.

4.3 Conclusions

We synthesized and fully characterized an unprecedented cavitand **C24** derived from resorcin[4]arene and decorated with one terpyridine ligand covalently attached to one of its aromatic walls. The terpyridine cavitand **C24** was metallated with $RuCl_3$ yielding the paramagnetic metallocavitand Ru^{III}•Cl_3•**C24** (**C25**). The coordination of the ancillary 2-(phenylazo)pyridine (**azpy**, **42**) bidentate ligand to the Ru^{III} metal center in the presence of triethylamine produced the concomitant reduction to Ru^{II} affording the metallocavitand **azpy**•Ru^{II}•Cl•**C24** (**C26**). Finally, the substitution of the chloro ligand in the metallocavitand **azpy**•Ru^{II}•Cl•**C24** (**C26**) by a water molecule produced the metallocavitand **azpy**•Ru^{II}•(H_2O)•**C24** (**C27**). Owing to the paramagnetic property of the metallocavitand Ru^{III}•Cl_3•**C24** (**C25**) and its existence in the solution as a mixture of conformers, its characterization by ^{1}H NMR spectroscopy was impossible. Likewise, the existence in solution of metallocavitands **azpy**•Ru^{II}•Cl•**C24** (**C26**) and **azpy**•Ru^{II}•(H_2O)•**C24** (**C27**) as a mixture of enantiomers[41] and conformers, produced ^{1}H NMR spectra with broad an ill-defined signals that were not appropriate for their characterization using this spectroscopy. Additional characterization methods (XRD, IR, DPV, UV/Vis) for the Ru^{II}-metallocavitands were assayed that proved beyond any reasonable doubt the assignment of their structures. Additionally, we assayed the metallocavitand **azpy**•Ru^{II}•(H_2O)•**C24** (**C27**) as a catalyst for the epoxidation reaction of alkenes and the oxidation of primary alcohols to aldehydes. Our aim was to show the possible involvement of the structure of the metallocavitand **azpy**•Ru^{II}•(H_2O)•**C24** as a supramolecular catalyst owing to the close proximity of the binding site and the catalytic center. The deep aromatic cavity of the metallocavitand **azpy**•Ru^{II}•(H_2O)•**C24** was explored for the selective complexation of substrates decorated with a trimethylalkylammonium knob. The obtained results indicate that the level of supramolecular catalysis that might be operative in the studied systems is reduced. We have not detected significant selectivity in the series of substrates used in epoxidation and oxidations reaction catalyzed by **azpy**•Ru^{II}•(H_2O)•**C24** (**C27**). In the case of the epoxidation reaction of alkenes, organometallic complex **azpy**•Ru^{II}•(H_2O)•**tpy** (**47**) used as reference catalyst was as efficient as the metallocavitand **azpy**•Ru^{II}•(H_2O)•**C24** (**C27**). On the other hand, in the oxidation reaction of alcohols, catalyst **azpy**•Ru^{II}•(H_2O)•**C24** (**C27**) outperformed reference catalyst **azpy**•Ru^{II}•(H_2O)•**tpy** (**47**) but did not show any selectivity. We ascribed this difference of reactivity in the latter case to the preferential reaction of

azpy•Ru^{II}•(H_2O)•**tpy** (**47**) for oxidant decomposition.[61,62] Catalysts **azpy**•Ru^{II}•(H_2O)•**C24** (**C27**) and **azpy**•Ru^{II}•(H_2O)•**tpy** (**47**) are significantly faster in the epoxidation of alkenes than in the oxidation of primary alcohols. Finally, we believe that the presence of weakly coordinating compounds, such as ketones (byproducts of Meinwald epoxide rearrangement), could have a significance in limiting the rate of excessive oxidant consumption, although more research is required to fully understand these implications.

4.4 Experimental section

4.4.1 General information and instrumentation

All reagents and solvents were obtained from commercial suppliers and used without further purification unless otherwise stated. All NMR spectra were recorded with a Bruker Avance 400 or a Bruker Avance 500 spectrometer. All deuterated solvents (Sigma–Aldrich) were used without any further purification. Chemical shifts are given in ppm and peaks are referenced relative to the solvent residual peak (δ_{CH2Cl2} = 5.32 ppm, δ_{CHCl3} = 7.26 ppm, δ_{DMSO} = 2.49 ppm, δ_{D2O} = 4.65 ppm). All NMR *J* values are given in Hz and are uncorrected. All MS were recorded on Bruker MALDI-TOF Autoflex, Bruker HPLC-MicroTOF Focus, Bruker HPLC-QqTOF and Waters HPLC-TOF. All IR spectra were recorded with Alpha-P FTIR-ATR TR2. UV/Vis spectra were recorded on Shimadzu UV-2401 with temperature control unit. All DPV experiments were performed on an IJ-Cambria CHI-660 potentiostat, using glassy carbon electrode (d = 2 mm) as a working electrode, platinum wire as an auxiliary electrode, and $Hg/HgSO_4$ as a reference electrode. All samples were weighed on Mettler Toledo MX5 microbalance. HPLC analyses were performed on Agilent 1200 Series using Agilent Eclipse XDB-C18 analytical column coupled with Agilent G1315D or Agilent Quadrupole LC/MS 6130 detector. XRD samples were recorded on Bruker Kappa Apex II.

4.4.2 Synthetic procedures

2-(phenylazo)pyridine ligand (azpy, 42): The synthesis of **azpy** was performed according to published procedure and consisted of adding 2-aminopyridine (4.00 g, 42.1 mmol) to emulsion prepared by mixing sodium hydroxide (20.00 g, 490 mmol) in water (20 mL) and benzene (2.6 mL). Over 10 minute period, solid nitrosobenzene (4.74 g, 42.1 mmol) was added and reaction mixture carried out in oil bath at 90-100 °C, followed by additional 10 minutes heating at 100 °C. Crude product was extracted using benzene (3 x 75 mL) and resulting solution treated with active carbon. Evaporation of solvent yielded dark red oily compound, and desired product was recrystallized from petroleum ether (315 mL) at -20

°C, producing dark red crystals (5.30 g, 28.9 mmol, 68.8%). M.p. = 32 - 34 °C. ^{1}H NMR (500 MHz, CD_2Cl_2): δ = 8.72 (ddd, *J* = 4.8, 1.8, 0.8 Hz, 1H), 8.04 - 7.98 (m, 2H), 7.91 (ddd, *J* = 8.0, 7.4, 1.9 Hz, 1H), 7.77 (dt, *J* = 8.0, 1.0 Hz, 1H), 7.60 - 7.55 (m, 1H), 7.58 - 7.54 (m, 2H), 7.42 (ddd, *J* = 7.4, 4.8, 1.1 Hz, 1H) ppm. ^{13}C NMR (100 MHz, CD_2Cl_2): δ = 163.30, 152.43, 149.41, 138.21, 132.08, 129.21, 125.20, 123.31, 113.99 ppm. FTIR: $\tilde{\upsilon}$ = ν(-N=N-) 1420; ν(Py) 1441, 1463, 1476; ν(Ar/Py) 1470, 1580 cm^{-1}.

Ethyl 2,6-dibromoisonicotinate (43b): The solid 2,6-dihydroxyisonicotinic acid (**43a**, 4.00 g, 25.8 mmol) and solid phosphorous oxybromide (11.65 g, 40.6 mmol) were mixed with spatula in a two-necked flask (under the flow of nitrogen). Reaction flask was placed in the oil bath, gradually heated to 185 ºC and kept at that temperature untill hydrogen bromide stopped evolving (≈ 2 h). Then, the temperature was reduced to 70 ºC, followed by slow and careful addition of anhydrous ethanol (20 mL, exothermic!). Reaction mixture was equipped with magnetic stirbar and mixed for 30 min at 60 ºC. Then, the solid sodium bicarbonate was added until gas evolved. Ethanol was evacuated affording the thick black sludge. The product, ethyl 2,6-dibromoisonicotinate (**43b**), was extracted using methylene chloride (6 x 40 mL) by decanting the organic phase. Methylene chloride fractions were combined, solvent evacuated and crude product purified by flash chromatography on silica using 1:1 hexanes and methylene chloride as eluent (4.02 g, 13.0 mmol; 50.4%). ^{1}H NMR (400 MHz, $CDCl_3$): δ = 7.97 (s, 2H), 4.40 (q, *J* = 7.1 Hz, 2H), 1.39 (t, *J* = 7.1 Hz, 3H) ppm. ^{13}C NMR (126 MHz, $CDCl_3$): δ = 162.46, 141.88, 141.48, 126.69, 62.69, 14.14 ppm. GC/MS (EI, -): calcd for $C_8H_7Br_2NO_2$ 306.9; found 306.9.

(2,6-dibromopyridin-4-yl)methanol (43c): Ethyl 2,6-dibromoisonicotinate (**43b**, 4.02 g, 13.0 mmol) was dissolved in anhydrous ethanol (30 mL) followed by slow addition of the solid sodium borohydride (2.60 g, 68.7 mmol). Reaction mixture was refluxed for 2 h, cooled to room temperature and hydrochloric acid (2 M) slowly added until gas stopped evolving. The solvent was removed, water (2 mL) added and solution basified with solid potassium hydroxide. Obtained white precipitate was extracted with methylene chloride, dried over anhydrous magnesium sulfate and solvent evacuated yielding (2,6-dibromopyridin-4-yl)methanol (**43c**) as a white solid that required no further purification (2.92 g, 10.9 mmol, 84%). ^{1}H NMR (400 MHz, $CDCl_3$): δ = 7.44 (t, *J* = 0.8 Hz, 2H), 4.69 (s, 2H), 2.56 (bs, 1H) ppm. ^{13}C NMR (126 MHz, $CDCl_3$): δ = 155.57, 140.81, 124.35, 62.14 ppm. GC/MS (EI, -): calcd for $C_6H_5Br_2NO$ 264.9; found 264.9.

2,6-dibromoisonicotinaldehyde (43d): In the two-necked flask kept under the nitrogen flow, oxalyl chloride (200 μL, 2.37 mmol) and dry methylene chloride (20 mL) were added and cooled down to -78 ºC. Then, DMSO (270 μL, 3.8 mmol) dissolved in dry methylene chloride (5 mL) was added drop-wise to cooled solution and reaction mixture stirred for 10 min. To the obtained reaction mixture a solution prepared by dissolving dried (2,6-dibromopyridin-4-yl)methanol (**43c**, 420 mg, 1.57 mmol) in dry methylene chloride (10 mL) was added and reaction carried out for 15 min. Reaction was quenched by addition of triethylamine (1.12 mL), cooling bath was removed and water added when the room

temperature was reached. The crude product was extracted with methylene chloride, dried over anhydrous magnesium sulfate and solvent evacuated. Obtained white solid was purified by flash chromatography on silica using 1:1 methylene chloride and hexanes as an eluent (375 mg, 1.42 mmol, 90%). ^{1}H NMR (400 MHz, $CDCl_3$): δ = 9.95 (s, 1H), 7.83 (s, 2H) ppm. ^{13}C NMR (100 MHz, $CDCl_3$): δ = 188.00, 145.17, 142.29, 125.99 ppm. GC/MS (EI, -): calcd for $C_6H_3Br_2NO$ 262.9; found 262.9.

[2,2':6',2''-terpyridine]-4'-carbaldehyde (43): Dry 2,6-dibromoisonicotinaldehyde (**43d**, 300 mg, 1.13 mmol) and freshly distilled 2-(tributylstannyl)pyridine (750 μL, 2.32 mmol) were transferred in the two-necked flask equipped with condenser connected to nitrogen line and with the septum. System was evacuated (until there was no more bubbling of viscous liquid) and purged with nitrogen few times. Then, the catalyst tetrakis(triphenylphosphin)-palladium(0) (28.1 mg, 24 μmol) dissolved in dry toluene (1 mL) was added to the reaction mixture. Additional amount of dry toluene (19 mL) was added and reaction mixture refluxed overnight under nitrogen atmosphere. The reaction mixture was filtered over celite, solvent evacuated and crude product purified by flash chromatography on silica, first with pure methylene chloride followed by isocratic 5% ethyl acetate (242.6 mg, 0.93 mmol, 82%). ^{1}H NMR (500 MHz, $CDCl_3$): δ = 10.25 (s, 1H), 8.86 (s, 2H), 8.72 (ddd, *J* = 4.8, 1.8, 0.9 Hz, 2H), 8.61 (dt, *J* = 7.9, 1.0 Hz, 2H), 7.87 (td, *J* = 7.7, 1.8 Hz, 2H), 7.37 (ddd, *J* = 7.5, 4.8, 1.2 Hz, 2H) ppm. ^{13}C NMR (126 MHz, $CDCl_3$): δ = 191.75, 157.20, 155.15, 149.39, 143.96, 137.00, 124.37, 121.30, 119.75 ppm. GC/MS (EI, -): calcd for $C_{16}H_{11}N_3O$ 261.1; found 261.1.

Cavitand C9: The hexaamidedinitro cavitand **C8** (150 mg, 0.106 mmol) was dissolved in THF (4 mL) and transferred to 25 mL two-necked amber glass flask. To this solution was suspended catalytic amount of Raney-Ni (washed four times with THF, followed by separation with a magnet and decantation). System was purged with hydrogen and reaction carried under hydrogen (1 atm) at 40 °C for 4 h. The catalyst was separated from the resulting solution using magnet, and the afforded solution of hexaamidediamine cavitand **C9** filtered through a 0.45 μm syringe filter to remove remaining catalyst particles. Solvent was evacuated at 35 °C under vacuum and obtained cavitand **C9** immediately used in the next step without further purification (oxidizible by air on longer exposition).

Cavitand C24: In 25 mL pressure tube, terpyridine aldehyde **43** (27.7 mg, 106 μmol), was added followed by hexaamidediamine cavitand **C9** dissolved in minimal amount of dry dioxane (200 - 400 μL; dried over molecular sieves). The pressure vessel was sealed, placed in 100 °C pre-heated oil bath, and reaction carried out for around 16 h (reaction was monitored by HPLC). Then, solvent was evacuated, solid dissolved in a small amount of methylene chloride and drop-wise added to hexane (≈ 10 mL). The obtained pale yellowish precipitate was collected by filtration and washed with hexanes (removes most of the unreacted terpyridine aldehyde **43**), and material purified by flash chromatography on silica, first eluting with methylene chloride, followed by gradient up to 5% methanol and the isocratic elution with 5% methanol (152.3 4 mg, 0.096 mmol, 90% calculated on

cavitand **C8**). ^{1}H NMR (500 MHz, CD_2Cl_2): δ = 12.36 (s, 1H), 10.20 (s, 1H), 9.98 (s, 1H), 9.56 (s, 1H), 9.01 (s, 2H), 8.88 (s, 1H), 8.72 (d, *J* = 4.2 Hz, 2H), 8.69 (d, *J* = 7.9 Hz, 2H), 8.32 (s, 1H), 8.16 (s, 1H), 7.93 (td, *J* = 7.8, 1.7 Hz, 2H), 7.73 (s, 1H), 7.72 (s, 1H), 7.70 (s, 1H), 7.65 (s, 1H), 7.53 (s, 1H), 7.50 (s, 1H), 7.45 (s, 1H), 7.44 - 7.40 (m, 2H), 7.36 (s, 1H), 7.35 (s, 1H), 7.28 (s, 1H), 7.23 (s, 1H), 7.22 (s, 1H), 7.21 (s, 1H), 7.18 (s, 1H), 7.17 (s, 1H), 5.68 (t, *J* = 8.3 Hz, 1H), 5.63 - 5.56 (m, 3H), 3.16 - 2.14 (m, 18H), 1.74 - 1.55 (m, 2H), 1.44 (t, *J* = 7.6 Hz, 3H), 1.26 (t, *J* = 7.5 Hz, 3H), 1.18 (t, *J* = 7.6 Hz, 3H), 1.12 (t, *J* = 7.7 Hz, 3H), 1.08 - 1.02 (m, 9H), 1.00 (t, *J* = 7.3 Hz, 6H), 0.68 (t, *J* = 7.7 Hz, 3H) ppm. MS (ESI, +): calcd for $C_{94}H_{87}N_{11}O_{14} + H^+$ 1594.6512; found 1594.6518. DPV (in acetonitrile): 1.27 V vs $Hg/HgSO_4$. See the supporting information for crystal structure details.

Metallocavitand Ru^{III}•Cl_3•C24 (C25): To the solution made of $RuCl_3 \times 3H_2O$ (8.2 mg, 31 μmol) dissolved in absolute ethanol (2.5 mL), a solution made of terpyridine cavitand **C24** (50 mg, 31 μmol) dissolved in ethanol (5 mL) was added drop-wise. Reaction mixture was refluxed for 4 h, followed by cooling to room temperature and filtration of the brown precipitate. The solid material was washed with cold ethanol, dissolved in methylene chloride and filtered through 0.45 μm syringe filter. After solvent evacuation the brown metallocavitand Ru^{III}•Cl_3•**C24** (**C25**) was obtained as a solid (47 mg, 26 μmol, 83%). MS (MALDI, +): calcd for $C_{94}H_{87}Cl_3N_{11}O_{14}Ru$ - Cl^- 1767.4875; found 1767.5127. See the supporting information for crystal structure details.

Metallocavitand azpy•Ru^{II}•Cl•C24 (C26): Suspension made of metallocavitand Ru^{III}•Cl_3•**C24** (**C25**, 35.2 mg, 20 μmol), triethylamine (14.1 μL, 0.1 mmol), lithium chloride (8.6 mg, 0.2 mmol) and **azpy** (**42**, 14.7 mg, 27 μmol) in 4:1 mixture of ethanol/water (2.5 mL) was refluxed overnight. Obtained deep purple solution was filtered hot, followed by addition to saturated water solution (2 mL) of ammonium hexafluorophosphate. Precipitate was washed with water, dried and purified by column chromatography on alumina, eluting first unreacted **azpy** and blue isomeric forms of (**azpy**)$_2$•Ru^{II}•Cl_2 with 9:1 methylene chloride / acetone, followed by elution with 10:85:5 methylene chloride / acetone / methanol separating dark pink band of the **azpy**•Ru^{II}•Cl•**C24** (**C26**) metallocavitand (35.2 mg, 17 μmol, 88%). ^{31}P NMR (162 MHz, CD_2Cl_2): δ = -139.18 (hept, *J* = 712.2 Hz) ppm. ^{19}F NMR (376 MHz, CD_2Cl_2): δ = -72.48 (d, *J* = 711.4 Hz) ppm. MS (MALDI, +): calcd for $C_{105}H_{96}ClF_6N_{14}O_{14}PRu$ - PF_6^- 1907.5995; found 1907.5933. DPV (in acetonitrile): 1.08 V (highest intensity wave) vs $Hg/HgSO_4$. FTIR: ῡ = ν(PF_6^-) 557, 840; ν(-NH···O=) 3243; ν(C-N) 1401; ν(C=O) 1668, 1663, 1653; ν(N=N) 1272; ν(Ar) 1602, 840 cm^{-1}.

Metallocavitand azpy•Ru^{II}•(H_2O)•C24 (C27): The metallocavitand **azpy**•Ru^{II}•Cl•**C24** (**C26**, 25 mg, 12 μmol) was dissolved in mixture of acetone (3 mL) and water (10 drops) followed by addition of silver hexafluorophosphate (10 mg, 40 μmol) dissolved in acetone solution (1 mL). Reaction was stirred at 60 °C overnight in the absence of light. Precipitated silver chloride was separated using 0.45 μm syringe filter and obtained solution drop-wise added to water (50 mL). The obtained maroon colored precipitate of

metallocavitand **azpy**•Ru^{II}•(H_2O)•**C24** (**C27**) was rinsed with water and dried under vacuum overnight (26.4 mg, 12 μmol, 99%). ^{31}P NMR (162 MHz, CD_2Cl_2): δ = -139.34 (hept, *J* = 713.3 Hz) ppm. ^{19}F NMR (376 MHz, CD_2Cl_2): δ = -69.50 (d, *J* = 711.1 Hz) ppm. MS (MALDI, +): calcd for $C_{105}H_{98}F_{12}N_{14}O_{15}P_2Ru$ - $2PF_6^-$ - H^+ 1895.6331; found 1895.6301. DPV (in chloroform): 1.18 V (highest intensity wave) vs Hg/$HgSO_4$. FTIR: ῡ = ν(PF_6^-) 556, 837; ν(-NH···O=) 3244; ν(C-N) 1401; ν(C=O) 1669, 1662, 1653; ν(N=N) 1272; ν(Ar) 1602, 837; ν(Ru-H_2O) 3393 cm^{-1}.

Organometallic complex Ru^{III}•Cl_3•tpy (45):[63] In solution made of $RuCl_3 \times 3H_2O$ (56 mg, 0.21 mmol) and absolute ethanol (15 mL), an ethanol solution (30 mL) of 2,2':6',2"-terpyridine (**tpy**, **44**, 50 mg, 0.21 mmol) was added drop-wise. Reaction mixture was refluxed overnight. The obtained suspension was cooled down to a room temperature, brown solid collected by filtration, washed with ethanol and methylene chloride, and dried on vacuum affording Ru^{III}•Cl_3•**tpy** (**C25**) complex (93 mg, 0.21 mmol, 99%).

Organometallic complex azpy•Ru^{II}•Cl•tpy (46):[40] The organometallic complex Ru^{III}•Cl_3•**tpy** (**45**, 200 mg, 0.45 mmol) was suspended in 1:1 mixture of ethanol and water (50 mL). Suspension was refluxed for 5 min followed by addition of **azpy** (**42**, 83.2 mg, 0.45 mmol), lithium chloride (200 mg, 4.72 mmol) and triethylamine (3 mL, 21.31 mmol). Solution was refluxed for 5 h. The solvent was removed under reduced pressure and dry residue dissolved in minimum amount of acetonitrile, to which was then added saturated water solution (5 mL) of sodium perchlorate. The solution was refrigerated overnight and obtained solid collected by filtration, washed with a small amount of ice-cold water and dried on vacuum. Finally, the afforded material was purified by column chromatography on silica, eluting first with 4:1 mixture of methylene chloride and acetonitrile to separate unreacted ligand **azpy** and all blue isomeric complexes with general formula (**azpy**)$_2$•Ru^{II}•Cl_2, followed by elution using 2:1 mixture of methylene chloride and acetonitrile to elute dark pink band of the organometallic complex **azpy**•Ru^{II}•Cl•**tpy** (302.0 mg, 0.43 mmol, 95%). ^1H NMR (400 MHz, DMSO-d_6): δ = 9.75 (d, *J* = 5.2 Hz, 1H), 8.87 (d, *J* = 7.6 Hz, 1H), 8.61 (d, *J* = 7.9 Hz, 4H), 8.45 (t, *J* = 7.8 Hz, 1H), 8.25 (t, *J* = 6.5 Hz, 1H), 8.21 (t, *J* = 4.1 Hz, 1H), 8.15 (t, *J* = 7.8 Hz, 2H), 7.49 (t, *J* = 6.5 Hz, 2H), 7.30 (d, *J* = 4.8 Hz, 2H), 7.22 (d, *J* = 7.6 Hz, 1H), 7.04 (t, *J* = 7.5 Hz, 2H), 6.21 (d, *J* = 7.5 Hz, 2H) ppm. MS (MALDI, +): calcd for $C_{29}H_{27}Cl_2N_6O_4Ru$ − ClO_4^- 547.0514; found 547.0505, DPV (in acetonitrile): 0.99 V vs Hg/$HgSO_4$. FTIR: ῡ = ν(ClO_4^-) 620, 1080; ν(N=N) 1296 cm^{-1}.

Organometallic complex azpy•Ru^{II}•(H_2O)•tpy (47):[40] The organometallic complex **azpy**•Ru^{II}•Cl•**tpy** (**46**, 60 mg, 92 μmol) was dissolved in water (10 mL) and to this solution added water solution (2 mL) of silver nitrate (63 mg, 0.37 mmol). Solution was refluxed for 2 h followed by 1 h refrigeration. Precipitated silver chloride was filtered off and in addition, solution passed through 0.45 uL syringe filter to remove any remaining particles of silver chloride. Volume of solution was reduced to 3 mL, followed by addition of saturated water solution of sodium perchlorate (2.5 mL). The solution was refrigerated

overnight. The brown precipitate was collected, washed with small amount of ice-cold water and dried on vacuum (46.1 mg, 63 μmol, 68.3%). ^{1}H NMR (500 MHz, D_2O): δ = 9.35 (d, *J* = 4.9 Hz, 1H), 8.73 (d, *J* = 7.9 Hz, 1H), 8.42 (td, *J* = 7.9, 1.5 Hz, 1H), 8.34 (d, *J* = 8.0 Hz, 2H), 8.30 (d, *J* = 8.2 Hz, 2H), 8.22 - 8.15 (m, 1H), 8.10 (t, *J* = 7.7 Hz, 1H), 8.10 (d, *J* = 16.0 Hz, 2H), 7.46 - 7.40 (m, 4H), 7.20 (t, *J* = 7.5 Hz, 1H), 7.03 - 6.93 (m, 2H), 6.16 (dd, *J* = 8.5, 1.1 Hz, 2H) ppm. MS (ESI, +): calcd for $C_{26}H_{22}Cl_2N_6O_9Ru$ – $2ClO_4^-$ - H^+ 529.0853; found 529.0847. DPV (in water): 0.65 V (pH 7), 0.73 V (pH 1 adjusted with $HClO_4$) vs $Hg/HgSO_4$. FTIR: ῡ = ν(ClO_4^-) 618, 1050; ν(N=N) 1289; ν(Ru-H_2O) 3390 cm^{-1}.

***Z*-alkene 50b:** The phosphonium salt **50a** (1 g, 2.335 mmol) was suspended in dry THF (25 mL) under the nitrogen atmosphere. Suspension was cooled at -78 ºC, followed by drop-wise addition of hexane solution of *n*-butyl lithium (2.5 M, 0.97 mL, 2.425 mmol). After 1 h of stirring, benzaldehyde (0.23 mL, 2.240 mmol) was added and solution allowed to warm up to room temperature followed by stirring for 1 h more. Reaction mixture was quenched with water (10 mL) and THF evacuated. Crude product was extracted with methylene chloride, organic phase dried over anhydrous magnesium sulfate and remaining oily product centrifuged. Clear fraction of *Z*-alkene **50b** was decanted (106.6 mg, 0.608 mmol, 26.1%). ^{1}H NMR (400 MHz, acetone-d_6): δ = 7.40 - 7.20 (m, 5H), 6.47 (d, *J* = 11.7 Hz, 1H), 5.73 (dt, *J* = 11.7, 7.1 Hz, 1H), 2.54 - 2.45 (m, 2H), 2.40 - 2.34 (m, 2H), 2.17 (s, 6H) ppm. MS (ESI, +): calcd for $C_{12}H_{17}N + H^+$ 176.1439; found 176.1431.

***Z*-alkene 50c**: *Z*-alkene **50b** (106.6 mg, 0.608 mmol) was dissolved in ethyl acetate (3 mL) followed by addition of iodomethane (1.4 mL, 22.49 mmol). The white precipitate appears immediately and solution was left to stir overnight. The precipitate was collected by filtration, washed with ethyl acetate and dried under reduced pressure (158 mg, 0.498 mmol, 82%). ^{1}H NMR (400 MHz, $CDCl_3$): δ = 7.46 - 7.21 (m, 5H), 6.70 (d, *J* = 11.4 Hz, 1H), 5.70 (dt, *J* = 11.4, 7.1 Hz, 1H), 3.84 - 3.76 (m, 2H), 3.42 (s, 9H), 2.84 (q, *J* = 7.3 Hz, 2H) ppm. ^{13}C NMR (126 MHz, $CDCl_3$): δ = 135.90, 133.63, 128.76, 128.51, 127.65, 124.31, 66.22, 53.89, 30.93, 22.83 ppm. MS (ESI, +): calcd for $C_{13}H_{20}IN$ - I^- 190.1596; found 190.1589.

***Z*-alkene 50**: *Z*-alkene **50c** (100 mg, 0.315 mmol) was dissolved in minimal amount of acetone and to it added silver hexafluorophosphate (85 mg, 0.333 mmol) dissolved in minimal amount of acetone. Solution was left to stir for 1 hour in the absence of light followed by separation of precipitated silver iodide. The solvent was evacuated yielding product as a white solid (105.6 mg, 0.315 mmol, 100%). ^{1}H NMR (400 MHz, CD_3CN): δ = 7.48 - 7.23 (m, 5H), 6.65 (d, *J* = 11.6 Hz, 1H), 5.53 (dt, *J* = 11.6, 7.1 Hz, 1H), 3.37 - 3.29 (m, 2H), 3.00 (s, 9H), 2.81 - 2.70 (m, 2H) ppm. ^{13}C NMR (101 MHz, CD_3CN): δ = 136.40, 132.50, 128.58, 128.52, 127.39, 124.62, 65.55, 52.94, 22.42 ppm. ^{31}P NMR (162 MHz, CD_3CN): δ = -141.52 (hept, *J* = 706.5 Hz) ppm. ^{19}F NMR (376 MHz, CD_3CN): δ = -72.96 (d, *J* = 706.4 Hz) ppm. MS (ESI, +): calcd for $C_{13}H_{20}F_6NP$ - PF_6^- 190.1596; found 190.1584.

Epoxide 53: *m*-CPBA (4.2 mg, 19 μmol) was transferred to NMR tube and dissolved in methylene chloride-*d2* (700 μL). The solution was cooled at 0 - (-5) °C and methylene chloride-*d2* (900 μL) solution of *Z*-alkene **50** (6 mg, 18 μmol) slowly added. The NMR tube was stored in refrigerator and reaction checked periodically. Conversion reached its maximum after 2.5 days of reaction and was estimated to be ≈ 70 % accomplished. Obtained product was purified by analytical HPLC (reverse phase C18 column, 0 - 5 min. 100% water, 20 min gradient to 100% of acetonitrile, 25 min 100% acetonitrile). ^{1}H NMR (500 MHz, CD_2Cl_2): δ = 8.02 - 7.99 (m, 1H), 7.91 (dt, *J* = 7.5, 1.3 Hz, 1H), 7.47 - 7.27 (m, 6H), 4.24 (d, *J* = 4.2 Hz, 1H), 3.83 - 3.61 (m, 2H), 3.42 (dt, *J* = 7.3, 4.6 Hz, 1H), 3.19 (s, 9H), 1.91 - 1.68 (m, 2H) ppm. MS (ESI, +): calcd for $C_{20}H_{24}ClNO_3$ - $C_7H_4ClO_2^-$ 206.1539; found 206.1544.

General procedure for the synthesis of alcohols 58b, 58, 59b, 59, 60b and 60. A typical synthetic procedure is described. 6-bromohexan-1-ol (**58a**, 100 mg, 0.552 mmol) was added to water (5 mL) and to stirred emulsion 45% water solution of trimethylamine (1 mL, 7.61 mmol) added. The solution was stirred at room temperature until reaction mixture became homogenous. Solvent was evacuated and white solid product of **58b** dried over phosphorous pentoxide (130 mg, 0.541 mmol, 98%).

To the water solution (1 mL) of the alcohol **58b** (50 mg, 0.208 mmol) drop-wise was added a water solution (0.5 mL) of the silver hexafluorophosphate (55 mg, 0.215 mmol). Solution was stirred for 2 h followed by filtration over 0.45 μm syringe filter, evacuation of water and drying over phosphorous pentoxide yielding alcohol **58** as a white solid (62 mg, 0.203 mmol, 98%).

By use of similar experimental procedures the alcohol **59b** was isolated in 99% yield, **59** in 97% yield, **60b** in 98% yield and **60** in 93% yield.

Alcohol 58b: ^{1}H NMR (500 MHz, D_2O): δ = 3.49 (t, *J* = 6.6 Hz, 2H), 3.25 - 3.12 (m, 2H), 2.99 (s, 9H), 1.69 (p, *J* = 7.5 Hz, 2H), 1.45 (p, *J* = 6.8 Hz, 2H), 1.35 - 1.21 (m, 4H) ppm. ^{13}C NMR (126 MHz, D_2O): δ = 66.63, 61.53, 30.91, 25.18, 24.52, 22.18 ppm. MS (ESI, +): calcd for $C_9H_{22}BrNO$ - Br^- 160.1701; found 160.1696.

Alcohol 58: ^{1}H NMR (400 MHz, CD_3CN): δ = 3.48 (q, *J* = 6.3 Hz, 2H) ppm, 3.23 - 3.12 (m, 2H), 2.98 (s, 9H), 1.77 - 1.64 (m, 2H), 1.53 - 1.44 (m, 2H), 1.44 - 1.28 (m, 4H) ppm. ^{13}C NMR (101 MHz, CD_3CN): δ = 66.57, 61.29, 52.84, 32.11, 25.57, 25.06, 22.45 ppm. ^{31}P NMR (162 MHz, CD_3CN): δ = -141.53 (hept, *J* = 706.3 Hz) ppm. ^{19}F NMR (376 MHz, CD_3CN): δ = -72.99 (d, *J* = 706.4 Hz) ppm. MS (ESI, +): calcd for $C_9H_{22}F_6NOP$ - PF_6^- 160.1701; found 160.1697.

Alcohol 59b: ^{1}H NMR (500 MHz, D_2O): δ = 3.48 (t, *J* = 6.6 Hz, 2H), 3.22 - 3.14 (m, 2H), 2.98 (s, 9H), 1.71 - 1.60 (m, 2H), 1.49 - 1.35 (m, 2H), 1.30 - 1.18 (m, 8H) ppm. ^{13}C NMR (126 MHz, D_2O): δ = 66.71, 61.79, 31.16, 28.10, 28.01, 25.29, 24.83, 22.17 ppm. MS (ESI, +): calcd for $C_{11}H_{26}BrNO$ - Br^- 188.2009; found 188.2010.

Alcohol 59: ^{1}H NMR (400 MHz, D_2O): δ = 3.47 (t, *J* = 6.6 Hz, 2H), 3.20 - 3.13 (m, 2H), 2.97 (s, 9H), 1.66 (dd, *J* = 10.5, 6.1 Hz, 2H), 1.42 (p, *J* = 6.6 Hz, 2H), 1.29 - 1.18 (m, 8H) ppm. ^{13}C NMR (101 MHz, D_2O): δ = 66.75, 61.79, 31.16, 28.10, 28.01, 25.29, 24.83, 22.16 ppm. ^{31}P NMR (162 MHz, D_2O): δ = -141.96 (hept, *J* = 708.7 Hz) ppm. ^{19}F NMR (376 MHz, D_2O): δ = -72.17 (d, *J* = 708.7 Hz) ppm. MS (MS, +): calcd for $C_{11}H_{26}F_6NOP$ - PF_6^- 188.2009; found 188.2011.

Alcohol 60b: ^{1}H NMR (500 MHz, D_2O): δ = 3.48 (t, *J* = 6.7 Hz, 2H), 3.23 - 3.15 (m, 2H), 2.98 (s, 9H), 1.67 (dt, *J* = 8.0, 4.5 Hz, 2H), 1.42 (q, *J* = 6.8 Hz, 2H), 1.27 - 1.14 (m, 12H) ppm. ^{13}C NMR (126 MHz, D_2O): δ = 67.40, 62.48, 31.85, 29.07, 29.01, 28.91, 28.68, 25.97, 25.59, 22.80 ppm. MS (ESI, +): calcd for $C_{13}H_{30}BrNO$ - Br^- 216.2327; found 216.2324.

Alcohol 60: ^{1}H NMR (500 MHz, D_2O): δ = 3.48 (t, *J* = 6.7 Hz, 2H), 3.22 - 3.14 (m, 2H), 2.98 (s, 9H), 1.70 - 1.54 (m, 2H), 1.47 - 1.38 (m, 2H), 1.29 - 1.04 (m, 12H) ppm. ^{13}C NMR (126 MHz, D_2O): δ = 66.78, 61.86, 31.23, 30.21, 28.44, 28.28, 28.05, 25.34, 24.96, 22.17 ppm. ^{31}P NMR (203 MHz, D_2O): δ = -141.99 (hept, *J* = 708.3 Hz) ppm. ^{19}F NMR (471 MHz, D_2O): δ = -72.10 (d, *J* = 708.7 Hz) ppm. MS (ESI, +): calcd for $C_{13}H_{30}F_6NOP$ - PF_6^- 216.2327; found 216.2321.

Synthesis of aldehyde 63: In the two-necked flask kept under the nitrogen, oxalyl chloride (20μL, 236 μmol) was dissolved in dry methylene chloride (1 mL) and cooled down to -78 ºC. Then, DMSO (20 μL, 282 μmol) dissolved in dry methylene chloride (500 μL) was added slowly to cooled solution and reaction mixture stirred for 10 min. To this mixture was added a suspension prepared by dispersion a dried alcohol **59** in dry methylene chloride (1 mL) and reaction carried out for 15 min. Reaction was quenched by addition of triethylamine (100 μL), cooling bath removed and few drops of water added. Since reaction mixture contained both, product (seen by aldehyde signal in ^{1}H NMR spectrum) and starting material, crude reaction mixture was separated by HPLC (gradient H_2O/CH_3OH with a 0.1% of TFA; C18 column) and fractions analyzed by MS. HPLC/MS (+): calcd for $C_{11}H_{24}F_6NOP$ - PF_6^- 186.2; found 186.2.

4.4.3 Catalytic procedures

Epoxidation: A typical NMR-scale epoxidation experiment consisted of dissolving the appropriate alkene (3.00 μmol), the appropriate Ru^{II}•(H_2O) catalyst (0.15 μmol) and water (22.00 μmol) in methylene chloride-d_2 (550 μL). Then, the solid iodosobenzene diacetate (6.10 μmol) was added and ^{1}H NMR software programmed to record spectrum every 120 s (sw = 12; ns = 16). Using Bruker TopSpin v2.1 each individual spectrum had corrected phase and baseline before performing batch absolute integration of diagnostic signals (regions). Diagnostic region for iodosobenzene diacetate *ortho* aromatic protons (2H) was

8.177 - 8.088 ppm. The oxidant integral initial value was normalized to 1H and used as a reference to convert integrals to concentrations. Components that possesed more diagnostic signals were averaged and used for construction of kinetic diagrams. Using linear fitting for the first 17 min of reaction, we calculated the initial reaction rates.

Diagnostic signals (regions) for styrene (48) epoxidation: styrene (**48**, 1H) 6.823 - 6.718, 5.850 - 5.750 and 5.312 - 5.247 ppm; styrene oxide (**51**, 1H) 3.894 - 3.854, 3.176 - 3.125 and 2.841 - 2.790 ppm (**Fig. 90**).

Diagnostic signals (regions) for *trans*-β-methylstyrene (49) epoxidation: *trans*-β-methylstyrene (**49**, 1H) 6.508 - 6.393 and 6.361 - 6.247 ppm; 1-phenylpropylene oxide (**52**, 1H) 3.622 - 3.552 and 3.090 - 3.016 ppm (**Fig. 101**).

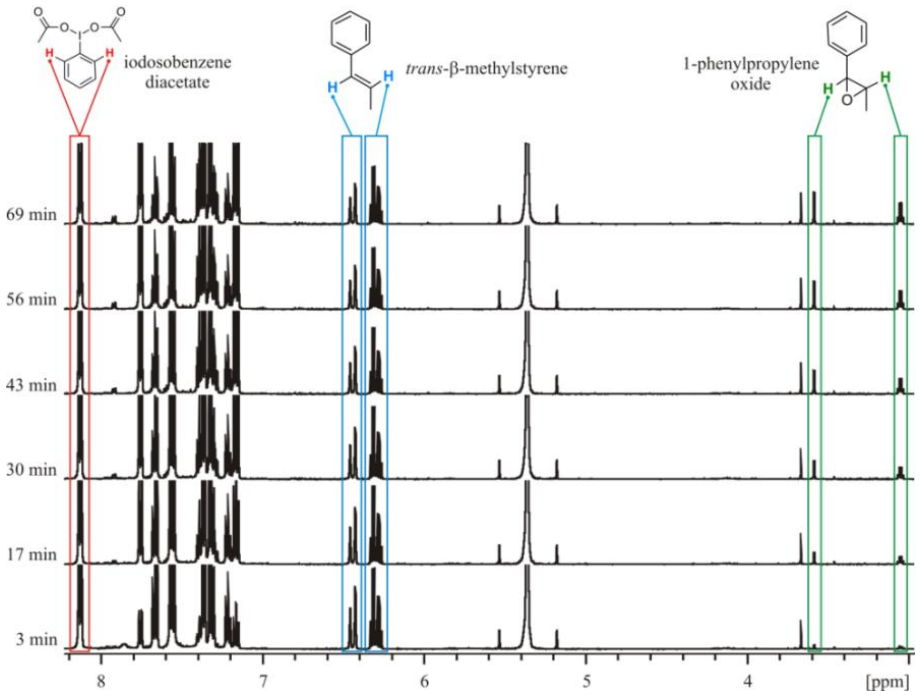

Fig. 101. Few time dependent ^{1}H NMR spectra for catalytic epoxidation of *trans*-β-methylstyrene (**49**, 5.5 mM) catalyzed by **azpy**•Ru^{II}•(H_2O)•**C24** (**C27**, 5 mol-%) in the presence of iodosobenzene diacetate (11 mM) and water (40 mM) in CD_2Cl_2 (550 μL).

Diagnostic signals (regions) for *Z*-alkene 50 epoxidation: Z-alkene **50** (1H) 6.855 - 6.740 and 5.672 - 5.570 ppm; epoxide **53** (1H) 4.306 - 4.254 ppm (**Fig. 102**).

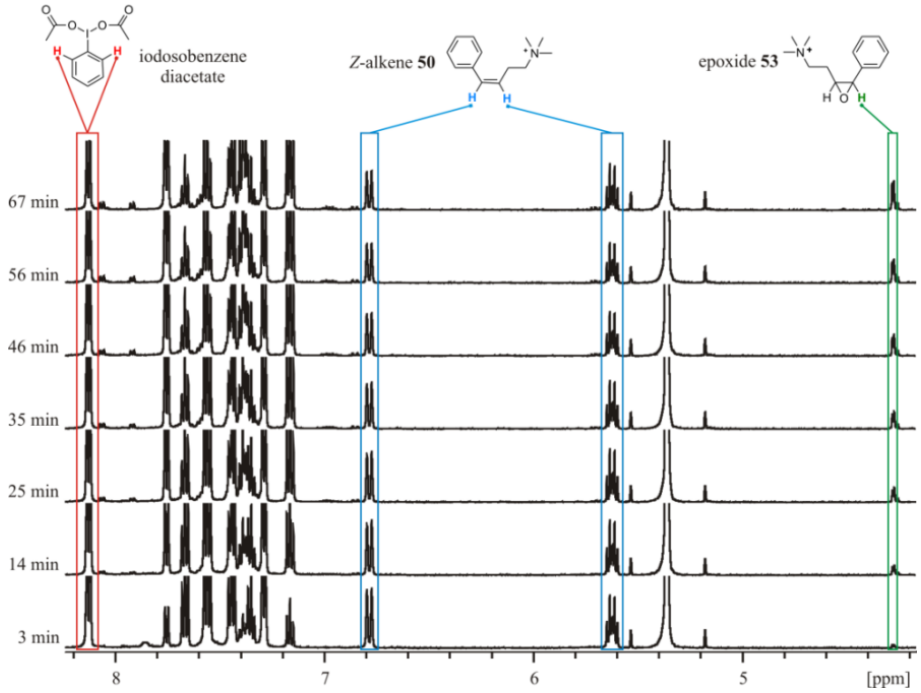

Fig. 102. Few time dependent ^{1}H NMR spectra for catalytic epoxidation of *Z*-alkene **50** (5.5 mM) catalyzed by **azpy**•Ru^{II}•(H_2O)•**C24** (**C27**, 5 mol-%) in the presence of iodosobenzene diacetate (11 mM) and water (40 mM) in CD_2Cl_2 (550 μL).

Oxidation of alcohols: A typical NMR-scale epoxidation experiment consisted of dissolving the appropriate alcohol (3.00 μmol), and the appropriate Ru^{II}•(H_2O) catalyst (0.15 μmol) in methylene chloride-d_2 (500 μL). Then, the solid iodosobenzene diacetate (9.00 μmol) was added and ^{1}H NMR software programmed to record spectrum every 300 s (sw = 12; ns = 16). Using Bruker TopSpin v2.1 each individual spectrum had corrected phase and baseline before performing batch absolute integration of diagnostic signals (regions). Diagnostic region for iodosobenzene diacetate *ortho* aromatic protons (2H) was 8.177 - 8.088 ppm. The oxidant integral initial value was normalized to 1H and used as a reference to convert integrals to concentrations. Using linear fitting for the first 60 min of reaction (except in the cases when reaction was very slow where all values were taken into account), we calculated the initial reaction rates.

Diagnostic signals (regions) for analyzed aldehydes: octanal (**61**, 1H) 9.776 to - 9.7440 ppm; aldehyde **62** (1H) 9.814 - 9.740 ppm; aldehyde **63** (1H) 9.802 - 9.708 ppm (**Fig. 97**); aldehyde **64** (1H) 9.784 - 9.722 ppm.

4.5 Supporting information

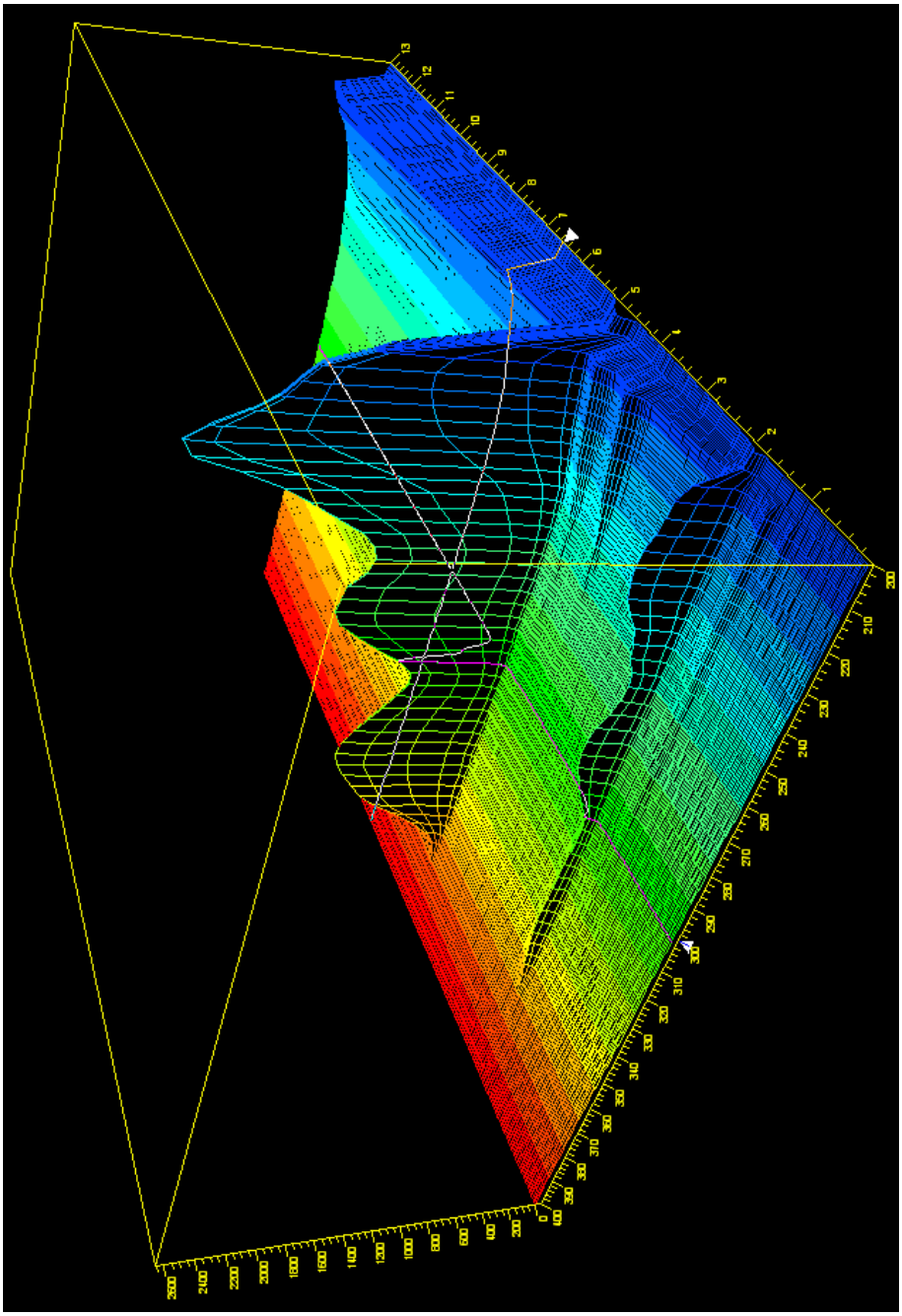

Fig. 103. HPLC trace for the crude reaction mixture of the cavitand **C24**.

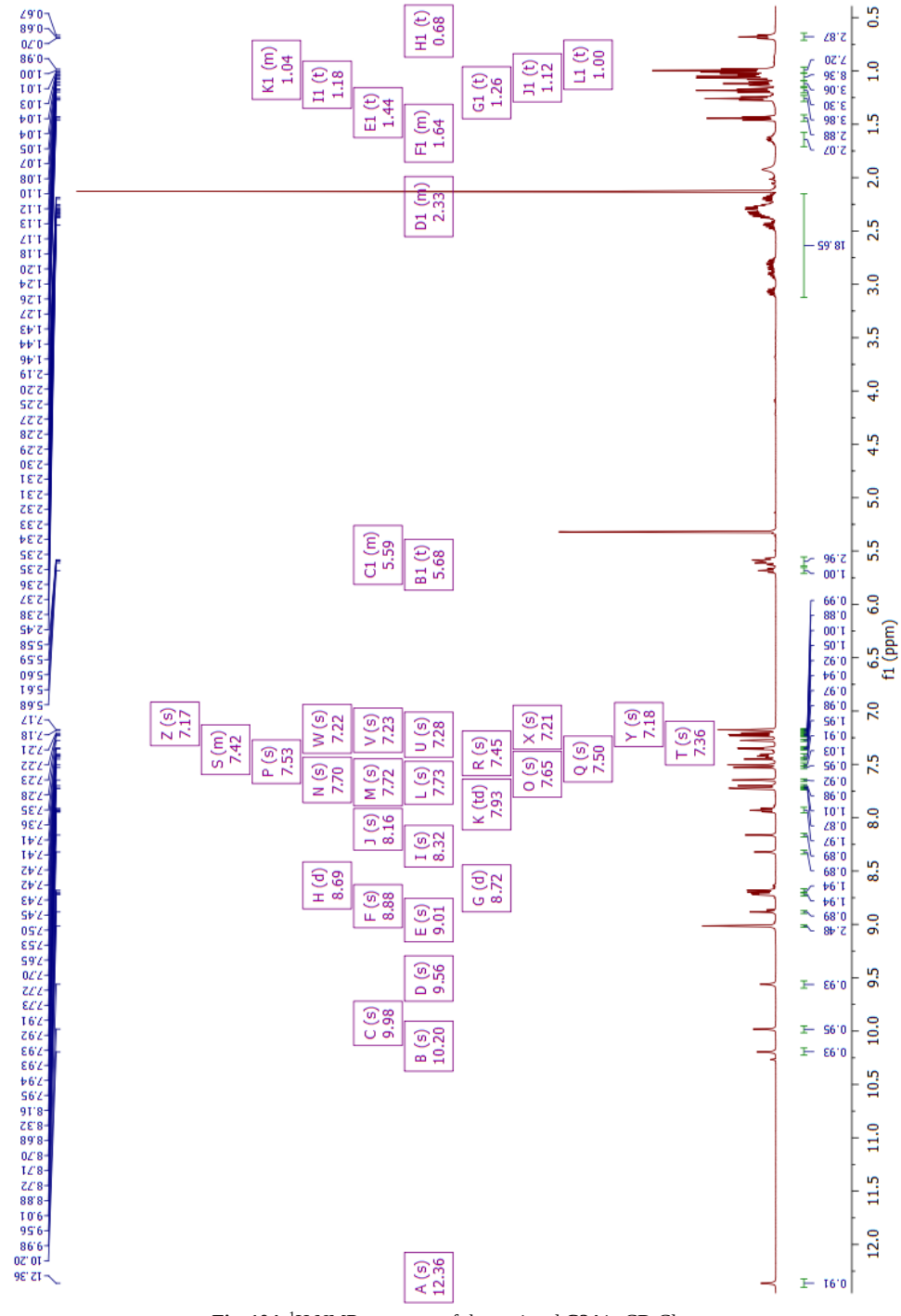

Fig. 104. ^{1}H NMR spectrum of the cavitand **C24** in CD_2Cl_2.

Table 7. Crystal data and structure refinement for the cavitand **C24**.

Empirical formula	$C_{97}\ H_{93}\ C_{l6}\ N_{11}\ O_{14}$	
Formula weight	1849.52	
Temperature	100(2) K	
Wavelength	0.71073 Å	
Crystal system	Triclinic	
Space group	P-1	
Unit cell dimensions	a = 15.6530(14)Å	a = 97.556(4)°.
	b = 16.8518(17)Å	b = 101.633(4)°.
	c = 21.323(3)Å	g = 117.144(3)°.
Volume	4738.4(9) $Å^3$	
Z	2	
Density (calculated)	1.296 Mg/m^3	
Absorption coefficient	0.250 mm^{-1}	
F(000)	1932	
Crystal size	0.40 x 0.30 x 0.10 mm^3	
Theta range for data collection	1.009 to 31.861°.	
Index ranges	-14<=h<=23,-24<=k<=25,-25<=l<=28	
Reflections collected	45658	
Independent reflections	26215[R(int) = 0.0306]	
Completeness to theta =31.861°	80.6%	
Absorption correction	Empirical	
Max. and min. transmission	0.975 and 0.75	
Refinement method	Full-matrix least-squares on F^2	
Data / restraints / parameters	26215/ 381/ 1367	
Goodness-of-fit on F^2	1.962	
Final R indices [I>2sigma(I)]	R1 = 0.1114, wR2 = 0.3108	
R indices (all data)	R1 = 0.1543, wR2 = 0.3323	
Largest diff. peak and hole	2.558 and -1.308 $e.Å^{-3}$	

Bond lengths [Å] and angles [°]

Bond lengths (part 1)		Bond lengths (part 2)		Bond lengths (part 3)		Bond lengths (part 4)	
C1-C2	1.373(5)	C23-C26	1.522(4)	C45-C46	1.502(6)	C68-C69	1.399(5)
C1-O1	1.388(4)	C23-C93	1.533(5)	C47-C48	1.389(4)	C69-C70	1.396(4)
C1-C7	1.414(5)	C23-C24	1.535(5)	C47-C52	1.408(4)	C69-O6	1.399(3)
C2-C3	1.382(5)	C24-C25	1.528(5)	C48-O4	1.394(4)	C70-C71	1.389(4)
C3-N1	1.385(5)	C26-C31	1.391(4)	C48-C49	1.396(5)	C71-C72	1.390(5)
C3-C5	1.400(5)	C26-C27	1.393(4)	C49-C50	1.386(4)	C71-O7	1.411(4)
C4-N2	1.320(5)	C27-C28	1.382(5)	C50-C51	1.393(4)	C72-C73	1.403(4)
C4-N1	1.369(4)	C27-O2	1.400(3)	C50-O5	1.395(4)	C72-C86	1.537(4)
C4-C8	1.465(5)	C28-C29	1.381(4)	C51-C52	1.385(5)	C74-O7	1.382(4)
C5-N2	1.388(4)	C29-C30	1.388(4)	C51-C65	1.528(4)	C74-C75	1.391(5)
C5-C6	1.393(5)	C29-O3	1.411(4)	C53-O5	1.375(4)	C74-C79	1.395(4)
C6-C7	1.385(5)	C30-C31	1.402(4)	C53-C58	1.393(5)	C75-C76	1.392(4)
C7-O2	1.409(4)	C30-C44	1.529(4)	C53-C54	1.398(4)	C76-C77	1.402(5)
C8-C12	1.390(5)	C32-C33	1.389(4)	C54-C55	1.380(5)	C76-N10	1.411(5)
C8-C9	1.407(5)	C32-O3	1.394(4)	C55-C56	1.390(5)	C77-C78	1.386(5)
C9-C10	1.381(5)	C32-C37	1.398(4)	C55-N8	1.432(4)	C77-N11	1.421(4)
C10-N4	1.342(4)	C33-C34	1.394(5)	C56-C57	1.399(5)	C78-C79	1.392(5)
C10-C13	1.489(5)	C34-C35	1.402(4)	C56-N9	1.413(5)	C79-O8	1.388(4)
C11-N4	1.354(5)	C34-N6	1.426(4)	C57-C58	1.366(5)	C80-O13	1.237(5)
C11-C12	1.393(5)	C35-C36	1.392(4)	C58-O6	1.398(4)	C80-N10	1.367(5)
C11-C18	1.468(5)	C35-N7	1.421(4)	C59-O11	1.231(5)	C80-C81	1.502(6)
C13-N3	1.345(5)	C36-C37	1.380(5)	C59-N8	1.349(4)	C81-C82'	1.505(9)
C13-C14	1.388(5)	C37-O4	1.398(4)	C59-C60	1.516(5)	C81-C82	1.511(8)
C14-C15	1.382(5)	C38-O9	1.225(4)	C60-C61	1.520(8)	C83-O14	1.229(5)
C15-C16	1.361(6)	C38-N6	1.353(4)	C62-O12	1.239(5)	C83-N11	1.343(5)
C16-C17	1.386(6)	C38-C39	1.508(4)	C62-N9	1.337(5)	C83-C84	1.514(6)
C17-N3	1.338(5)	C39-C40	1.492(6)	C62-C63	1.501(6)	C84-C85	1.477(7)
C18-N5	1.344(5)	C41-O10	1.218(4)	C63-C64'	1.513(8)	C86-C89	1.515(4)
C18-C19	1.413(6)	C41-N7	1.350(4)	C63-C64	1.548(8)	C86-C87	1.531(5)
C19-C20	1.392(7)	C41-C42	1.531(5)	C65-C68	1.526(4)	C87-C88	1.504(5)
C20-C21	1.419(9)	C42-C43	1.503(6)	C65-C66	1.531(4)	C89-C90	1.402(5)
C21-C22	1.357(9)	C44-C47	1.520(5)	C66-C67	1.528(4)	C89-C94	1.412(5)
C22-N5	1.328(6)	C44-C45	1.535(4)	C68-C73	1.394(4)	C90-C91	1.382(5)

Bond lengths (part 5)		Bond lengths (part 6)		Bond lengths (part 7)		Bond lengths (part 8)	
C90-O8	1.399(4)	Cl1A-C1A	1.772(9)	C1R-Cl1R	1.756(9)	C1X-Cl1X	1.682(8)
C91-C92	1.372(5)	Cl2A-C1A	1.736(9)	Cl1T-C1T	1.788(9)	C1X-Cl2X	1.758(7)
C92-C93	1.401(5)	Cl1C-C1C	1.799(13)	Cl2T-C1T	1.727(9)	Cl2X-Cl2X#1	2.106(7)
C92-O1	1.410(4)	Cl2C-C1C	1.738(13)	C1U-Cl2U	1.770(10)	C1Y-Cl2Y	1.765(10)
C93-C94	1.395(4)	Cl1D-C1D	1.786(13)	C1U-Cl1U	1.772(10)	C1Y-Cl1Y	1.767(10)
Cl1B-C1B	1.745(10)	Cl2D-C1D	1.758(13)	C1W-Cl1W	1.768(10)		
Cl2B-C1B	1.760(10)	C1R-Cl2R	1.677(8)	C1W-Cl2W	1.803(10)		

Angles (part 1)		Angles (part 2)		Angles (part 3)	
C2-C1-O1	121.2(3)	O3-C32-C37	120.8(3)	C68-C65-C66	113.8(2)
C2-C1-C7	120.8(3)	C32-C33-C34	120.9(3)	C51-C65-C66	113.3(3)
O1-C1-C7	117.9(3)	C33-C34-C35	119.7(3)	C67-C66-C65	112.0(3)
C1-C2-C3	117.3(3)	C33-C34-N6	119.0(3)	C73-C68-C69	117.4(3)
C2-C3-N1	131.4(3)	C35-C34-N6	121.3(3)	C73-C68-C65	122.2(3)
C2-C3-C5	122.9(3)	C36-C35-C34	119.5(3)	C69-C68-C65	120.4(3)
N1-C3-C5	105.6(3)	C36-C35-N7	123.8(3)	C70-C69-C68	121.8(3)
N2-C4-N1	113.9(3)	C34-C35-N7	116.6(3)	C70-C69-O6	117.9(3)
N2-C4-C8	125.8(3)	C37-C36-C35	120.0(3)	C68-C69-O6	120.0(3)
N1-C4-C8	120.2(3)	C36-C37-C32	121.3(3)	C71-C70-C69	118.6(3)
N2-C5-C6	130.1(3)	C36-C37-O4	121.9(3)	C70-C71-C72	122.2(3)
N2-C5-C3	110.3(3)	C32-C37-O4	116.6(3)	C70-C71-O7	118.1(3)
C6-C5-C3	119.6(3)	O9-C38-N6	120.8(3)	C72-C71-O7	119.5(3)
C7-C6-C5	117.9(3)	O9-C38-C39	122.8(3)	C71-C72-C73	117.3(3)
C6-C7-O2	120.5(3)	N6-C38-C39	116.4(3)	C71-C72-C86	120.5(3)
C6-C7-C1	121.4(3)	C40-C39-C38	114.9(3)	C73-C72-C86	122.2(3)
O2-C7-C1	118.1(3)	O10-C41-N7	123.6(3)	C68-C73-C72	122.8(3)
C12-C8-C9	118.1(3)	O10-C41-C42	122.4(3)	O7-C74-C75	120.1(3)
C12-C8-C4	121.1(3)	N7-C41-C42	114.0(3)	O7-C74-C79	120.1(3)
C9-C8-C4	120.7(3)	C43-C42-C41	111.2(3)	C75-C74-C79	119.5(3)
C10-C9-C8	119.3(3)	C47-C44-C30	110.2(3)	C74-C75-C76	121.5(3)
N4-C10-C9	122.9(3)	C47-C44-C45	113.2(2)	C75-C76-C77	118.6(3)
N4-C10-C13	116.2(3)	C30-C44-C45	113.3(3)	C75-C76-N10	118.1(3)
C9-C10-C13	120.7(3)	C46-C45-C44	113.0(3)	C77-C76-N10	123.3(3)
N4-C11-C12	122.9(3)	C48-C47-C52	116.6(3)	C78-C77-C76	119.9(3)
N4-C11-C18	116.7(3)	C48-C47-C44	121.0(3)	C78-C77-N11	120.9(3)
C12-C11-C18	120.3(3)	C52-C47-C44	122.4(3)	C76-C77-N11	119.1(3)
C8-C12-C11	118.9(3)	C47-C48-O4	119.0(3)	C77-C78-C79	121.2(3)
N3-C13-C14	122.9(3)	C47-C48-C49	122.2(3)	O8-C79-C78	121.5(3)
N3-C13-C10	116.0(3)	O4-C48-C49	118.3(3)	O8-C79-C74	118.9(3)
C14-C13-C10	121.1(3)	C50-C49-C48	118.7(3)	C78-C79-C74	119.2(3)
C15-C14-C13	118.5(4)	C49-C50-C51	121.8(3)	O13-C80-N10	122.4(4)
C16-C15-C14	119.5(4)	C49-C50-O5	119.6(3)	O13-C80-C81	121.4(4)
C15-C16-C17	118.5(4)	C51-C50-O5	118.3(3)	N10-C80-C81	116.1(3)
N3-C17-C16	123.8(4)	C52-C51-C50	117.5(3)	C80-C81-C82'	113.2(10)
N5-C18-C19	123.1(4)	C52-C51-C65	123.3(3)	C80-C81-C82	111.6(7)
N5-C18-C11	116.9(4)	C50-C51-C65	119.2(3)	O14-C83-N11	122.3(3)
C19-C18-C11	119.8(4)	C51-C52-C47	123.2(3)	O14-C83-C84	122.4(3)
C20-C19-C18	117.8(5)	O5-C53-C58	119.7(3)	N11-C83-C84	115.3(4)
C19-C20-C21	118.5(6)	O5-C53-C54	120.9(3)	C85-C84-C83	120.4(4)
C22-C21-C20	118.0(5)	C58-C53-C54	119.2(3)	C89-C86-C87	113.3(3)
N5-C22-C21	125.5(5)	C55-C54-C53	120.1(3)	C89-C86-C72	109.6(2)
C26-C23-C93	111.2(3)	C54-C55-C56	120.7(3)	C87-C86-C72	113.7(2)
C26-C23-C24	112.3(3)	C54-C55-N8	116.5(3)	C88-C87-C86	113.1(3)
C93-C23-C24	113.8(3)	C56-C55-N8	122.8(3)	C90-C89-C94	116.6(3)
C25-C24-C23	111.9(3)	C55-C56-C57	118.6(3)	C90-C89-C86	121.0(3)
C31-C26-C27	116.8(3)	C55-C56-N9	119.7(3)	C94-C89-C86	122.4(3)
C31-C26-C23	122.5(3)	C57-C56-N9	121.6(3)	C91-C90-O8	119.0(3)
C27-C26-C23	120.8(3)	C58-C57-C56	121.0(3)	C91-C90-C89	121.6(3)
C28-C27-C26	121.4(3)	C57-C58-C53	120.3(3)	O8-C90-C89	119.0(3)
C28-C27-O2	118.1(3)	C57-C58-O6	121.0(3)	C92-C91-C90	119.6(3)
C26-C27-O2	120.5(3)	C53-C58-O6	118.4(3)	C91-C92-C93	122.4(3)
C29-C28-C27	119.9(3)	O11-C59-N8	123.5(3)	C91-C92-O1	119.2(3)
C28-C29-C30	121.3(3)	O11-C59-C60	121.6(3)	C93-C92-O1	118.3(3)
C28-C29-O3	117.9(3)	N8-C59-C60	114.9(3)	C94-C93-C92	116.5(3)
C30-C29-O3	120.8(2)	C59-C60-C61	110.9(4)	C94-C93-C23	122.0(3)
C29-C30-C31	116.8(3)	O12-C62-N9	123.6(4)	C92-C93-C23	121.4(3)
C29-C30-C44	120.9(3)	O12-C62-C63	122.5(4)	C93-C94-C89	123.2(3)
C31-C30-C44	122.3(3)	N9-C62-C63	113.9(4)	C4-N1-C3	105.9(3)
C26-C31-C30	123.6(3)	C62-C63-C64'	120.1(7)	C4-N2-C5	104.2(3)
C33-C32-O3	120.8(3)	C62-C63-C64	107.3(7)	C17-N3-C13	116.8(3)
C33-C32-C37	118.5(3)	C68-C65-C51	109.1(2)	C10-N4-C11	117.8(3)

Angles (part 4)		Angles (part 5)		Angles (part 6)	
C22-N5-C18	117.1(4)	C32-O3-C29	111.1(2)	Cl2D-C1D-Cl1D	103.9(10)
C38-N6-C34	121.3(3)	C48-O4-C37	118.2(2)	Cl2R-C1R-Cl1R	114.4(6)
C41-N7-C35	128.7(3)	C53-O5-C50	117.5(2)	Cl2T-C1T-Cl1T	115.0(7)
C59-N8-C55	126.6(3)	C58-O6-C69	116.2(2)	Cl2U-C1U-Cl1U	116.3(8)
C62-N9-C56	127.1(3)	C74-O7-C71	116.4(2)	Cl1W-C1W-Cl2W	108.7(8)
C80-N10-C76	125.1(3)	C79-O8-C90	118.2(2)	Cl1X-C1X-Cl2X	114.8(5)
C83-N11-C77	127.0(3)	Cl1B-C1B-Cl2B	111.1(8)	C1X-Cl2X-Cl2X#1	147.7(5)
C1-O1-C92	113.3(2)	Cl2A-C1A-Cl1A	109.8(6)	Cl2Y-C1Y-Cl1Y	106.1(7)
C27-O2-C7	111.1(2)	Cl2C-C1C-Cl1C	102.0(10)		
Symmetry transformations used to generate equivalent atoms: #1 -x+3, -y+2, -z+1					

Torsion angles [°]

Part 1		Part 2		Part 3	
O1-C1-C2-C3	-178.5(3)	C26-C27-C28-C29	5.5(5)	C48-C47-C52-C51	3.3(4)
C7-C1-C2-C3	3.1(4)	O2-C27-C28-C29	-173.5(3)	C44-C47-C52-C51	-174.3(3)
C1-C2-C3-N1	176.6(3)	C27-C28-C29-C30	-4.5(5)	O5-C53-C54-C55	174.2(3)
C1-C2-C3-C5	-2.6(5)	C27-C28-C29-O3	174.9(3)	C58-C53-C54-C55	0.2(4)
C2-C3-C5-N2	178.6(3)	C28-C29-C30-C31	1.0(5)	C53-C54-C55-C56	-1.7(4)
N1-C3-C5-N2	-0.8(3)	O3-C29-C30-C31	-178.5(3)	C53-C54-C55-N8	176.8(3)
C2-C3-C5-C6	-0.1(5)	C28-C29-C30-C44	179.1(3)	C54-C55-C56-C57	1.2(5)
N1-C3-C5-C6	-179.5(3)	O3-C29-C30-C44	-0.4(5)	N8-C55-C56-C57	-177.2(3)
N2-C5-C6-C7	-176.2(3)	C27-C26-C31-C30	-0.8(5)	C54-C55-C56-N9	-174.9(3)
C3-C5-C6-C7	2.2(4)	C23-C26-C31-C30	-179.8(3)	N8-C55-C56-N9	6.7(5)
C5-C6-C7-O2	177.9(3)	C29-C30-C31-C26	1.7(5)	C55-C56-C57-C58	0.9(5)
C5-C6-C7-C1	-1.7(4)	C44-C30-C31-C26	-176.4(3)	N9-C56-C57-C58	176.9(3)
C2-C1-C7-C6	-1.0(4)	O3-C32-C33-C34	-176.5(3)	C56-C57-C58-C53	-2.4(4)
O1-C1-C7-C6	-179.5(3)	C37-C32-C33-C34	3.4(4)	C56-C57-C58-O6	-176.6(3)
C2-C1-C7-O2	179.4(3)	C32-C33-C34-C35	-2.7(5)	O5-C53-C58-C57	-172.3(3)
O1-C1-C7-O2	0.9(4)	C32-C33-C34-N6	178.8(3)	C54-C53-C58-C57	1.8(4)
N2-C4-C8-C12	20.9(5)	C33-C34-C35-C36	0.0(5)	O5-C53-C58-O6	2.1(4)
N1-C4-C8-C12	-162.5(3)	N6-C34-C35-C36	178.6(3)	C54-C53-C58-O6	176.2(2)
N2-C4-C8-C9	-155.2(3)	C33-C34-C35-N7	-178.7(3)	O11-C59-C60-C61	43.6(6)
N1-C4-C8-C9	21.5(4)	N6-C34-C35-N7	-0.2(4)	N8-C59-C60-C61	-136.6(5)
C12-C8-C9-C10	-1.7(5)	C34-C35-C36-C37	1.8(5)	O12-C62-C63-C64'	138.5(9)
C4-C8-C9-C10	174.5(3)	N7-C35-C36-C37	-179.5(3)	N9-C62-C63-C64'	-41.3(9)
C8-C9-C10-N4	1.5(5)	C35-C36-C37-C32	-1.0(5)	O12-C62-C63-C64	98.2(9)
C8-C9-C10-C13	-173.5(3)	C35-C36-C37-O4	-175.8(3)	N9-C62-C63-C64	-81.6(9)
C9-C8-C12-C11	1.2(5)	C33-C32-C37-C36	-1.5(5)	C52-C51-C65-C68	89.5(3)
C4-C8-C12-C11	-175.0(3)	O3-C32-C37-C36	178.4(3)	C50-C51-C65-C68	-90.0(3)
N4-C11-C12-C8	-0.5(5)	C33-C32-C37-O4	173.5(3)	C52-C51-C65-C66	-38.4(4)
C18-C11-C12-C8	176.8(3)	O3-C32-C37-O4	-6.6(4)	C50-C51-C65-C66	142.2(3)
N4-C10-C13-N3	-177.9(3)	O9-C38-C39-C40	-2.4(6)	C68-C65-C66-C67	174.1(3)
C9-C10-C13-N3	-2.5(5)	N6-C38-C39-C40	176.3(4)	C51-C65-C66-C67	-60.5(4)
N4-C10-C13-C14	0.4(5)	O10-C41-C42-C43	68.7(5)	C51-C65-C68-C73	-84.6(3)
C9-C10-C13-C14	175.8(3)	N7-C41-C42-C43	-109.2(4)	C66-C65-C68-C73	43.0(4)
N3-C13-C14-C15	-1.6(5)	C29-C30-C44-C47	-97.5(4)	C51-C65-C68-C69	94.2(3)
C10-C13-C14-C15	-179.7(3)	C31-C30-C44-C47	80.5(4)	C66-C65-C68-C69	-138.2(3)
C13-C14-C15-C16	1.0(6)	C29-C30-C44-C45	134.4(3)	C73-C68-C69-C70	-1.3(4)
C14-C15-C16-C17	-0.1(6)	C31-C30-C44-C45	-47.6(4)	C65-C68-C69-C70	179.8(2)
C15-C16-C17-N3	-0.4(6)	C47-C44-C45-C46	169.8(3)	C73-C68-C69-O6	-175.1(2)
N4-C11-C18-N5	-166.1(3)	C30-C44-C45-C46	-63.7(4)	C65-C68-C69-O6	6.1(4)
C12-C11-C18-N5	16.4(5)	C30-C44-C47-C48	88.4(3)	C68-C69-C70-C71	1.4(4)
N4-C11-C18-C19	17.8(5)	C45-C44-C47-C48	-143.5(3)	O6-C69-C70-C71	175.3(2)
C12-C11-C18-C19	-159.6(4)	C30-C44-C47-C52	-94.0(3)	C69-C70-C71-C72	-1.2(4)
N5-C18-C19-C20	-1.7(7)	C45-C44-C47-C52	34.0(4)	C69-C70-C71-O7	-176.1(2)
C11-C18-C19-C20	174.1(4)	C52-C47-C48-O4	-175.1(2)	C70-C71-C72-C73	0.9(4)
C18-C19-C20-C21	3.3(8)	C44-C47-C48-O4	2.6(4)	O7-C71-C72-C73	175.7(2)
C19-C20-C21-C22	-2.3(9)	C52-C47-C48-C49	-3.5(4)	C70-C71-C72-C86	179.8(3)
C20-C21-C22-N5	-0.6(10)	C44-C47-C48-C49	174.2(3)	O7-C71-C72-C86	-5.5(4)
C26-C23-C24-C25	173.4(3)	C47-C48-C49-C50	1.2(4)	C69-C68-C73-C72	1.1(4)
C93-C23-C24-C25	-59.3(4)	O4-C48-C49-C50	172.8(2)	C65-C68-C73-C72	179.9(3)
C93-C23-C26-C31	-83.8(4)	C48-C49-C50-C51	1.7(4)	C71-C72-C73-C68	-0.9(4)
C24-C23-C26-C31	44.9(4)	C48-C49-C50-O5	-172.5(3)	C86-C72-C73-C68	-179.7(3)
C93-C23-C26-C27	97.3(4)	C49-C50-C51-C52	-1.9(4)	O7-C74-C75-C76	174.5(3)
C24-C23-C26-C27	-134.0(3)	O5-C50-C51-C52	172.4(2)	C79-C74-C75-C76	0.1(5)
C31-C26-C27-C28	-2.9(5)	C49-C50-C51-C65	177.6(2)	C74-C75-C76-C77	1.1(5)
C23-C26-C27-C28	176.1(3)	O5-C50-C51-C65	-8.1(4)	C74-C75-C76-N10	-179.9(3)
C31-C26-C27-O2	176.1(3)	C50-C51-C52-C47	-0.7(4)	C75-C76-C77-C78	-1.9(5)
C23-C26-C27-O2	-4.9(5)	C65-C51-C52-C47	179.8(3)	N10-C76-C77-C78	179.2(3)

Part 4		Part 5		Part 6	
C75-C76-C77-N11	-179.8(3)	C24-C23-C93-C92	139.8(3)	C75-C76-N10-C80	126.9(3)
N10-C76-C77-N11	1.3(5)	C92-C93-C94-C89	-0.8(4)	C77-C76-N10-C80	-54.2(5)
C76-C77-C78-C79	1.4(5)	C23-C93-C94-C89	176.6(3)	O14-C83-N11-C77	-0.2(6)
N11-C77-C78-C79	179.3(3)	C90-C89-C94-C93	0.5(4)	C84-C83-N11-C77	179.8(4)
C77-C78-C79-O8	-173.3(3)	C86-C89-C94-C93	-178.3(3)	C78-C77-N11-C83	48.9(5)
C77-C78-C79-C74	-0.1(5)	N2-C4-N1-C3	-0.6(3)	C76-C77-N11-C83	-133.3(4)
O7-C74-C79-O8	-1.7(5)	C8-C4-N1-C3	-177.7(3)	C2-C1-O1-C92	74.3(4)
C75-C74-C79-O8	172.6(3)	C2-C3-N1-C4	-178.5(3)	C7-C1-O1-C92	-107.3(3)
O7-C74-C79-C78	-175.0(3)	C5-C3-N1-C4	0.8(3)	C91-C92-O1-C1	-79.2(4)
C75-C74-C79-C78	-0.6(5)	N1-C4-N2-C5	0.2(3)	C93-C92-O1-C1	103.9(3)
O13-C80-C81-C82'	71.3(11)	C8-C4-N2-C5	177.0(3)	C28-C27-O2-C7	77.6(4)
N10-C80-C81-C82'	-106.2(10)	C6-C5-N2-C4	178.9(3)	C26-C27-O2-C7	-101.4(3)
O13-C80-C81-C82	95.2(7)	C3-C5-N2-C4	0.4(3)	C6-C7-O2-C27	-76.8(3)
N10-C80-C81-C82	-82.3(6)	C16-C17-N3-C13	-0.1(6)	C1-C7-O2-C27	102.8(3)
O14-C83-C84-C85	169.7(4)	C14-C13-N3-C17	1.1(5)	C33-C32-O3-C29	86.2(3)
N11-C83-C84-C85	-10.4(6)	C10-C13-N3-C17	179.3(3)	C37-C32-O3-C29	-93.7(3)
C71-C72-C86-C89	-93.0(4)	C9-C10-N4-C11	-0.9(5)	C28-C29-O3-C32	-73.5(3)
C73-C72-C86-C89	85.8(3)	C13-C10-N4-C11	174.4(3)	C30-C29-O3-C32	105.9(3)
C71-C72-C86-C87	139.2(3)	C12-C11-N4-C10	0.3(5)	C47-C48-O4-C37	-106.3(3)
C73-C72-C86-C87	-42.1(4)	C18-C11-N4-C10	-177.1(3)	C49-C48-O4-C37	81.8(3)
C89-C86-C87-C88	167.7(3)	C21-C22-N5-C18	2.3(8)	C36-C37-O4-C48	-76.0(4)
C72-C86-C87-C88	-66.4(4)	C19-C18-N5-C22	-1.1(7)	C32-C37-O4-C48	108.9(3)
C87-C86-C89-C90	-140.0(3)	C11-C18-N5-C22	-177.0(4)	C58-C53-O5-C50	-102.3(3)
C72-C86-C89-C90	91.9(3)	O9-C38-N6-C34	12.4(5)	C54-C53-O5-C50	83.7(3)
C87-C86-C89-C94	38.7(4)	C39-C38-N6-C34	-166.4(3)	C49-C50-O5-C53	-72.7(3)
C72-C86-C89-C94	-89.4(3)	C33-C34-N6-C38	101.6(4)	C51-C50-O5-C53	112.9(3)
C94-C89-C90-C91	-1.2(4)	C35-C34-N6-C38	-76.9(4)	C57-C58-O6-C69	-90.9(3)
C86-C89-C90-C91	177.6(3)	O10-C41-N7-C35	-1.1(6)	C53-C58-O6-C69	94.7(3)
C94-C89-C90-O8	-174.3(2)	C42-C41-N7-C35	176.7(3)	C70-C69-O6-C58	76.7(3)
C86-C89-C90-O8	4.5(4)	C36-C35-N7-C41	16.5(5)	C68-C69-O6-C58	-109.3(3)
O8-C90-C91-C92	175.3(3)	C34-C35-N7-C41	-164.8(3)	C75-C74-O7-C71	88.8(4)
C89-C90-C91-C92	2.2(5)	O11-C59-N8-C55	8.6(6)	C79-C74-O7-C71	-96.9(3)
C90-C91-C92-C93	-2.5(5)	C60-C59-N8-C55	-171.2(4)	C70-C71-O7-C74	-75.8(3)
C90-C91-C92-O1	-179.4(3)	C54-C55-N8-C59	124.6(4)	C72-C71-O7-C74	109.2(3)
C91-C92-C93-C94	1.8(4)	C56-C55-N8-C59	-56.9(5)	C78-C79-O8-C90	-86.6(4)
O1-C92-C93-C94	178.7(3)	O12-C62-N9-C56	1.1(6)	C74-C79-O8-C90	100.3(3)
C91-C92-C93-C23	-175.6(3)	C63-C62-N9-C56	-179.1(3)	C91-C90-O8-C79	78.6(4)
O1-C92-C93-C23	1.2(4)	C55-C56-N9-C62	-144.5(3)	C89-C90-O8-C79	-108.2(3)
C26-C23-C93-C94	90.4(3)	C57-C56-N9-C62	39.5(5)	Cl1X-C1X-Cl2X-Cl2X#1	-166.7(6)
C24-C23-C93-C94	-37.5(4)	O13-C80-N10-C76	6.6(5)		
C26-C23-C93-C92	-92.3(3)	C81-C80-N10-C76	-175.9(3)		

Symmetry transformations used to generate equivalent atoms: #1 -x+3, -y+2, -z+1

Table 8. Crystal data and structure refinement for the metallocavitand Ru^{III}•Cl_3•**C24** (**C25**).

Empirical formula	$C_{586}\ H_{580}\ C_{118}\ N_{66}\ O_{100.20}\ Ru_6$	
Formula weight	11394.85	
Temperature	100(2) K	
Wavelength	0.71073 Å	
Crystal system	Orthorhombic	
Space group	Pbcn	
Unit cell dimensions	a = 67.017(3)Å	a = 90°.
	b = 31.4138(15)Å	b = 90°.
	c = 32.1376(17)Å	g = 90°.
Volume	67658(6) $Å^3$	
Z	4	
Density (calculated)	1.119 Mg/m^3	
Absorption coefficient	0.270 mm^{-1}	
F(000)	23718	
Crystal size	0.12 x 0.12 x 0.08 mm^3	
Theta range for data collection	0.716 to 24.850°.	
Index ranges	-78<=h<=66,-30<=k<=37,-25<=l<=37	
Reflections collected	242108	
Independent reflections	58142[R(int) = 0.0735]	
Completeness to theta =24.850°	99.2%	
Absorption correction	Empirical	
Max. and min. transmission	0.979 and 0.818	
Refinement method	Full-matrix least-squares on F^2	
Data / restraints / parameters	58142/ 7870/ 4163	
Goodness-of-fit on F^2	1.306	
Final R indices [I>2sigma(I)]	R1 = 0.1203, wR2 = 0.3444	
R indices (all data)	R1 = 0.1581, wR2 = 0.3671	
Largest diff. peak and hole	2.135 and -1.077 e.$Å^{-3}$	

Bond lengths [Å] and angles [°]

Bond lengths (part 1)		Bond lengths (part 2)		Bond lengths (part 3)		Bond lengths (part 4)	
Ru1A-N4A	1.976(6)	C18A-C19A	1.392(10)	N7A-C41A	1.363(9)	C53A-C54A	1.341(10)
Ru1A-N5A	2.044(6)	C19A-C20A	1.393(10)	O10A-C41A	1.212(9)	C53A-C58A	1.376(10)
Ru1A-N3A	2.080(6)	C20A-C21A	1.412(11)	C41A-C42A	1.546(9)	C53A-O4A	1.392(8)
Ru1A-Cl3A	2.336(2)	C21A-C22A	1.374(11)	C42A-C43A	1.540(9)	C54A-C55A	1.397(10)
Ru1A-Cl1A	2.3482(19)	C22A-N5A	1.364(9)	O2A'-C32'	1.24(3)	C55A-C56A	1.392(10)
Ru1A-Cl2A	2.3694(18)	C23A-C26A	1.525(10)	O3A'-C37'	1.36(3)	C55A-N8A	1.413(9)
C1A-O8A	1.380(5)	C23A-C24A	1.527(9)	O3A'-C48A	1.415(15)	C56A-C57A	1.363(11)
C1A-C2A	1.3900	C23A-C93A	1.531(10)	C32'-C37'	1.38(3)	C56A-N9A	1.438(10)
C1A-C6A	1.3900	C24A-C25A	1.535(10)	C32'-C33'	1.40(3)	C57A-C58A	1.387(10)
C2A-C3A	1.3900	C26A-C27A	1.379(10)	C33'-C34'	1.31(3)	C58A-O5A	1.389(9)
C3A-N1A	1.331(6)	C26A-C31A	1.401(10)	C34'-N6A'	1.410(9)	C59A-O11A	1.204(7)
C3A-C4A	1.3900	C27A-O1A	1.377(8)	C34'-C35'	1.41(2)	C59A-N8A	1.355(6)
C4A-N2A	1.357(6)	C27A-C28A	1.405(10)	C35'-C36'	1.38(2)	C59A-C60A	1.503(7)
C4A-C5A	1.3900	C28A-C29A	1.349(10)	C35'-N7A'	1.415(9)	C60A-C61A	1.534(7)
C5A-C6A	1.3900	C29A-C30A	1.398(10)	C36'-C37'	1.45(3)	C62A-O12A	1.228(7)
C6A-O1A	1.399(6)	C29A-O2A'	1.415(18)	N6A'-C38'	1.356(9)	C62A-N9A	1.367(6)
C7A-N2A	1.364(9)	C29A-O2A	1.42(2)	O9A'-C38'	1.224(9)	C62A-C63A	1.510(7)
C7A-N1A	1.370(9)	C30A-C31A	1.381(10)	C38'-C39'	1.525(9)	C63A-C64A	1.536(7)
C7A-C8A	1.466(10)	C30A-C44A	1.561(10)	C39'-C40'	1.525(10)	C65A-C68A	1.538(10)
C8A-C9A	1.384(10)	O2A-C32A	1.58(4)	N7A'-C41'	1.350(9)	C65A-C66A	1.540(10)
C8A-C12A	1.397(10)	O3A-C48A	1.40(2)	O10'-C41'	1.212(8)	C66A-C67A	1.433(14)
C9A-C10A	1.344(10)	O3A-C37A	1.53(4)	C41'-C42'	1.511(9)	C68A-C69A	1.361(10)
C10A-N4A	1.367(9)	C32A-C37A	1.34(4)	C42'-C43'	1.533(8)	C68A-C73A	1.415(10)
C10A-C13A	1.469(10)	C32A-C33A	1.51(4)	C44A-C47A	1.527(10)	C69A-O5A	1.403(9)
C11A-N4A	1.326(9)	C33A-C34A	1.50(4)	C44A-C45A	1.536(10)	C69A-C70A	1.408(10)
C11A-C12A	1.358(10)	C34A-C35A	1.36(4)	C45A-C46A	1.533(10)	C70A-C71A	1.357(10)
C11A-C18A	1.495(10)	C34A-N6A	1.412(10)	C47A-C52A	1.393(10)	C71A-C72A	1.358(10)
C13A-N3A	1.389(9)	C35A-N7A	1.417(10)	C47A-C48A	1.407(10)	C71A-O6A	1.416(8)
C13A-C14A	1.403(10)	C35A-C36A	1.47(4)	C48A-C49A	1.374(10)	C72A-C73A	1.396(10)
C14A-C15A	1.348(11)	C36A-C37A	1.33(4)	C49A-C50A	1.358(10)	C72A-C86A	1.519(10)
C15A-C16A	1.418(11)	N6A-C38A	1.346(9)	C50A-C51A	1.423(10)	C74A-C79A	1.368(10)
C16A-C17A	1.364(11)	O9A-C38A	1.200(9)	C50A-O4A	1.424(8)	C74A-C75A	1.387(10)
C17A-N3A	1.301(10)	C38A-C39A	1.518(9)	C51A-C52A	1.377(9)	C74A-O6A	1.415(8)
C18A-N5A	1.348(9)	C39A-C40A	1.536(10)	C51A-C65A	1.499(10)	C75A-C76A	1.412(10)

Bond lengths (part 5)		Bond lengths (part 6)		Bond lengths (part 7)		Bond lengths (part 8)	
C76A-C77A	1.371(10)	C27B-O2B	1.447(9)	C59"-O11"	1.211(5)	C10C-N4C	1.348(8)
C76A-N10A	1.428(7)	C28B-C29B	1.363(11)	C59"-N8B"	1.352(4)	C10C-C13C	1.485(10)
C77A-C78A	1.420(10)	C29B-O3B	1.410(10)	C59"-C60"	1.519(3)	C11C-N4C	1.342(8)
C77A-N11A	1.423(6)	C29B-C30B	1.412(11)	C60"-C61"	1.544(3)	C11C-C12C	1.401(9)
C78A-C79A	1.361(10)	C30B-C31B	1.407(11)	C62"-O12"	1.205(5)	C11C-C18C	1.461(9)
C79A-O7A	1.403(8)	C30B-C44B	1.488(10)	C62"-N9B"	1.360(4)	C13C-N3C	1.340(10)
C80A-O13A	1.236(7)	C32B-C37B	1.337(11)	C62"-C63"	1.539(4)	C13C-C14C	1.364(10)
C80A-N10A	1.348(7)	C32B-C33B	1.373(12)	C63"-C64"	1.539(4)	C14C-C15C	1.383(12)
C80A-C81A	1.504(7)	C32B-O3B	1.411(10)	O6B"-C69B	1.419(11)	C15C-C16C	1.359(14)
C81A-C82A	1.515(8)	C33B-C34B	1.379(13)	C65B-C66B	1.526(10)	C16C-C17C	1.370(12)
C83A-O14A	1.217(6)	C34B-C35B	1.387(12)	C65B-C68B	1.536(11)	C17C-N3C	1.331(10)
C83A-N11A	1.351(6)	C34B-N6B	1.416(8)	C66B-C67B	1.521(12)	C18C-C19C	1.360(9)
C83A-C84A	1.531(7)	C35B-C36B	1.366(12)	C68B-C73B	1.384(10)	C18C-N5C	1.380(8)
C84A-C85A	1.530(7)	C35B-N7B	1.411(9)	C68B-C69B	1.400(10)	C19C-C20C	1.378(10)
C86A-C89A	1.492(10)	C35B-N7B"	1.465(16)	C69B-C70B	1.326(11)	C20C-C21C	1.374(10)
C86A-C87A	1.549(9)	C36B-C37B	1.442(12)	C70B-C71B	1.398(10)	C21C-C22C	1.393(10)
C87A-C88A	1.437(12)	C37B-O4B	1.379(10)	C71B-C72B	1.365(10)	C22C-N5C	1.324(9)
C89A-C90A	1.368(9)	N6B-C38B	1.352(7)	C71B-O7B	1.402(9)	C23C-C24C	1.508(9)
C89A-C94A	1.422(10)	C38B-O9B	1.227(7)	C72B-C73B	1.367(10)	C23C-C93C	1.537(10)
C90A-O7A	1.414(9)	C38B-C39B	1.506(8)	C72B-C86B	1.518(10)	C23C-C26C	1.553(10)
C90A-C91A	1.416(10)	C39B-C40B	1.513(8)	C74B-C79B	1.3215	C24C-C25*	1.532(5)
C91A-C92A	1.369(10)	N7B"-C41"	1.358(9)	C74B-C75B	1.3911	C24C-C25C	1.535(5)
C92A-O8A	1.374(8)	O10"-C41"	1.208(9)	C74B-O7B	1.403(4)	C26C-C31C	1.379(9)
C92A-C93A	1.389(9)	C41"-C42"	1.526(9)	C75B-C76B	1.4414	C26C-C27C	1.384(10)
C93A-C94A	1.391(10)	C42"-C43"	1.550(9)	C76B-C77B	1.3883	C27C-O2C	1.400(8)
Ru1B-N4B	1.961(5)	N7B-C41B	1.358(9)	C76B-N10B	1.4295	C27C-C28C	1.402(11)
Ru1B-N5B	2.057(5)	O10B-C41B	1.205(9)	C77B-N11B	1.402(4)	C28C-C29C	1.361(10)
Ru1B-N3B	2.077(5)	C41B-C42B	1.520(9)	C77B-C78B	1.4241	C29C-C30C	1.383(10)
Ru1B-Cl3B	2.3305(18)	C42B-C43B	1.530(9)	C78B-C79B	1.3945	C29C-O3C	1.426(9)
Ru1B-Cl1B	2.3456(18)	C44B-C45B	1.544(10)	C79B-O8B	1.432(4)	C30C-C31C	1.379(10)
Ru1B-Cl2B	2.3870(18)	C44B-C47B	1.547(10)	C80B-O13B	1.218(5)	C30C-C44C	1.510(9)
C1B-C2B	1.370(10)	C45B-C46B	1.521(10)	C80B-N10B	1.3466	C32C-O3C	1.360(9)
C1B-O1B	1.372(9)	C47B-C48B	1.392(10)	C80B-C81B	1.5184	C32C-C37C	1.390(9)
C1B-C6B	1.460(11)	C47B-C52B	1.402(10)	C81B-C82B	1.5448	C32C-C33C	1.391(10)
C2B-C3B	1.395(10)	C48B-C49B	1.367(10)	C83B-O14B	1.207(4)	C33C-C34C	1.356(11)
C3B-N1B	1.346(8)	C48B-O4B	1.389(9)	C83B-N11B	1.351(4)	C34C-C35C	1.361(10)
C3B-C4B	1.411(11)	C49B-C50B	1.390(11)	C83B-C84B	1.5354	C34C-N6C	1.405(7)
C4B-N2B	1.364(9)	C50B-O5B	1.354(14)	C84B-C85B	1.5425	C35C-C36C	1.407(10)
C4B-C5B	1.430(10)	C50B-O5B"	1.400(13)	O8B-C90B	1.389(9)	C35C-N7C	1.423(7)
C5B-C6B	1.357(11)	C50B-C51B	1.402(10)	C86B-C89B	1.499(11)	C36C-C37C	1.354(10)
C6B-O2B	1.397(8)	C51B-C52B	1.412(10)	C86B-C87B	1.573(10)	C37C-O4C	1.401(8)
C7B-N2B	1.302(9)	C51B-C65B	1.527(11)	C87B-C88B	1.509(12)	C38C-O9C	1.222(7)
C7B-N1B	1.379(9)	C53B-C58B	1.325(4)	C89B-C90B	1.393(10)	C38C-N6C	1.340(7)
C7B-C8B	1.444(9)	C53B-C54B	1.393(4)	C89B-C94B	1.437(11)	C38C-C39C	1.520(8)
C8B-C12B	1.401(10)	C53B-O5B	1.403(5)	C90B-C91B	1.396(11)	C39C-C40C	1.515(8)
C8B-C9B	1.420(9)	C54B-C55B	1.440(4)	C91B-C92B	1.355(11)	C41C-O10C	1.220(7)
C9B-C10B	1.388(9)	C55B-C56B	1.390(4)	C92B-C93B	1.350(10)	C41C-N7C	1.359(7)
C10B-N4B	1.328(8)	C55B-N8B	1.408(4)	C92B-O1B	1.418(9)	C41C-C42*	1.36(2)
C10B-C13B	1.481(9)	C56B-N9B	1.402(5)	C93B-C94B	1.387(10)	C41C-C42C	1.510(9)
C11B-N4B	1.339(8)	C56B-C57B	1.421(4)	Ru1C-N4C	1.968(6)	C42C-C43C	1.516(8)
C11B-C12B	1.373(9)	C57B-C58B	1.393(4)	Ru1C-N5C	2.059(5)	C42*-C43*	1.508(12)
C11B-C18B	1.479(9)	C58B-O6B	1.429(5)	Ru1C-N3C	2.065(6)	C44C-C47C	1.505(9)
C13B-N3B	1.349(8)	C59B-O11B	1.213(5)	Ru1C-Cl3C	2.331(2)	C44C-C45C	1.561(10)
C13B-C14B	1.408(9)	C59B-N8B	1.352(4)	Ru1C-Cl1C	2.352(2)	C45C-C46C	1.529(10)
C14B-C15B	1.373(9)	C59B-C60B	1.522(4)	Ru1C-Cl2C	2.384(2)	C47C-C52C	1.400(9)
C15B-C16B	1.383(10)	C60B-C61B	1.545(4)	C1C-C6C	1.335(10)	C47C-C48C	1.404(9)
C16B-C17B	1.384(10)	C62B-O12B	1.212(5)	C1C-C2C	1.410(10)	C48C-C49C	1.371(9)
C17B-N3B	1.323(8)	C62B-N9B	1.363(4)	C1C-O1C	1.414(9)	C48C-O4C	1.411(8)
C18B-N5B	1.370(8)	C62B-C63B	1.542(4)	C2C-C3C	1.411(10)	C49C-C50C	1.366(9)
C18B-C19B	1.398(9)	C63B-C64B	1.541(3)	C3C-N1C	1.379(9)	C50C-C51C	1.396(10)
C19B-C20B	1.398(10)	O6B-C69B	1.443(12)	C3C-C4C	1.381(10)	C50C-O5C	1.407(7)
C20B-C21B	1.392(10)	C53"-C58"	1.324(4)	C4C-C5C	1.390(10)	C51C-C52C	1.370(9)
C21B-C22B	1.394(10)	C53"-C54"	1.392(4)	C4C-N2C	1.402(9)	C51C-C65C	1.562(9)
C22B-N5B	1.345(9)	C53"-O5B"	1.404(5)	C5C-C6C	1.392(10)	C53C-O5C	1.369(8)
C23B-C93B	1.529(11)	C54"-C55"	1.441(4)	C6C-O2C	1.417(8)	C53C-C54C	1.388(10)
C23B-C24B	1.546(10)	C55"-C56"	1.387(4)	C7C-N2C	1.307(9)	C53C-C58C	1.411(10)
C23B-C26B	1.558(12)	C55"-N8B"	1.409(4)	C7C-N1C	1.384(9)	C54C-C55C	1.351(11)
C24B-C25B	1.555(14)	C56"-N9B"	1.408(5)	C7C-C8C	1.472(10)	C55C-C56C	1.385(12)
C26B-C31B	1.354(10)	C56"-C57"	1.420(4)	C8C-C12C	1.388(9)	C55C-N8C	1.461(10)
C26B-C27B	1.416(11)	C57"-C58"	1.393(4)	C8C-C9C	1.390(9)	C56C-N9C	1.390(10)
C27B-C28B	1.348(12)	C58"-O6B"	1.428(5)	C9C-C10C	1.380(9)	C56C-C57C	1.400(12)

Bond lengths (part 9)		Bond lengths (part 10)		Bond lengths (part 11)		Bond lengths (part 12)	
C57C-C58C	1.377(10)	C69C-C70C	1.361(9)	O13*-C80*	1.198(18)	O1T-C1T	1.438(8)
C58C-O6C	1.362(9)	C69C-O6C	1.436(8)	C80*-C81*	1.513(19)	C1T-C2T	1.517(9)
N8C-C59*	1.373(7)	C70C-C71C	1.395(10)	C81*-C82*	1.45(2)	O1U-C1U	1.412(9)
N8C-C59C	1.381(7)	C71C-C72C	1.356(10)	C83C-O14C	1.227(6)	C1U-C2U	1.506(9)
O11C-C59C	1.219(9)	C71C-O7C	1.428(8)	C83C-N11C	1.349(7)	O1V-C1V	1.423(9)
C59C-C60C	1.527(9)	C72C-C73C	1.395(10)	C83C-C84C	1.490(7)	C1V-C2V	1.525(9)
C60C-C61C	1.562(9)	C72C-C86C	1.521(10)	C84C-C85*	1.505(9)	O1N-C1N'	1.394(9)
O11*-C59*	1.206(9)	C74C-C75C	1.371(11)	C84C-C85C	1.516(6)	O1N-C1N	1.415(9)
C59*-C60*	1.519(9)	C74C-C79C	1.402(11)	C86C-C89C	1.514(10)	C1N-C2N	1.519(9)
C60*-C61*	1.561(10)	C74C-O7C	1.417(9)	C86C-C87C	1.551(10)	C1N'-C2N'	1.515(9)
N9C-C62C	1.380(7)	C75C-C76C	1.410(11)	C87C-C88C	1.475(11)	O1X-C1X	1.410(9)
N9C-C62*	1.419(9)	C76C-C77C	1.373(10)	C89C-C94C	1.351(10)	C1X-C2X	1.534(9)
O12C-C62C	1.221(9)	C76C-N10C	1.420(8)	C89C-C90C	1.434(10)	O1Y-C1Y	1.421(10)
C62C-C63C	1.544(9)	C76C-N10*	1.426(14)	C90C-C91C	1.374(10)	C1Y-C2Y	1.539(10)
C63C-C64C	1.557(9)	C77C-N11C	1.429(7)	C90C-O8C	1.385(9)	O1Z-C1Z	1.448(10)
O12*-C62*	1.217(9)	C77C-C78C	1.435(11)	C91C-C92C	1.358(10)	C1Z-C2Z	1.529(10)
C62*-C63*	1.533(9)	C78C-C79C	1.367(10)	C92C-O1C	1.409(9)	O1Z'-C1Z'	1.418(10)
C63*-C64*	1.536(10)	C79C-O8C	1.368(9)	C92C-C93C	1.414(10)	C1Z'-C2Z'	1.534(10)
C65C-C68C	1.527(9)	N10C-C80C	1.346(9)	C93C-C94C	1.403(10)	O1M-C1M	1.422(9)
C65C-C66C	1.542(10)	O13C-C80C	1.213(9)	O1R-C1R	1.433(10)	C1M-C2M	1.524(10)
C66C-C67C	1.505(10)	C80C-C81C	1.521(9)	C1R-C2R	1.524(10)		
C68C-C73C	1.377(10)	C81C-C82C	1.542(9)	O1S-C1S	1.422(9)		
C68C-C69C	1.388(9)	N10*-C80*	1.35(2)	C1S-C2S	1.516(9)		

Angles (part 1)		Angles (part 2)		Angles (part 3)	
N4A-Ru1A-N5A	79.3(2)	C14A-C13A-C10A	125.5(6)	C36A-C37A-C32A	119(3)
N4A-Ru1A-N3A	80.9(2)	C15A-C14A-C13A	122.1(7)	C36A-C37A-O3A	126(3)
N5A-Ru1A-N3A	159.9(2)	C14A-C15A-C16A	117.7(8)	C32A-C37A-O3A	115(3)
N4A-Ru1A-Cl3A	84.76(17)	C17A-C16A-C15A	118.2(8)	C38A-N6A-C34A	122(2)
N5A-Ru1A-Cl3A	89.65(18)	N3A-C17A-C16A	124.2(8)	O9A-C38A-N6A	121.9(13)
N3A-Ru1A-Cl3A	91.96(18)	N5A-C18A-C19A	123.2(7)	O9A-C38A-C39A	122.2(13)
N4A-Ru1A-Cl1A	89.90(17)	N5A-C18A-C11A	114.9(6)	N6A-C38A-C39A	115.9(10)
N5A-Ru1A-Cl1A	88.86(17)	C19A-C18A-C11A	121.9(7)	C38A-C39A-C40A	113.1(9)
N3A-Ru1A-Cl1A	87.68(17)	C18A-C19A-C20A	118.4(7)	C41A-N7A-C35A	131.1(18)
Cl3A-Ru1A-Cl1A	174.64(7)	C19A-C20A-C21A	118.7(7)	O10A-C41A-N7A	117.5(17)
N4A-Ru1A-Cl2A	178.18(18)	C22A-C21A-C20A	119.2(7)	O10A-C41A-C42A	129.3(17)
N5A-Ru1A-Cl2A	100.94(17)	N5A-C22A-C21A	122.3(7)	N7A-C41A-C42A	112.5(9)
N3A-Ru1A-Cl2A	98.97(17)	C26A-C23A-C24A	113.0(6)	C43A-C42A-C41A	110.2(8)
Cl3A-Ru1A-Cl2A	93.42(7)	C26A-C23A-C93A	110.6(6)	C32'-O2A'-C29A	133.9(14)
Cl1A-Ru1A-Cl2A	91.92(7)	C24A-C23A-C93A	113.1(6)	C37'-O3A'-C48A	121.5(13)
O8A-C1A-C2A	121.3(3)	C23A-C24A-C25A	109.6(6)	O2A'-C32'-C37'	120.2(19)
O8A-C1A-C6A	118.7(3)	C27A-C26A-C31A	117.8(7)	O2A'-C32'-C33'	128.4(17)
C2A-C1A-C6A	120.0	C27A-C26A-C23A	122.0(6)	C37'-C32'-C33'	111.3(18)
C3A-C2A-C1A	120.0	C31A-C26A-C23A	120.0(6)	C34'-C33'-C32'	128.6(17)
N1A-C3A-C4A	107.6(4)	O1A-C27A-C26A	119.7(7)	C33'-C34'-N6A'	118.7(17)
N1A-C3A-C2A	132.3(4)	O1A-C27A-C28A	120.1(6)	C33'-C34'-C35'	118.6(13)
C4A-C3A-C2A	120.0	C26A-C27A-C28A	120.2(7)	N6A'-C34'-C35'	122.5(15)
N2A-C4A-C5A	129.1(4)	C29A-C28A-C27A	120.2(7)	C36'-C35'-C34'	119.7(14)
N2A-C4A-C3A	110.9(4)	C28A-C29A-C30A	121.7(7)	C36'-C35'-N7A'	114.6(14)
C5A-C4A-C3A	120.0	C28A-C29A-O2A'	115.5(9)	C34'-C35'-N7A'	125.5(14)
C6A-C5A-C4A	120.0	C30A-C29A-O2A'	122.6(9)	C35'-C36'-C37'	116.4(17)
C5A-C6A-C1A	120.0	C28A-C29A-O2A	112.6(11)	O3A'-C37'-C32'	122.4(17)
C5A-C6A-O1A	121.0(3)	C30A-C29A-O2A	124.0(11)	O3A'-C37'-C36'	112.1(16)
C1A-C6A-O1A	118.6(3)	C31A-C30A-C29A	117.3(7)	C32'-C37'-C36'	124(2)
N2A-C7A-N1A	112.7(6)	C31A-C30A-C44A	120.1(6)	C38'-N6A'-C34'	127.8(14)
N2A-C7A-C8A	123.4(7)	C29A-C30A-C44A	122.6(7)	O9A'-C38'-N6A'	121.4(14)
N1A-C7A-C8A	123.8(7)	C30A-C31A-C26A	122.7(7)	O9A'-C38'-C39'	121.6(14)
C9A-C8A-C12A	120.2(7)	C29A-O2A-C32A	111.5(17)	N6A'-C38'-C39'	114.0(9)
C9A-C8A-C7A	121.5(7)	C48A-O3A-C37A	107.7(18)	C38'-C39'-C40'	100.0(13)
C12A-C8A-C7A	118.3(7)	C37A-C32A-C33A	127(3)	C41'-N7A'-C35'	125.0(12)
C10A-C9A-C8A	119.0(7)	C37A-C32A-O2A	139(3)	O10'-C41'-N7A'	126.4(11)
C9A-C10A-N4A	119.3(7)	C33A-C32A-O2A	94(2)	O10'-C41'-C42'	119.4(11)
C9A-C10A-C13A	127.3(7)	C34A-C33A-C32A	108(2)	N7A'-C41'-C42'	114.2(8)
N4A-C10A-C13A	113.3(6)	C35A-C34A-N6A	114(2)	C41'-C42'-C43'	119.8(9)
N4A-C11A-C12A	119.6(7)	C35A-C34A-C33A	124.0(18)	C47A-C44A-C45A	114.5(6)
N4A-C11A-C18A	112.0(6)	N6A-C34A-C33A	122(2)	C47A-C44A-C30A	105.5(5)
C12A-C11A-C18A	128.4(7)	C34A-C35A-N7A	127(2)	C45A-C44A-C30A	112.0(6)
C11A-C12A-C8A	118.8(7)	C34A-C35A-C36A	119.3(18)	C46A-C45A-C44A	109.9(6)
N3A-C13A-C14A	117.9(7)	N7A-C35A-C36A	113(2)	C52A-C47A-C48A	116.4(6)
N3A-C13A-C10A	116.5(6)	C37A-C36A-C35A	121(3)	C52A-C47A-C44A	123.7(6)

Angles (part 4)		Angles (part 5)		Angles (part 6)	
C48A-C47A-C44A	119.8(6)	O14A-C83A-N11A	124.0(6)	N2B-C7B-N1B	111.8(6)
C49A-C48A-O3A	109.9(9)	O14A-C83A-C84A	122.5(6)	N2B-C7B-C8B	123.4(7)
C49A-C48A-C47A	122.3(6)	N11A-C83A-C84A	113.5(5)	N1B-C7B-C8B	124.7(6)
O3A-C48A-C47A	127.0(10)	C85A-C84A-C83A	111.6(6)	C12B-C8B-C9B	118.5(6)
C49A-C48A-O3A'	120.4(7)	C89A-C86A-C72A	110.3(6)	C12B-C8B-C7B	120.3(6)
C47A-C48A-O3A'	117.0(7)	C89A-C86A-C87A	114.5(6)	C9B-C8B-C7B	121.2(6)
C50A-C49A-C48A	119.0(7)	C72A-C86A-C87A	112.6(6)	C10B-C9B-C8B	117.5(6)
C49A-C50A-C51A	122.2(7)	C88A-C87A-C86A	113.6(7)	N4B-C10B-C9B	121.2(6)
C49A-C50A-O4A	117.5(6)	C90A-C89A-C94A	115.4(7)	N4B-C10B-C13B	113.0(6)
C51A-C50A-O4A	120.1(6)	C90A-C89A-C86A	121.0(7)	C9B-C10B-C13B	125.8(6)
C52A-C51A-C50A	116.4(6)	C94A-C89A-C86A	123.6(6)	N4B-C11B-C12B	118.7(6)
C52A-C51A-C65A	123.7(6)	C89A-C90A-O7A	118.1(6)	N4B-C11B-C18B	114.0(5)
C50A-C51A-C65A	119.7(6)	C89A-C90A-C91A	123.2(7)	C12B-C11B-C18B	127.2(6)
C51A-C52A-C47A	123.6(6)	O7A-C90A-C91A	118.5(6)	C11B-C12B-C8B	120.8(6)
C54A-C53A-C58A	121.5(7)	C92A-C91A-C90A	118.4(6)	N3B-C13B-C14B	120.9(6)
C54A-C53A-O4A	120.3(7)	C91A-C92A-O8A	120.2(6)	N3B-C13B-C10B	115.9(6)
C58A-C53A-O4A	118.2(7)	C91A-C92A-C93A	121.9(7)	C14B-C13B-C10B	123.2(6)
C53A-C54A-C55A	120.2(7)	O8A-C92A-C93A	117.6(6)	C15B-C14B-C13B	117.7(6)
C56A-C55A-C54A	118.3(7)	C92A-C93A-C94A	117.5(7)	C14B-C15B-C16B	121.4(7)
C56A-C55A-N8A	118.9(7)	C92A-C93A-C23A	118.5(6)	C15B-C16B-C17B	117.3(7)
C54A-C55A-N8A	122.7(7)	C94A-C93A-C23A	123.9(6)	N3B-C17B-C16B	122.8(7)
C57A-C56A-C55A	120.7(7)	C93A-C94A-C89A	123.5(6)	N5B-C18B-C19B	122.1(6)
C57A-C56A-N9A	121.1(7)	C3A-N1A-C7A	105.9(5)	N5B-C18B-C11B	114.5(5)
C55A-C56A-N9A	117.9(7)	C4A-N2A-C7A	102.9(5)	C19B-C18B-C11B	123.4(6)
C56A-C57A-C58A	119.8(7)	C17A-N3A-C13A	119.6(7)	C20B-C19B-C18B	117.6(7)
C53A-C58A-C57A	119.2(7)	C17A-N3A-Ru1A	128.7(5)	C21B-C20B-C19B	120.5(7)
C53A-C58A-O5A	126.6(7)	C13A-N3A-Ru1A	111.4(5)	C20B-C21B-C22B	118.5(7)
C57A-C58A-O5A	114.2(6)	C11A-N4A-C10A	123.0(6)	N5B-C22B-C21B	122.2(7)
O11A-C59A-N8A	123.0(6)	C11A-N4A-Ru1A	118.6(5)	C93B-C23B-C24B	113.1(7)
O11A-C59A-C60A	120.9(6)	C10A-N4A-Ru1A	117.2(5)	C93B-C23B-C26B	112.6(6)
N8A-C59A-C60A	116.1(5)	C18A-N5A-C22A	118.1(7)	C24B-C23B-C26B	111.2(6)
C59A-C60A-C61A	113.3(6)	C18A-N5A-Ru1A	114.2(5)	C23B-C24B-C25B	111.2(7)
O12A-C62A-N9A	123.1(6)	C22A-N5A-Ru1A	127.6(5)	C31B-C26B-C27B	116.4(8)
O12A-C62A-C63A	122.9(6)	C59A-N8A-C55A	126.9(6)	C31B-C26B-C23B	122.3(7)
N9A-C62A-C63A	113.7(6)	C62A-N9A-C56A	125.3(6)	C27B-C26B-C23B	121.3(7)
C62A-C63A-C64A	113.0(6)	C80A-N10A-C76A	123.8(6)	C28B-C27B-C26B	121.6(7)
C51A-C65A-C68A	107.8(6)	C83A-N11A-C77A	126.1(6)	C28B-C27B-O2B	119.6(7)
C51A-C65A-C66A	115.0(6)	C27A-O1A-C6A	113.9(5)	C26B-C27B-O2B	118.8(8)
C68A-C65A-C66A	113.2(6)	C53A-O4A-C50A	112.9(5)	C27B-C28B-C29B	120.1(8)
C67A-C66A-C65A	119.0(8)	C58A-O5A-C69A	123.0(5)	C28B-C29B-O3B	114.6(7)
C69A-C68A-C73A	116.5(7)	C74A-O6A-C71A	116.4(5)	C28B-C29B-C30B	122.2(8)
C69A-C68A-C65A	125.9(7)	C79A-O7A-C90A	118.1(5)	O3B-C29B-C30B	123.0(7)
C73A-C68A-C65A	117.6(6)	C92A-O8A-C1A	115.7(5)	C31B-C30B-C29B	114.6(7)
C68A-C69A-O5A	125.1(7)	N4B-Ru1B-N5B	80.3(2)	C31B-C30B-C44B	121.7(7)
C68A-C69A-C70A	120.6(7)	N4B-Ru1B-N3B	79.9(2)	C29B-C30B-C44B	123.7(8)
O5A-C69A-C70A	114.1(6)	N5B-Ru1B-N3B	160.1(2)	C26B-C31B-C30B	124.9(8)
C71A-C70A-C69A	120.2(7)	N4B-Ru1B-Cl3B	87.90(16)	C37B-C32B-C33B	121.9(9)
C70A-C71A-C72A	122.3(7)	N5B-Ru1B-Cl3B	88.79(16)	C37B-C32B-O3B	124.8(8)
C70A-C71A-O6A	118.0(6)	N3B-Ru1B-Cl3B	92.31(15)	C33B-C32B-O3B	113.2(8)
C72A-C71A-O6A	119.6(7)	N4B-Ru1B-Cl1B	89.50(16)	C32B-C33B-C34B	118.9(9)
C71A-C72A-C73A	116.7(7)	N5B-Ru1B-Cl1B	88.12(16)	C33B-C34B-C35B	120.7(8)
C71A-C72A-C86A	122.9(7)	N3B-Ru1B-Cl1B	89.89(15)	C33B-C34B-N6B	120.7(9)
C73A-C72A-C86A	120.4(6)	Cl3B-Ru1B-Cl1B	176.25(6)	C35B-C34B-N6B	118.6(9)
C72A-C73A-C68A	123.4(7)	N4B-Ru1B-Cl2B	178.60(17)	C36B-C35B-C34B	120.6(8)
C79A-C74A-C75A	121.5(7)	N5B-Ru1B-Cl2B	100.48(16)	C36B-C35B-N7B	112.6(9)
C79A-C74A-O6A	119.6(6)	N3B-Ru1B-Cl2B	99.35(15)	C34B-C35B-N7B	126.6(10)
C75A-C74A-O6A	118.7(6)	Cl3B-Ru1B-Cl2B	90.98(6)	C36B-C35B-N7B"	117.1(10)
C74A-C75A-C76A	118.6(7)	Cl1B-Ru1B-Cl2B	91.66(7)	C34B-C35B-N7B"	121.9(10)
C77A-C76A-C75A	120.2(6)	C2B-C1B-O1B	122.6(8)	C35B-C36B-C37B	117.8(9)
C77A-C76A-N10A	120.6(6)	C2B-C1B-C6B	120.2(7)	C32B-C37B-O4B	122.7(8)
C75A-C76A-N10A	119.1(7)	O1B-C1B-C6B	117.2(6)	C32B-C37B-C36B	120.0(8)
C76A-C77A-C78A	119.1(6)	C1B-C2B-C3B	117.6(7)	O4B-C37B-C36B	117.3(8)
C76A-C77A-N11A	118.5(6)	N1B-C3B-C2B	132.5(7)	C38B-N6B-C34B	124.0(7)
C78A-C77A-N11A	122.4(6)	N1B-C3B-C4B	105.6(6)	O9B-C38B-N6B	122.0(7)
C79A-C78A-C77A	120.5(7)	C2B-C3B-C4B	121.8(6)	O9B-C38B-C39B	123.6(7)
C78A-C79A-C74A	120.0(7)	N2B-C4B-C3B	109.2(6)	N6B-C38B-C39B	114.3(6)
C78A-C79A-O7A	119.9(7)	N2B-C4B-C5B	129.7(8)	C38B-C39B-C40B	116.9(8)
C74A-C79A-O7A	120.0(6)	C3B-C4B-C5B	120.9(7)	C41"-N7B"-C35B	129.1(13)
O13A-C80A-N10A	122.6(7)	C6B-C5B-C4B	116.1(8)	O10"-C41"-N7B"	126.6(14)
O13A-C80A-C81A	118.5(7)	C5B-C6B-O2B	120.8(8)	O10"-C41"-C42"	120.3(13)
N10A-C80A-C81A	118.9(6)	C5B-C6B-C1B	122.6(7)	N7B"-C41"-C42"	113.2(8)
C80A-C81A-C82A	116.9(6)	O2B-C6B-C1B	116.6(7)	C41"-C42"-C43"	111.6(8)

Angles (part 7)		Angles (part 8)		Angles (part 9)	
C41B-N7B-C35B	125.9(12)	C64"-C63"-C62"	111.8(5)	C17B-N3B-Ru1B	127.7(5)
O10B-C41B-N7B	121.7(12)	C59"-N8B"-C55"	128.9(4)	C13B-N3B-Ru1B	112.2(4)
O10B-C41B-C42B	124.3(11)	C62"-N9B"-C56"	121.9(5)	C10B-N4B-C11B	123.3(6)
N7B-C41B-C42B	114.0(8)	C50B-O5B"-C53"	116.6(9)	C10B-N4B-Ru1B	118.7(4)
C41B-C42B-C43B	113.9(9)	C69B-O6B"-C58"	126.6(7)	C11B-N4B-Ru1B	117.8(4)
C30B-C44B-C45B	114.1(6)	C66B-C65B-C51B	114.3(6)	C22B-N5B-C18B	119.0(6)
C30B-C44B-C47B	107.8(6)	C66B-C65B-C68B	112.8(7)	C22B-N5B-Ru1B	127.8(5)
C45B-C44B-C47B	113.1(6)	C51B-C65B-C68B	106.6(6)	C18B-N5B-Ru1B	113.1(4)
C46B-C45B-C44B	112.3(6)	C67B-C66B-C65B	112.3(7)	C1B-O1B-C92B	116.5(5)
C48B-C47B-C52B	117.1(7)	C73B-C68B-C69B	116.0(7)	C6B-O2B-C27B	109.2(5)
C48B-C47B-C44B	119.8(7)	C73B-C68B-C65B	119.7(6)	C29B-O3B-C32B	127.1(6)
C52B-C47B-C44B	122.9(6)	C69B-C68B-C65B	124.1(7)	C37B-O4B-C48B	118.2(6)
C49B-C48B-O4B	116.7(6)	C70B-C69B-C68B	121.4(7)	N4C-Ru1C-N5C	80.3(2)
C49B-C48B-C47B	122.4(7)	C70B-C69B-O6B"	115.2(8)	N4C-Ru1C-N3C	79.4(2)
O4B-C48B-C47B	120.2(6)	C68B-C69B-O6B"	122.1(9)	N5C-Ru1C-N3C	159.5(2)
C48B-C49B-C50B	119.3(7)	C70B-C69B-O6B	112.5(8)	N4C-Ru1C-Cl3C	87.02(17)
O5B-C50B-C49B	114.1(8)	C68B-C69B-O6B	126.0(8)	N5C-Ru1C-Cl3C	90.37(16)
C49B-C50B-O5B"	120.5(8)	C69B-C70B-C71B	120.4(7)	N3C-Ru1C-Cl3C	92.0(2)
O5B-C50B-C51B	122.9(8)	C72B-C71B-C70B	121.0(7)	N4C-Ru1C-Cl1C	89.37(17)
C49B-C50B-C51B	121.9(7)	C72B-C71B-O7B	120.8(7)	N5C-Ru1C-Cl1C	88.30(16)
O5B"-C50B-C51B	117.5(8)	C70B-C71B-O7B	118.2(7)	N3C-Ru1C-Cl1C	88.06(19)
C50B-C51B-C52B	116.5(7)	C71B-C72B-C73B	116.7(7)	Cl3C-Ru1C-Cl1C	176.32(8)
C50B-C51B-C65B	119.9(6)	C71B-C72B-C86B	120.5(7)	N4C-Ru1C-Cl2C	177.78(17)
C52B-C51B-C65B	123.6(6)	C73B-C72B-C86B	122.6(6)	N5C-Ru1C-Cl2C	100.77(16)
C47B-C52B-C51B	122.6(7)	C72B-C73B-C68B	124.3(7)	N3C-Ru1C-Cl2C	99.58(18)
C58B-C53B-C54B	120.9(4)	C79B-C74B-C75B	120.7	Cl3C-Ru1C-Cl2C	91.04(8)
C58B-C53B-O5B	121.7(5)	C79B-C74B-O7B	122.3(2)	Cl1C-Ru1C-Cl2C	92.58(8)
C54B-C53B-O5B	117.3(5)	C75B-C74B-O7B	116.9(2)	C6C-C1C-C2C	123.0(7)
C53B-C54B-C55B	117.9(4)	C74B-C75B-C76B	117.0	C6C-C1C-O1C	120.4(7)
C56B-C55B-N8B	123.0(5)	C77B-C76B-N10B	124.4	C2C-C1C-O1C	116.5(7)
C56B-C55B-C54B	119.8(4)	C77B-C76B-C75B	121.4	C1C-C2C-C3C	114.9(7)
N8B-C55B-C54B	117.0(5)	N10B-C76B-C75B	114.2	N1C-C3C-C4C	107.4(6)
C55B-C56B-N9B	118.7(4)	C76B-C77B-N11B	119.0(2)	N1C-C3C-C2C	130.8(7)
C55B-C56B-C57B	120.1(4)	C76B-C77B-C78B	119.2	C4C-C3C-C2C	121.8(7)
N9B-C56B-C57B	121.0(5)	N11B-C77B-C78B	121.8(2)	C3C-C4C-C5C	121.0(7)
C58B-C57B-C56B	117.2(5)	C79B-C78B-C77B	116.5	C3C-C4C-N2C	109.3(6)
C53B-C58B-C57B	123.8(4)	C74B-C79B-C78B	125.1	C5C-C4C-N2C	129.6(7)
C53B-C58B-O6B	122.0(5)	C74B-C79B-O8B	119.2(2)	C4C-C5C-C6C	117.1(7)
C57B-C58B-O6B	113.4(5)	C78B-C79B-O8B	115.4(2)	C1C-C6C-C5C	121.9(7)
O11B-C59B-N8B	126.0(6)	O13B-C80B-N10B	124.0(3)	C1C-C6C-O2C	118.9(7)
O11B-C59B-C60B	119.1(6)	O13B-C80B-C81B	119.5(3)	C5C-C6C-O2C	119.2(7)
N8B-C59B-C60B	114.4(4)	N10B-C80B-C81B	114.8	N2C-C7C-N1C	114.0(6)
C59B-C60B-C61B	112.1(5)	C80B-C81B-C82B	112.4	N2C-C7C-C8C	123.7(7)
O12B-C62B-N9B	127.0(8)	O14B-C83B-N11B	127.3(3)	N1C-C7C-C8C	122.3(6)
O12B-C62B-C63B	114.9(7)	O14B-C83B-C84B	119.0(3)	C12C-C8C-C9C	119.5(6)
N9B-C62B-C63B	111.9(5)	N11B-C83B-C84B	113.74(19)	C12C-C8C-C7C	118.6(6)
C64B-C63B-C62B	111.3(4)	C83B-C84B-C85B	112.0	C9C-C8C-C7C	121.8(6)
C59B-N8B-C55B	130.1(6)	C80B-N10B-C76B	124.4	C10C-C9C-C8C	119.5(6)
C62B-N9B-C56B	124.9(6)	C83B-N11B-C77B	124.0(3)	N4C-C10C-C9C	118.9(6)
C50B-O5B-C53B	114.2(10)	C71B-O7B-C74B	116.0(5)	N4C-C10C-C13C	112.9(6)
C58B-O6B-C69B	126.6(8)	C90B-O8B-C79B	118.0(5)	C9C-C10C-C13C	128.2(6)
C58"-C53"-C54"	120.7(4)	C89B-C86B-C72B	111.5(6)	N4C-C11C-C12C	117.3(6)
C58"-C53"-O5B"	122.0(5)	C89B-C86B-C87B	114.1(6)	N4C-C11C-C18C	115.1(6)
C54"-C53"-O5B"	117.2(5)	C72B-C86B-C87B	110.7(6)	C12C-C11C-C18C	127.5(6)
C53"-C54"-C55"	118.0(4)	C88B-C87B-C86B	114.4(6)	C8C-C12C-C11C	120.2(6)
C56"-C55"-N8B"	124.2(4)	C90B-C89B-C94B	116.3(7)	N3C-C13C-C14C	122.2(7)
C56"-C55"-C54"	120.1(4)	C90B-C89B-C86B	121.1(7)	N3C-C13C-C10C	115.0(6)
N8B"-C55"-C54"	115.7(4)	C94B-C89B-C86B	122.5(6)	C14C-C13C-C10C	122.6(7)
C55"-C56"-N9B"	119.0(4)	O8B-C90B-C89B	118.2(7)	C13C-C14C-C15C	117.9(8)
C55"-C56"-C57"	119.9(4)	O8B-C90B-C91B	120.0(6)	C16C-C15C-C14C	119.0(9)
N9B"-C56"-C57"	121.1(4)	C89B-C90B-C91B	121.7(8)	C15C-C16C-C17C	121.1(9)
C58"-C57"-C56"	117.1(5)	C92B-C91B-C90B	118.4(7)	N3C-C17C-C16C	119.4(9)
C53"-C58"-C57"	124.2(4)	C93B-C92B-C91B	123.7(8)	C19C-C18C-N5C	119.7(6)
C53"-C58"-O6B"	122.1(5)	C93B-C92B-O1B	117.7(7)	C19C-C18C-C11C	126.1(6)
C57"-C58"-O6B"	113.4(5)	C91B-C92B-O1B	118.3(7)	N5C-C18C-C11C	114.2(5)
O11"-C59"-N8B"	125.2(5)	C92B-C93B-C94B	118.4(8)	C18C-C19C-C20C	120.6(7)
O11"-C59"-C60"	120.0(5)	C92B-C93B-C23B	120.8(7)	C21C-C20C-C19C	119.6(7)
N8B"-C59"-C60"	114.8(3)	C94B-C93B-C23B	120.7(6)	C20C-C21C-C22C	117.9(7)
C59"-C60"-C61"	112.4(3)	C93B-C94B-C89B	121.2(7)	N5C-C22C-C21C	122.4(7)
O12"-C62"-N9B"	126.4(7)	C3B-N1B-C7B	107.1(6)	C24C-C23C-C93C	111.9(6)
O12"-C62"-C63"	117.1(6)	C7B-N2B-C4B	106.3(6)	C24C-C23C-C26C	111.7(6)
N9B"-C62"-C63"	113.5(4)	C17B-N3B-C13B	120.0(6)	C93C-C23C-C26C	111.3(5)

Angles (part 10)		Angles (part 11)		Angles (part 12)	
C23C-C24C-C25*	112.2(6)	C56C-C55C-N8C	118.8(7)	N10C-C80C-C81C	114.6(8)
C23C-C24C-C25C	113.8(7)	C55C-C56C-N9C	121.9(8)	C80C-C81C-C82C	111.7(8)
C31C-C26C-C27C	116.7(7)	C55C-C56C-C57C	119.6(7)	C80*-N10*-C76C	128.2(13)
C31C-C26C-C23C	120.6(6)	N9C-C56C-C57C	118.5(8)	O13*-C80*-N10*	124.8(14)
C27C-C26C-C23C	122.7(6)	C58C-C57C-C56C	120.2(8)	O13*-C80*-C81*	120.2(15)
C26C-C27C-O2C	120.6(7)	O6C-C58C-C57C	116.3(7)	N10*-C80*-C81*	114.7(12)
C26C-C27C-C28C	120.4(6)	O6C-C58C-C53C	124.6(6)	C82*-C81*-C80*	118.8(11)
O2C-C27C-C28C	119.0(6)	C57C-C58C-C53C	119.1(7)	O14C-C83C-N11C	122.5(6)
C29C-C28C-C27C	119.3(7)	C59*-N8C-C55C	125.6(8)	O14C-C83C-C84C	121.4(6)
C28C-C29C-C30C	122.7(7)	C59C-N8C-C55C	126.6(8)	N11C-C83C-C84C	116.1(5)
C28C-C29C-O3C	113.4(6)	O11C-C59C-N8C	120.1(9)	C83C-C84C-C85*	117.5(7)
C30C-C29C-O3C	123.7(6)	O11C-C59C-C60C	124.6(11)	C83C-C84C-C85C	116.9(7)
C31C-C30C-C29C	115.6(6)	N8C-C59C-C60C	112.7(8)	C89C-C86C-C72C	110.3(6)
C31C-C30C-C44C	118.5(6)	C59C-C60C-C61C	112.2(9)	C89C-C86C-C87C	113.2(6)
C29C-C30C-C44C	125.6(7)	O11*-C59*-N8C	114.0(11)	C72C-C86C-C87C	112.7(6)
C30C-C31C-C26C	125.0(7)	O11*-C59*-C60*	132.2(12)	C88C-C87C-C86C	114.1(6)
O3C-C32C-C37C	125.1(6)	N8C-C59*-C60*	112.7(8)	C94C-C89C-C90C	117.4(7)
O3C-C32C-C33C	116.9(6)	C59*-C60*-C61*	112.6(9)	C94C-C89C-C86C	124.4(6)
C37C-C32C-C33C	118.0(7)	C62C-N9C-C56C	129.0(9)	C90C-C89C-C86C	118.1(7)
C34C-C33C-C32C	121.2(7)	C56C-N9C-C62*	118.8(9)	C91C-C90C-O8C	121.0(6)
C33C-C34C-C35C	120.5(6)	O12C-C62C-N9C	118.4(12)	C91C-C90C-C89C	119.7(7)
C33C-C34C-N6C	120.9(7)	O12C-C62C-C63C	130.1(13)	O8C-C90C-C89C	119.2(7)
C35C-C34C-N6C	118.5(7)	N9C-C62C-C63C	111.3(8)	C92C-C91C-C90C	121.0(7)
C34C-C35C-C36C	119.6(6)	C62C-C63C-C64C	109.6(8)	C91C-C92C-O1C	119.9(6)
C34C-C35C-N7C	122.4(7)	O12*-C62*-N9C	134.9(13)	C91C-C92C-C93C	121.6(7)
C36C-C35C-N7C	118.0(6)	O12*-C62*-C63*	124.8(15)	O1C-C92C-C93C	118.2(7)
C37C-C36C-C35C	119.5(6)	N9C-C62*-C63*	99.8(11)	C94C-C93C-C92C	115.7(7)
C36C-C37C-C32C	121.1(7)	C62*-C63*-C64*	112.4(9)	C94C-C93C-C23C	123.0(6)
C36C-C37C-O4C	120.4(6)	C68C-C65C-C66C	113.6(6)	C92C-C93C-C23C	121.0(6)
C32C-C37C-O4C	118.4(6)	C68C-C65C-C51C	106.9(5)	C89C-C94C-C93C	124.5(7)
O9C-C38C-N6C	120.5(7)	C66C-C65C-C51C	113.5(5)	C3C-N1C-C7C	104.7(6)
O9C-C38C-C39C	126.0(8)	C67C-C66C-C65C	111.5(6)	C7C-N2C-C4C	104.5(6)
N6C-C38C-C39C	113.3(6)	C73C-C68C-C69C	116.2(6)	C17C-N3C-C13C	120.2(7)
C40C-C39C-C38C	114.9(8)	C73C-C68C-C65C	120.6(6)	C17C-N3C-Ru1C	125.3(6)
O10C-C41C-N7C	118.8(7)	C69C-C68C-C65C	123.1(7)	C13C-N3C-Ru1C	114.2(5)
O10C-C41C-C42*	121.8(12)	C70C-C69C-C68C	123.1(7)	C11C-N4C-C10C	124.5(6)
N7C-C41C-C42*	118.3(11)	C70C-C69C-O6C	113.7(6)	C11C-N4C-Ru1C	117.0(4)
O10C-C41C-C42C	126.1(10)	C68C-C69C-O6C	122.4(6)	C10C-N4C-Ru1C	118.3(5)
N7C-C41C-C42C	115.1(8)	C69C-C70C-C71C	117.0(7)	C22C-N5C-C18C	119.6(6)
C41C-C42C-C43C	115.8(9)	C72C-C71C-C70C	123.6(7)	C22C-N5C-Ru1C	127.3(5)
C41C-C42*-C43*	110.1(15)	C72C-C71C-O7C	119.9(6)	C18C-N5C-Ru1C	113.1(4)
C47C-C44C-C30C	109.2(5)	C70C-C71C-O7C	116.1(6)	C38C-N6C-C34C	129.0(7)
C47C-C44C-C45C	114.1(6)	C71C-C72C-C73C	115.9(7)	C41C-N7C-C35C	123.5(6)
C30C-C44C-C45C	113.7(6)	C71C-C72C-C86C	121.9(7)	C83C-N11C-C77C	126.7(6)
C46C-C45C-C44C	110.7(6)	C73C-C72C-C86C	122.2(7)	C92C-O1C-C1C	114.2(5)
C52C-C47C-C48C	116.4(6)	C68C-C73C-C72C	123.8(7)	C27C-O2C-C6C	112.3(5)
C52C-C47C-C44C	123.7(6)	C75C-C74C-C79C	120.5(7)	C32C-O3C-C29C	126.8(5)
C48C-C47C-C44C	119.5(6)	C75C-C74C-O7C	118.4(7)	C37C-O4C-C48C	116.0(5)
C49C-C48C-C47C	122.0(6)	C79C-C74C-O7C	121.0(7)	C53C-O5C-C50C	115.5(5)
C49C-C48C-O4C	116.4(6)	C74C-C75C-C76C	120.7(7)	C58C-O6C-C69C	124.7(5)
C47C-C48C-O4C	121.2(5)	C77C-C76C-C75C	119.3(7)	C74C-O7C-C71C	116.2(5)
C50C-C49C-C48C	119.0(6)	C77C-C76C-N10C	130.3(9)	C79C-O8C-C90C	116.3(5)
C49C-C50C-C51C	122.0(6)	C75C-C76C-N10C	109.7(8)	O1R-C1R-C2R	109.1(9)
C49C-C50C-O5C	117.0(6)	C77C-C76C-N10*	113.8(8)	O1S-C1S-C2S	109.9(9)
C51C-C50C-O5C	120.9(6)	C75C-C76C-N10*	126.8(9)	O1T-C1T-C2T	109.1(7)
C52C-C51C-C50C	117.5(6)	C76C-C77C-N11C	121.8(7)	O1U-C1U-C2U	110.8(8)
C52C-C51C-C65C	123.4(6)	C76C-C77C-C78C	119.5(7)	O1V-C1V-C2V	110.2(8)
C50C-C51C-C65C	118.8(6)	N11C-C77C-C78C	118.5(7)	O1N-C1N-C2N	112.7(9)
C51C-C52C-C47C	123.0(6)	C79C-C78C-C77C	120.4(7)	O1N-C1N'-C2N'	109.2(8)
O5C-C53C-C54C	121.3(6)	C78C-C79C-O8C	120.7(7)	O1X-C1X-C2X	109.8(9)
O5C-C53C-C58C	119.2(6)	C78C-C79C-C74C	119.5(7)	O1Y-C1Y-C2Y	108.3(9)
C54C-C53C-C58C	119.5(7)	O8C-C79C-C74C	119.5(7)	O1Z-C1Z-C2Z	108.3(9)
C55C-C54C-C53C	120.8(7)	C80C-N10C-C76C	124.2(10)	O1Z'-C1Z'-C2Z'	109.0(9)
C54C-C55C-C56C	120.6(8)	O13C-C80C-N10C	122.4(11)	O1M-C1M-C2M	108.5(9)
C54C-C55C-N8C	120.4(8)	O13C-C80C-C81C	123.0(11)		

Torsion angles [°]

Part 1		Part 2		Part 3	
O8A-C1A-C2A-C3A	178.0(4)	C23A-C26A-C31A-C30A	-173.4(6)	C29A-C30A-C44A-C47A	-104.9(7)
C6A-C1A-C2A-C3A	0.0	C28A-C29A-O2A-C32A	-130.2(17)	C31A-C30A-C44A-C45A	-52.8(8)
C1A-C2A-C3A-N1A	175.3(6)	C30A-C29A-O2A-C32A	65(2)	C29A-C30A-C44A-C45A	130.0(7)
C1A-C2A-C3A-C4A	0.0	C29A-O2A-C32A-C37A	12(5)	C47A-C44A-C45A-C46A	176.4(6)
N1A-C3A-C4A-N2A	2.1(5)	C29A-O2A-C32A-C33A	-175.5(19)	C30A-C44A-C45A-C46A	-63.7(8)
C2A-C3A-C4A-N2A	178.4(4)	C37A-C32A-C33A-C34A	-6(4)	C45A-C44A-C47A-C52A	7.6(10)
N1A-C3A-C4A-C5A	-176.3(4)	O2A-C32A-C33A-C34A	180(2)	C30A-C44A-C47A-C52A	-115.9(7)
C2A-C3A-C4A-C5A	0.0	C32A-C33A-C34A-C35A	1(4)	C45A-C44A-C47A-C48A	-176.2(7)
N2A-C4A-C5A-C6A	-178.1(5)	C32A-C33A-C34A-N6A	-176(3)	C30A-C44A-C47A-C48A	60.2(8)
C3A-C4A-C5A-C6A	0.0	N6A-C34A-C35A-N7A	-15(5)	C37A-O3A-C48A-C49A	-123.1(15)
C4A-C5A-C6A-C1A	0.0	C33A-C34A-C35A-N7A	167(3)	C37A-O3A-C48A-C47A	66(2)
C4A-C5A-C6A-O1A	173.2(4)	N6A-C34A-C35A-C36A	174(3)	C52A-C47A-C48A-C49A	2.7(11)
O8A-C1A-C6A-C5A	-178.1(4)	C33A-C34A-C35A-C36A	-3(5)	C44A-C47A-C48A-C49A	-173.7(7)
C2A-C1A-C6A-C5A	0.0	C34A-C35A-C36A-C37A	11(4)	C52A-C47A-C48A-O3A	172.1(13)
O8A-C1A-C6A-O1A	8.6(5)	N7A-C35A-C36A-C37A	-161(3)	C44A-C47A-C48A-O3A	-4.4(16)
C2A-C1A-C6A-O1A	-173.4(4)	C35A-C36A-C37A-C32A	-15(4)	C52A-C47A-C48A-O3A'	176.1(9)
N2A-C7A-C8A-C9A	158.7(7)	C35A-C36A-C37A-O3A	163(3)	C44A-C47A-C48A-O3A'	-0.3(12)
N1A-C7A-C8A-C9A	-20.7(11)	C33A-C32A-C37A-C36A	14(5)	C37'-O3A'-C48A-C49A	-119.0(13)
N2A-C7A-C8A-C12A	-19.0(10)	O2A-C32A-C37A-C36A	-175(3)	C37'-O3A'-C48A-C47A	67.6(16)
N1A-C7A-C8A-C12A	161.7(7)	C33A-C32A-C37A-O3A	-165(3)	O3A-C48A-C49A-C50A	-171.0(11)
C12A-C8A-C9A-C10A	-3.3(10)	O2A-C32A-C37A-O3A	6(5)	C47A-C48A-C49A-C50A	-0.1(11)
C7A-C8A-C9A-C10A	179.1(6)	C48A-O3A-C37A-C36A	69(3)	O3A'-C48A-C49A-C50A	-173.2(9)
C8A-C9A-C10A-N4A	2.7(10)	C48A-O3A-C37A-C32A	-113(3)	C48A-C49A-C50A-C51A	-2.0(11)
C8A-C9A-C10A-C13A	-176.0(7)	C35A-C34A-N6A-C38A	138(3)	C48A-C49A-C50A-O4A	173.0(6)
N4A-C11A-C12A-C8A	-2.9(10)	C33A-C34A-N6A-C38A	-44(4)	C49A-C50A-C51A-C52A	1.2(11)
C18A-C11A-C12A-C8A	178.8(7)	C34A-N6A-C38A-O9A	11(4)	O4A-C50A-C51A-C52A	-173.7(6)
C9A-C8A-C12A-C11A	3.3(10)	C34A-N6A-C38A-C39A	-171(2)	C49A-C50A-C51A-C65A	176.6(7)
C7A-C8A-C12A-C11A	-178.9(6)	O9A-C38A-C39A-C40A	-35(3)	O4A-C50A-C51A-C65A	1.8(10)
C9A-C10A-C13A-N3A	172.5(7)	N6A-C38A-C39A-C40A	147(2)	C50A-C51A-C52A-C47A	1.8(11)
N4A-C10A-C13A-N3A	-6.3(9)	C34A-C35A-N7A-C41A	-45(5)	C65A-C51A-C52A-C47A	-173.5(7)
C9A-C10A-C13A-C14A	-10.0(12)	C36A-C35A-N7A-C41A	126(3)	C48A-C47A-C52A-C51A	-3.6(11)
N4A-C10A-C13A-C14A	171.2(7)	C35A-N7A-C41A-O10A	12(4)	C44A-C47A-C52A-C51A	172.6(7)
N3A-C13A-C14A-C15A	0.3(11)	C35A-N7A-C41A-C42A	-177(2)	C58A-C53A-C54A-C55A	-0.9(11)
C10A-C13A-C14A-C15A	-177.2(8)	O10A-C41A-C42A-C43A	141(2)	O4A-C53A-C54A-C55A	179.7(6)
C13A-C14A-C15A-C16A	2.4(12)	N7A-C41A-C42A-C43A	-29(2)	C53A-C54A-C55A-C56A	-3.0(11)
C14A-C15A-C16A-C17A	-4.0(12)	C28A-C29A-O2A'-C32'	-130(2)	C53A-C54A-C55A-N8A	179.5(7)
C15A-C16A-C17A-N3A	3.0(13)	C30A-C29A-O2A'-C32'	54(2)	C54A-C55A-C56A-C57A	5.3(11)
N4A-C11A-C18A-N5A	8.2(9)	C29A-O2A'-C32'-C37'	12(3)	N8A-C55A-C56A-C57A	-177.0(7)
C12A-C11A-C18A-N5A	-173.3(7)	C29A-O2A'-C32'-C33'	-164.9(17)	C54A-C55A-C56A-N9A	-168.2(7)
N4A-C11A-C18A-C19A	-172.9(7)	O2A'-C32'-C33'-C34'	-178(2)	N8A-C55A-C56A-N9A	9.5(10)
C12A-C11A-C18A-C19A	5.5(12)	C37'-C32'-C33'-C34'	5(3)	C55A-C56A-C57A-C58A	-3.7(11)
N5A-C18A-C19A-C20A	-1.7(11)	C32'-C33'-C34'-N6A'	172(2)	N9A-C56A-C57A-C58A	169.6(6)
C11A-C18A-C19A-C20A	179.6(7)	C32'-C33'-C34'-C35'	-3(4)	C54A-C53A-C58A-C57A	2.6(11)
C18A-C19A-C20A-C21A	-1.7(11)	C33'-C34'-C35'-C36'	5(3)	O4A-C53A-C58A-C57A	-178.1(6)
C19A-C20A-C21A-C22A	3.3(11)	N6A'-C34'-C35'-C36'	-169.9(19)	C54A-C53A-C58A-O5A	-177.5(7)
C20A-C21A-C22A-N5A	-1.7(11)	C33'-C34'-C35'-N7A'	178(2)	O4A-C53A-C58A-O5A	1.8(10)
C26A-C23A-C24A-C25A	62.4(9)	N6A'-C34'-C35'-N7A'	3(3)	C56A-C57A-C58A-C53A	-0.2(10)
C93A-C23A-C24A-C25A	-171.1(7)	C34'-C35'-C36'-C37'	-8(3)	C56A-C57A-C58A-O5A	179.9(6)
C24A-C23A-C26A-C27A	-127.3(7)	N7A'-C35'-C36'-C37'	177.7(16)	O11A-C59A-C60A-C61A	-18.0(14)
C93A-C23A-C26A-C27A	104.9(8)	C48A-O3A'-C37'-C32'	-122.7(19)	N8A-C59A-C60A-C61A	160.5(8)
C24A-C23A-C26A-C31A	46.6(9)	C48A-O3A'-C37'-C36'	68(2)	O12A-C62A-C63A-C64A	21.4(13)
C93A-C23A-C26A-C31A	-81.2(8)	O2A'-C32'-C37'-O3A'	6(3)	N9A-C62A-C63A-C64A	-152.8(8)
C31A-C26A-C27A-O1A	174.5(6)	C33'-C32'-C37'-O3A'	-176.6(19)	C52A-C51A-C65A-C68A	118.0(8)
C23A-C26A-C27A-O1A	-11.4(10)	O2A'-C32'-C37'-C36'	174.1(19)	C50A-C51A-C65A-C68A	-57.1(8)
C31A-C26A-C27A-C28A	-3.8(10)	C33'-C32'-C37'-C36'	-9(3)	C52A-C51A-C65A-C66A	-9.3(10)
C23A-C26A-C27A-C28A	170.3(6)	C35'-C36'-C37'-O3A'	179.9(17)	C50A-C51A-C65A-C66A	175.6(6)
O1A-C27A-C28A-C29A	-174.9(6)	C35'-C36'-C37'-C32'	11(3)	C51A-C65A-C66A-C67A	-70.3(10)
C26A-C27A-C28A-C29A	3.4(11)	C33'-C34'-N6A'-C38'	33(3)	C68A-C65A-C66A-C67A	165.2(8)
C27A-C28A-C29A-C30A	0.1(11)	C35'-C34'-N6A'-C38'	-152(2)	C51A-C65A-C68A-C69A	103.9(8)
C27A-C28A-C29A-O2A'	-175.7(8)	C34'-N6A'-C38'-O9A'	23(3)	C66A-C65A-C68A-C69A	-127.8(7)
C27A-C28A-C29A-O2A	-165.6(11)	C34'-N6A'-C38'-C39'	-176.1(19)	C51A-C65A-C68A-C73A	-74.5(7)
C28A-C29A-C30A-C31A	-3.0(11)	O9A'-C38'-C39'-C40'	-46(3)	C66A-C65A-C68A-C73A	53.9(8)
O2A'-C29A-C30A-C31A	172.5(9)	N6A'-C38'-C39'-C40'	153.1(17)	C73A-C68A-C69A-O5A	-169.3(6)
O2A-C29A-C30A-C31A	161.0(11)	C36'-C35'-N7A'-C41'	-151.6(15)	C65A-C68A-C69A-O5A	12.4(11)
C28A-C29A-C30A-C44A	174.4(6)	C34'-C35'-N7A'-C41'	35(3)	C73A-C68A-C69A-C70A	5.4(10)
O2A'-C29A-C30A-C44A	-10.2(12)	C35'-N7A'-C41'-O10'	9(2)	C65A-C68A-C69A-C70A	-172.9(6)
O2A-C29A-C30A-C44A	-21.7(14)	C35'-N7A'-C41'-C42'	-167.0(14)	C68A-C69A-C70A-C71A	-5.2(11)
C29A-C30A-C31A-C26A	2.5(10)	O10'-C41'-C42'-C43'	-88.1(16)	O5A-C69A-C70A-C71A	170.0(6)
C44A-C30A-C31A-C26A	-174.9(6)	N7A'-C41'-C42'-C43'	88.5(15)	C69A-C70A-C71A-C72A	1.3(11)
C27A-C26A-C31A-C30A	0.8(10)	C31A-C30A-C44A-C47A	72.3(8)	C69A-C70A-C71A-O6A	-176.7(6)

Part 4		Part 5		Part 6	
C70A-C71A-C72A-C73A	1.9(10)	C12A-C11A-N4A-C10A	2.5(10)	N2B-C7B-C8B-C9B	162.7(6)
O6A-C71A-C72A-C73A	179.9(6)	C18A-C11A-N4A-C10A	-178.9(6)	N1B-C7B-C8B-C9B	-16.2(10)
C70A-C71A-C72A-C86A	-174.6(6)	C12A-C11A-N4A-Ru1A	169.9(5)	C12B-C8B-C9B-C10B	-1.6(9)
O6A-C71A-C72A-C86A	3.4(10)	C18A-C11A-N4A-Ru1A	-11.5(8)	C7B-C8B-C9B-C10B	179.7(6)
C71A-C72A-C73A-C68A	-1.6(10)	C9A-C10A-N4A-C11A	-2.4(10)	C8B-C9B-C10B-N4B	1.6(9)
C86A-C72A-C73A-C68A	175.1(6)	C13A-C10A-N4A-C11A	176.5(6)	C8B-C9B-C10B-C13B	179.6(6)
C69A-C68A-C73A-C72A	-2.1(10)	C9A-C10A-N4A-Ru1A	-170.0(5)	N4B-C11B-C12B-C8B	-2.1(9)
C65A-C68A-C73A-C72A	176.4(6)	C13A-C10A-N4A-Ru1A	8.9(8)	C18B-C11B-C12B-C8B	-179.5(6)
C79A-C74A-C75A-C76A	2.1(11)	C19A-C18A-N5A-C22A	3.3(10)	C9B-C8B-C12B-C11B	1.9(10)
O6A-C74A-C75A-C76A	177.5(6)	C11A-C18A-N5A-C22A	-177.9(6)	C7B-C8B-C12B-C11B	-179.4(6)
C74A-C75A-C76A-C77A	-1.8(11)	C19A-C18A-N5A-Ru1A	179.6(6)	N4B-C10B-C13B-N3B	-6.2(8)
C74A-C75A-C76A-N10A	175.9(6)	C11A-C18A-N5A-Ru1A	-1.5(8)	C9B-C10B-C13B-N3B	175.7(6)
C75A-C76A-C77A-C78A	1.0(11)	C21A-C22A-N5A-C18A	-1.6(10)	N4B-C10B-C13B-C14B	175.8(6)
N10A-C76A-C77A-C78A	-176.7(6)	C21A-C22A-N5A-Ru1A	-177.3(5)	C9B-C10B-C13B-C14B	-2.4(11)
C75A-C76A-C77A-N11A	-176.6(6)	O11A-C59A-N8A-C55A	-1.4(15)	N3B-C13B-C14B-C15B	2.1(10)
N10A-C76A-C77A-N11A	5.7(10)	C60A-C59A-N8A-C55A	-179.9(8)	C10B-C13B-C14B-C15B	-179.9(6)
C76A-C77A-C78A-C79A	-0.4(11)	C56A-C55A-N8A-C59A	-178.0(8)	C13B-C14B-C15B-C16B	-2.0(10)
N11A-C77A-C78A-C79A	177.0(7)	C54A-C55A-N8A-C59A	-0.4(12)	C14B-C15B-C16B-C17B	0.8(11)
C77A-C78A-C79A-C74A	0.8(11)	O12A-C62A-N9A-C56A	10.1(14)	C15B-C16B-C17B-N3B	0.5(11)
C77A-C78A-C79A-O7A	-175.1(6)	C63A-C62A-N9A-C56A	-175.7(8)	N4B-C11B-C18B-N5B	2.3(8)
C75A-C74A-C79A-C78A	-1.6(11)	C57A-C56A-N9A-C62A	45.3(12)	C12B-C11B-C18B-N5B	179.7(6)
O6A-C74A-C79A-C78A	-177.0(6)	C55A-C56A-N9A-C62A	-141.2(8)	N4B-C11B-C18B-C19B	-177.1(6)
C75A-C74A-C79A-O7A	174.2(6)	O13A-C80A-N10A-C76A	2.8(14)	C12B-C11B-C18B-C19B	0.4(10)
O6A-C74A-C79A-O7A	-1.1(10)	C81A-C80A-N10A-C76A	-178.3(8)	N5B-C18B-C19B-C20B	-0.7(9)
O13A-C80A-C81A-C82A	169.0(10)	C77A-C76A-N10A-C80A	-128.9(9)	C11B-C18B-C19B-C20B	178.6(6)
N10A-C80A-C81A-C82A	-10.0(14)	C75A-C76A-N10A-C80A	53.4(11)	C18B-C19B-C20B-C21B	-0.9(10)
O14A-C83A-C84A-C85A	-2.4(10)	O14A-C83A-N11A-C77A	-7.7(12)	C19B-C20B-C21B-C22B	1.0(10)
N11A-C83A-C84A-C85A	176.1(6)	C84A-C83A-N11A-C77A	173.8(7)	C20B-C21B-C22B-N5B	0.6(10)
C71A-C72A-C86A-C89A	-99.6(8)	C76A-C77A-N11A-C83A	-132.8(8)	C93B-C23B-C24B-C25B	-58.9(9)
C73A-C72A-C86A-C89A	84.0(8)	C78A-C77A-N11A-C83A	49.7(10)	C26B-C23B-C24B-C25B	173.2(7)
C71A-C72A-C86A-C87A	131.2(7)	C26A-C27A-O1A-C6A	-96.3(7)	C93B-C23B-C26B-C31B	-79.4(8)
C73A-C72A-C86A-C87A	-45.2(9)	C28A-C27A-O1A-C6A	82.0(7)	C24B-C23B-C26B-C31B	48.7(9)
C89A-C86A-C87A-C88A	62.6(9)	C5A-C6A-O1A-C27A	-78.4(5)	C93B-C23B-C26B-C27B	99.4(8)
C72A-C86A-C87A-C88A	-170.4(7)	C1A-C6A-O1A-C27A	94.9(5)	C24B-C23B-C26B-C27B	-132.4(7)
C72A-C86A-C89A-C90A	89.0(8)	C54A-C53A-O4A-C50A	-61.9(8)	C31B-C26B-C27B-C28B	-5.1(11)
C87A-C86A-C89A-C90A	-142.9(7)	C58A-C53A-O4A-C50A	118.8(7)	C23B-C26B-C27B-C28B	176.0(7)
C72A-C86A-C89A-C94A	-92.5(8)	C49A-C50A-O4A-C53A	115.6(7)	C31B-C26B-C27B-O2B	174.2(6)
C87A-C86A-C89A-C94A	35.7(10)	C51A-C50A-O4A-C53A	-69.3(8)	C23B-C26B-C27B-O2B	-4.7(10)
C94A-C89A-C90A-O7A	-172.6(6)	C53A-C58A-O5A-C69A	-25.5(10)	C26B-C27B-C28B-C29B	2.5(11)
C86A-C89A-C90A-O7A	6.1(10)	C57A-C58A-O5A-C69A	154.3(6)	O2B-C27B-C28B-C29B	-176.8(6)
C94A-C89A-C90A-C91A	2.9(10)	C68A-C69A-O5A-C58A	-48.0(10)	C27B-C28B-C29B-O3B	-172.1(7)
C86A-C89A-C90A-C91A	-178.4(6)	C70A-C69A-O5A-C58A	137.0(7)	C27B-C28B-C29B-C30B	2.3(11)
C89A-C90A-C91A-C92A	-0.6(10)	C79A-C74A-O6A-C71A	-96.0(8)	C28B-C29B-C30B-C31B	-4.1(10)
O7A-C90A-C91A-C92A	174.9(6)	C75A-C74A-O6A-C71A	88.5(8)	O3B-C29B-C30B-C31B	169.9(6)
C90A-C91A-C92A-O8A	-176.4(6)	C70A-C71A-O6A-C74A	-80.8(8)	C28B-C29B-C30B-C44B	173.5(7)
C90A-C91A-C92A-C93A	-2.0(10)	C72A-C71A-O6A-C74A	101.1(7)	O3B-C29B-C30B-C44B	-12.5(11)
C91A-C92A-C93A-C94A	1.9(10)	C78A-C79A-O7A-C90A	-82.2(8)	C27B-C26B-C31B-C30B	3.2(11)
O8A-C92A-C93A-C94A	176.5(6)	C74A-C79A-O7A-C90A	101.9(8)	C23B-C26B-C31B-C30B	-177.9(6)
C91A-C92A-C93A-C23A	-173.3(6)	C89A-C90A-O7A-C79A	-108.6(7)	C29B-C30B-C31B-C26B	1.2(10)
O8A-C92A-C93A-C23A	1.2(9)	C91A-C90A-O7A-C79A	75.7(8)	C44B-C30B-C31B-C26B	-176.5(7)
C26A-C23A-C93A-C92A	-90.7(8)	C91A-C92A-O8A-C1A	-81.1(8)	C37B-C32B-C33B-C34B	-1.2(13)
C24A-C23A-C93A-C92A	141.5(7)	C93A-C92A-O8A-C1A	104.2(7)	O3B-C32B-C33B-C34B	-179.2(7)
C26A-C23A-C93A-C94A	94.3(8)	C2A-C1A-O8A-C92A	67.3(6)	C32B-C33B-C34B-C35B	-0.5(13)
C24A-C23A-C93A-C94A	-33.5(10)	C6A-C1A-O8A-C92A	-114.7(5)	C32B-C33B-C34B-N6B	-179.2(8)
C92A-C93A-C94A-C89A	0.6(11)	O1B-C1B-C2B-C3B	178.2(6)	C33B-C34B-C35B-C36B	0.1(14)
C23A-C93A-C94A-C89A	175.6(7)	C6B-C1B-C2B-C3B	-3.1(10)	N6B-C34B-C35B-C36B	178.9(8)
C90A-C89A-C94A-C93A	-3.0(10)	C1B-C2B-C3B-N1B	178.3(7)	C33B-C34B-C35B-N7B	175.0(10)
C86A-C89A-C94A-C93A	178.4(7)	C1B-C2B-C3B-C4B	-4.2(10)	N6B-C34B-C35B-N7B	-6.3(15)
C4A-C3A-N1A-C7A	-1.8(6)	N1B-C3B-C4B-N2B	0.4(8)	C33B-C34B-C35B-N7B"	-172.3(10)
C2A-C3A-N1A-C7A	-177.5(4)	C2B-C3B-C4B-N2B	-177.7(6)	N6B-C34B-C35B-N7B"	6.5(14)
N2A-C7A-N1A-C3A	1.0(8)	N1B-C3B-C4B-C5B	-174.2(6)	C34B-C35B-C36B-C37B	1.7(13)
C8A-C7A-N1A-C3A	-179.6(6)	C2B-C3B-C4B-C5B	7.8(11)	N7B-C35B-C36B-C37B	-173.8(9)
C5A-C4A-N2A-C7A	176.8(4)	N2B-C4B-C5B-C6B	-176.7(7)	N7B"-C35B-C36B-C37B	174.5(9)
C3A-C4A-N2A-C7A	-1.4(6)	C3B-C4B-C5B-C6B	-3.4(10)	C33B-C32B-C37B-O4B	-175.3(7)
N1A-C7A-N2A-C4A	0.3(7)	C4B-C5B-C6B-O2B	177.8(6)	O3B-C32B-C37B-O4B	2.5(12)
C8A-C7A-N2A-C4A	-179.1(6)	C4B-C5B-C6B-C1B	-4.0(10)	C33B-C32B-C37B-C36B	3.1(12)
C16A-C17A-N3A-C13A	-0.2(12)	C2B-C1B-C6B-C5B	7.5(11)	O3B-C32B-C37B-C36B	-179.1(7)
C16A-C17A-N3A-Ru1A	174.2(6)	O1B-C1B-C6B-C5B	-173.7(6)	C35B-C36B-C37B-C32B	-3.3(13)
C14A-C13A-N3A-C17A	-1.5(10)	C2B-C1B-C6B-O2B	-174.2(6)	C35B-C36B-C37B-O4B	175.1(8)
C10A-C13A-N3A-C17A	176.2(7)	O1B-C1B-C6B-O2B	4.6(9)	C33B-C34B-N6B-C38B	49.8(13)
C14A-C13A-N3A-Ru1A	-176.8(5)	N2B-C7B-C8B-C12B	-16.0(10)	C35B-C34B-N6B-C38B	-128.9(10)
C10A-C13A-N3A-Ru1A	0.9(8)	N1B-C7B-C8B-C12B	165.1(6)	C34B-N6B-C38B-O9B	-3.3(16)

Part 7		Part 8		Part 9	
C34B-N6B-C38B-C39B	179.8(9)	C49B-C50B-O5B-C53B	117.6(9)	C65B-C68B-C73B-C72B	177.0(7)
O9B-C38B-C39B-C40B	-29.3(17)	C51B-C50B-O5B-C53B	-74.4(11)	C79B-C74B-C75B-C76B	-1.3
N6B-C38B-C39B-C40B	147.6(11)	C58B-C53B-O5B-C50B	114.6(14)	O7B-C74B-C75B-C76B	175.3(3)
C36B-C35B-N7B"-C41"	130.2(12)	C54B-C53B-O5B-C50B	-62.1(17)	C74B-C75B-C76B-C77B	-0.9
C34B-C35B-N7B"-C41"	-57.2(16)	C53B-C58B-O6B-C69B	-34(2)	C74B-C75B-C76B-N10B	177.0
C35B-N7B"-C41"-O10"	7.9(13)	C57B-C58B-O6B-C69B	155.8(13)	N10B-C76B-C77B-N11B	5.2(3)
C35B-N7B"-C41"-C42"	-172.1(13)	C58"-C53"-C54"-C55"	-0.1(3)	C75B-C76B-C77B-N11B	-177.1(3)
O10"-C41"-C42"-C43"	-150.9(16)	O5B"-C53"-C54"-C55"	-174.8(7)	N10B-C76B-C77B-C78B	-175.8
N7B"-C41"-C42"-C43"	29.0(16)	C53"-C54"-C55"-C56"	-0.1(3)	C75B-C76B-C77B-C78B	2.0
C36B-C35B-N7B-C41B	129.5(11)	C53"-C54"-C55"-N8B"	-179.9(2)	C76B-C77B-C78B-C79B	-0.8
C34B-C35B-N7B-C41B	-45.7(17)	N8B"-C55"-C56"-N9B"	-0.4(6)	N11B-C77B-C78B-C79B	178.2(3)
C35B-N7B-C41B-O10B	6.0(13)	C54"-C55"-C56"-N9B"	179.8(3)	C75B-C74B-C79B-C78B	2.6
C35B-N7B-C41B-C42B	-173.9(12)	N8B"-C55"-C56"-C57"	179.8(4)	O7B-C74B-C79B-C78B	-173.8(3)
O10B-C41B-C42B-C43B	29.0(15)	C54"-C55"-C56"-C57"	0.0(6)	C75B-C74B-C79B-O8B	176.6(3)
N7B-C41B-C42B-C43B	-151.0(15)	C55"-C56"-C57"-C58"	0.2(7)	O7B-C74B-C79B-O8B	0.2(4)
C31B-C30B-C44B-C45B	-52.9(9)	N9B"-C56"-C57"-C58"	-179.6(5)	C77B-C78B-C79B-C74B	-1.5
C29B-C30B-C44B-C45B	129.7(8)	C54"-C53"-C58"-C57"	0.2(6)	C77B-C78B-C79B-O8B	-175.7(3)
C31B-C30B-C44B-C47B	73.6(8)	O5B"-C53"-C58"-C57"	174.7(8)	O13B-C80B-C81B-C82B	70.6(4)
C29B-C30B-C44B-C47B	-103.8(8)	C54"-C53"-C58"-O6B"	174.0(9)	N10B-C80B-C81B-C82B	-95.3
C30B-C44B-C45B-C46B	-163.9(7)	O5B"-C53"-C58"-O6B"	-11.5(12)	O14B-C83B-C84B-C85B	-56.4(4)
C47B-C44B-C45B-C46B	72.5(8)	C56"-C57"-C58"-C53"	-0.3(8)	N11B-C83B-C84B-C85B	123.1(3)
C30B-C44B-C47B-C48B	62.5(9)	C56"-C57"-C58"-O6B"	-174.6(8)	O13B-C80B-N10B-C76B	11.5(4)
C45B-C44B-C47B-C48B	-170.4(7)	O11"-C59"-C60"-C61"	-7.8(7)	C81B-C80B-N10B-C76B	176.7
C30B-C44B-C47B-C52B	-113.1(8)	N8B"-C59"-C60"-C61"	172.2(6)	C77B-C76B-N10B-C80B	-60.2
C45B-C44B-C47B-C52B	14.0(10)	O12"-C62"-C63"-C64"	144.9(17)	C75B-C76B-N10B-C80B	121.9
C52B-C47B-C48B-C49B	3.2(11)	N9B"-C62"-C63"-C64"	-16.9(17)	O14B-C83B-N11B-C77B	-5.2(9)
C44B-C47B-C48B-C49B	-172.6(7)	O11"-C59"-N8B"-C55"	20.1(7)	C84B-C83B-N11B-C77B	175.4(4)
C52B-C47B-C48B-O4B	173.1(7)	C60"-C59"-N8B"-C55"	-159.9(7)	C76B-C77B-N11B-C83B	-130.8(4)
C44B-C47B-C48B-O4B	-2.7(10)	C56"-C55"-N8B"-C59"	35.2(7)	C78B-C77B-N11B-C83B	50.2(6)
O4B-C48B-C49B-C50B	-172.6(7)	C54"-C55"-N8B"-C59"	-144.9(6)	C72B-C71B-O7B-C74B	98.9(7)
C47B-C48B-C49B-C50B	-2.3(12)	O12"-C62"-N9B"-C56"	16(2)	C70B-C71B-O7B-C74B	-83.3(8)
C48B-C49B-C50B-O5B	169.8(7)	C63"-C62"-N9B"-C56"	175.9(9)	C79B-C74B-O7B-C71B	-98.1(5)
C48B-C49B-C50B-O5B"	177.8(7)	C55"-C56"-N9B"-C62"	146.1(10)	C75B-C74B-O7B-C71B	85.3(5)
C48B-C49B-C50B-C51B	1.6(12)	C57"-C56"-N9B"-C62"	-34.2(12)	C74B-C79B-O8B-C90B	101.5(5)
O5B-C50B-C51B-C52B	-169.0(7)	C49B-C50B-O5B"-C53"	122.8(9)	C78B-C79B-O8B-C90B	-83.9(5)
C49B-C50B-C51B-C52B	-1.9(11)	C51B-C50B-O5B"-C53"	-60.9(11)	C71B-C72B-C86B-C89B	-100.1(8)
O5B"-C50B-C51B-C52B	-178.2(7)	C58"-C53"-O5B"-C50B	126.9(7)	C73B-C72B-C86B-C89B	84.6(9)
O5B-C50B-C51B-C65B	7.5(11)	C54"-C53"-O5B"-C50B	-58.4(10)	C71B-C72B-C86B-C87B	131.7(7)
C49B-C50B-C51B-C65B	174.6(7)	C53"-C58"-O6B"-C69B	-16.8(17)	C73B-C72B-C86B-C87B	-43.6(10)
O5B"-C50B-C51B-C65B	-1.6(11)	C57"-C58"-O6B"-C69B	157.5(10)	C89B-C86B-C87B-C88B	171.8(7)
C48B-C47B-C52B-C51B	-3.5(11)	C50B-C51B-C65B-C66B	173.1(7)	C72B-C86B-C87B-C88B	-61.4(9)
C44B-C47B-C52B-C51B	172.2(7)	C52B-C51B-C65B-C66B	-10.7(10)	C72B-C86B-C89B-C90B	90.0(8)
C50B-C51B-C52B-C47B	2.9(11)	C50B-C51B-C65B-C68B	-61.6(9)	C87B-C86B-C89B-C90B	-143.6(7)
C65B-C51B-C52B-C47B	-173.5(7)	C52B-C51B-C65B-C68B	114.6(7)	C72B-C86B-C89B-C94B	-88.1(8)
C58B-C53B-C54B-C55B	6(2)	C51B-C65B-C66B-C67B	-177.7(7)	C87B-C86B-C89B-C94B	38.3(10)
O5B-C53B-C54B-C55B	-177.5(14)	C68B-C65B-C66B-C67B	60.3(9)	C79B-O8B-C90B-C89B	-105.8(6)
C53B-C54B-C55B-C56B	-4(2)	C66B-C65B-C68B-C73B	52.1(9)	C79B-O8B-C90B-C91B	77.7(7)
C53B-C54B-C55B-N8B	-178.3(14)	C51B-C65B-C68B-C73B	-74.2(8)	C94B-C89B-C90B-O8B	-176.5(6)
N8B-C55B-C56B-N9B	-11(3)	C66B-C65B-C68B-C69B	-132.0(8)	C86B-C89B-C90B-O8B	5.3(10)
C54B-C55B-C56B-N9B	175.1(15)	C51B-C65B-C68B-C69B	101.8(8)	C94B-C89B-C90B-C91B	-0.1(10)
N8B-C55B-C56B-C57B	175.4(15)	C73B-C68B-C69B-C70B	0.7(12)	C86B-C89B-C90B-C91B	-178.3(6)
C54B-C55B-C56B-C57B	1(3)	C65B-C68B-C69B-C70B	-175.4(8)	O8B-C90B-C91B-C92B	179.3(6)
C55B-C56B-C57B-C58B	0(2)	C73B-C68B-C69B-O6B"	-165.9(8)	C89B-C90B-C91B-C92B	3.0(10)
N9B-C56B-C57B-C58B	-174.1(15)	C65B-C68B-C69B-O6B"	18.0(12)	C90B-C91B-C92B-C93B	-6.0(11)
C54B-C53B-C58B-C57B	-5(2)	C73B-C68B-C69B-O6B	-175.7(8)	C90B-C91B-C92B-O1B	-179.6(6)
O5B-C53B-C58B-C57B	178.1(15)	C65B-C68B-C69B-O6B	8.2(13)	C91B-C92B-C93B-C94B	5.8(11)
C54B-C53B-C58B-O6B	-174.1(14)	C58"-O6B"-C69B-C70B	142.2(11)	O1B-C92B-C93B-C94B	179.5(6)
O5B-C53B-C58B-O6B	9(2)	C58"-O6B"-C69B-C68B	-50.5(16)	C91B-C92B-C93B-C23B	-171.1(7)
C56B-C57B-C58B-C53B	2(2)	C58B-O6B-C69B-C70B	142.9(12)	O1B-C92B-C93B-C23B	2.5(10)
C56B-C57B-C58B-O6B	172.1(14)	C58B-O6B-C69B-C68B	-40.5(17)	C24B-C23B-C93B-C92B	141.8(7)
O11B-C59B-C60B-C61B	2(2)	C68B-C69B-C70B-C71B	-0.1(13)	C26B-C23B-C93B-C92B	-91.1(8)
N8B-C59B-C60B-C61B	-170.7(16)	O6B"-C69B-C70B-C71B	167.3(8)	C24B-C23B-C93B-C94B	-35.1(10)
O12B-C62B-C63B-C64B	-66.1(12)	O6B-C69B-C70B-C71B	176.7(8)	C26B-C23B-C93B-C94B	92.0(8)
N9B-C62B-C63B-C64B	88.3(9)	C69B-C70B-C71B-C72B	-1.9(12)	C92B-C93B-C94B-C89B	-2.6(10)
O11B-C59B-N8B-C55B	-4(3)	C69B-C70B-C71B-O7B	-179.7(7)	C23B-C93B-C94B-C89B	174.4(6)
C60B-C59B-N8B-C55B	167.7(14)	C70B-C71B-C72B-C73B	3.1(11)	C90B-C89B-C94B-C93B	-0.1(10)
C56B-C55B-N8B-C59B	145.5(16)	O7B-C71B-C72B-C73B	-179.2(6)	C86B-C89B-C94B-C93B	178.1(6)
C54B-C55B-N8B-C59B	-40(2)	C70B-C71B-C72B-C86B	-172.5(7)	C2B-C3B-N1B-C7B	177.5(7)
O12B-C62B-N9B-C56B	-41(2)	O7B-C71B-C72B-C86B	5.3(11)	C4B-C3B-N1B-C7B	-0.3(7)
C63B-C62B-N9B-C56B	168.9(13)	C71B-C72B-C73B-C68B	-2.5(11)	N2B-C7B-N1B-C3B	0.1(8)
C55B-C56B-N9B-C62B	-21(2)	C86B-C72B-C73B-C68B	172.9(7)	C8B-C7B-N1B-C3B	179.1(6)
C57B-C56B-N9B-C62B	153.1(15)	C69B-C68B-C73B-C72B	0.7(11)	N1B-C7B-N2B-C4B	0.2(8)

Part 10		Part 11		Part 12	
C8B-C7B-N2B-C4B	-178.9(6)	C10C-C13C-C14C-C15C	-173.5(8)	C44C-C47C-C48C-O4C	2.2(9)
C3B-C4B-N2B-C7B	-0.3(8)	C13C-C14C-C15C-C16C	-0.1(15)	C47C-C48C-C49C-C50C	0.6(10)
C5B-C4B-N2B-C7B	173.6(7)	C14C-C15C-C16C-C17C	-3.1(17)	O4C-C48C-C49C-C50C	-172.8(6)
C16B-C17B-N3B-C13B	-0.4(10)	C15C-C16C-C17C-N3C	5.1(17)	C48C-C49C-C50C-C51C	-3.0(10)
C16B-C17B-N3B-Ru1B	175.4(5)	N4C-C11C-C18C-C19C	-178.4(6)	C48C-C49C-C50C-O5C	174.4(6)
C14B-C13B-N3B-C17B	-0.9(9)	C12C-C11C-C18C-C19C	-1.0(11)	C49C-C50C-C51C-C52C	3.1(10)
C10B-C13B-N3B-C17B	-179.1(6)	N4C-C11C-C18C-N5C	4.8(8)	O5C-C50C-C51C-C52C	-174.3(6)
C14B-C13B-N3B-Ru1B	-177.3(5)	C12C-C11C-C18C-N5C	-177.9(6)	C49C-C50C-C51C-C65C	177.0(6)
C10B-C13B-N3B-Ru1B	4.6(7)	N5C-C18C-C19C-C20C	-5.7(10)	O5C-C50C-C51C-C65C	-0.4(9)
C9B-C10B-N4B-C11B	-1.9(10)	C11C-C18C-C19C-C20C	177.6(6)	C50C-C51C-C52C-C47C	-0.7(10)
C13B-C10B-N4B-C11B	179.8(5)	C18C-C19C-C20C-C21C	4.1(10)	C65C-C51C-C52C-C47C	-174.3(6)
C9B-C10B-N4B-Ru1B	-176.9(5)	C19C-C20C-C21C-C22C	-2.2(10)	C48C-C47C-C52C-C51C	-1.5(10)
C13B-C10B-N4B-Ru1B	4.8(7)	C20C-C21C-C22C-N5C	2.0(10)	C44C-C47C-C52C-C51C	170.7(6)
C12B-C11B-N4B-C10B	2.1(9)	C93C-C23C-C24C-C25*	-107.2(7)	O5C-C53C-C54C-C55C	-176.0(7)
C18B-C11B-N4B-C10B	179.8(6)	C26C-C23C-C24C-C25*	127.3(7)	C58C-C53C-C54C-C55C	5.6(12)
C12B-C11B-N4B-Ru1B	177.2(5)	C93C-C23C-C24C-C25C	-172.6(7)	C53C-C54C-C55C-C56C	-5.7(13)
C18B-C11B-N4B-Ru1B	-5.1(7)	C26C-C23C-C24C-C25C	61.8(8)	C53C-C54C-C55C-N8C	178.6(7)
C21B-C22B-N5B-C18B	-2.2(10)	C24C-C23C-C26C-C31C	42.8(8)	C54C-C55C-C56C-N9C	-179.5(8)
C21B-C22B-N5B-Ru1B	179.7(5)	C93C-C23C-C26C-C31C	-83.1(7)	N8C-C55C-C56C-N9C	-3.8(13)
C19B-C18B-N5B-C22B	2.3(9)	C24C-C23C-C26C-C27C	-136.1(7)	C54C-C55C-C56C-C57C	1.3(13)
C11B-C18B-N5B-C22B	-177.1(6)	C93C-C23C-C26C-C27C	98.1(7)	N8C-C55C-C56C-C57C	177.1(8)
C19B-C18B-N5B-Ru1B	-179.3(5)	C31C-C26C-C27C-O2C	174.2(6)	C55C-C56C-C57C-C58C	3.2(13)
C11B-C18B-N5B-Ru1B	1.3(7)	C23C-C26C-C27C-O2C	-7.0(10)	N9C-C56C-C57C-C58C	-176.0(8)
C2B-C1B-O1B-C92B	65.1(9)	C31C-C26C-C27C-C28C	-4.7(9)	C56C-C57C-C58C-O6C	174.8(7)
C6B-C1B-O1B-C92B	-113.7(7)	C23C-C26C-C27C-C28C	174.2(6)	C56C-C57C-C58C-C53C	-3.2(11)
C93B-C92B-O1B-C1B	104.4(7)	C26C-C27C-C28C-C29C	0.9(10)	O5C-C53C-C58C-O6C	2.7(11)
C91B-C92B-O1B-C1B	-81.5(8)	O2C-C27C-C28C-C29C	-177.9(6)	C54C-C53C-C58C-O6C	-178.9(7)
C5B-C6B-O2B-C27B	-82.3(8)	C27C-C28C-C29C-C30C	2.8(10)	O5C-C53C-C58C-C57C	-179.5(6)
C1B-C6B-O2B-C27B	99.4(7)	C27C-C28C-C29C-O3C	-172.4(6)	C54C-C53C-C58C-C57C	-1.1(11)
C28B-C27B-O2B-C6B	76.9(8)	C28C-C29C-C30C-C31C	-2.5(9)	C54C-C55C-N8C-C59*	-68.9(14)
C26B-C27B-O2B-C6B	-102.5(8)	O3C-C29C-C30C-C31C	172.3(6)	C56C-C55C-N8C-C59*	115.3(13)
C28B-C29B-O3B-C32B	-133.1(7)	C28C-C29C-C30C-C44C	170.0(6)	C54C-C55C-N8C-C59C	27.1(15)
C30B-C29B-O3B-C32B	52.5(10)	O3C-C29C-C30C-C44C	-15.2(10)	C56C-C55C-N8C-C59C	-148.7(11)
C37B-C32B-O3B-C29B	17.0(12)	C29C-C30C-C31C-C26C	-1.7(9)	C55C-N8C-C59C-O11C	20(2)
C33B-C32B-O3B-C29B	-165.0(7)	C44C-C30C-C31C-C26C	-174.8(6)	C55C-N8C-C59C-C60C	-177.5(9)
C32B-C37B-O4B-C48B	-117.7(8)	C27C-C26C-C31C-C30C	5.2(10)	O11C-C59C-C60C-C61C	-122(2)
C36B-C37B-O4B-C48B	63.9(9)	C23C-C26C-C31C-C30C	-173.7(6)	N8C-C59C-C60C-C61C	76.7(18)
C49B-C48B-O4B-C37B	-120.9(8)	O3C-C32C-C33C-C34C	179.2(7)	C55C-N8C-C59*-O11*	7(2)
C47B-C48B-O4B-C37B	68.6(9)	C37C-C32C-C33C-C34C	-1.5(11)	C55C-N8C-C59*-C60*	176.0(9)
C6C-C1C-C2C-C3C	1.7(10)	C32C-C33C-C34C-C35C	1.0(12)	O11*-C59*-C60*-C61*	81(2)
O1C-C1C-C2C-C3C	178.2(6)	C32C-C33C-C34C-N6C	-174.7(7)	N8C-C59*-C60*-C61*	-85.5(18)
C1C-C2C-C3C-N1C	175.4(6)	C33C-C34C-C35C-C36C	0.2(12)	C55C-C56C-N9C-C62C	-53.1(16)
C1C-C2C-C3C-C4C	-5.0(9)	N6C-C34C-C35C-C36C	175.9(7)	C57C-C56C-N9C-C62C	126.0(13)
N1C-C3C-C4C-C5C	-176.5(6)	C33C-C34C-C35C-N7C	-179.2(7)	C55C-C56C-N9C-C62*	48.5(15)
C2C-C3C-C4C-C5C	3.9(10)	N6C-C34C-C35C-N7C	-3.4(12)	C57C-C56C-N9C-C62*	-132.3(11)
N1C-C3C-C4C-N2C	0.5(7)	C34C-C35C-C36C-C37C	-0.7(11)	C56C-N9C-C62C-O12C	12(2)
C2C-C3C-C4C-N2C	-179.1(6)	N7C-C35C-C36C-C37C	178.7(7)	C56C-N9C-C62C-C63C	-162.8(10)
C3C-C4C-C5C-C6C	0.7(10)	C35C-C36C-C37C-C32C	0.1(11)	O12C-C62C-C63C-C64C	-75(3)
N2C-C4C-C5C-C6C	-175.6(6)	C35C-C36C-C37C-O4C	179.1(6)	N9C-C62C-C63C-C64C	99.0(18)
C2C-C1C-C6C-C5C	2.8(11)	O3C-C32C-C37C-C36C	-179.8(7)	C56C-N9C-C62*-O12*	20(3)
O1C-C1C-C6C-C5C	-173.6(6)	C33C-C32C-C37C-C36C	1.0(11)	C56C-N9C-C62*-C63*	-167.4(10)
C2C-C1C-C6C-O2C	-175.8(6)	O3C-C32C-C37C-O4C	1.2(11)	O12*-C62*-C63*-C64*	-83(3)
O1C-C1C-C6C-O2C	7.9(9)	C33C-C32C-C37C-O4C	-178.0(6)	N9C-C62*-C63*-C64*	102.9(18)
C4C-C5C-C6C-C1C	-4.0(10)	O9C-C38C-C39C-C40C	22(2)	C52C-C51C-C65C-C68C	115.4(7)
C4C-C5C-C6C-O2C	174.5(6)	N6C-C38C-C39C-C40C	-162.9(13)	C50C-C51C-C65C-C68C	-58.1(8)
N2C-C7C-C8C-C12C	-18.8(10)	O10C-C41C-C42C-C43C	-83.2(18)	C52C-C51C-C65C-C66C	-10.6(9)
N1C-C7C-C8C-C12C	160.4(6)	N7C-C41C-C42C-C43C	95.6(16)	C50C-C51C-C65C-C66C	175.8(6)
N2C-C7C-C8C-C9C	157.2(7)	O10C-C41C-C42*-C43*	-64(2)	C68C-C65C-C66C-C67C	63.5(8)
N1C-C7C-C8C-C9C	-23.6(10)	N7C-C41C-C42*-C43*	128.1(15)	C51C-C65C-C66C-C67C	-174.1(6)
C12C-C8C-C9C-C10C	-3.8(10)	C31C-C30C-C44C-C47C	71.8(8)	C66C-C65C-C68C-C73C	51.5(9)
C7C-C8C-C9C-C10C	-179.8(6)	C29C-C30C-C44C-C47C	-100.5(8)	C51C-C65C-C68C-C73C	-74.5(8)
C8C-C9C-C10C-N4C	1.7(10)	C31C-C30C-C44C-C45C	-57.0(8)	C66C-C65C-C68C-C69C	-132.3(7)
C8C-C9C-C10C-C13C	-179.5(7)	C29C-C30C-C44C-C45C	130.7(7)	C51C-C65C-C68C-C69C	101.7(8)
C9C-C8C-C12C-C11C	4.6(10)	C47C-C44C-C45C-C46C	174.8(6)	C73C-C68C-C69C-C70C	3.5(10)
C7C-C8C-C12C-C11C	-179.3(6)	C30C-C44C-C45C-C46C	-58.9(8)	C65C-C68C-C69C-C70C	-172.9(7)
N4C-C11C-C12C-C8C	-3.2(10)	C30C-C44C-C47C-C52C	-114.9(7)	C73C-C68C-C69C-O6C	-166.3(6)
C18C-C11C-C12C-C8C	179.5(6)	C45C-C44C-C47C-C52C	13.7(9)	C65C-C68C-C69C-O6C	17.3(10)
N4C-C10C-C13C-N3C	-4.9(9)	C30C-C44C-C47C-C48C	57.1(8)	C68C-C69C-C70C-C71C	-1.2(11)
C9C-C10C-C13C-N3C	176.3(7)	C45C-C44C-C47C-C48C	-174.3(6)	O6C-C69C-C70C-C71C	169.3(6)
N4C-C10C-C13C-C14C	170.4(7)	C52C-C47C-C48C-C49C	1.5(9)	C69C-C70C-C71C-C72C	-4.3(11)
C9C-C10C-C13C-C14C	-8.4(12)	C44C-C47C-C48C-C49C	-171.0(6)	C69C-C70C-C71C-O7C	-177.1(6)
N3C-C13C-C14C-C15C	1.4(13)	C52C-C47C-C48C-O4C	174.7(6)	C70C-C71C-C72C-C73C	7.0(11)

Part 13		Part 14		Part 15	
O7C-C71C-C72C-C73C	179.4(6)	C87C-C86C-C89C-C94C	38.7(10)	C19C-C18C-N5C-Ru1C	-178.2(5)
C70C-C71C-C72C-C86C	-173.8(7)	C72C-C86C-C89C-C90C	94.4(8)	C11C-C18C-N5C-Ru1C	-1.2(7)
O7C-C71C-C72C-C86C	-1.3(10)	C87C-C86C-C89C-C90C	-138.3(7)	O9C-C38C-N6C-C34C	-7(2)
C69C-C68C-C73C-C72C	-0.5(10)	C94C-C89C-C90C-C91C	2.9(10)	C39C-C38C-N6C-C34C	177.8(10)
C65C-C68C-C73C-C72C	176.0(7)	C86C-C89C-C90C-C91C	-179.9(6)	C33C-C34C-N6C-C38C	-38.3(15)
C71C-C72C-C73C-C68C	-4.5(10)	C94C-C89C-C90C-O8C	-174.6(6)	C35C-C34C-N6C-C38C	145.9(11)
C86C-C72C-C73C-C68C	176.3(7)	C86C-C89C-C90C-O8C	2.6(9)	O10C-C41C-N7C-C35C	9.3(14)
C79C-C74C-C75C-C76C	-3.7(11)	O8C-C90C-C91C-C92C	177.2(6)	C42*-C41C-N7C-C35C	177.5(11)
O7C-C74C-C75C-C76C	172.0(6)	C89C-C90C-C91C-C92C	-0.2(11)	C42C-C41C-N7C-C35C	-169.6(8)
C74C-C75C-C76C-C77C	4.2(11)	C90C-C91C-C92C-O1C	-176.8(6)	C34C-C35C-N7C-C41C	-70.7(11)
C74C-C75C-C76C-N10C	176.1(8)	C90C-C91C-C92C-C93C	-2.4(11)	C36C-C35C-N7C-C41C	109.9(9)
C74C-C75C-C76C-N10*	179.5(9)	C91C-C92C-C93C-C94C	2.1(10)	O14C-C83C-N11C-C77C	-8.0(12)
C75C-C76C-C77C-N11C	-178.7(6)	O1C-C92C-C93C-C94C	176.6(6)	C84C-C83C-N11C-C77C	169.3(7)
N10C-C76C-C77C-N11C	11.3(14)	C91C-C92C-C93C-C23C	-171.5(6)	C76C-C77C-N11C-C83C	-127.1(8)
N10*-C76C-C77C-N11C	5.4(12)	O1C-C92C-C93C-C23C	3.0(9)	C78C-C77C-N11C-C83C	57.5(10)
C75C-C76C-C77C-C78C	-3.4(11)	C24C-C23C-C93C-C94C	-29.0(9)	C91C-C92C-O1C-C1C	-85.2(8)
N10C-C76C-C77C-C78C	-173.4(9)	C26C-C23C-C93C-C94C	96.7(8)	C93C-C92C-O1C-C1C	100.1(7)
N10*-C76C-C77C-C78C	-179.3(9)	C24C-C23C-C93C-C92C	144.1(6)	C6C-C1C-O1C-C92C	-112.5(7)
C76C-C77C-C78C-C79C	2.1(11)	C26C-C23C-C93C-C92C	-90.1(7)	C2C-C1C-O1C-C92C	70.9(8)
N11C-C77C-C78C-C79C	177.5(6)	C90C-C89C-C94C-C93C	-3.2(10)	C26C-C27C-O2C-C6C	-98.9(7)
C77C-C78C-C79C-O8C	-174.9(6)	C86C-C89C-C94C-C93C	179.7(6)	C28C-C27C-O2C-C6C	80.0(7)
C77C-C78C-C79C-C74C	-1.5(11)	C92C-C93C-C94C-C89C	0.8(10)	C1C-C6C-O2C-C27C	97.4(7)
C75C-C74C-C79C-C78C	2.3(11)	C23C-C93C-C94C-C89C	174.3(6)	C5C-C6C-O2C-C27C	-81.2(8)
O7C-C74C-C79C-C78C	-173.2(6)	C4C-C3C-N1C-C7C	-0.4(7)	C37C-C32C-O3C-C29C	22.3(11)
C75C-C74C-C79C-O8C	175.8(6)	C2C-C3C-N1C-C7C	179.2(7)	C33C-C32C-O3C-C29C	-158.5(7)
O7C-C74C-C79C-O8C	0.2(10)	N2C-C7C-N1C-C3C	0.2(8)	C28C-C29C-O3C-C32C	-134.8(7)
C77C-C76C-N10C-C80C	-52.9(19)	C8C-C7C-N1C-C3C	-179.0(6)	C30C-C29C-O3C-C32C	50.0(10)
C75C-C76C-N10C-C80C	136.4(13)	N1C-C7C-N2C-C4C	0.1(8)	C36C-C37C-O4C-C48C	62.8(8)
C76C-N10C-C80C-O13C	-6(2)	C8C-C7C-N2C-C4C	179.3(6)	C32C-C37C-O4C-C48C	-118.2(7)
C76C-N10C-C80C-C81C	176.3(11)	C3C-C4C-N2C-C7C	-0.4(7)	C49C-C48C-O4C-C37C	-120.3(6)
O13C-C80C-C81C-C82C	83.5(19)	C5C-C4C-N2C-C7C	176.3(7)	C47C-C48C-O4C-C37C	66.2(8)
N10C-C80C-C81C-C82C	-98.4(15)	C16C-C17C-N3C-C13C	-3.8(14)	C54C-C53C-O5C-C50C	-61.5(9)
C77C-C76C-N10*-C80*	-59.6(18)	C16C-C17C-N3C-Ru1C	169.5(7)	C58C-C53C-O5C-C50C	116.8(7)
C75C-C76C-N10*-C80*	124.9(15)	C14C-C13C-N3C-C17C	0.5(13)	C49C-C50C-O5C-C53C	113.2(7)
C76C-N10*-C80*-O13*	13(3)	C10C-C13C-N3C-C17C	175.9(7)	C51C-C50C-O5C-C53C	-69.3(8)
C76C-N10*-C80*-C81*	-173.4(13)	C14C-C13C-N3C-Ru1C	-173.4(7)	C57C-C58C-O6C-C69C	162.2(6)
O13*-C80*-C81*-C82*	165.9(17)	C10C-C13C-N3C-Ru1C	1.9(9)	C53C-C58C-O6C-C69C	-20.0(11)
N10*-C80*-C81*-C82*	-9(2)	C12C-C11C-N4C-C10C	1.0(10)	C70C-C69C-O6C-C58C	132.6(7)
O14C-C83C-C84C-C85*	156.3(11)	C18C-C11C-N4C-C10C	178.7(6)	C68C-C69C-O6C-C58C	-56.8(10)
N11C-C83C-C84C-C85*	-21.0(14)	C12C-C11C-N4C-Ru1C	176.1(5)	C75C-C74C-O7C-C71C	87.6(8)
O14C-C83C-C84C-C85C	-20.6(14)	C18C-C11C-N4C-Ru1C	-6.3(7)	C79C-C74C-O7C-C71C	-96.7(8)
N11C-C83C-C84C-C85C	162.2(10)	C9C-C10C-N4C-C11C	-0.4(10)	C72C-C71C-O7C-C74C	101.6(8)
C71C-C72C-C86C-C89C	-97.5(8)	C13C-C10C-N4C-C11C	-179.3(6)	C70C-C71C-O7C-C74C	-85.3(8)
C73C-C72C-C86C-C89C	81.7(8)	C9C-C10C-N4C-Ru1C	-175.3(5)	C78C-C79C-O8C-C90C	-85.0(8)
C71C-C72C-C86C-C87C	134.9(7)	C13C-C10C-N4C-Ru1C	5.7(8)	C74C-C79C-O8C-C90C	101.6(8)
C73C-C72C-C86C-C87C	-45.9(10)	C21C-C22C-N5C-C18C	-3.7(10)	C91C-C90C-O8C-C79C	75.1(8)
C89C-C86C-C87C-C88C	61.3(9)	C21C-C22C-N5C-Ru1C	-179.4(5)	C89C-C90C-O8C-C79C	-107.5(7)
C72C-C86C-C87C-C88C	-172.7(7)	C19C-C18C-N5C-C22C	5.5(9)		
C72C-C86C-C89C-C94C	-88.5(8)	C11C-C18C-N5C-C22C	-177.5(6)		

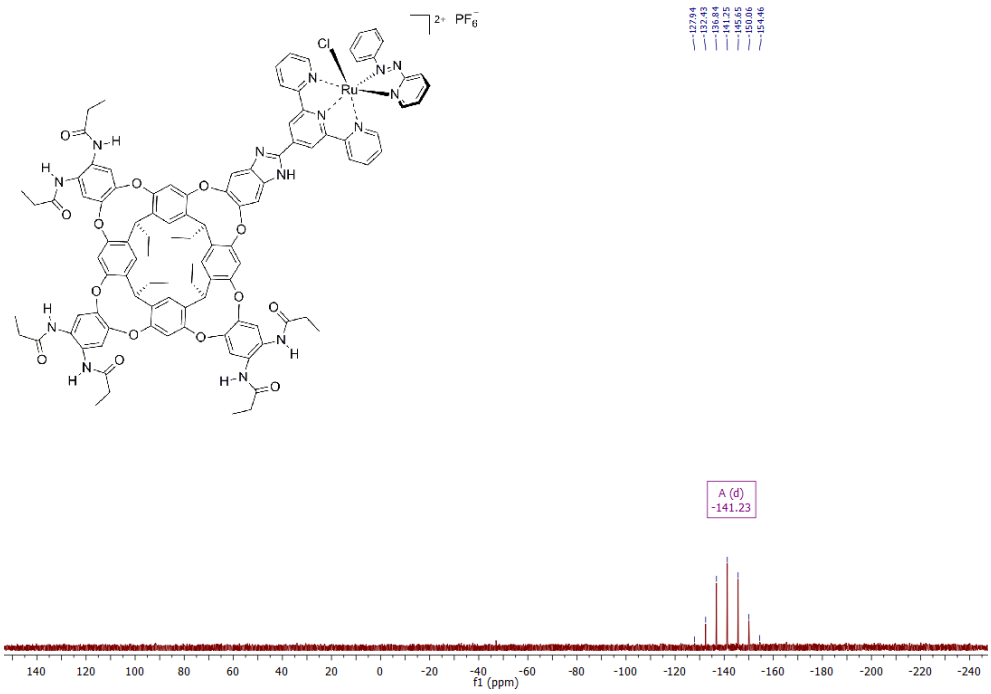

Fig. 105. ^{31}P NMR spectrum of the metallocavitand **azpy**•Ru^{II}•Cl•**C24** (**C26**) in $CDCl_3$.

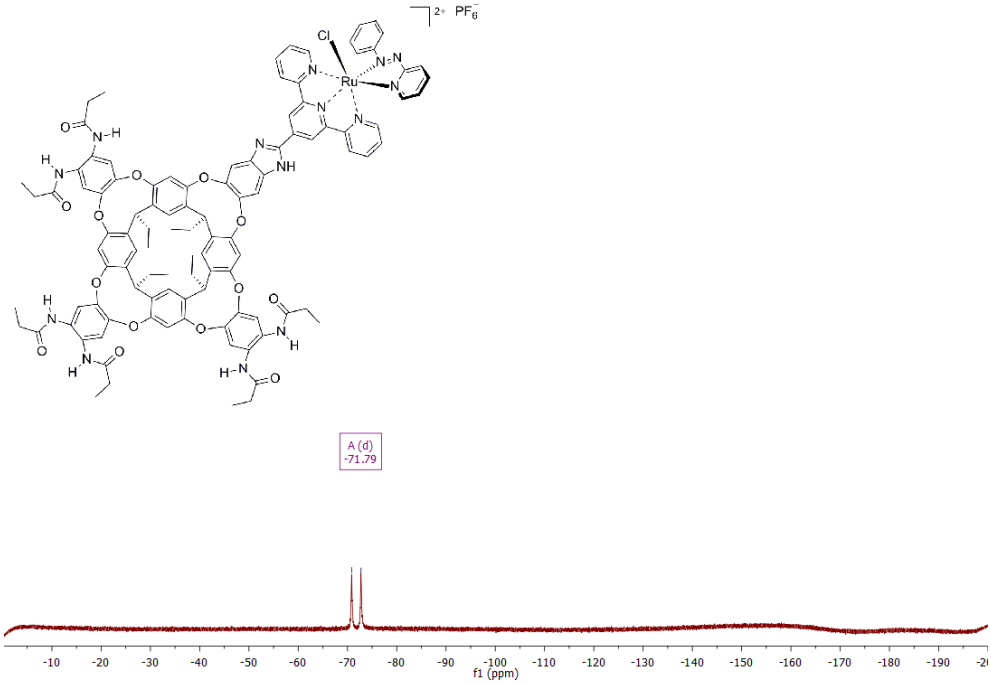

Fig. 106. ^{19}F NMR spectrum of the metallocavitand cavitand **azpy**•Ru^{II}•Cl•**C24** (**C26**) in $CDCl_3$.

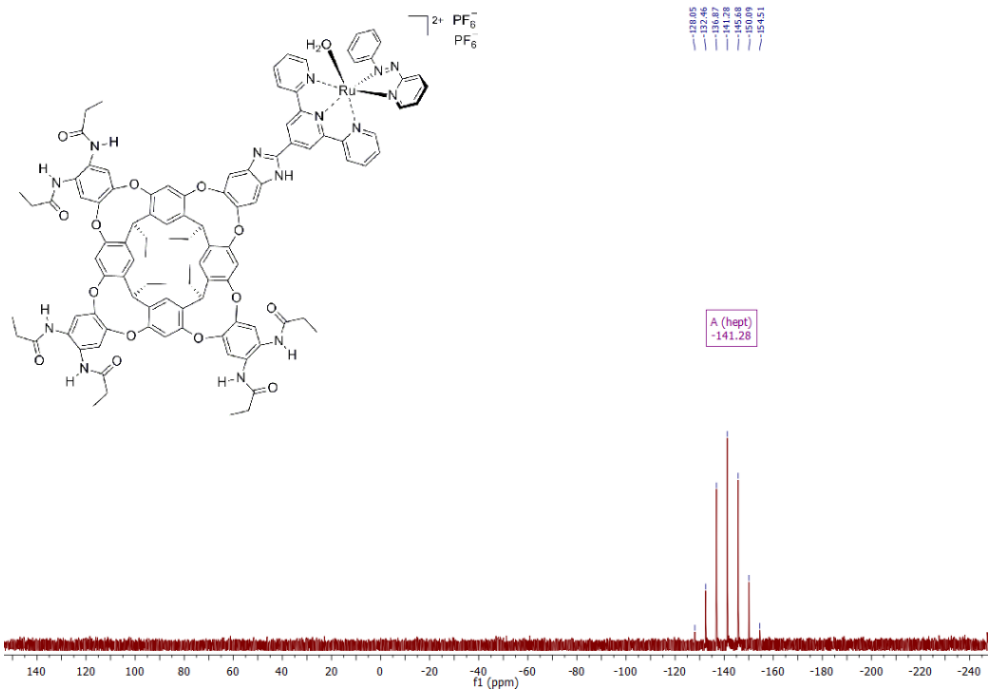

Fig. 107. ^{31}P NMR spectrum of the metallocavitand **azpy**•Ru^{II}•(H_2O)•**C24 (C27)** in $CDCl_3$.

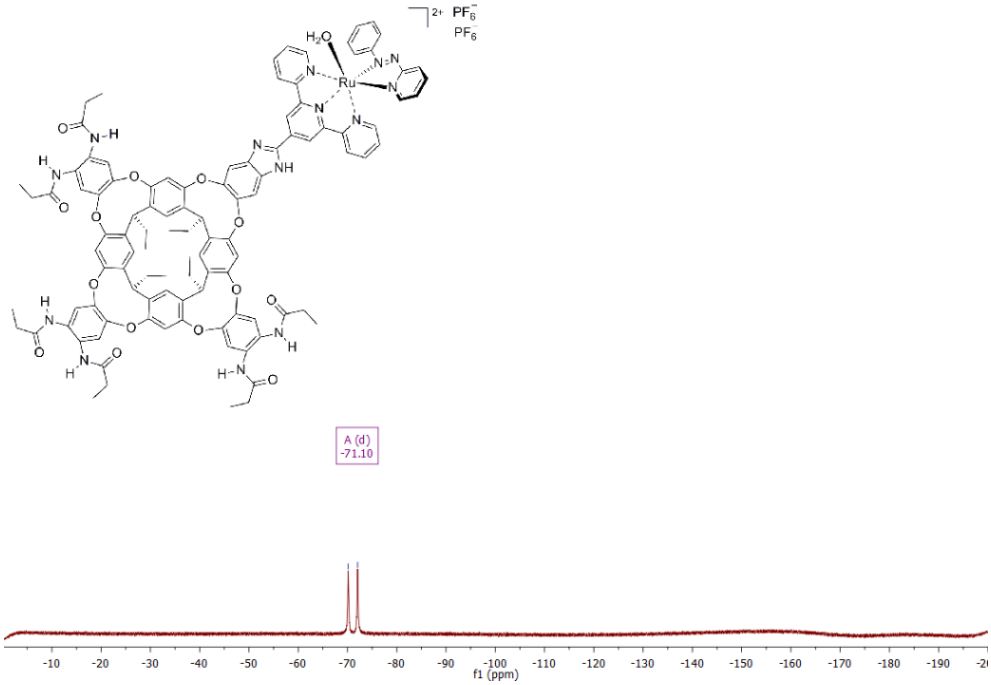

Fig. 108. ^{19}F NMR spectrum of the metallocavitand **azpy**•Ru^{II}•(H_2O)•**C24 (C27)** in $CDCl_3$.

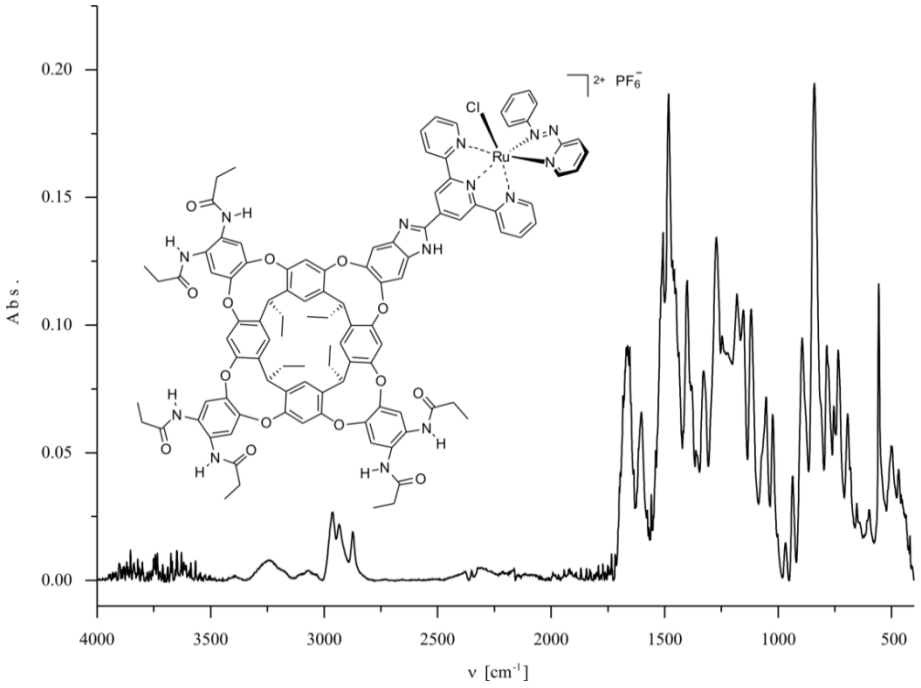

Fig. 109. ATR FT-IR spectrum of **azpy**•Ru^{II}•Cl•**C24** (**C26**).

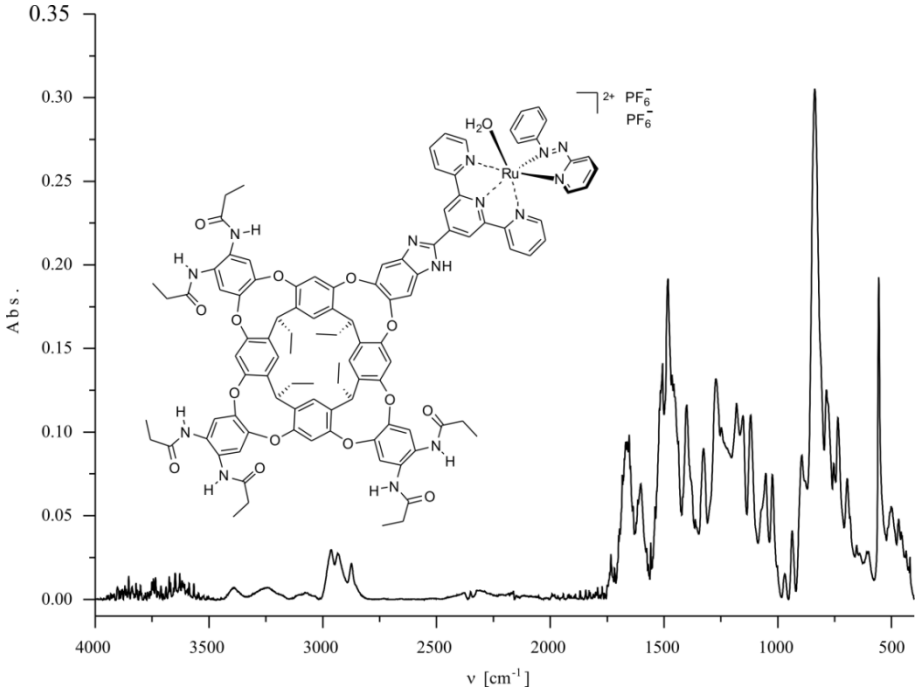

Fig. 110. ATR FT-IR spectrum of **azpy**•Ru^{II}•(H_2O)•**C24** (**C27**).

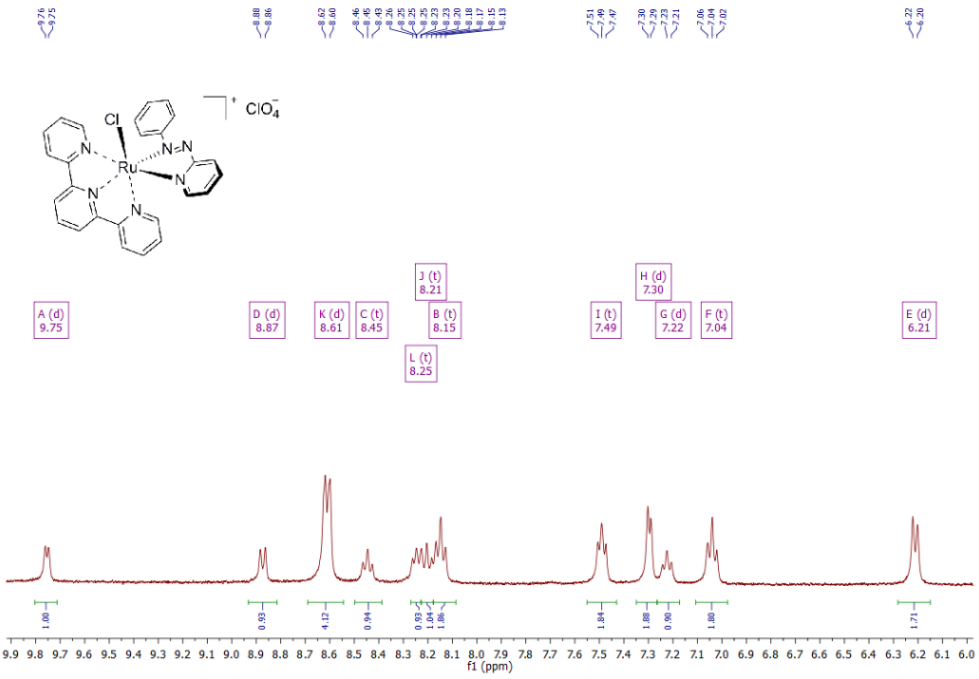

Fig. 111. ^{1}H NMR spectrum of the organometallic complex **azpy**•Ru^{II}•Cl•**tpy** (**46**) in DMSO-d_6.

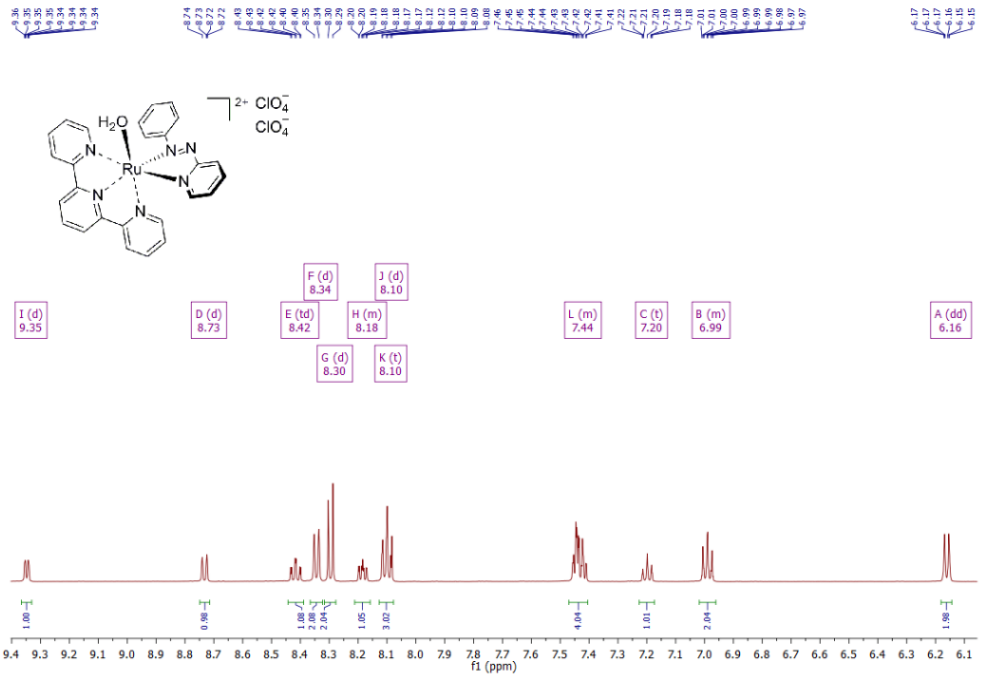

Fig. 112. ^{1}H NMR spectrum of the organometallic complex **azpy**•Ru^{II}•(H_2O)•**tpy** (**47**) in D_2O.

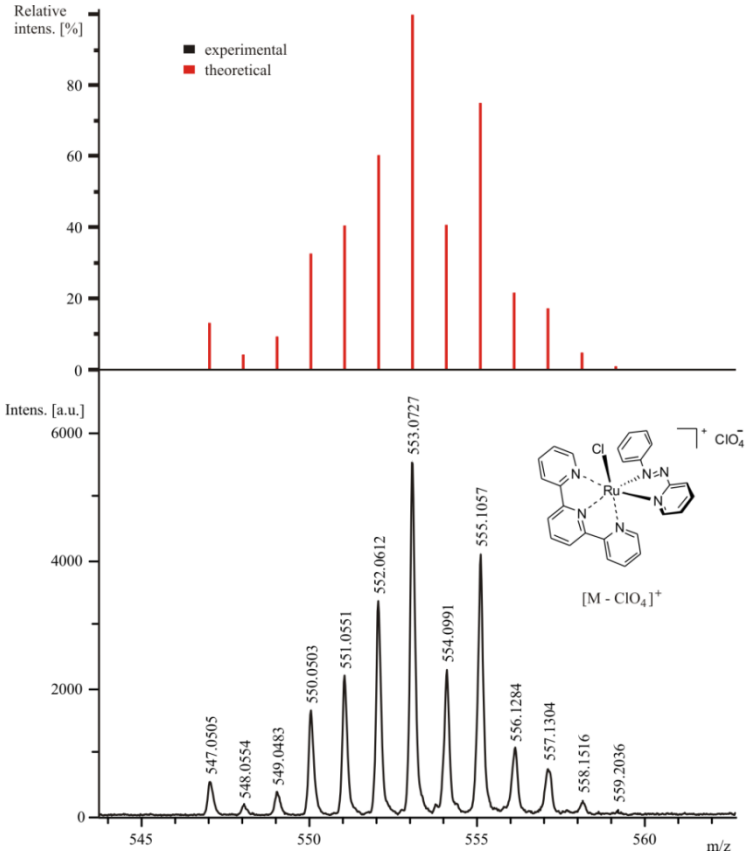

Fig. 113. MALDI-MS (+) isotopic pattern for the organometallic complex *trans*-**azpy**•Ru^{II}•Cl•**tpy** (**46**).

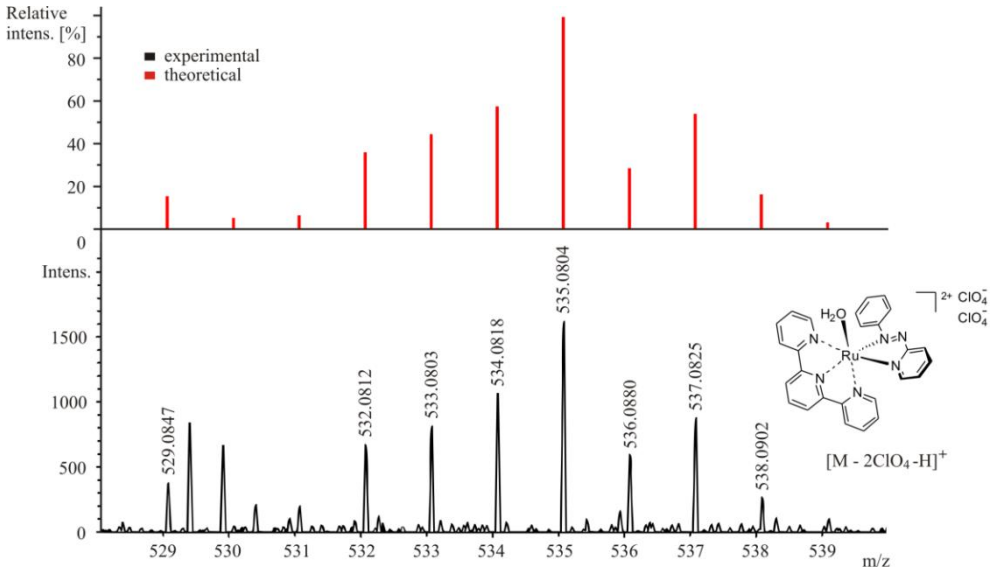

Fig. 114. ESI-MS (+) isotopic pattern for the organometallic complex *trans*-**azpy**•Ru^{II}•(H_2O)•**tpy** (**47**).

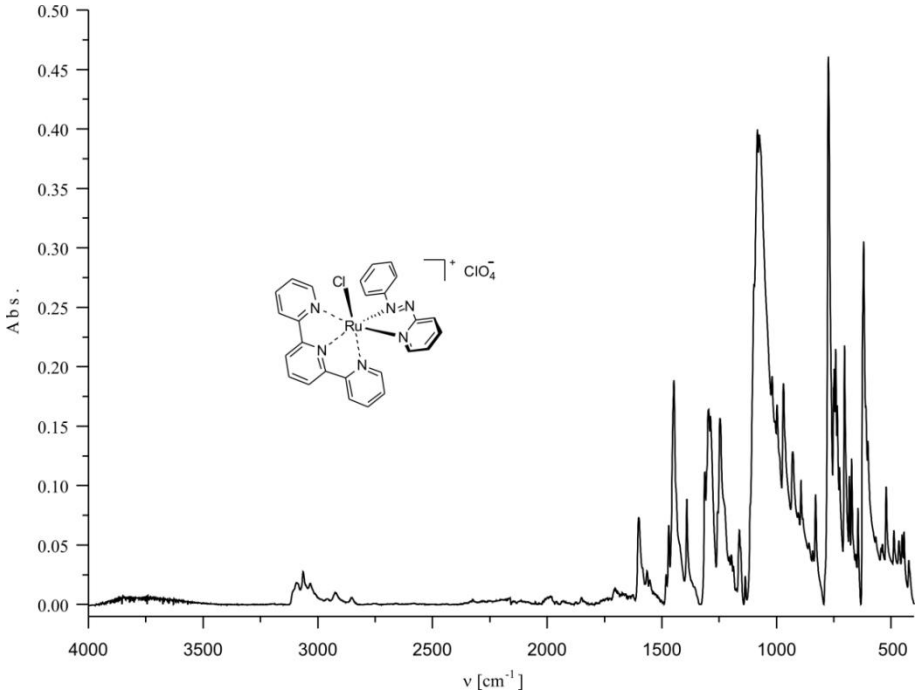

Fig. 115. ATR FT-IR spectrum of the organometallic complex *trans*-**azpy**•Ru^{II}•Cl•**tpy** (**46**).

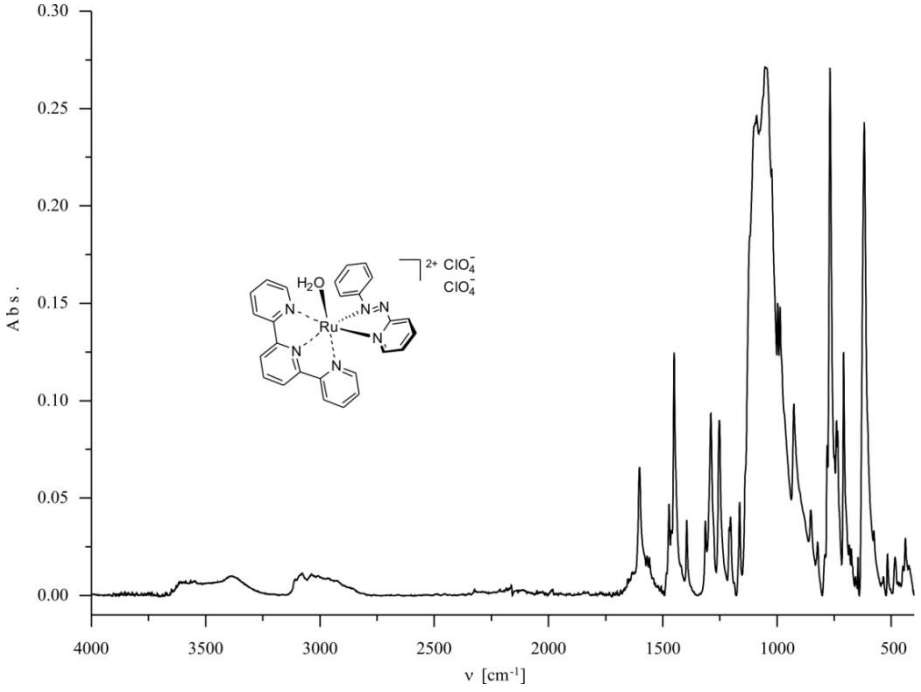

Fig. 116. ATR FT-IR spectrum of the organometallic complex *trans*-**azpy**•Ru^{II}•(H_2O)•**tpy** (**47**).

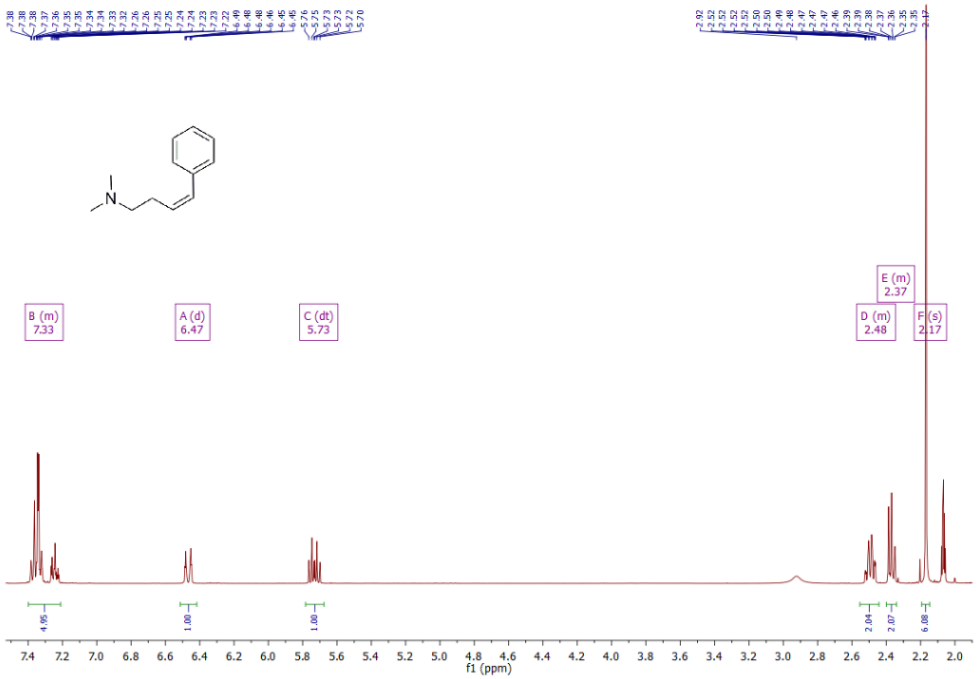

Fig. 117. ^{1}H NMR spectrum of **50b** in acetone-d_6.

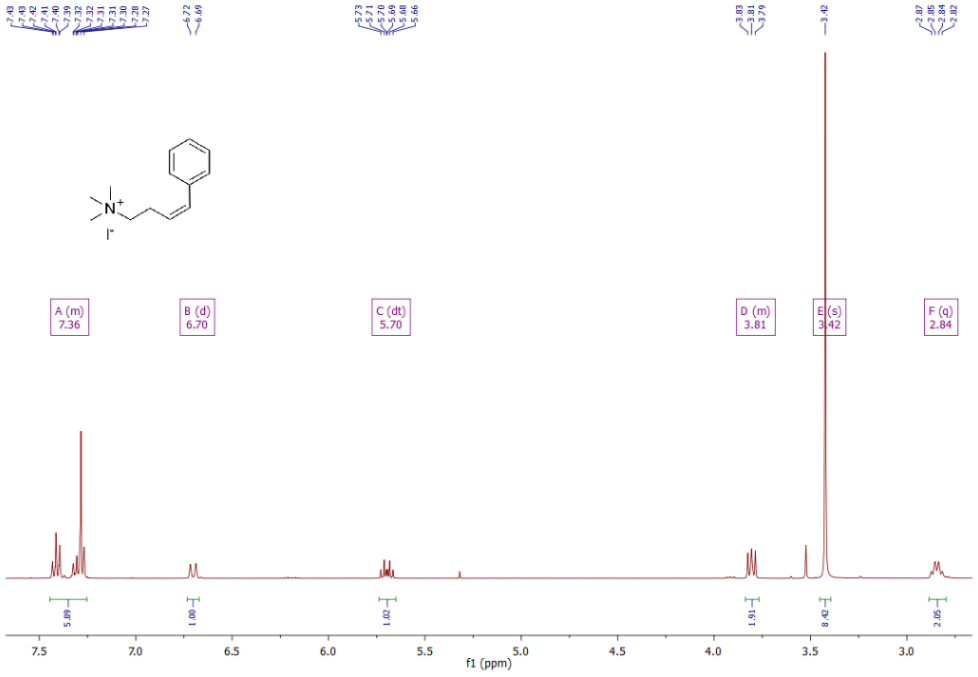

Fig. 118. ^{1}H NMR spectrum of **50c** in $CDCl_3$.

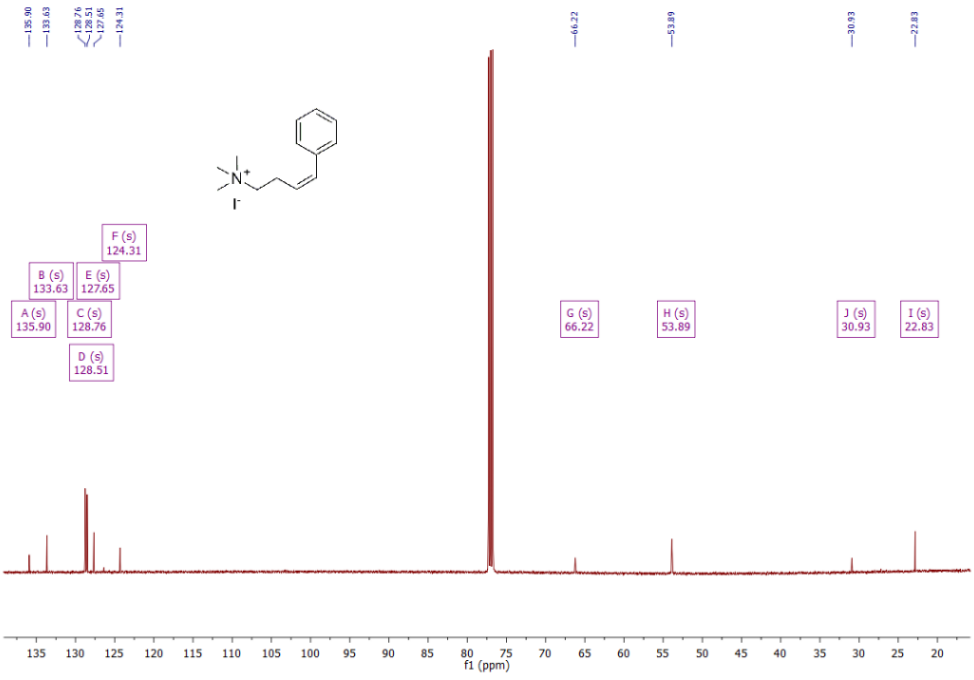

Fig. 119. ^{13}C NMR spectrum of **50c** in $CDCl_3$.

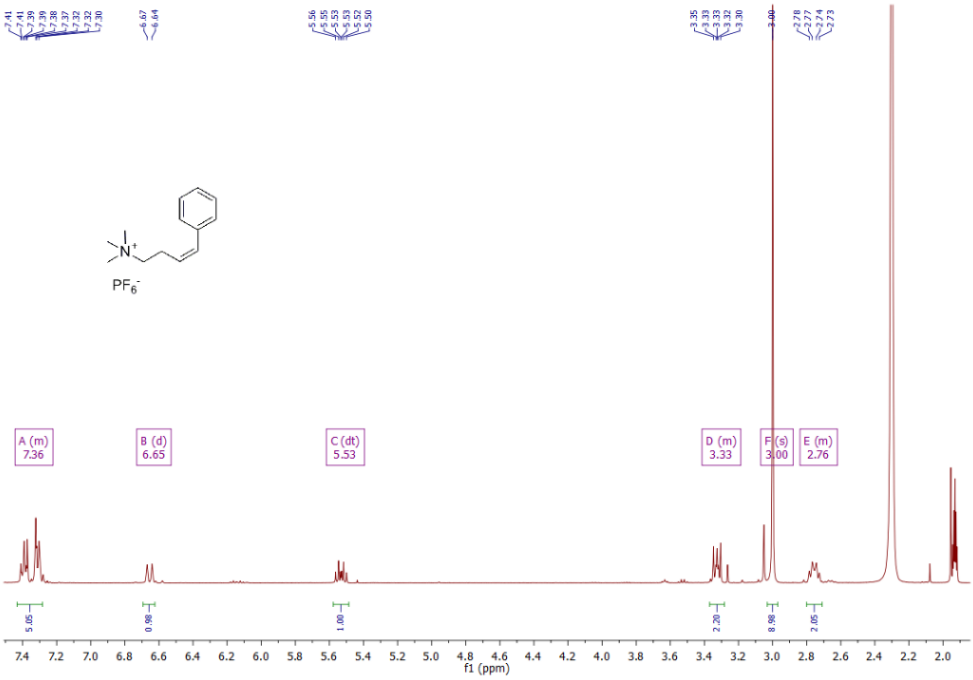

Fig. 120. ^{1}H NMR spectrum of **50** in CD_3CN.

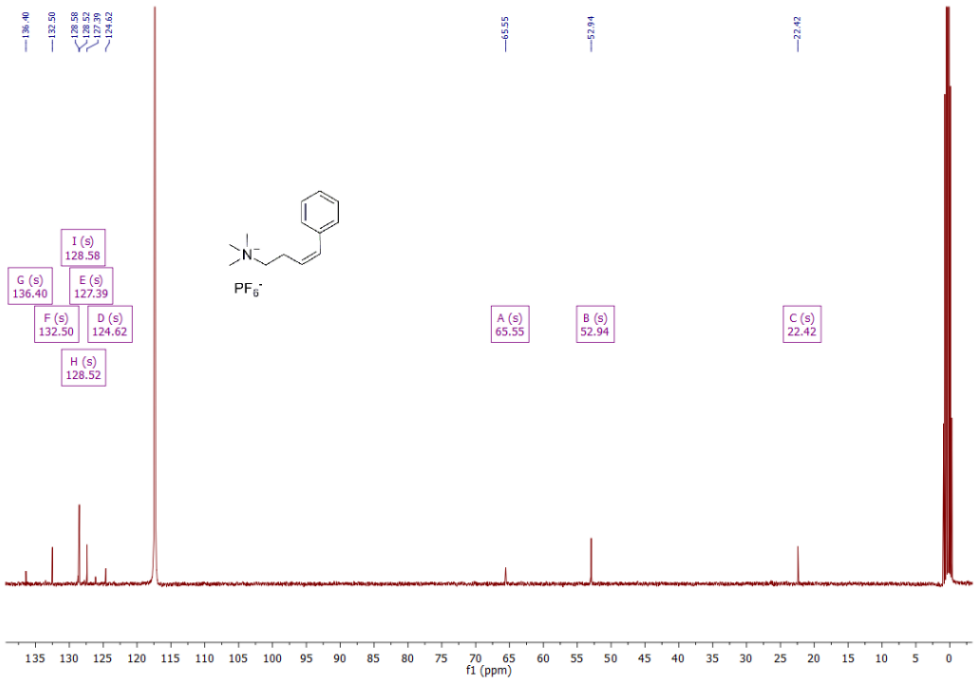

Fig. 121. ^{13}C NMR spectrum of **50** in CD_3CN.

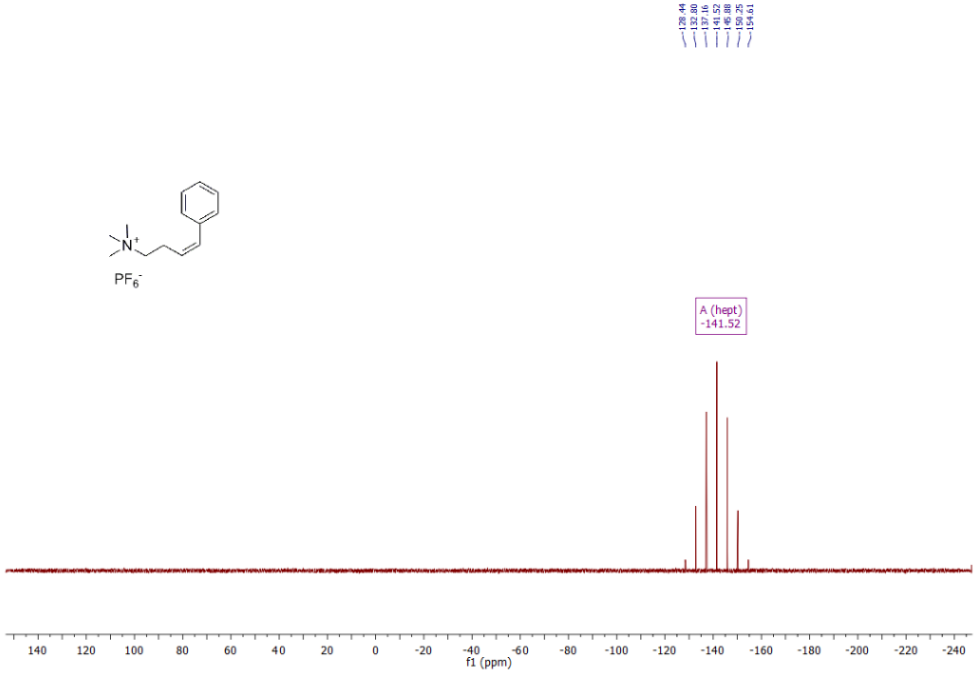

Fig. 122. ^{31}P NMR spectrum of **50** in CD_3CN.

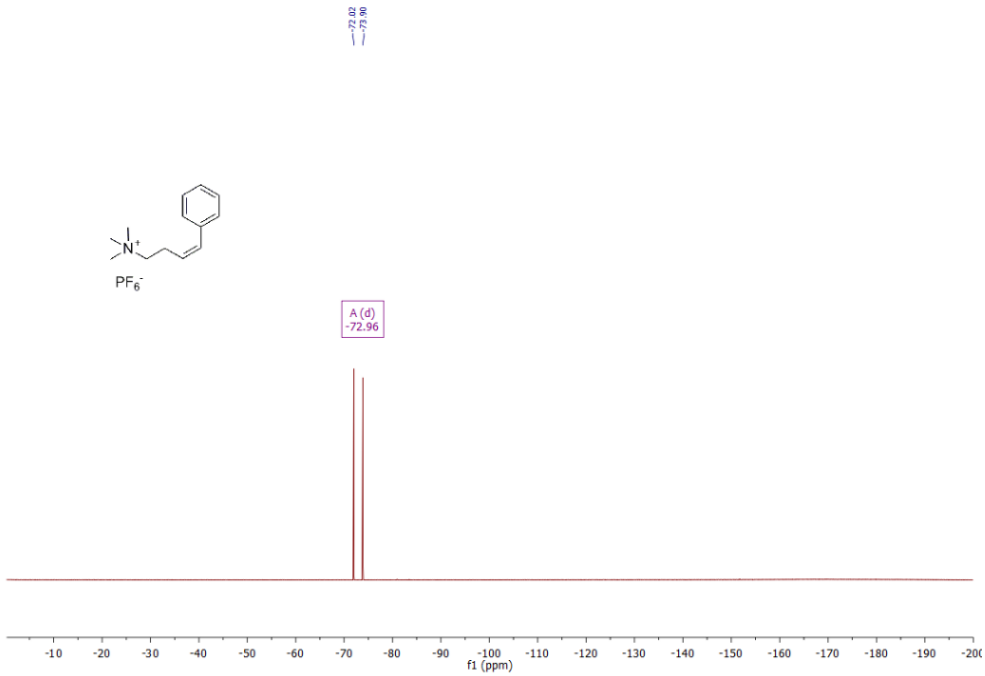

Fig. 123. ^{19}F NMR spectrum of **50** in CD_3CN.

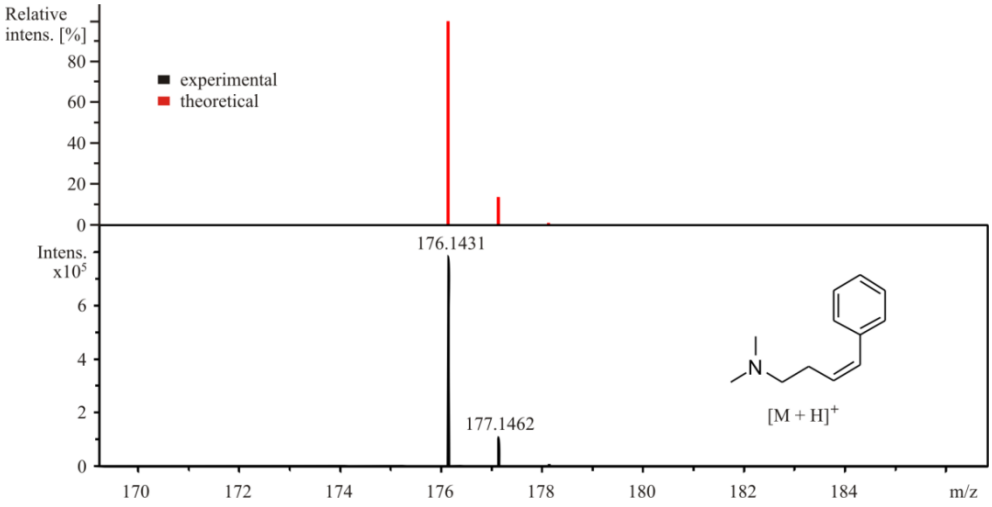

Fig. 124. ESI-MS isotopic pattern for **50b**.

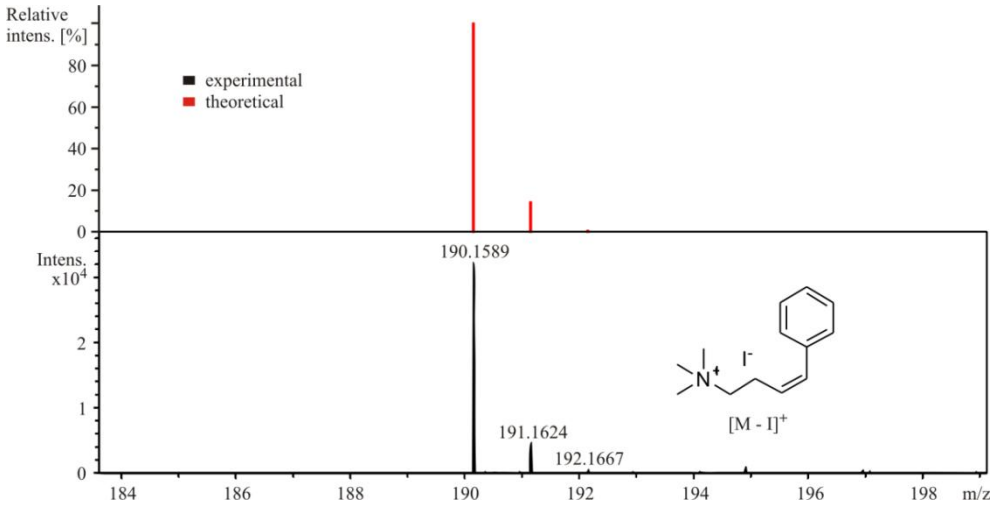

Fig. 125. ESI-MS isotopic pattern for **50c**.

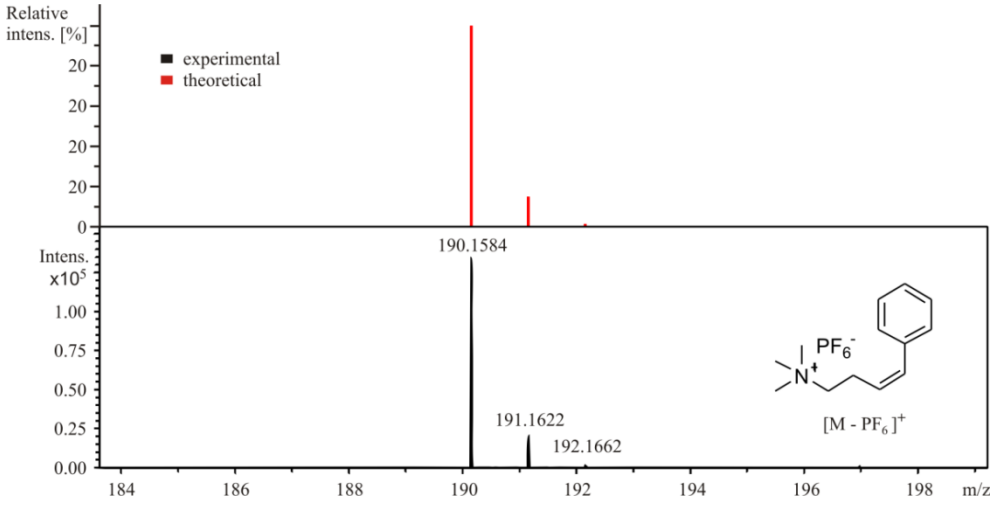

Fig. 126. ESI-MS isotopic pattern for **50**.

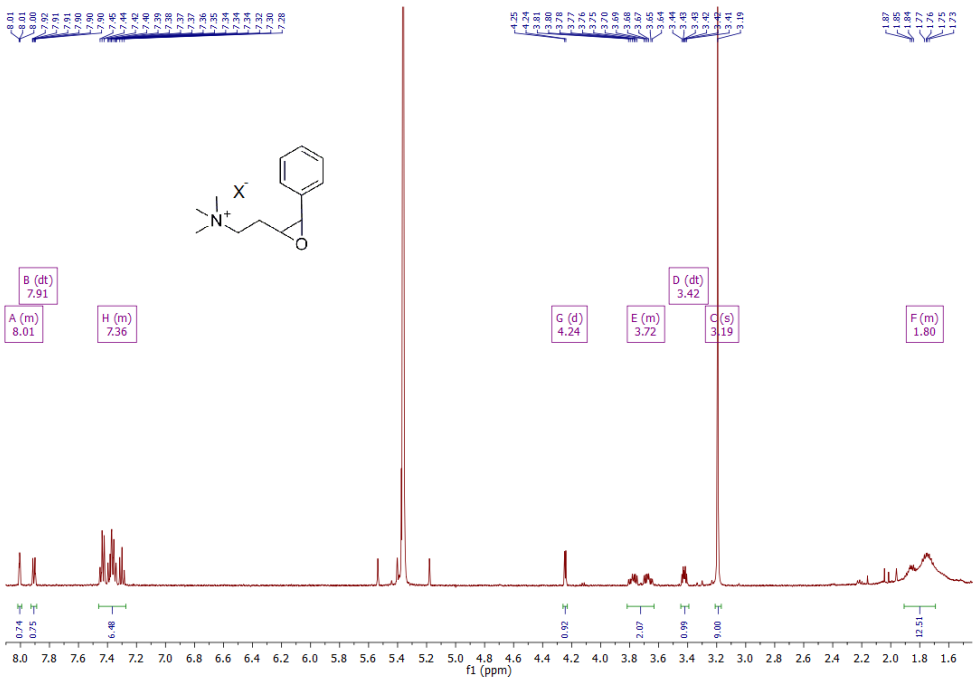

Fig. 127. ^{1}H NMR **53** in CD_2Cl_2. X = PF_6 or *meta*-chlorobenzoate.

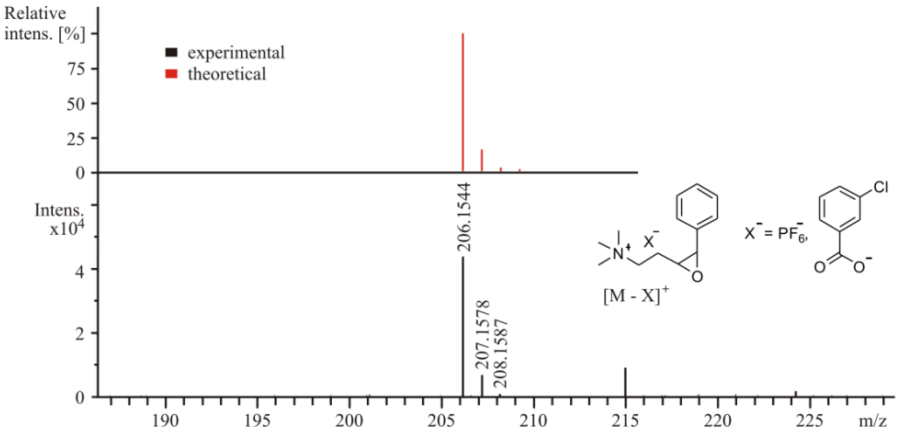

Fig. 128. ESI-MS (+) isotopic pattern for **53**. X = PF_6 or *meta*-chlorobenzoate.

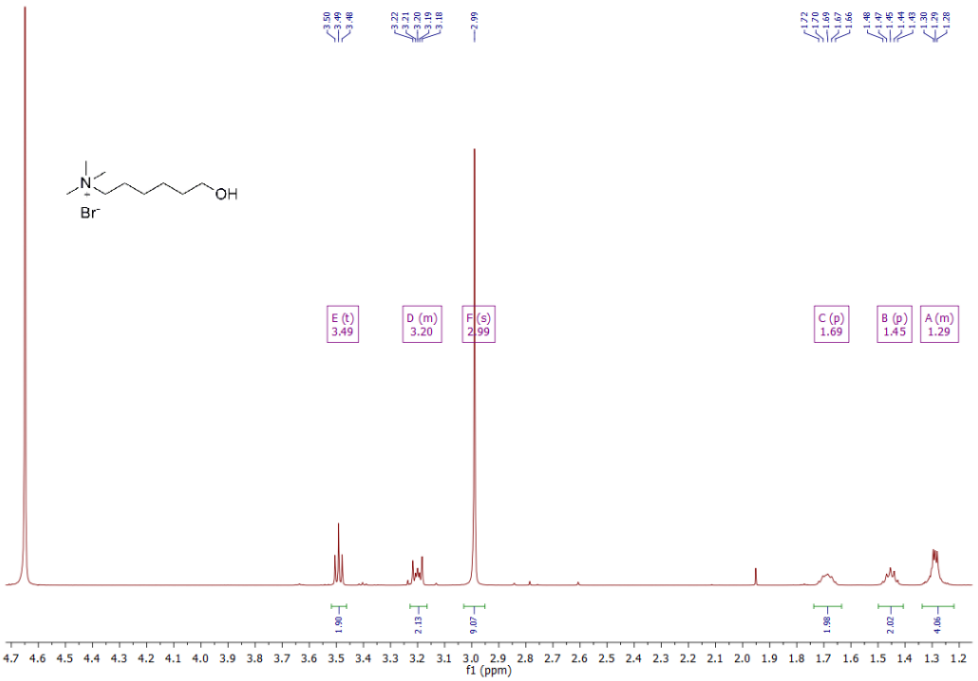

Fig. 129. ^{1}H NMR of of the alcohol **58b** in D_2O.

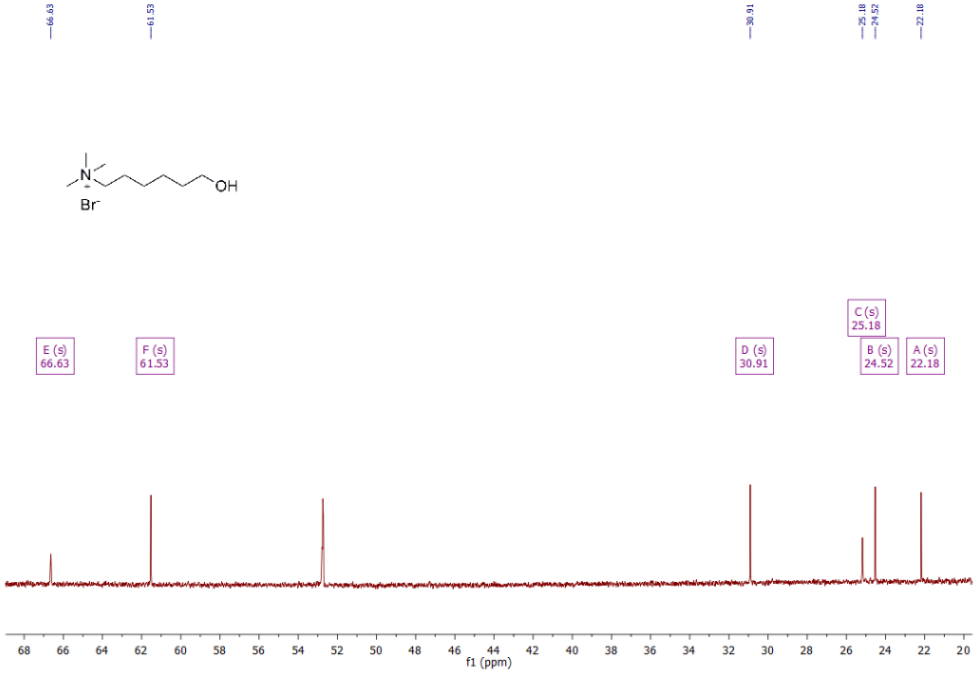

Fig. 130. ^{13}C NMR of the alcohol **58b** in D_2O.

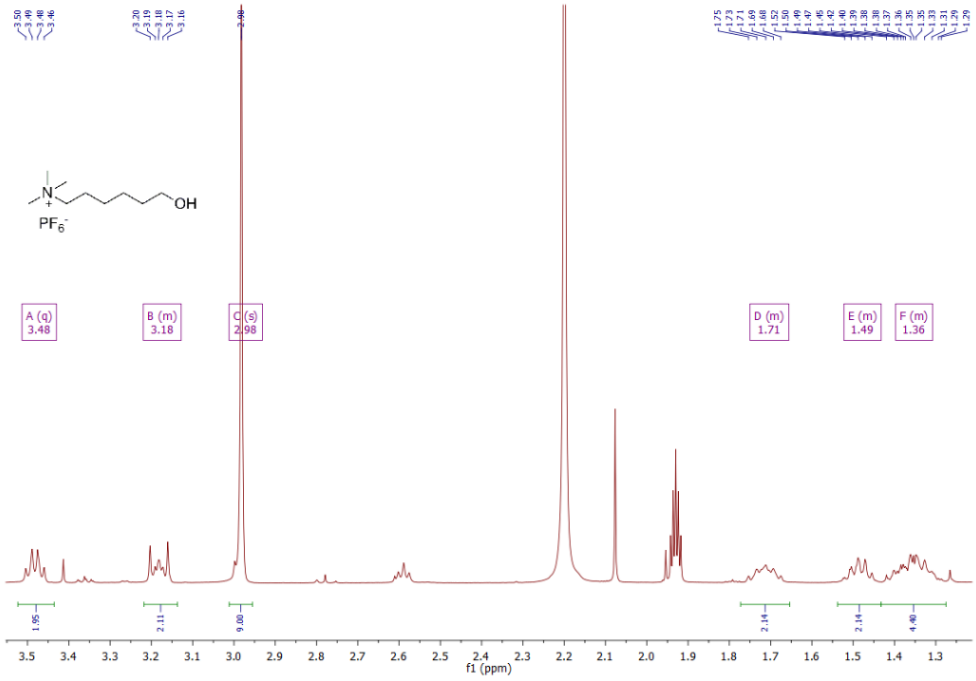

Fig. 131. ^{1}H NMR of the alcohol **58** in CD_3CN.

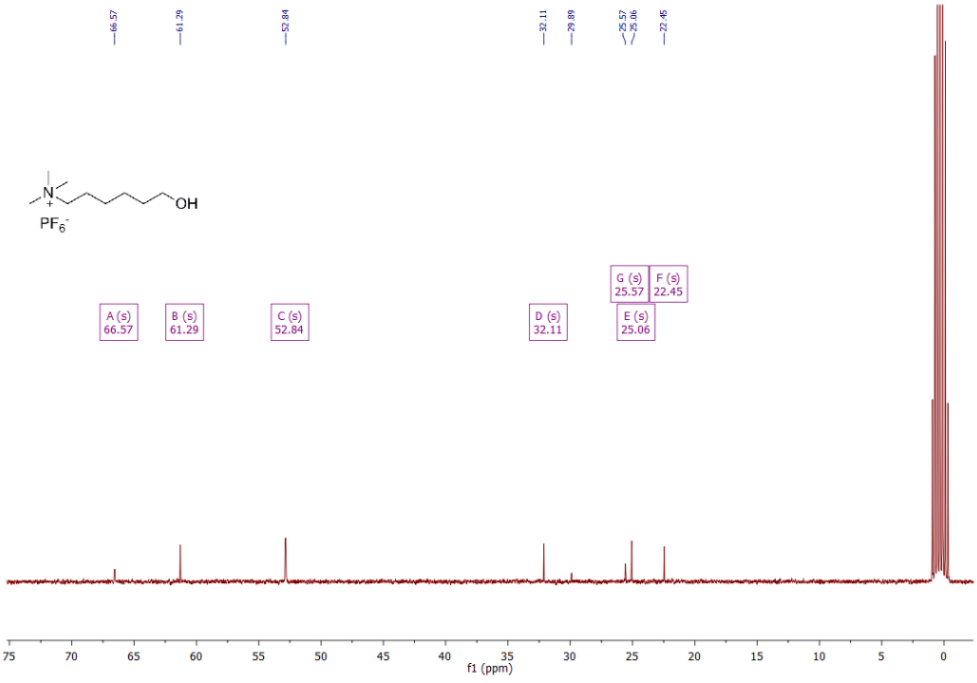

Fig. 132. ^{13}C NMR of the alcohol **58** in CD_3CN.

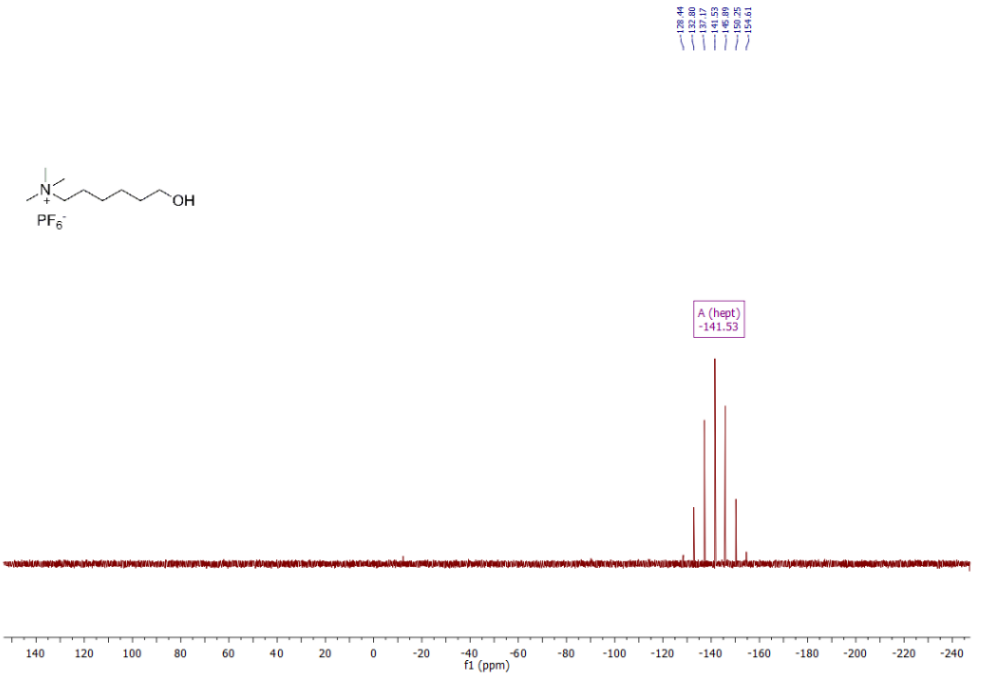

Fig. 133. ^{31}P NMR of the alcohol **58** in CD_3CN.

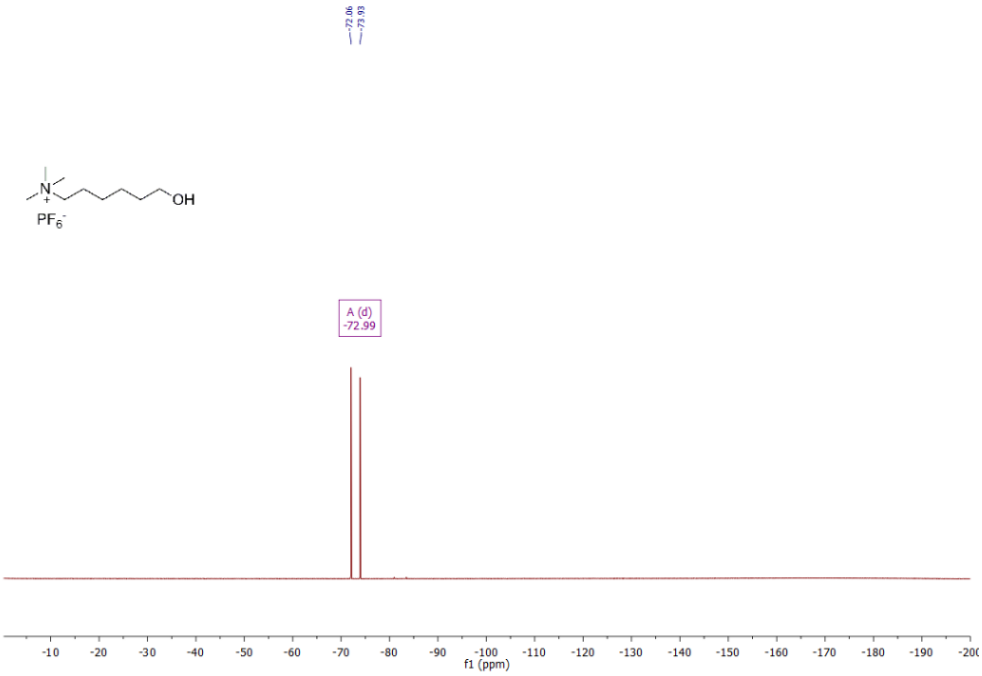

Fig. 134. ^{19}F NMR of the alcohol **58** in CD_3CN.

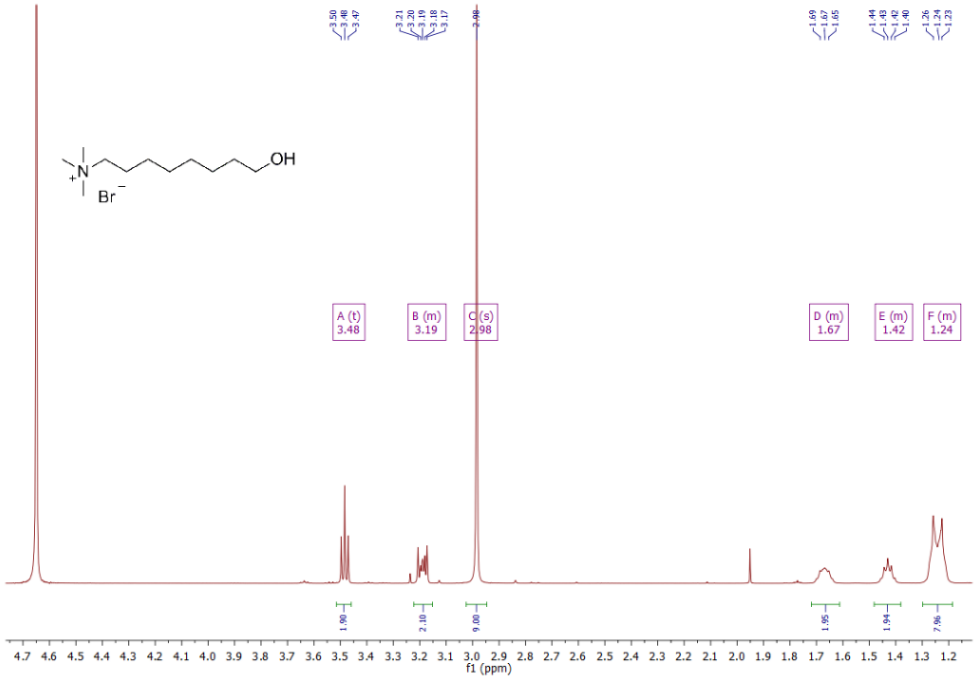

Fig. 135. ^{1}H NMR of the alcohol **59b** in D_2O.

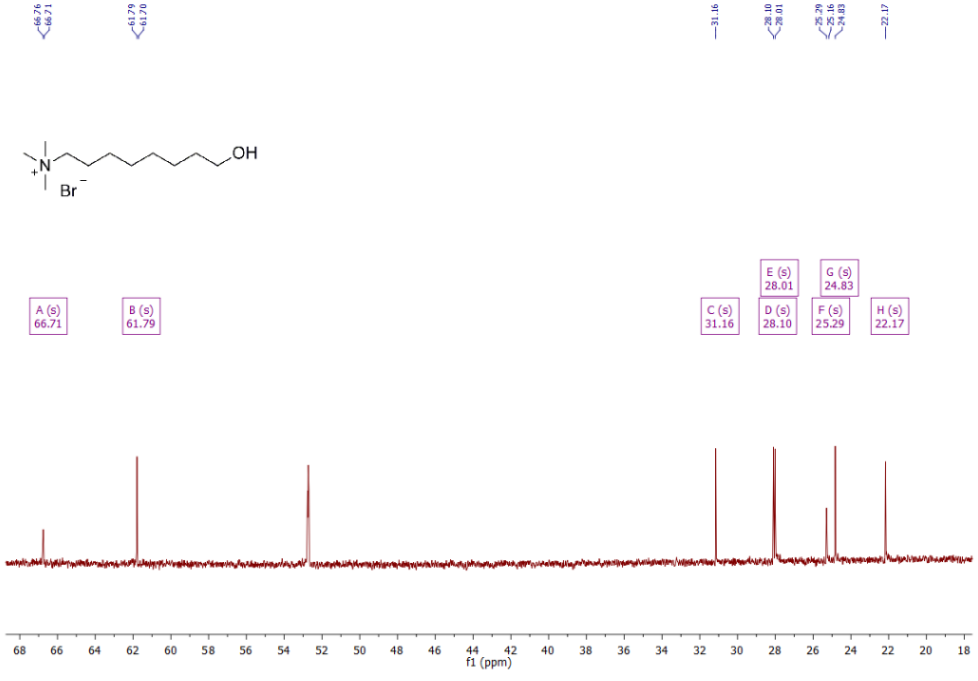

Fig. 136. ^{13}C NMR of the alcohol **59b** in D_2O.

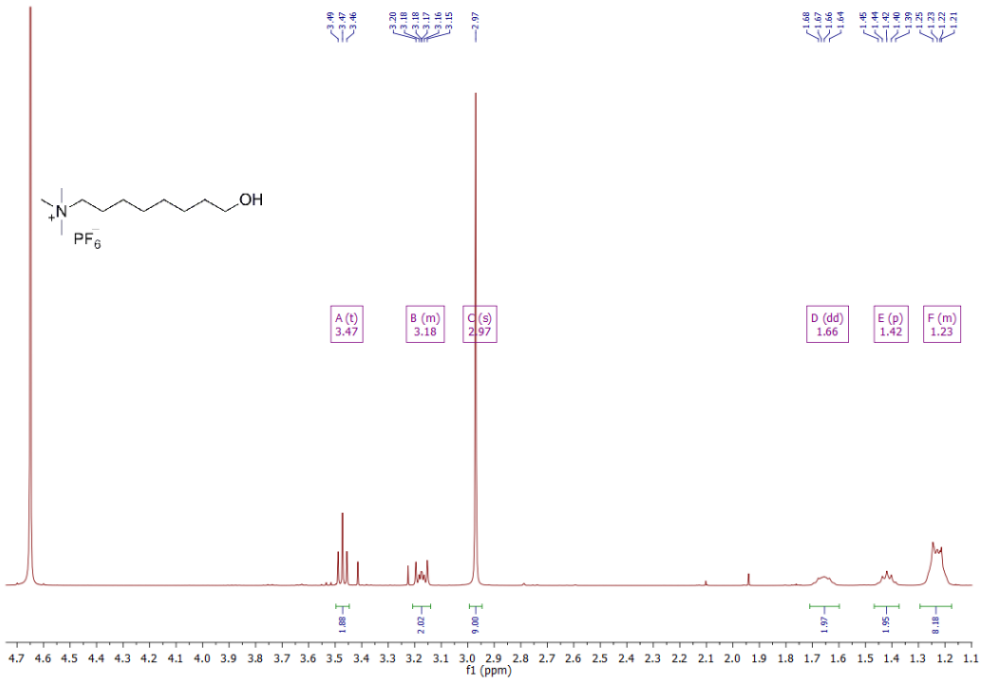

Fig. 137. ^{1}H NMR of the alcohol **59** in D_2O.

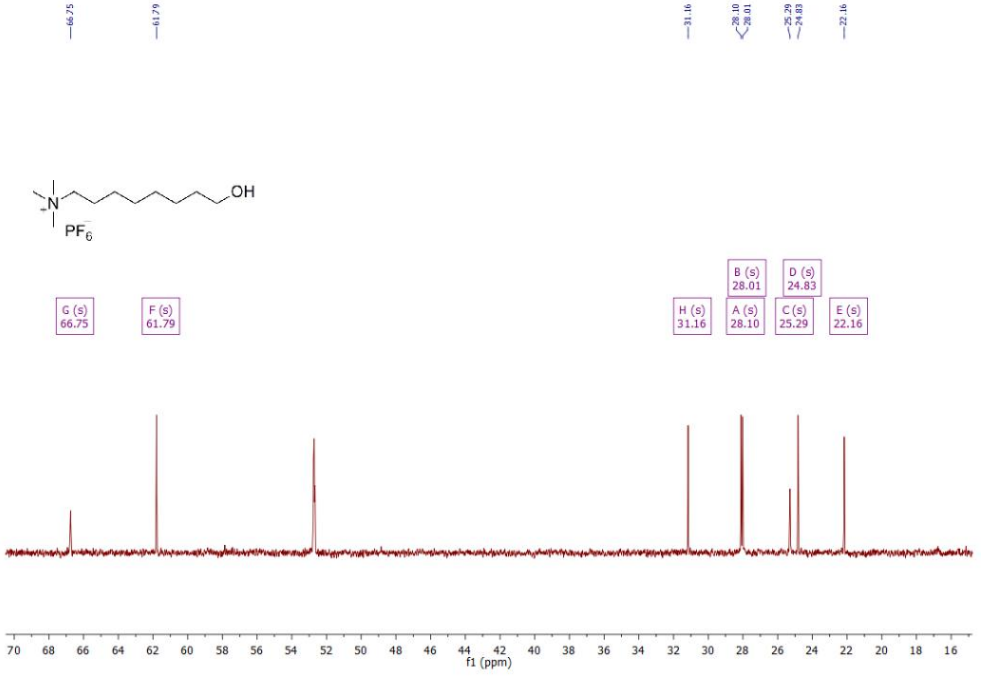

Fig. 138. ^{13}C NMR of the alcohol **59** in D_2O.

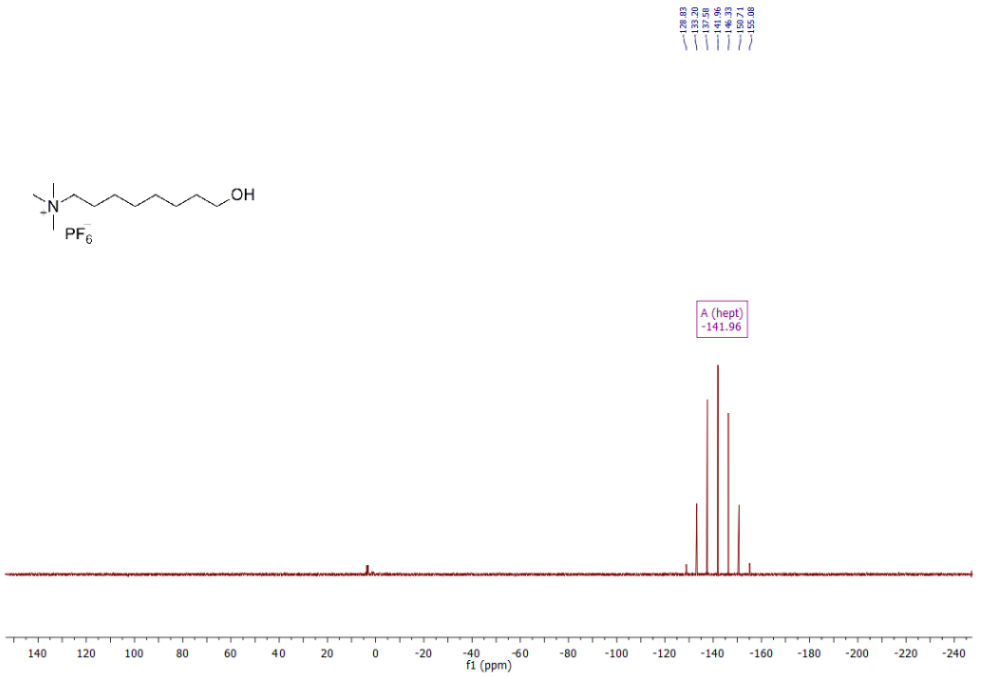

Fig. 139. ^{31}P NMR of the alcohol **59** in D_2O.

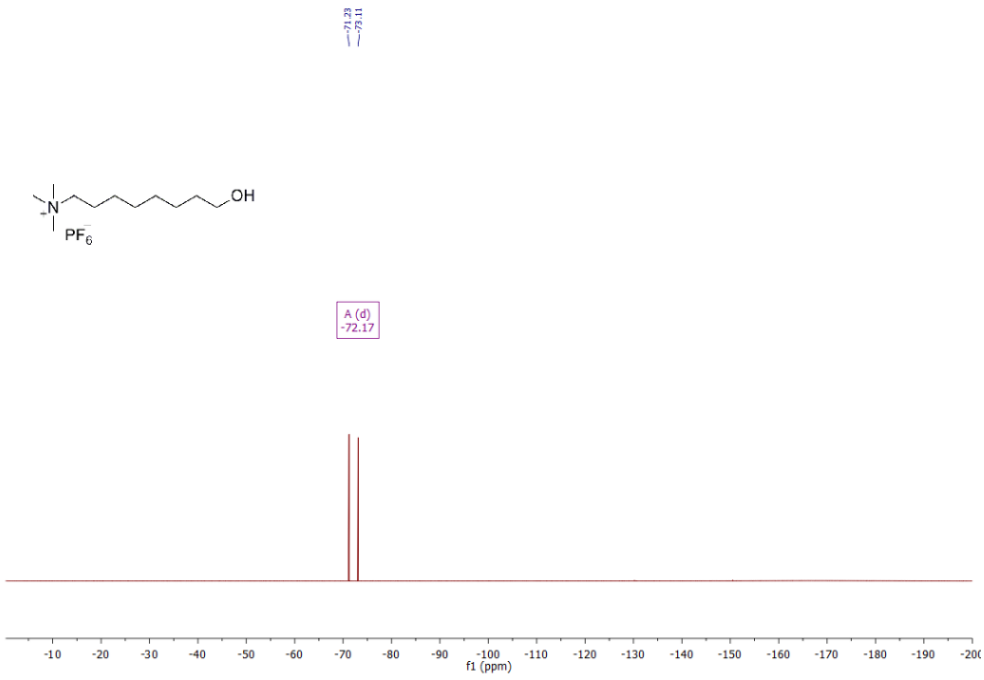

Fig. 140. ^{19}F NMR of the alcohol **59** in D_2O.

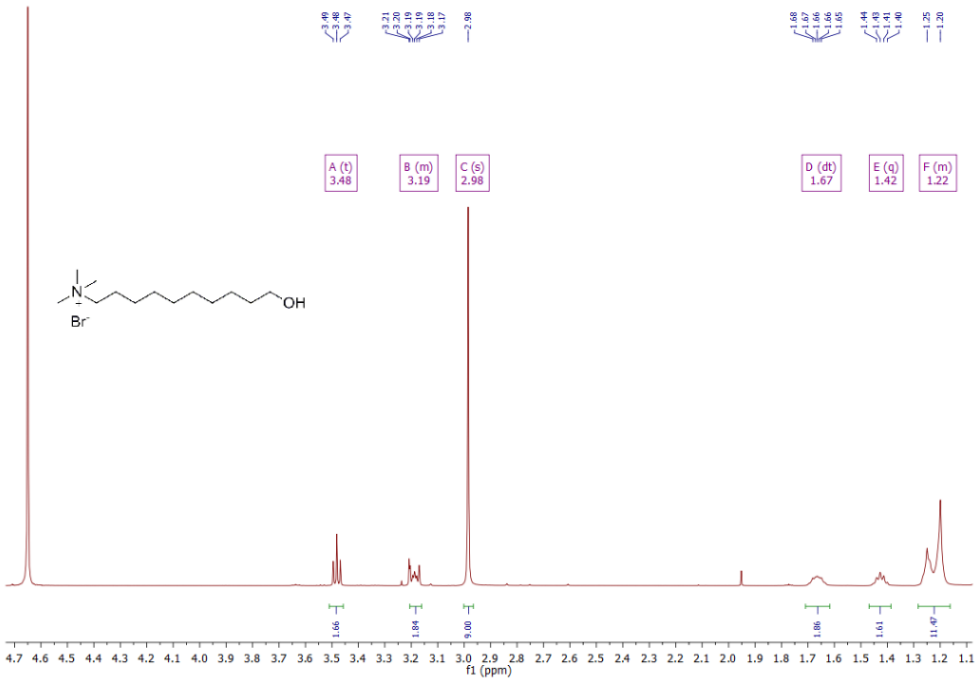

Fig. 141. ^{1}H NMR of the alcohol **60b** in D_2O.

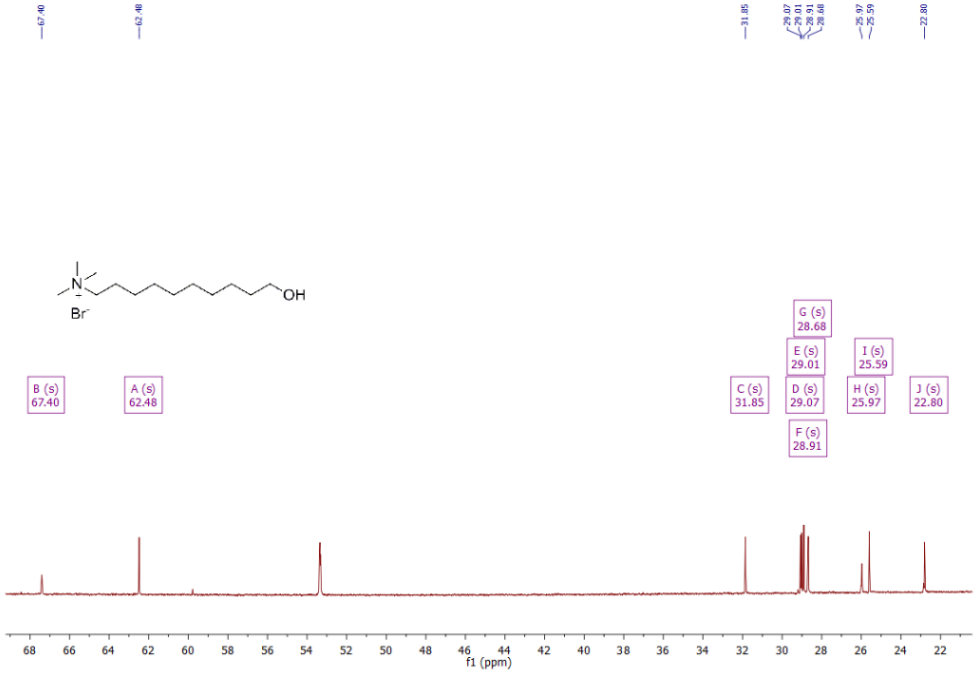

Fig. 142. ^{13}C NMR of the alcohol **60b** in D_2O.

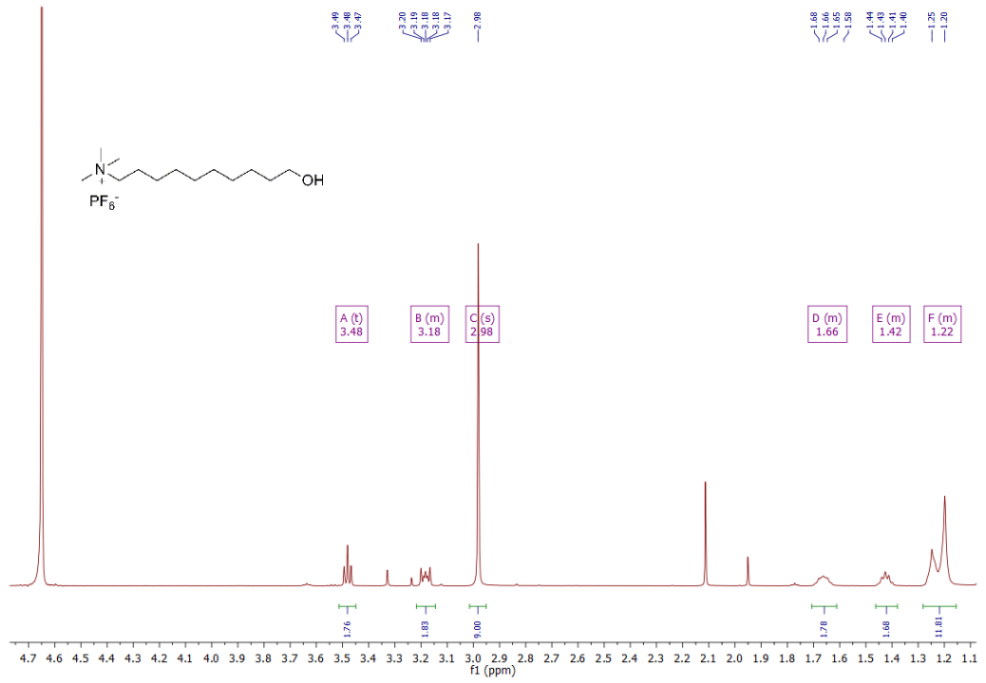

Fig. 143. ^{1}H NMR of the alcohol **60** in D_2O.

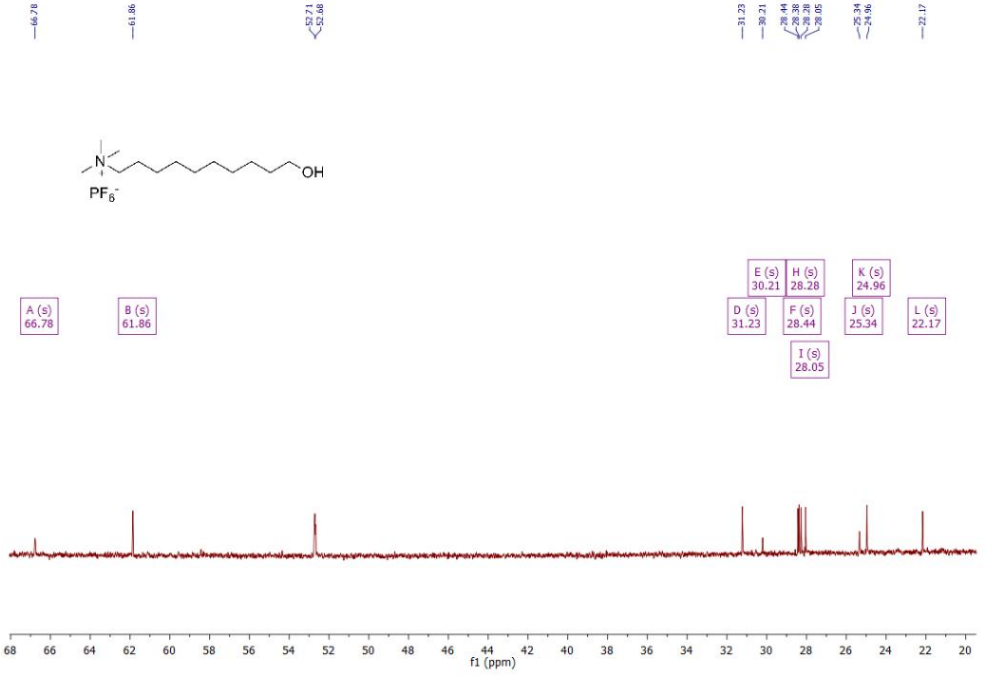

Fig. 144. ^{13}C NMR of the alcohol **60** in D_2O.

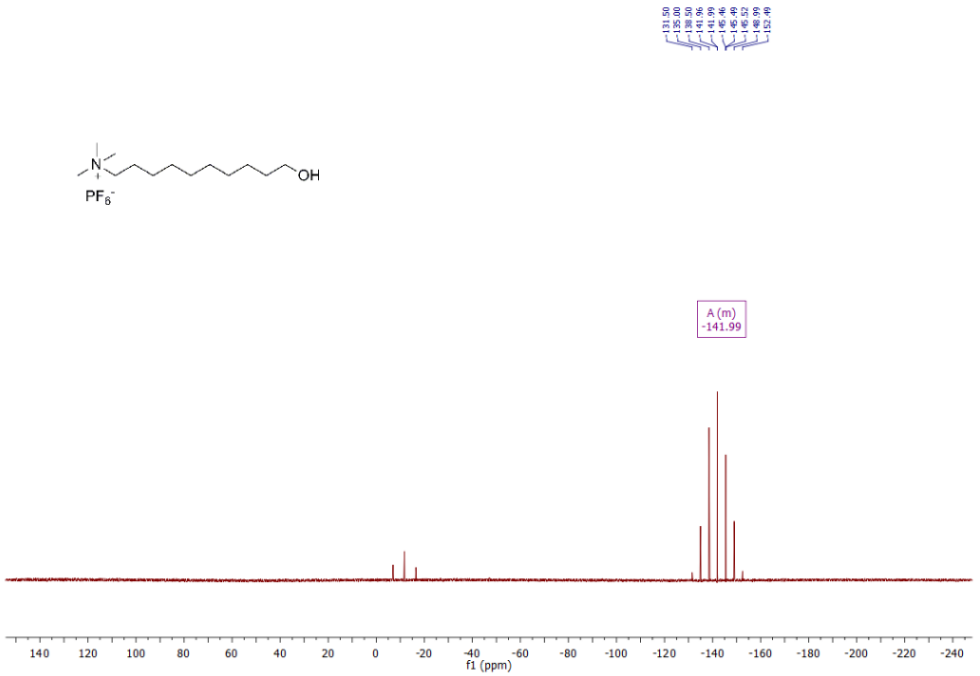

Fig. 145. ^{31}P NMR of the alcohol **60** in D_2O.

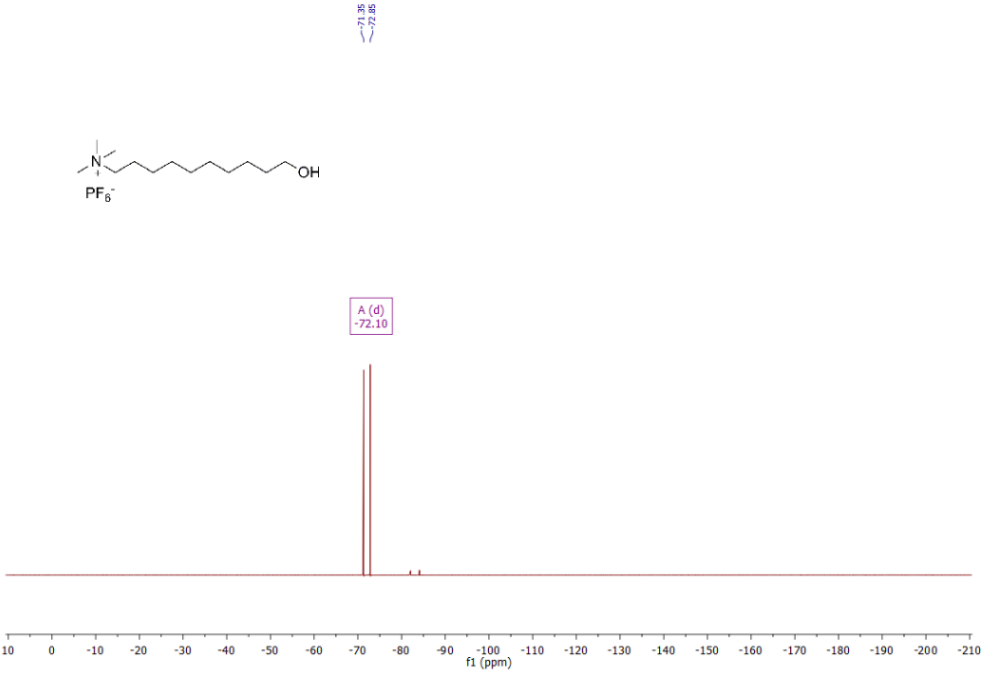

Fig. 146. ^{19}F NMR of the alcohol **60** in D_2O.

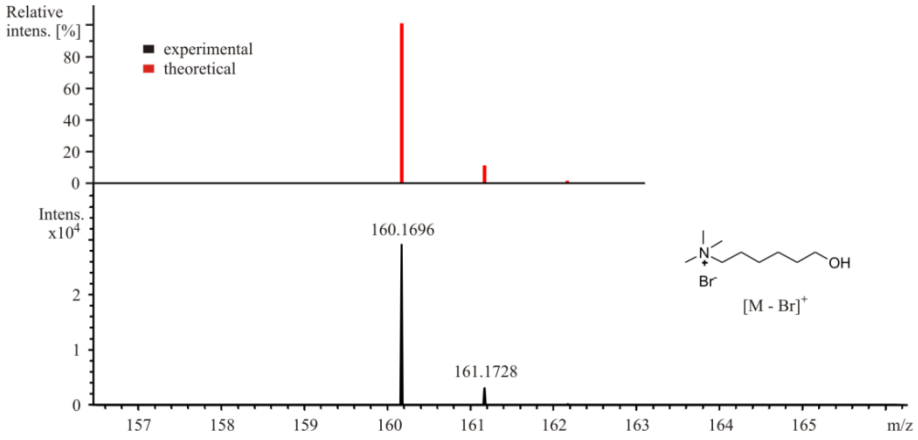

Fig. 147. ESI-MS (+) isotopic pattern for the alcohol **58b**.

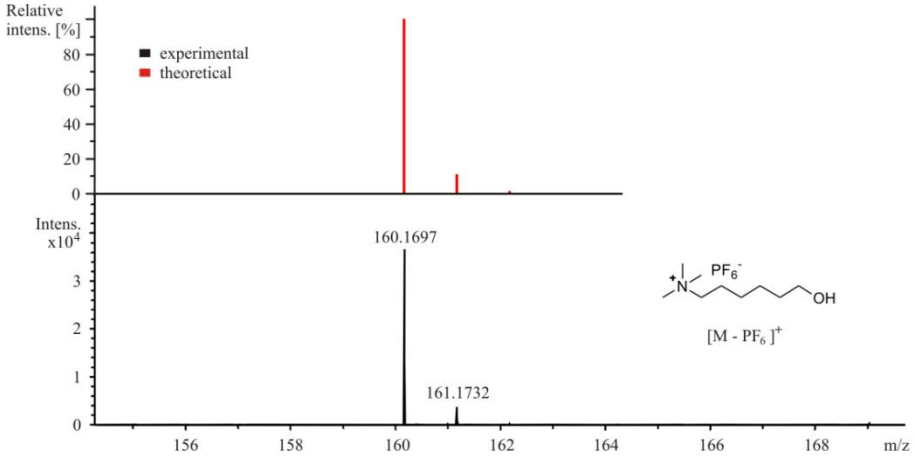

Fig. 148. ESI-MS (+) isotopic pattern for the alcohol **58**.

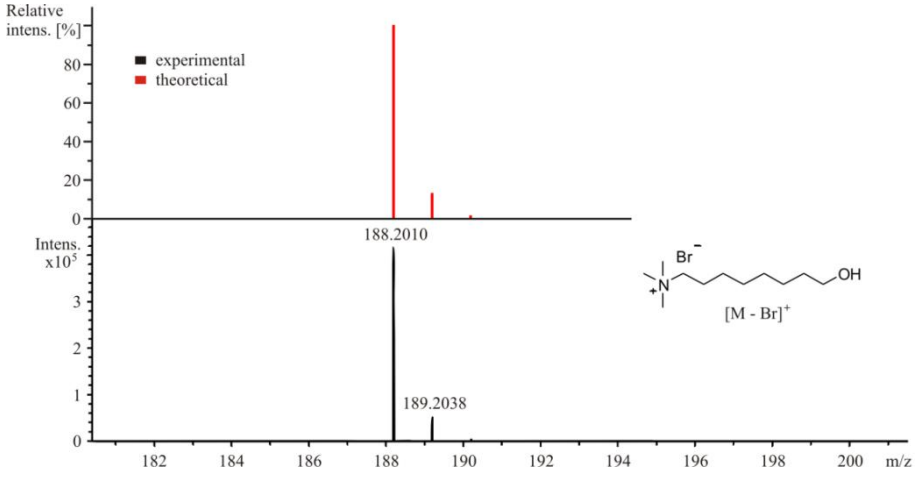

Fig. 149. ESI-MS (+) isotopic pattern for the alcohol **59b**.

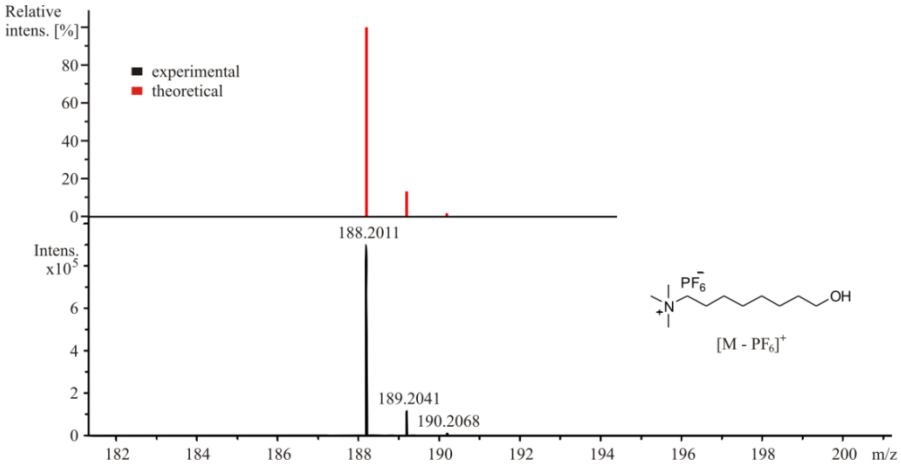

Fig. 150. ESI-MS (+) isotopic pattern for the alcohol **59**.

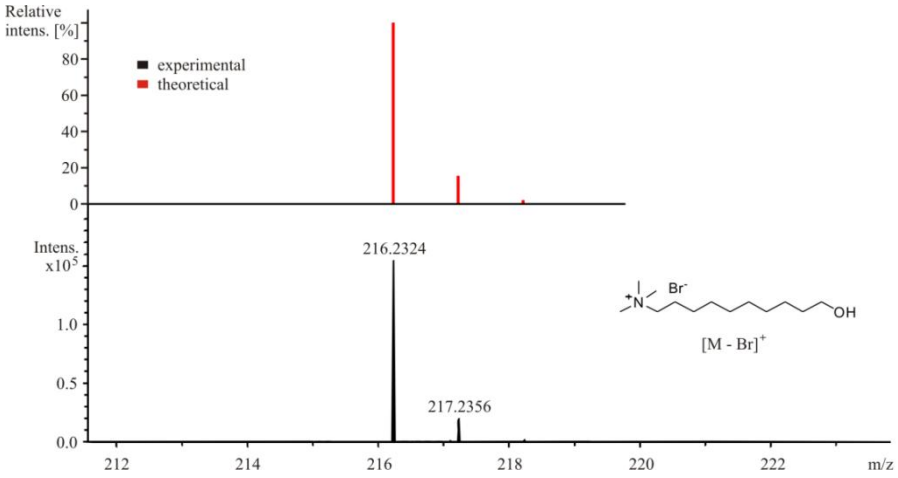

Fig. 151. ESI-MS (+) isotopic pattern for the alcohol **60b**.

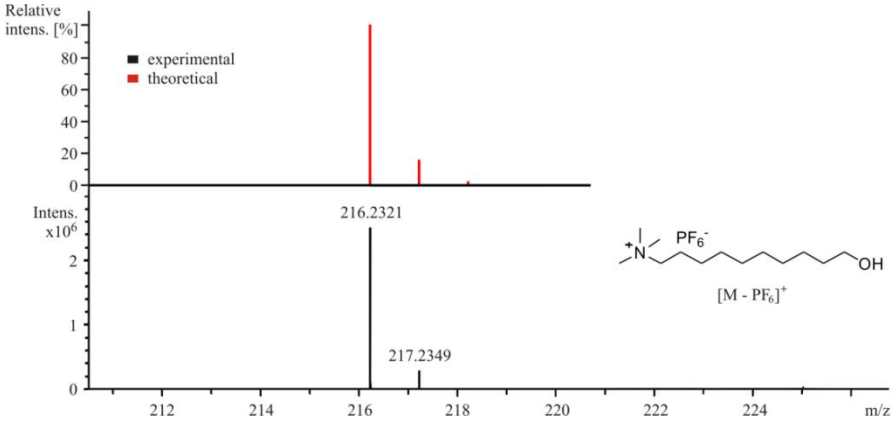

Fig. 152. ESI-MS (+) isotopic pattern for the alcohol **60**.

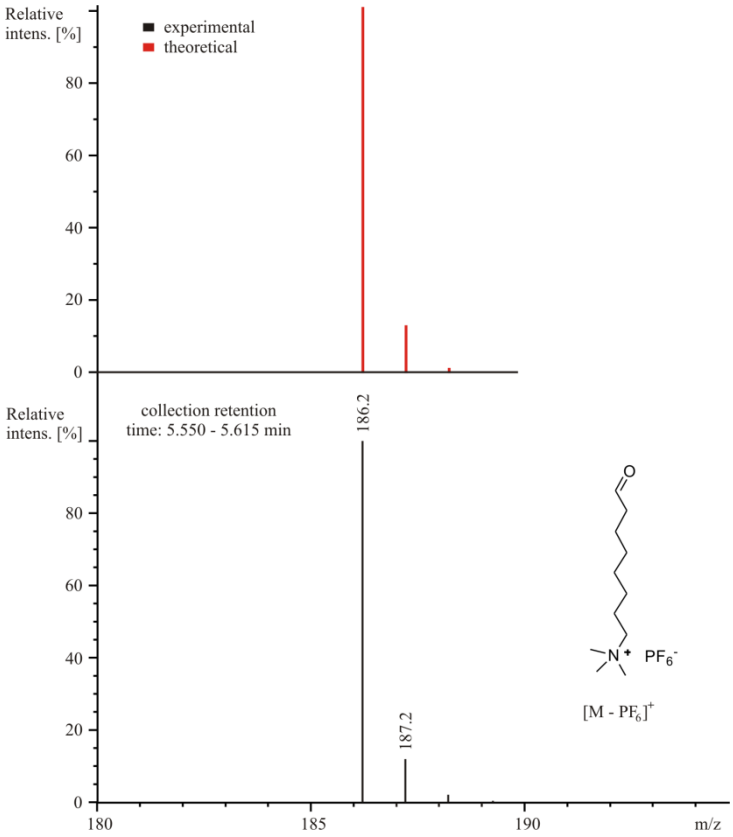

Fig. 153. HPLC/ESI-MS (+) isotopic pattern for the aldehyde **63**.

Kinetic data

Styrene (**48**) epoxidation:

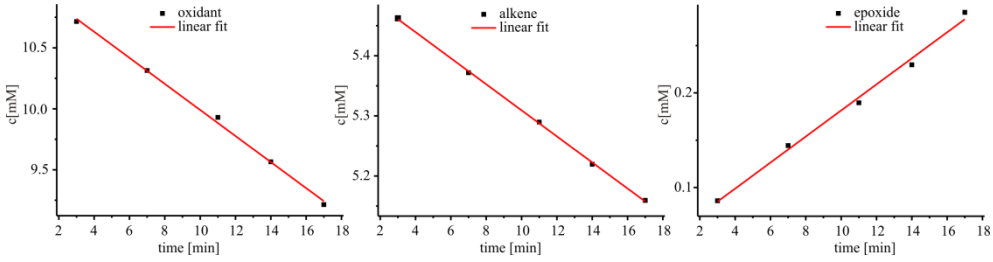

Fig. 154. Linear fittings for 17 min of reaction for iodosobenzene diacetate (left); styrene (middle) and styrene oxide (right) associated with the catalytic epoxidation of styrene (**48**, 5.5 mM) using **azpy**•Ru^{II}•(H_2O)•**tpy** (**47**, 5 mol-%) in the presence of iodosobenzene diacetate as an oxidant (11 mM) and water (40 mM) in CD_2Cl_2 (550 µL).

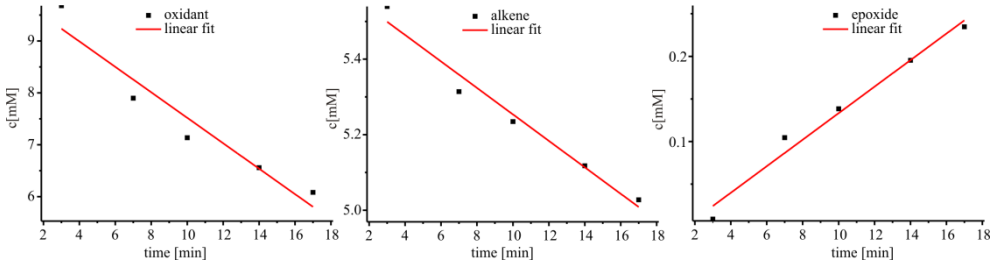

Fig. 155. Linear fittings for 17 min of reaction for iodosobenzene diacetate (left); styrene (**48**, middle) and styrene oxide (**51**, right) associated with the catalytic epoxidation of styrene (**48**, 5.5 mM) using **azpy**•Ru^{II}•(H_2O)•**C24** (**C27**, 5 mol-%) in the presence of iodosobenzene diacetate as an oxidant (11 mM) and water (40 mM) in CD_2Cl_2 (550 µL).

Table 9. Initial reaction rates derived from **Fig. 154** and **Fig. 155**.

Recorded reaction components	**47** (5 mol-%)		**C27** (5 mol-%)	
	rate [µM/min]	R^2	rate [µM/min]	R^2
styrene (**48**)	22	0.999	35	0.962
styrene oxide (**51**)	14	0.991	16	0.972
iodosobenzene diacetate	107	0.997	245	0.908

Iodosobenzene diacetate decomposition:

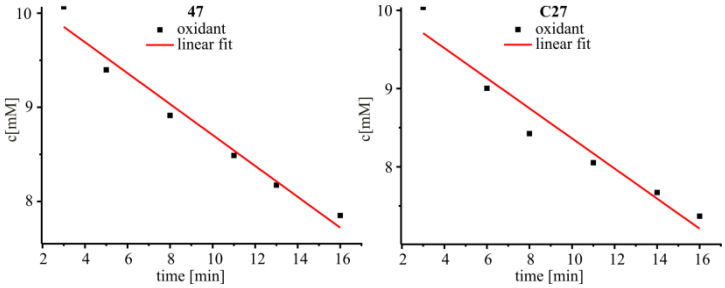

Fig. 156. Linear fittings for 17 min of reaction for iodosobenzene diacetate consumption using **azpy**•Ru^{II}•(H_2O)•**tpy** (**47**, 5 mol-%, left) and **azpy**•Ru^{II}•(H_2O)•**C24** (**C27**, 5 mol-%, right) in the presence water (40 mM) in CD_2Cl_2 (550 µL).

Table 10. Initial reaction rates derived from **Fig. 156**.

Recorded reaction components	**47** (5 mol-%)		**C27** (5 mol-%)	
	rate [µM/min]	R^2	rate [µM/min]	R^2
iodosobenzene diacetate	164	0.964	192	0.928

Trans-β-methylstyrene (**49**) epoxidation:

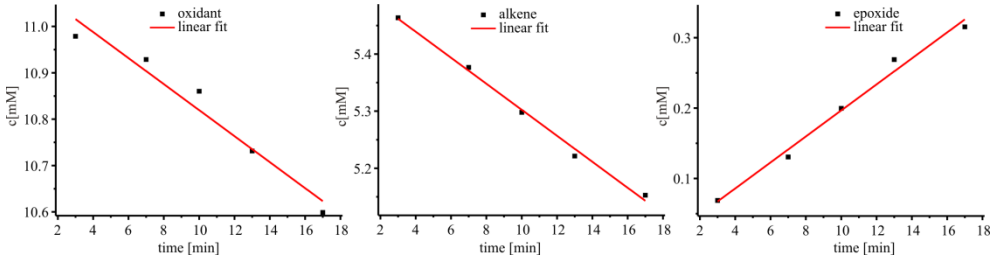

Fig. 157. Linear fittings for 17 min of reaction for iodosobenzene diacetate (left); *trans*-β-methylstyrene (**49**, middle) and 1-phenylpropylene oxide (**52**, right) associated with the catalytic epoxidation of *trans*-β-methylstyrene (**49**, 5.5 mM) using **azpy**•Ru^{II}•(H_2O)•**tpy** (**47**, 5 mol-%) in the presence of iodosobenzene diacetate as an oxidant (11 mM) and water (40 mM) in CD_2Cl_2 (550 μL).

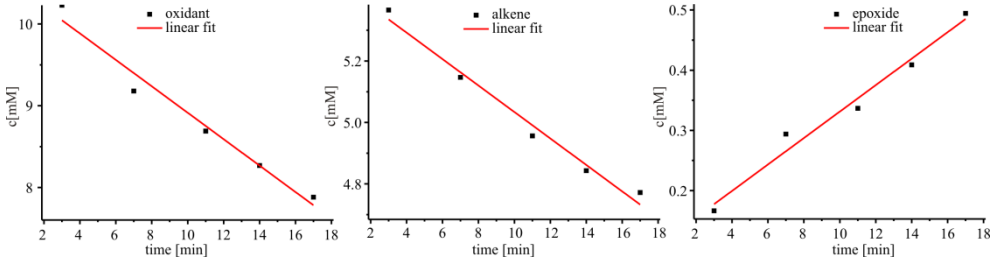

Fig. 158. Linear fittings for 17 min of reaction for iodosobenzene diacetate (left); *trans*-β-methylstyrene (**49**, middle) and 1-phenylpropylene oxide (**52**, right) associated with the catalytic epoxidation of *trans*-β-methylstyrene (**49**, 5.5 mM) using **azpy**•Ru^{II}•(H_2O)•**C24** (**C27**, 5 mol-%) in the presence of iodosobenzene diacetate as an oxidant (11 mM) and water (40 mM) in CD_2Cl_2 (550 μL).

Table 11. Initial reaction rates derived from **Fig. 157** and **Fig. 158**.

Recorded reaction components	**47** (5 mol-%)		**C27** (5 mol-%)	
	rate [μM/min]	R^2	rate [μM/min]	R^2
trans-β-methylstyrene (**49**)	23	0.993	43	0.975
1-phenylpropylene oxide (**52**)	18	0.983	22	0.969
iodosobenzene diacetate	28	0.940	162	0.962

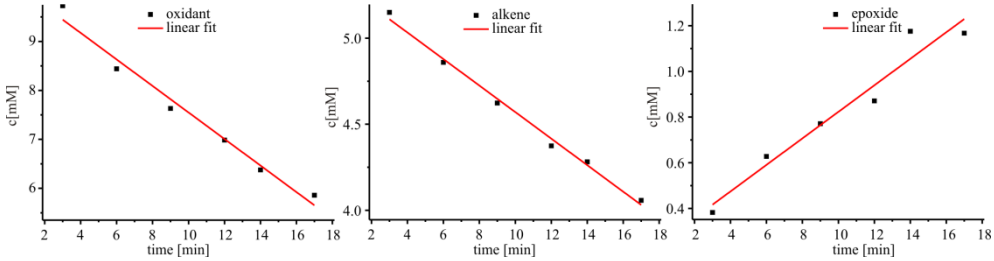

Fig. 159. Linear fittings for 17 min of reaction for iodosobenzene diacetate (left); *trans*-β-methylstyrene (**49**, middle) and 1-phenylpropylene oxide (**52**, right) associated with the catalytic epoxidation of *trans*-β-methylstyrene (**49**, 5.5 mM) using **azpy**•Ru^{II}•(H_2O)•**C24** (**C27**, 10 mol-%) in the presence of iodosobenzene diacetate as an oxidant (11 mM) and water (40 mM) in CD_2Cl_2 (550 μL).

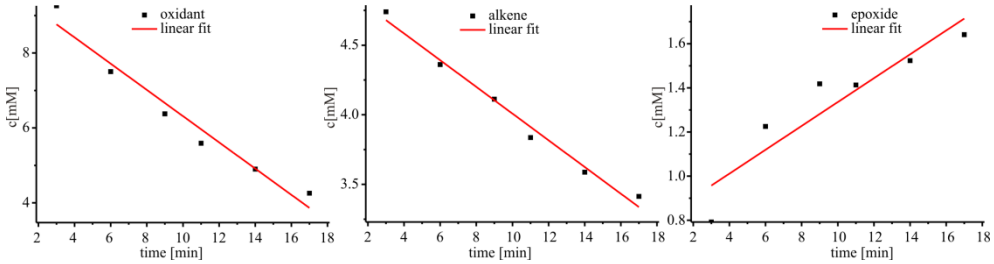

Fig. 160. Linear fittings for 17 min of reaction for iodosobenzene diacetate (left); *trans*-β-methylstyrene (**49**, middle) and 1-phenylpropylene oxide (**52**, right) associated with the catalytic epoxidation of *trans*-β-methylstyrene (**49**, 5.5 mM) using **azpy**•Ru^{II}•(H_2O)•**C24** (**C27**, 20 mol-%) in the presence of iodosobenzene diacetate as an oxidant (11 mM) and water (40 mM) in CD_2Cl_2 (550 μL).

Table 12. Initial reaction rates derived from **Fig. 159** and **Fig. 160**.

Recorded reaction components	**C27** (10 mol-%)		**C27** (20 mol-%)	
	rate [μM/min]	R^2	rate [μM/min]	R^2
trans-β-methylstyrene (**49**)	77	0.992	96	0.982
1-phenylpropylene oxide (**52**)	58	0.933	54	0.823
iodosobenzene diacetate	271	0.975	350	0.950

Z-alkene **50** epoxidation:

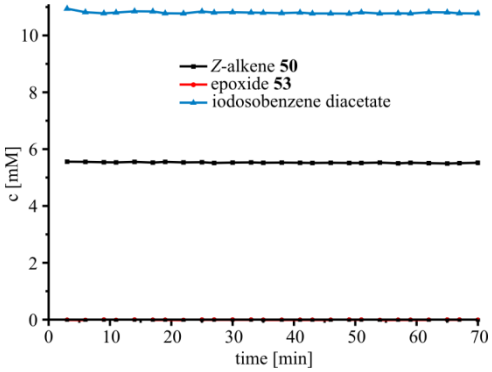

Fig. 161. Kinetic curve for the epoxidation of *Z*-alkene **50** (5.5 mM) in the absence of catalyst and in the presence of iodosobenzene diacetate as an oxidant (11 mM) and water (40 mM) in CD_2Cl_2 (550 μL).

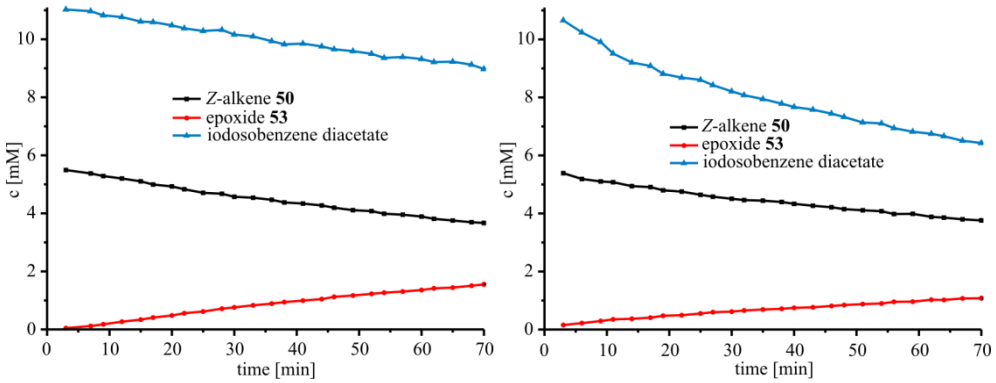

Fig. 162. Plots of the concentration changes observed for different species in the epoxidation reaction of *Z*-alkene **50** (5.5 mM) catalyzed by **azpy**•Ru^{II}•(H_2O)•**tpy** (**47**, 5 mol-%, left) and **azpy**•Ru^{II}•(H_2O)•**C24** (**C27**, 5 mol-%, right), in the presence of iodosobenzene diacetate as an oxidant (11 mM) and water (40 mM) in CD_2Cl_2 (550 µL).

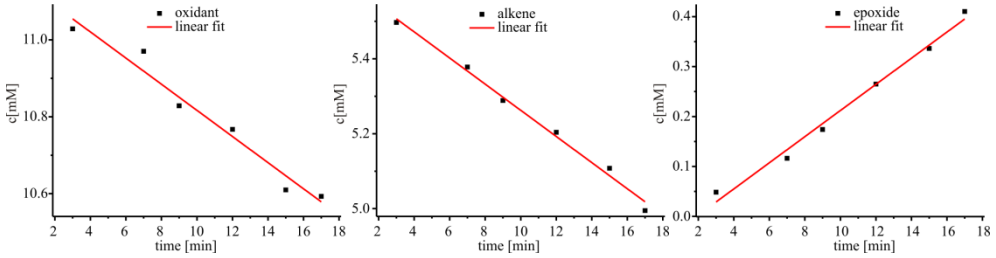

Fig. 163. Linear fittings for 17 min of reaction for iodosobenzene diacetate (left); *Z*-alkene **50** (middle) and epoxide **53** (right) associated with the catalytic epoxidation of *Z*-alkene **50** (5.5 mM) using **azpy**•Ru^{II}•(H_2O)•**tpy** (**47**, 5 mol-%) in the presence of iodosobenzene diacetate as an oxidant (11 mM) and water (40 mM) in CD_2Cl_2 (550 µL).

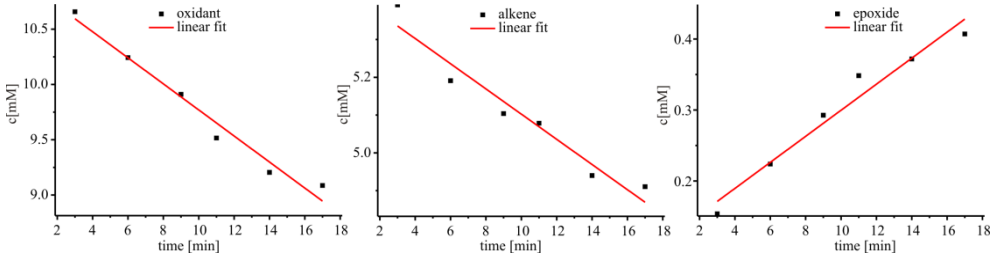

Fig. 164. Linear fittings for 17 min of reaction for iodosobenzene diacetate (left); *Z*-alkene **50** (middle) and epoxide **53** (right) associated with the catalytic epoxidation of *Z*-alkene **50** (5.5 mM) using **azpy**•Ru^{II}•(H_2O)•**C24** (**C27**, 5 mol-%) in the presence of iodosobenzene diacetate as an oxidant (11 mM) and water (40 mM) in CD_2Cl_2 (550 µL).

Table 13. Initial reaction rates derived from **Fig. 163** and **Fig. 164**.

Recorded reaction components	**47** (5 mol-%)		**C27** (5 mol-%)	
	rate [µM/min]	R^2	rate [µM/min]	R^2
Z-alkene **50**	35	0.990	33	0.929
epoxide **53**	26	0.986	18	0.951
iodosobenzene diacetate	34	0.956	118	0.966

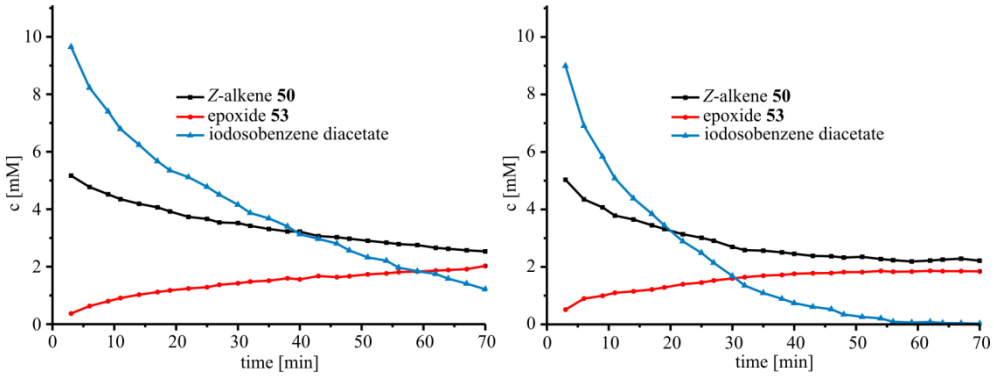

Fig. 165. Kinetic curves for epoxidation of *Z*-alkene **50** (5.5 mM) catalyzed by 10 mol-% (left) and 20 mol-% (right) of **azpy**•Ru^{II}•(H_2O)•**C24** (**C27**), in the presence of iodosobenzene diacetate as an oxidant (11 mM) and water (40 mM) in CD_2Cl_2 (550 µL).

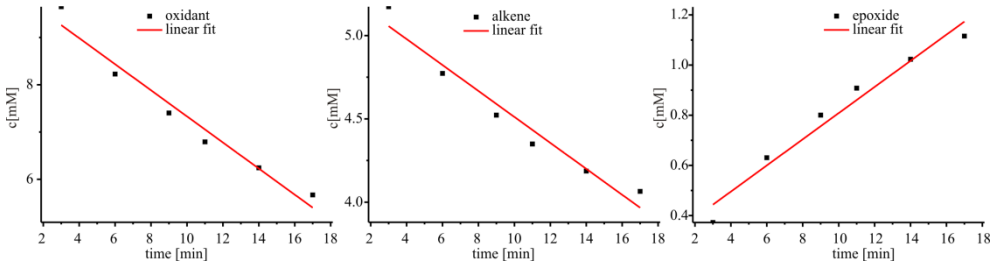

Fig. 166. Linear fittings for 17 min of reaction for iodosobenzene diacetate (left); *Z*-alkene **50** (middle) and epoxide **53** (right) associated with the catalytic epoxidation of *Z*-alkene **50** (5.5 mM) using of **azpy**•Ru^{II}•(H_2O)•**C24** (**C27**, 10 mol-%) in the presence of iodosobenzene diacetate as an oxidant (11 mM) and water (40 mM) in CD_2Cl_2 (550 µL).

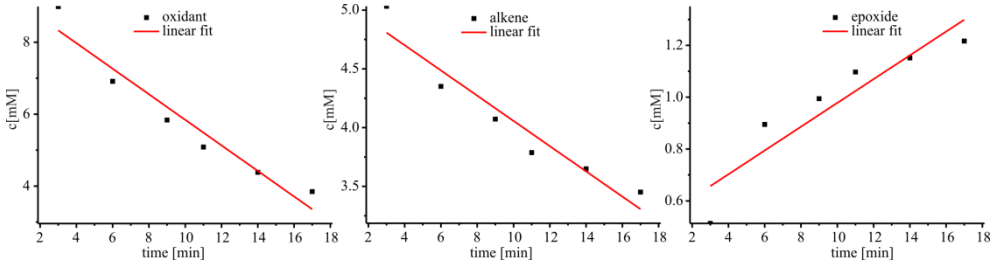

Fig. 167. Linear fittings for 17 min of reaction for iodosobenzene diacetate (left); *Z*-alkene **50** (middle) and epoxide **53** (right) associated with the catalytic epoxidation of *Z*-alkene **50** (5.5 mM) using of **azpy**•Ru^{II}•(H_2O)•**C24** (**C27**, 20 mol-%) in the presence of iodosobenzene diacetate as an oxidant (11 mM) and water (40 mM) in CD_2Cl_2 (550 µL).

Table 14. Initial reaction rates derived from **Fig. 166** and **Fig. 167**.

Recorded reaction components	**C27** (10 mol-%)		**C27** (20 mol-%)	
	rate [µM/min]	R^2	rate [µM/min]	R^2
Z-alkene **50**	78	0.944	107	0.905
epoxide **53**	52	0.954	46	0.819
iodosobenzene diacetate	276	0.955	355	0.923

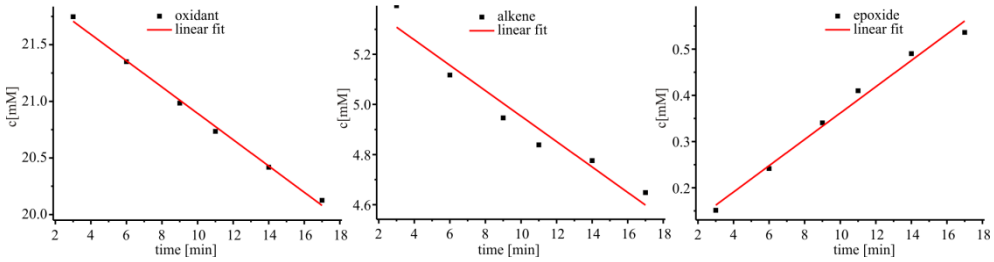

Fig. 168. Linear fittings for 17 min of reaction for iodosobenzene diacetate (left); *Z*-alkene **50** (middle) and epoxide **53** (right) associated with the catalytic epoxidation of *Z*-alkene **50** (5.5 mM) using of **azpy**•Ru^{II}•(H_2O)•**C24** (**C27**, 5 mol-%) in the presence of iodosobenzene diacetate as an oxidant (22 mM) and water (40 mM) in CD_2Cl_2 (550 µL).

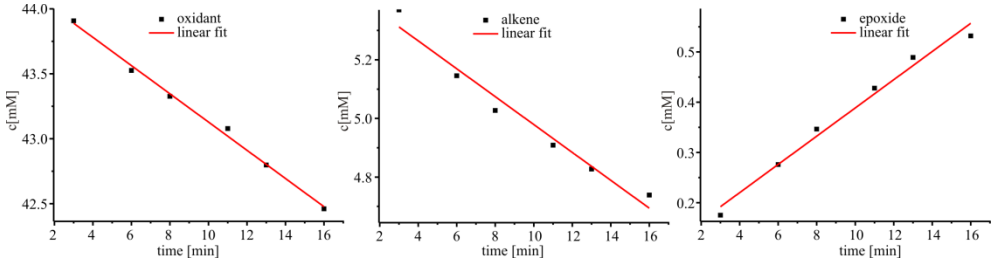

Fig. 169. Linear fittings for 17 min of reaction for iodosobenzene diacetate (left); *Z*-alkene **50** (middle) and epoxide **53** (right) associated with the catalytic epoxidation of *Z*-alkene **50** (5.5 mM) using of **azpy**•Ru^{II}•(H_2O)•**C24** (**C27**, 5 mol-%) in the presence of iodosobenzene diacetate as an oxidant (44 mM) and water (40 mM) in CD_2Cl_2 (550 µL).

Table 15. Initial reaction rates derived from **Fig. 168** and **Fig. 169**.

Recorded reaction components	oxidant (22 mM)		oxidant (44 mM)	
	rate [µM/min]	R^2	rate [µM/min]	R^2
Z-alkene **50**	51	0.932	48	0.959
epoxide **53**	28	0.983	28	0.979
iodosobenzene diacetate	116	0.996	109	0.994

Oxidation of octanol (57):

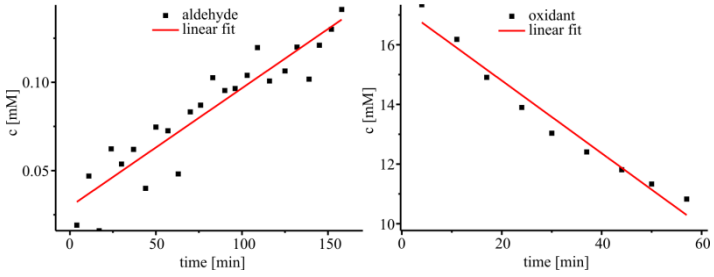

Fig. 170. Linear fittings for octanal **61** (left), and iodosobenzene diacetate (right) associated with the catalytic oxidation of octanol (**57**, 6 mM) using **azpy**•Ru^{II}•(H_2O)•**tpy** (**47**, 5 mol-%) in the presence of iodosobenzene diacetate as an oxidant (18 mM) in CD_2Cl_2 (500 µL).

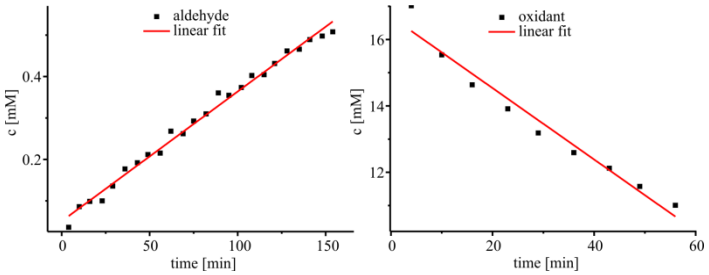

Fig. 171. Linear fittings for octanal **61** (left), and iodosobenzene diacetate (right) associated with the catalytic oxidation of octanol (**57**, 6 mM) using **azpy**•Ru^{II}•(H_2O)•**C24** (**C27**, 5 mol-%) in the presence of iodosobenzene diacetate as an oxidant (18 mM) in CD_2Cl_2 (500 µL).

Table 16. Reaction rates derived from **Fig. 170** and **Fig. 171**.

Recorded reaction components	**47** (5 mol-%)		**C27** (5 mol-%)	
	rate [µM/min]	R^2	rate [µM/min]	R^2
octanal (**61**)	0.7	0.857	3	0.990
iodosobenzene diacetate	122	0.960	107	0.958

Oxidation of alcohol **59**:

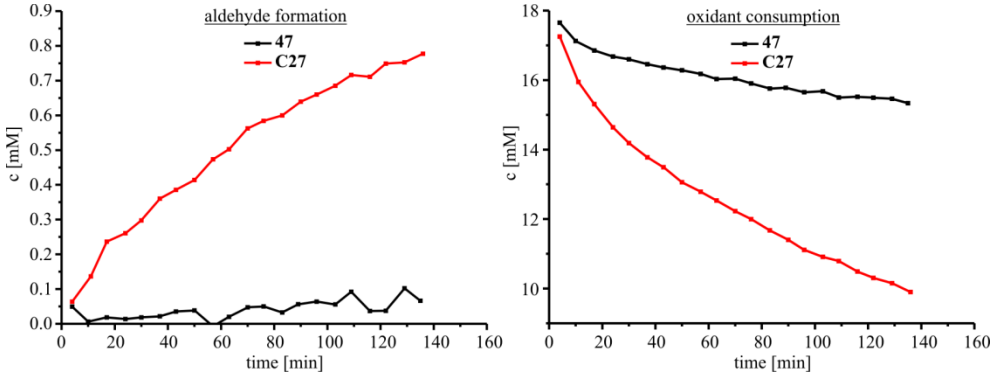

Fig. 172. Plots of changes in the concentration of the aldehyde **63** produced in the oxidation of the alcohol **59** (6 mM) catalyzed by **azpy**•Ru^{II}•(H_2O)•**tpy** (**47**, 5 mol-%, black) and **azpy**•Ru^{II}•(H_2O)•**C24** (**C27**, 5 mol-%, red) in the presence of iodosobenzene diacetate as an oxidant (18 mM) in CD_2Cl_2 (500 µL).

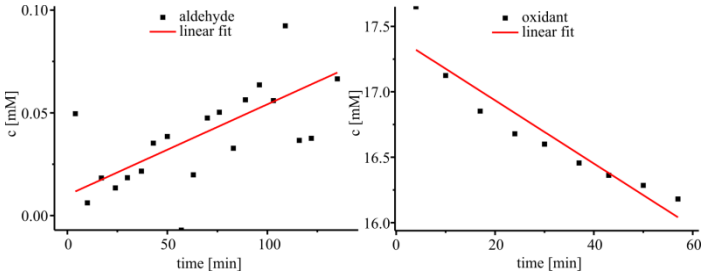

Fig. 173. Linear fittings for aldehyde **63** (left), and iodosobenzene diacetate (right) associated with the catalytic oxidation of alcohol **59** (6 mM) using **azpy**•Ru^{II}•(H_2O)•**tpy** (**47**, 5 mol-%) in the presence of iodosobenzene diacetate as an oxidant (18 mM) in CD_2Cl_2 (500 µL).

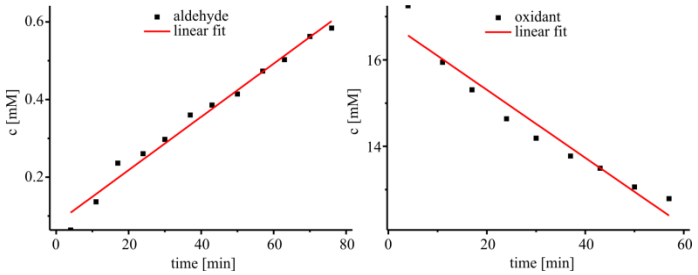

Fig. 174. Linear fittings for aldehyde **63** (left), and iodosobenzene diacetate (right) associated with the catalytic oxidation of alcohol **59** (6 mM) using **azpy**•Ru^{II}•(H_2O)•**C24** (**C27**, 5 mol-%) in the presence of iodosobenzene diacetate as an oxidant (18 mM) in CD_2Cl_2 (500 μL).

Table 17. Reaction rates derived from **Fig. 173** and **Fig. 174**.

Recorded reaction components	**47** (5 mol-%)		**C27** (5 mol-%)	
	rate [μM/min]	R^2	rate [μM/min]	R^2
aldehyde **63**	0.4	0.421	7	0.979
iodosobenzene diacetate	24	0.869	79	0.935

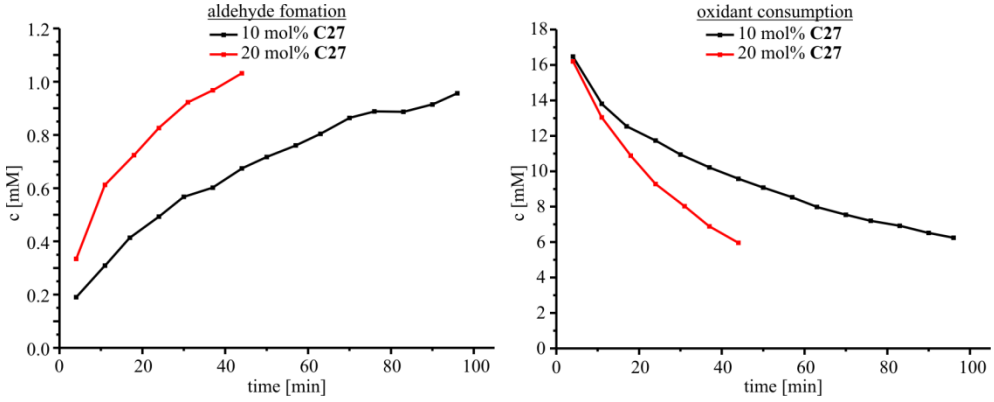

Fig. 175. Plots of changes in the concentration of the aldehyde **63** produced in the oxidation of the alcohol **59** (6 mM) catalyzed by 10 mol-% (black) and 20 mol-% (red) **azpy**•Ru^{II}•(H_2O)•**C24** (**C27**) in the presence of iodosobenzene diacetate as an oxidant (18 mM) in CD_2Cl_2 (500 μL).

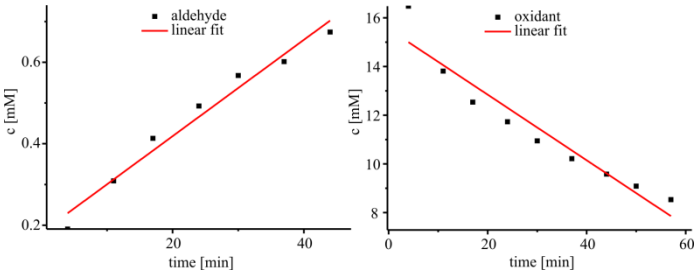

Fig. 176. Linear fittings for aldehyde **63** (left), and iodosobenzene diacetate (right) associated with the catalytic oxidation of alcohol **59** (6 mM) using **azpy**•Ru^{II}•(H_2O)•**C24** (**C27**, 10 mol-%) in the presence of iodosobenzene diacetate as an oxidant (18 mM) in CD_2Cl_2 (500 μL).

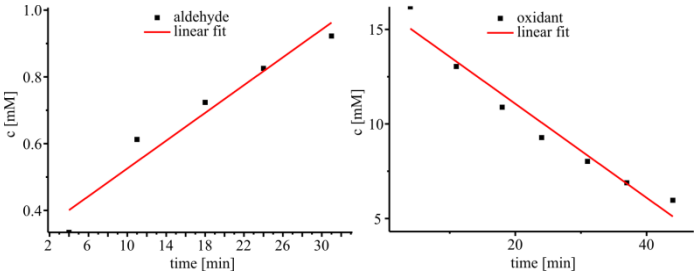

Fig. 177. Linear fittings for aldehyde **63** (left), and iodosobenzene diacetate (right) associated with the catalytic oxidation of alcohol **59** (6 mM) using **azpy**•Ru^{II}•(H_2O)•**C24** (**C27**, 20 mol-%) in the presence of iodosobenzene diacetate as an oxidant (18 mM) in CD_2Cl_2 (500 μL).

Table 18. Reaction rates derived from **Fig. 176** and **Fig. 177**.

Recorded reaction components	**C27** (10 mol-%)		**C27** (20 mol-%)	
	rate [μM/min]	R^2	rate [μM/min]	R^2
aldehyde **63**	12	0.965	21	0.926
iodosobenzene diacetate	135	0.911	248	0.949

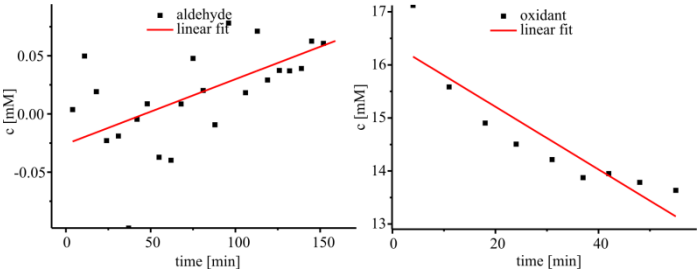

Fig. 178. Linear fittings for aldehyde **63** (left), and iodosobenzene diacetate (right) associated with the catalytic oxidation of alcohol **59** (6 mM) using **azpy**•Ru^{II}•(H_2O)•**tpy** (**47**, 5 mol-%) in the presence of iodosobenzene diacetate as an oxidant (18 mM) and water (112 mM) in CD_2Cl_2 (500 μL).

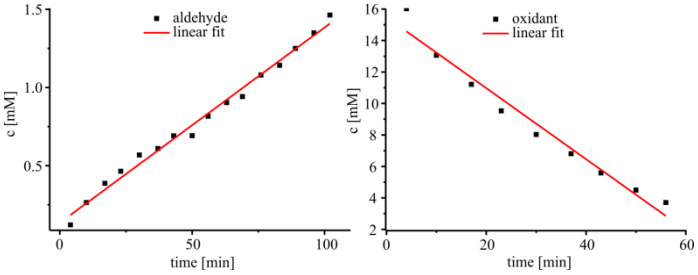

Fig. 179. Linear fittings for aldehyde **63** (left), and iodosobenzene diacetate (right) associated with the catalytic oxidation of alcohol **59** (6 mM) using **azpy**•Ru^{II}•(H_2O)•**C24** (**C27**, 5 mol-%) in the presence of iodosobenzene diacetate as an oxidant (18 mM) and water (112 mM) in CD_2Cl_2 (500 μL).

Table 19. Reaction rates derived from **Fig. 178** and **Fig. 179**.

Recorded reaction components	**47** (5 mol-%)		**C27** (5 mol-%)	
	rate [μM/min]	R^2	rate [μM/min]	R^2
aldehyde **63**	0.6	0.348	13	0.989
iodosobenzene diacetate	59	0.787	226	0.964

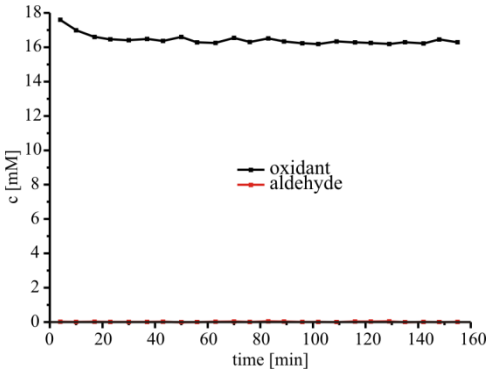

Fig. 180. Kinetic curve for the alcohol **59** (6 mM) oxidation in the absence of the catalyst and in the presence of iodosobenzene diacetate as an oxidant (18 mM) in CD_2Cl_2 (500 μL).

Oxidation of alcohol **58**:

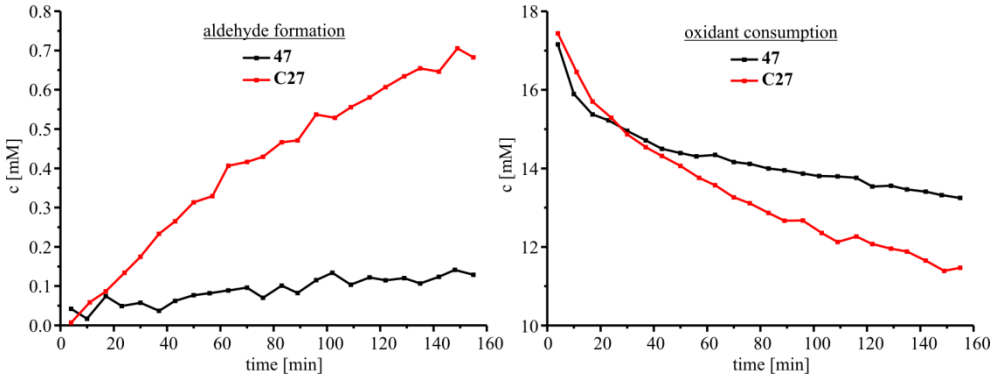

Fig. 181. Plots of changes in the concentration of the aldehyde **62** produced in the oxidation of the alcohol **58** (6 mM) catalyzed by **azpy**•Ru^{II}•(H_2O)•**tpy** (**47**, 5 mol-%, black) and **azpy**•Ru^{II}•(H_2O)•**C24** (**C27**, 5 mol-%, red) in the presence of iodosobenzene diacetate as an oxidant (18 mM) in CD_2Cl_2 (500 μL).

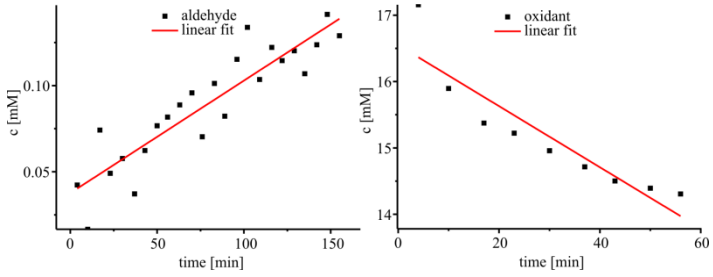

Fig. 182. Linear fittings for aldehyde **62** (left), and iodosobenzene diacetate (right) associated with the catalytic oxidation of alcohol **58** (6 mM) using **azpy**•Ru^{II}•(H_2O)•**tpy** (**47**, 5 mol-%) in the presence of iodosobenzene diacetate as an oxidant (18 mM) in CD_2Cl_2 (500 μL).

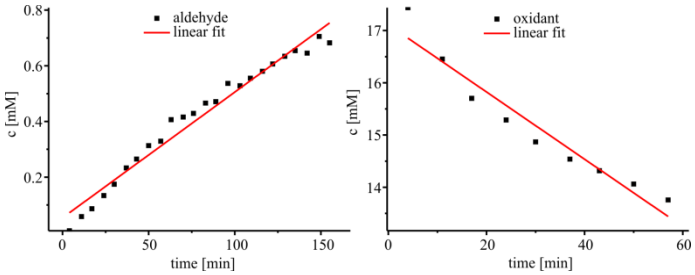

Fig. 183. Linear fittings for aldehyde **62** (left), and iodosobenzene diacetate (right) associated with the catalytic oxidation of alcohol **58** (6 mM) using **azpy**•Ru^{II}•(H_2O)•**C24** (**C27**, 5 mol-%) in the presence of iodosobenzene diacetate as an oxidant (18 mM) in CD_2Cl_2 (500 µL).

Table 20. Reaction rates derived from **Fig. 182** and **Fig. 183**.

Recorded reaction components	**47** (5 mol-%)		**C27** (5 mol-%)	
	rate [µM/min]	R^2	rate [µM/min]	R^2
aldehyde **62**	0.7	0.809	5	0.969
iodosobenzene diacetate	46	0.810	64	0.922

Oxidation of alcohol **60**:

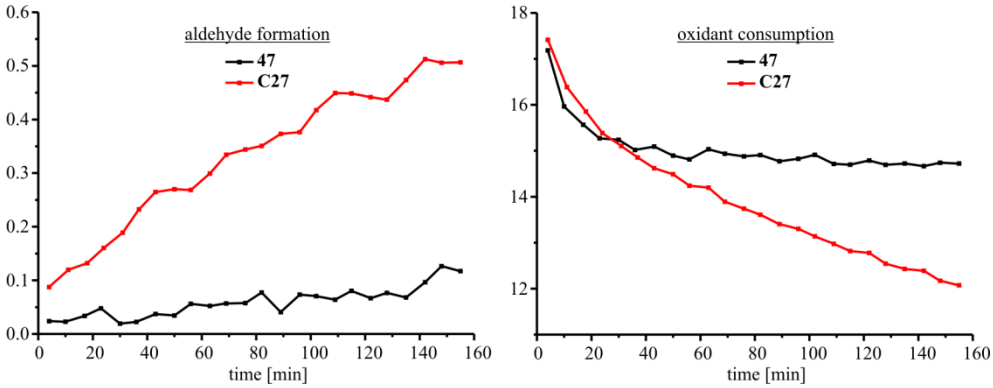

Fig. 184. Plots of changes in the concentration of the aldehyde **64** produced in the oxidation of the alcohol **60** (6 mM) catalyzed by **azpy**•Ru^{II}•(H_2O)•**tpy** (**47**, 5 mol-%, black) and **azpy**•Ru^{II}•(H_2O)•**C24** (**C27**, 5 mol-%, red) in the presence of iodosobenzene diacetate as an oxidant (18 mM) in CD_2Cl_2 (500 µL).

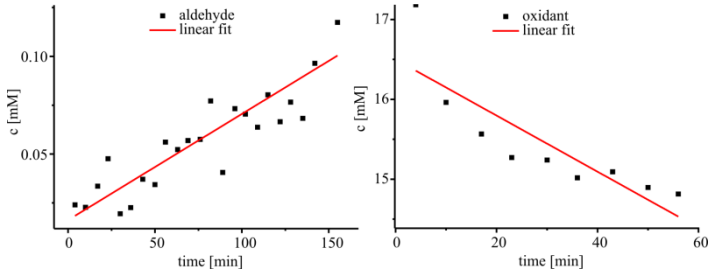

Fig. 185. Linear fittings for aldehyde **64** (left), and iodosobenzene diacetate (right) associated with the catalytic oxidation of alcohol **60** (6 mM) using **azpy**•Ru^{II}•(H_2O)•**tpy** (**47**, 5 mol-%) in the presence of iodosobenzene diacetate as an oxidant (18 mM) in CD_2Cl_2 (500 µL).

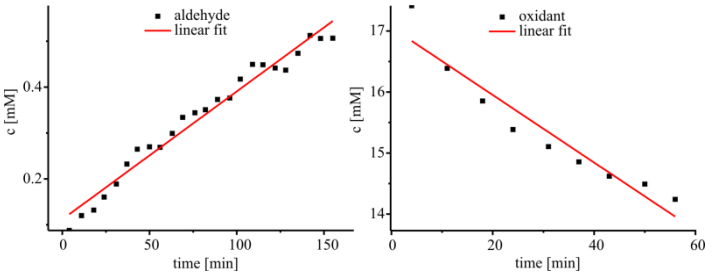

Fig. 186. Linear fittings for aldehyde **64** (left), and iodosobenzene diacetate (right) associated with the catalytic oxidation of alcohol **60** (6 mM) using **azpy**•Ru^{II}•(H_2O)•**C24** (**C27**, 5 mol-%) in the presence of iodosobenzene diacetate as an oxidant (18 mM) in CD_2Cl_2 (500 μL).

Table 21. Reaction rates derived from **Fig. 185** and **Fig. 186**.

Recorded reaction components	**47** (5 mol-%)		**C27** (5 mol-%)	
	rate [μM/min]	R^2	rate [μM/min]	R^2
aldehyde **64**	0.5	0.777	3	0.969
iodosobenzene diacetate	35	0.685	55	0.904

4.6 References and notes

[1] J.-M. Lehn, *Angew. Chem., Int. Ed. Engl.*, 1988, **27**, 89-112.
[2] A. R. Renslo, D. M. Rudkevich and J. Rebek, *J. Am. Chem. Soc.*, 1999, **121**, 7459-7460.
[3] C. Gibson and J. Rebek, *Org. Lett.*, 2002, **4**, 1887-1890.
[4] S. D. Starnes, D. M. Rudkevich and J. Rebek, *Org. Lett.*, 2000, **2**, 1995-1998.
[5] S. D. Starnes, D. M. Rudkevich and J. Rebek, *J. Am. Chem. Soc.*, 2001, **123**, 4659-4669.
[6] S. Richeter and Rebek, *J. Am. Chem. Soc.*, 2004, **126**, 16280-16281.
[7] F. H. Zelder and J. Rebek Jr, *Chem. Commun.*, 2006, 753-754.
[8] S. Korom and P. Ballester, *Eur. J. Org. Chem.*, 2014, **2014**, 4276-4282.
[9] K. E. Djernes, O. Moshe, M. Mettry, D. D. Richards and R. J. Hooley, *Org. Lett.*, 2012, **14**, 788-791.
[10] C. Bruneau and P. H. Dixneuf, *Ruthenium Catalysts and Fine Chemistry*, Springer Berlin Heidelberg, Berlin 2004.
[11] R. A. Krause and K. Krause, *Inorg. Chem.*, 1980, **19**, 2600-2603.
[12] J. S. Dewar, *Bull. Soc. Chim. Fr.*, 1951, **18**, C71-C79.
[13] J. Chatt and L. A. Duncanson, *J. Chem. Soc.*, 1953, 2939-2947.
[14] J. Chatt, L. A. Duncanson and L. M. Venanzi, *J. Chem. Soc.*, 1955, 4456-4460.
[15] C. Eskenazi, G. Balavoine, F. Meunier and H. Riviere, *J. Chem. Soc., Chem. Commun.*, 1985, 1111-1113.
[16] M. Okamura, M. Yoshida, R. Kuga, K. Sakai, M. Kondo and S. Masaoka, *Dalton Trans.*, 2012, **41**, 13081-13089.
[17] L. Vaquer, P. Riente, X. Sala, S. Jansat, J. Benet-Buchholz, A. Llobet and M. A. Pericas, *Catal. Sci. Tech.*, 2013, **3**, 706-714.

[18] T. R. Cundari and R. S. Drago, *Inorg. Chem.*, 1990, **29**, 487-493.
[19] A. D. Chowdhury, A. Das, I. K, S. M. Mobin and G. K. Lahiri, *Inorg. Chem.*, 2011, **50**, 1775-1785.
[20] C.-M. Che and J.-S. Huang, *Chem. Commun.*, 2009, 3996-4015.
[21] G. Balavoine, C. Eskenazi, F. Meunier and H. Rivière, *Tetrahedron Lett.*, 1984, **25**, 3187-3190.
[22] J. T. Groves and R. Quinn, *J. Am. Chem. Soc.*, 1985, **107**, 5790-5792.
[23] J. C. Dobson, W. K. Seok and T. J. Meyer, *Inorg. Chem.*, 1986, **25**, 1513-1514.
[24] C. L. Bailey and R. S. Drago, *J. Chem. Soc., Chem. Commun.*, 1987, 179-180.
[25] G. A. Barf and R. A. Sheldon, *J. Mol. Catal. A: Chem.*, 1995, **102**, 23-39.
[26] H. Nishiyama and Y. Motoyama, *Chem. Commun.*, 1997, 1863-1864.
[27] B. A. Moyer, M. S. Thompson and T. J. Meyer, *J. Am. Chem. Soc.*, 1980, **102**, 2310-2312.
[28] R. R. Gagne and D. N. Marks, *Inorg. Chem.*, 1984, **23**, 65-74.
[29] J. G. Muller, J. H. Acquaye and K. J. Takeuchi, *Inorg. Chem.*, 1992, **31**, 4552-4557.
[30] M. G. Bhowon, H. L. K. Wah and R. Narain, *Polyhedron*, 1998, **18**, 341-345.
[31] A. Miyata, M. Murakami, R. Irie and T. Katsuki, *Tetrahedron Lett.*, 2001, **42**, 7067-7070.
[32] Z. W. Yang, Q. X. Kang, F. Quan and Z. Q. Lei, *J. Mol. Catal. A: Chem.*, 2007, **261**, 190-195.
[33] D. A. Baldwin, A. B. P. Lever and R. V. Parish, *Inorg. Chem.*, 1969, **8**, 107-115.
[34] R. A. Fallahpour, *Synthesis*, 2000, 1665-1667.
[35] C. M. Amb and S. C. Rasmussen, *J. Org. Chem.*, 2006, **71**, 4696-4699.
[36] G. Ulrich, S. Bedel, C. Picard and P. Tisnès, *Tetrahedron Lett.*, 2001, **42**, 6113-6115.
[37] P. Amrhein, A. Shivanyuk, D. W. Johnson and J. Rebek, *J. Am. Chem. Soc.*, 2002, **124**, 10349-10358.
[38] A. R. Renslo, F. C. Tucci, D. M. Rudkevich and J. Rebek, *J. Am. Chem. Soc.*, 2000, **122**, 4573-4582.
[39] P. A. Adcock, F. R. Keene, R. S. Smythe and M. R. Snow, *Inorg. Chem.*, 1984, **23**, 2336-2343.
[40] B. Mondal, M. G. Walawalkar and G. Kumar Lahiri, *J. Chem. Soc., Dalton Trans.*, 2000, 4209-4217.
[41] *cis*- and *trans*- refer to the position phenyl group from the coordinated **azpy** (**42**) ligand relative to the monodentate ligand (Cl or H_2O).
[42] A.-J. DiMaio, A. L. Rheingold, T. T. Chin, D. T. Pierce and W. E. Geiger, *Organometallics*, 1998, **17**, 1169-1176.
[43] J. Meinwald, S. S. Labana and M. S. Chadha, *J. Am. Chem. Soc.*, 1963, **85**, 582-585.
[44] K. Maruoka, T. Ooi and H. Yamamoto, *Tetrahedron*, 1992, **48**, 3303-3312.
[45] Y. Kita, S. Kitagaki, Y. Yoshida, S. Mihara, D.-F. Fang, M. Kondo, S. Okamoto, R. Imai, S. Akai and H. Fujioka, *J. Org. Chem.*, 1997, **62**, 4991-4997.

[46] H. O. House, *J. Am. Chem. Soc.*, 1955, **77**, 3070-3075.
[47] B. Rickborn and R. M. Gerkin, *J. Am. Chem. Soc.*, 1971, **93**, 1693-1700.
[48] R. Sudha, K. Malola Narasimhan, V. Geetha Saraswathy and S. Sankararaman, *J. Org. Chem.*, 1996, **61**, 1877-1879.
[49] B. C. Ranu and U. Jana, *J. Org. Chem.*, 1998, **63**, 8212-8216.
[50] S. Kulasegaram and R. J. Kulawiec, *J. Org. Chem.*, 1997, **62**, 6547-6561.
[51] S. Kulasegaram and R. J. Kulawiec, *Tetrahedron*, 1998, **54**, 1361-1374.
[52] G. Jiang, J. Chen, H.-Y. Thu, J.-S. Huang, N. Zhu and C.-M. Che, *Angew. Chem., Int. Ed. Engl.*, 2008, **47**, 6638-6642.
[53] N. C. Pramanik and S. Bhattacharya, *Transition Met. Chem. (London)*, 1997, **22**, 524-526.
[54] J. J. Concepcion, M.-K. Tsai, J. T. Muckerman and T. J. Meyer, *J. Am. Chem. Soc.*, 2010, **132**, 1545-1557.
[55] L. Duan, F. Bozoglian, S. Mandal, B. Stewart, T. Privalov, A. Llobet and L. Sun, *Nature Chem.*, 2012, **4**, 418-423.
[56] L. Wang, L. Duan, Y. Wang, M. S. G. Ahlquist and L. Sun, *Chem. Commun.*, 2014, **50**, 12947-12950.
[57] Addition of 1 equiv. of *n*-BuLi by carrying reaction at -78 °C affords *Z*-alkene as a kinetic product (classical Wittig reaction), while addition of excess of base or salts or carrying reaction at room temperature affords *E*-alkene as a thermodynamic product (Schlosser modification).
[58] A. C. Gelebe and P. T. Kaye, *Synth. Commun.*, 1996, **26**, 4459-4475.
[59] A.-K. C. Schmidt and C. B. W. Stark, *Org. Lett.*, 2011, **13**, 4164-4167.
[60] E. L. Lebeau and T. J. Meyer, *Inorg. Chem.*, 1999, **38**, 2174-2181.
[61] M. Bressan and A. Morvillo, *Inorg. Chem.*, 1989, **28**, 950-953.
[62] T. Leung, B. R. James and D. Dolphin, *Inorg. Chim. Acta*, 1983, **79**, 180-181.
[63] B. P. Sullivan, J. M. Calvert and T. J. Meyer, *Inorg. Chem.*, 1980, **19**, 1404-1407.

APPENDIX

5.1 Synthesis of cavitand precursors

1,2-difluoro-4,5-dinitrobenzene[1]

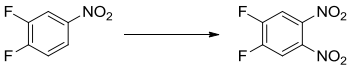

The fumic nitric acid (30 mL, 701 mmol) was poured into single-neck 1 L flask. The flask was equipped with magnetic stirrer and cooled down using ice-bath with salt, followed by careful addition of the fumic sulfuric acid - oleum (35 mL, 882 mmol). Then, 1,2-difluoro-4-nitrobenzene (10.0 mL, 90 mmol) was slowly and carefully added, followed by flask connection to long water-cooled condenser and on top of it Dewar-freeze gas trap with liquid nitrogen cooling. The reaction mixture was slowly warmed up to 60 ºC when bubbling of the reaction mixture starts. The temperature was maintained with ice between 63 - 66 ºC until bubbling stopped. Then, temperature was slowly raised and kept in the range of 70 - 72 ºC (at this point reaction can become highly exothermic, and if temperature is not maintained, it can abruptly increase to or above 100 ºC with rapid release of nitrogen dioxide). Once temperature stabilized, the water bath was changed with the oil bath and reaction carried out at 100 °C overnight. The reaction mixture was cooled to room temperature and obtained reaction mixture carefully poured over ice. The white solid was collected by filtration, rinsed with water, dissolved in ethyl acetate, dried over anhydrous magnesium sulfate and after solvent removal dried over phosphorous pentoxide (9.0526 g, 44.4 mmol, 49.5%). ^{1}H NMR (400 MHz, $CDCl_3$): δ = 7.83 (t, *J* = 7.5 Hz, 2H) ppm. ^{19}F NMR (376 MHz, $CDCl_3$): δ = -122.62 ppm.

Resorcin[4]arene[2]

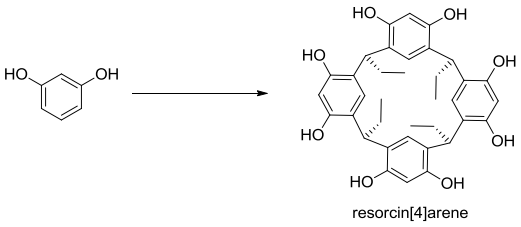

In the 1 L two-neck flask, resorcinol (66 g, 587 mmol) was dissolved in absolute ethanol (300 mL). To this solution, water (300 mL) and concentrated hydrochloric acid (150 mL) were added. The flask was purged with nitrogen and reaction mixture stirred while adding propanal drop-wise (36 mL, 875 mmol), followed by overnight stirring at the room temperature. Next day, the temperature was increased to 75 °C and reaction carried out for 2 h, followed by stirring at the room temperature for the next 4 days. The precipitate was collected by filtration, rinsed with 1:1 mixture of water and ethanol, dried on air and then in vacuum over phosphorous pentoxide (62.8176 g, 105 mmol, 71.2%). ^{1}H NMR (500

MHz, acetone-d_6): δ = 8.41 (s, 8H), 7.54 (s, 4H), 6.23 (s, 4H), 4.18 (t, *J* = 8.0 Hz, 4H), 2.31 (p, *J* = 7.3 Hz, 8H), 0.90 (t, *J* = 7.2 Hz, 12H) ppm.

Octanitro cavitand C6[3]

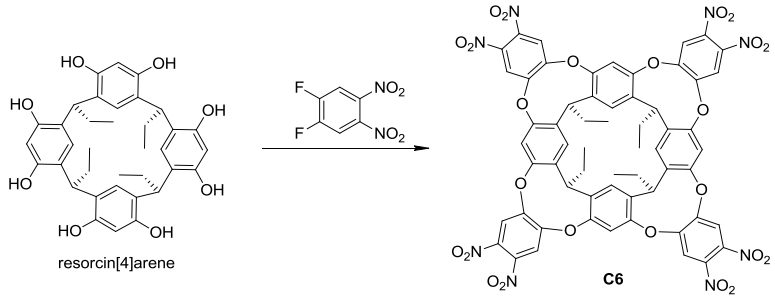

Under nitrogen atmosphere, dry resorcin[4]arene (1.2010 g, 2.000 mmol) and dry 1,2-difluoro-3,4-dinitrobenzene (1.7960 g, 8.800 mmol) were dissolved in anhydrous dimethylformamide (40 mL). To this solution anhydrous triethylamine (2.7 mL, 19.360 mmol) was added drop-wise. The solution was stirred at 120 °C for 3 days. The reaction mixture was poured into the water and the precipitate collected by filtration. The pale-yellow solid of the octanitro cavitand **C6** was rinsed with methylene chloride and small amount of acetone followed by overnight drying in vacuum (1.5516 g, 1.234 mmol, 61.7%). ^{1}H NMR (400 MHz, acetone-d_6): δ = 8.12 (s, 8H), 7.39 (s, 4H), 7.34 (s, 4H), 4.22 (s, 4H), 2.26 (s, 8H), 0.90 (t, *J* = 7.1 Hz, 12H) ppm.

Octaamide cavitand C5[4,5]

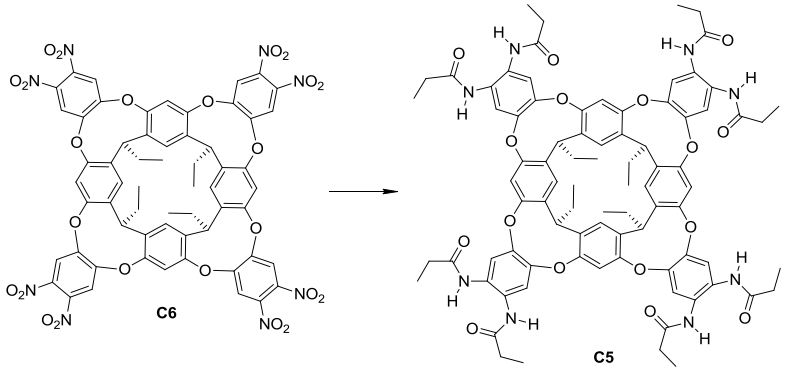

The octanitro cavitand **C6** (0.4 g, 0.318 mmol) and tin(II) chloride dihydrate (2.8 g, 12.410 mmol) were dissolved in absolute ethanol (15 mL) followed by addition of concentrated hydrochloric acid (8 mL) mixed with absolute ethanol (15 mL). The reaction mixture was purged with nitrogen and refluxed overnight. The ethanol was evacuated and to white slurry added ethyl acetate (50 mL), followed by slow addition of water solution

(40 mL) of potassium carbonate (7 g, 50.600 mmol) till carbon dioxide evolved. Finally, the additional amount of water solution (20 mL) of potassium carbonate (2 g) was added followed by drop-wise addition of propionyl chloride (1.5 mL, 16.920 mmol). The reaction mixture was stirred vigorously for one hour, followed by additional potion of propionyl chloride (1 mL, 11.280 mmol) and then stirring overnight. The organic phase was extracted, solution dried over anhydrous magnesium sulfate and product purified by flash chromatography on silica. Elution was performed first with pure methylene chloride, followed by ethyl acetate gradient 0 - 15% and isocratic elution with 15% of ethyl acetate (414.1 mg, 0.283 mmol, 89%). ^{1}H NMR (500 MHz, acetone-d_6): δ = 9.48 (s, 8H), 7.89 (s, 4H), 7.71 (s, 8H), 7.50 (s, 4H), 5.69 (t, *J* = 8.3 Hz, 4H), 2.48 (m, 24H), 1.22 (t, *J* = 7.6 Hz, 24H), 0.99 (t, *J* = 7.2 Hz, 12H) ppm.

Hexanitrodiol cavitand C7[6,7]

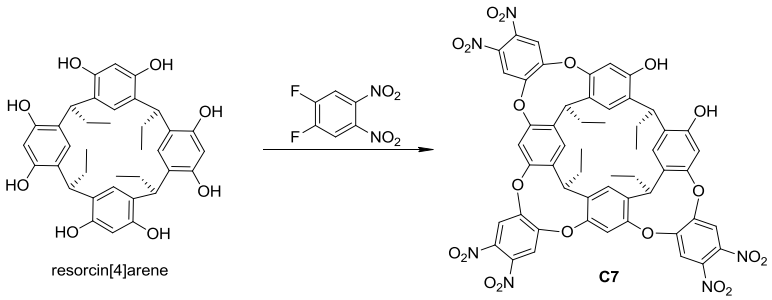

The dry resorcin[4]arene (1.5 g, 2.497 mmol) and dry 1,2-difluoro-3,4-dinitrobenzene (1.5 g, 7.350 mmol) were dissolved in anhydrous dimethylformamide (100 mL) under nitrogen atmosphere. Then, anhydrous triethylamine (2.3 mL, 16.490 mmol) was added drop-wise and reaction carried out at 85 ºC overnight. Dimethylformamide was evacuated, crude material triturated with methanol and solid separated by filtration. The octanitro cavitand (1.1399 g, 0.907 mmol, 36.3%) byproduct was separated from the precipitate by washing the remaining cavitands with methylene chloride and small amount of acetone. The collected solution contained the desired hexanitrodiol cavitand **C7** and was isolated from the mixture by flash chromatography on silica, eluting remaining octanitro cavitand with pure methylene chloride followed by 2% of ethyl acetate to elute desired product as a yellow solid (747.6 mg, 0.684 mmol, 27.5%). ^{1}H NMR (300 MHz, CD_2Cl_2): δ = 7.73 (s, 2H), 7.70 (s, 2H), 7.69 (s, 2H), 6.98 (s, 2H), 6.88 (s, 1H), 6.74 (s, 1H), 6.66 (s, 2H), 6.02 (s, 2H), 4.25 (t, *J* = 7.6 Hz, 1H), 3.91 (t, *J* = 7.5 Hz, 3H), 2.13 (d, *J* = 14.0 Hz, 8H), 1.04 - 0.83 (m, 12H) ppm.

Hexaamidediol cavitand C4[6,7]

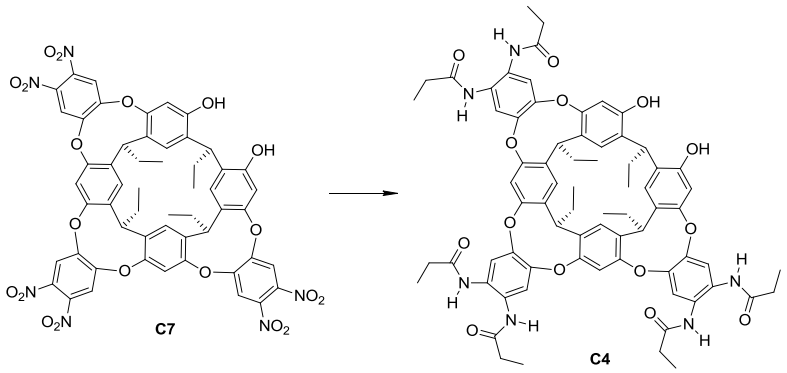

The hexanitrodiol cavitand **C7** (2 g, 1.830 mmol) and tin(II) chloride dihydrate (8.5 g, 37.7 mmol) were dissolved in a mixture made of absolute ethanol (115 mL) and concentrated hydrochloric acid (30 mL). The reaction mixture was stirred in nitrogen atmosphere at 70 °C overnight. The ethanol was evacuated and to obtained white slurry added ethyl acetate (350 mL), followed by slow addition of water solution (150 mL) of potassium carbonate (36.7 g, 265 mmol). The propionyl chloride (10.3 mL, 116 mmol) was added using syringe pump over period of 20 min. Reaction was stirred for additional 60 min and organic phase separated. The organic phase was dried over anhydrous magnesium sulfate and solvent evacuated yielding intermediate hexaamidediester cavitand (2.490 g, 1.829 mmol, 100%).

The ester was dissolved in a 1 : 1 mixture of toluene and ethanol (56 mL), followed by addition of hydrazine monohydrate (570 μL, dried over molecular sieves) and heated for 1 h at 70 °C. Volatiles were removed and residue triturated with methylene chloride yielding white precipitate of hexaamidediol cavitand **C4**. The remaining product (from solution after filtration) was isolated by flash chromatography on silica, performing elution with methylene chloride first, followed by gradient 2 - 3.4% of methanol (1.6902 g, 1.353 mmol, 73.9%). ^{1}H NMR (400 MHz, acetone-d_6): δ = 9.54 (s, 2H), 9.47 (s, 2H), 9.34 (s, 1H), 9.08 (s, 2H), 8.89 (s, 1H), 7.87 (s, 2H), 7.73 (s, 2H), 7.68 (s, 2H), 7.66 (s, 2H), 7.62 (s, 2H), 7.49 (s, 2H), 6.76 (s, 2H), 5.71 (t, *J* = 8.3 Hz, 1H), 5.59 (t, *J* = 8.3 Hz, 2H), 4.20 (t, *J* = 8.0 Hz, 1H), 2.61 - 2.18 (m, 20H), 1.30 - 0.79 (m, 30H) ppm.

Hexaamidedinitro cavitand C8[6,7]

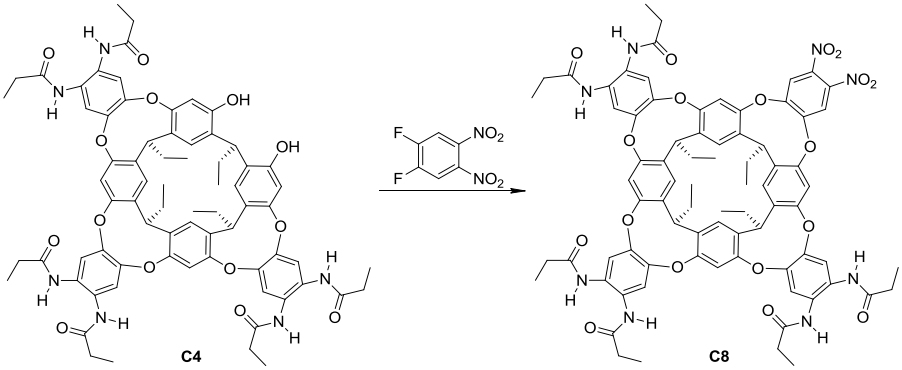

The dry hexaamidediol cavitand **C4** (1 g, 0.800 mmol) and dry 1,2-difluoro-3,4-dinitrobenzene (247 mg, 1.209 mmol) were transferred into 250 mL two-necked flask. The solid mixture was purged with nitrogen followed by addition of anhydrous dimethylformamide (150 mL). Once solids dissolved, dry triethylamine (500 μL, 3.58 mmol) was added and reaction carried out at 85 ºC for 24 h. Dimethylformamide was evacuated, solid residue dissolved in ethyl acetate, washed with hydrochloric acid (1 M) and dried over anhydrous sodium sulfate. The solvent was evacuated and crude material purified by flash chromatography on silica, performing elution with methylene chloride, increasing gradient to 10% ethyl acetate and finally, separating desired product with 20% ethyl acetate. After solvent evacuation, product was isolated as a pale orange solid (1.11 g, 0.785, 98%). ^{1}H NMR (400 MHz, CD_2Cl_2): δ = 9.40 (s, 2H), 9.28 (s, 2H), 8.16 (s, 2H), 8.09 (s, 2H), 7.63 (s, 2H), 7.54 (s, 4H), 7.37 (s, 2H), 7.34 (s, 2H), 7.33 (s, 2H), 7.26 (s, 2H), 5.68 (dt, *J* = 16.7, 8.3 Hz, 3H), 5.50 (t, *J* = 8.2 Hz, 1H), 2.53 - 2.21 (m, 20H), 1.27 - 1.17 (m, 18H), 1.08 - 0.94 (m, 12H) ppm.

Open-hexaamidemononitro cavitand C21[8]

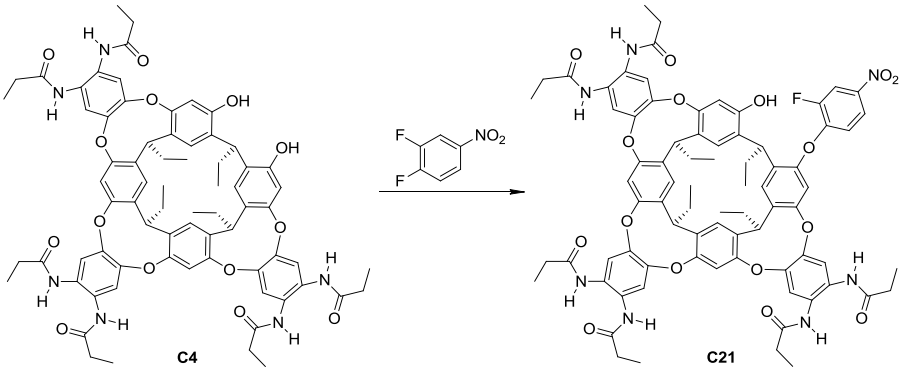

Under nitrogen atmosphere, dry hexaamidediol cavitand **C4** (570.0 mg, 0.456 mmol) and 1,2-difluoro-4-nitrobenzene (350 μL, 0.503 mmol) were dissolved in anhydrous dimethylformamide (14 mL). The solution was stirred at 60 °C for few minutes, followed by addition of dry triethylamine (1 mL, 0.726 mmol) and stirring reaction mixture for 16 h. The solvent was evacuated and the product purified by flash chromatography on silica applying gradient 10 - 30% ethyl acetate in methylene chloride. The open-hexaamidemononitro cavitand **C21** was isolated as a white solid (620.1 mg, 0.447 mmol, 98%). ^{1}H NMR (400 MHz, $CDCl_3$): δ = 9.64 (s, 1H), 9.43 (s, 1H), 9.34 (s, 1H), 9.18 (s, 1H), 8.15 (s, 1H), 8.09 (dd, *J* = 10.0, 2.6 Hz, 1H), 7.96 (s, 1H), 7.91 (s, 1H), 7.90 (s, 1H), 7.67 (s, 1H), 7.66 (s, 1H), 7.46 (s, 1H), 7.42 (s, 1H), 7.39 (s, 1H), 7.35 (s, 1H), 7.29 (s, 1H), 7.28 (s, 1H), 7.18 (s, 1H), 7.16 (s, 1H), 6.85 (s, 1H), 6.85 - 6.73 (m, 1H), 6.64 (s, 1H), 6.38 (s, 1H), 5.75 (t, *J* = 8.4 Hz, 1H), 5.68 (t, *J* = 8.3 Hz, 1H), 5.59 (t, *J* = 8.2 Hz, 1H), 4.19 (t, *J* = 8.0 Hz, 1H), 2.56 - 2.11 (m, 20H), 1.32 - 1.11 (m, 15H), 1.01 (ddt, *J* = 28.3, 10.4, 7.4 Hz, 12H), 0.86 (t, *J* = 7.2 Hz, 3H) ppm. ^{19}F NMR (376 MHz, $CDCl_3$): δ = -120.90 ppm.

Hexaamidemononitro cavitand C22[8]

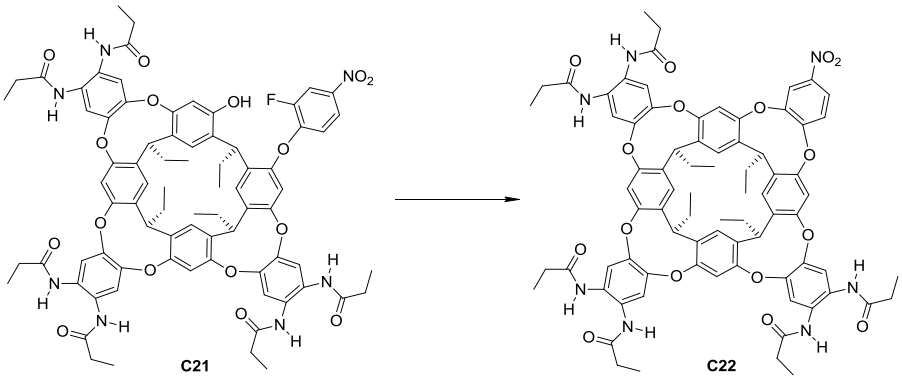

Under nitrogen atmosphere, the open-hexaamidemononitro cavitand **C21** (620.1 mg, 0.447 mmol) and dry cesium carbonate (450 mg, 1.369 mmol) were dissolved in anhydrous dimethylformamide (16 mL) and stirred at 60 °C for 16 h. The solvent was evacuated, residue dissolved in methylene chloride and washed with hydrochloric acid solution (40 mL, 0.1 M). The aqueous phase was extracted twice with methylene chloride, and combined organic phases dried with anhydrous sodium sulfate. The solvent was evacuated and product purified by flash chromatography on silica eluting product with 1% methanol in methylene chloride (427.8 mg, 0.313 mmol, 68.5% calculated on hexaamidediol cavitand **C4**). ^{1}H NMR (400 MHz, $CDCl_3$): δ = 9.80 (s, 1H), 9.74 (s, 1H), 9.05 (s, 1H), 8.96 (s, 1H), 8.58 (s, 1H), 8.20 (d, *J* = 2.8 Hz, 1H), 8.07 (d, *J* = 9.1 Hz, 1H), 8.00 (s, 1H), 7.98 (s, 2H), 7.85 (dd, *J* = 9.0, 2.8 Hz, 1H), 7.81 (s, 1H), 7.78 (s, 1H), 7.74 (s, 1H), 7.44 (s, 1H), 7.32 (s, 1H), 7.27 (s, 1H), 7.25 (s, 1H), 7.22 (s, 1H), 7.20 (s, 1H), 7.20 (s, 1H), 7.17 (s, 1H), 7.15 (s, 1H), 5.68 (t, *J* = 8.4 Hz, 1H), 5.64 (t, *J* = 8.2 Hz, 1H), 5.62 (t, *J* = 8.4 Hz, 1H), 5.53 (t, *J* =

8.3 Hz, 1H), 2.54 (q, *J* = 7.6 Hz, 2H), 2.51 - 2.17 (m, 18H), 1.30 - 1.16 (m, 18H), 0.99 (dtd, *J* = 13.6, 7.4, 3.2 Hz, 12H) ppm.

5.2 References and notes

[1] Z. Kazimierczuk, L. Dudycz, R. Stolarski and D. Shugar, *J. Carb.-Nucleos.-Nucl.*, 1981, **8**, 101-117.
[2] L. M. Tunstad, J. A. Tucker, E. Dalcanale, J. Weiser, J. A. Bryant, J. C. Sherman, R. C. Helgeson, C. B. Knobler and D. J. Cram, *J. Org. Chem.*, 1989, **54**, 1305-1312.
[3] D. J. Cram, H. J. Choi, J. A. Bryant and C. B. Knobler, *J. Am. Chem. Soc.*, 1992, **114**, 7748-7765.
[4] D. M. Rudkevich, G. Hilmersson and J. Rebek, *J. Am. Chem. Soc.*, 1998, **120**, 12216-12225.
[5] M. A. Sarmentero and P. Ballester, *Org. Biomol. Chem.*, 2007, **5**, 3046-3054.
[6] A. R. Renslo, F. C. Tucci, D. M. Rudkevich and J. Rebek, *J. Am. Chem. Soc.*, 2000, **122**, 4573-4582.
[7] P. Amrhein, A. Shivanyuk, D. W. Johnson and J. Rebek, *J. Am. Chem. Soc.*, 2002, **124**, 10349-10358.
[8] O. B. Berryman, A. C. Sather, A. Lledó and J. Rebek, *Angew. Chem., Int. Ed.*, 2011, **50**, 9400-9403.